UNIVERSITY OF OKLAHOMA

GRADUATE COLLEGE

POLARIMETRIC RADAR OBSERVATIONS AND NUMERICAL SIMULATIONS OF TORNADIC DEBRIS

A DISSERTATION

SUBMITTED TO THE GRADUATE FACULTY

in partial fulfillment of the requirements for the

Degree of

DOCTOR OF PHILOSOPHY

By

DAVID JOSEPH BODINE
Norman, Oklahoma
2014

POLARIMETRIC RADAR OBSERVATIONS AND NUMERICAL SIMULATIONS OF TORNADIC DEBRIS

A DISSERTATION APPROVED FOR THE SCHOOL OF METEOROLOGY

By

Dr. Robert D. Palmer

Dr. Michael I. Biggerstaff

Dr. Howard B. Bluestein

Dr. Pamela L. Heinselman

Dr. Mark B. Yeary

Dedication

This dissertation is dedicated to my late grandparents, Walt Bodine and Warren Hannon, for being great role models, instilling a strong work ethic in me, encouraging my interest in meteorology, and leaving an indelible impression on my life.

Acknowledgements

I would like to thank my Ph.D. advisor, Dr. Robert Palmer, for his excellent mentoring and advice, and the opportunities he gave me throughout my graduate education. I appreciate the freedom he gave me to pursue research topics which interested me, and the opportunities to participate in interesting projects ranging from building a unique phased array radar to leading field projects. Dr. Palmer encouraged me to pursue a cross-disciplinary education in meteorology and engineering, which helped me cultivate a valuable skill set and a deeper appreciation for the engineering underlying weather radar systems. Finally, he encouraged me to pursue a research experience in Japan that was very rewarding intellectually and personally. I look forward to continuing our collaboration throughout my career.

I am grateful to my doctoral committee members, Dr. Michael Biggerstaff, Dr. Howard Bluestein, Dr. Pamela Heinselman, and Dr. Mark Yeary, for their excellent guidance and feedback. I enjoyed long conversations with Dr. Biggerstaff and appreciate his advice about research, teaching and scientific funding. I also enjoyed the opportunities to work with him during VORTEX-2 and the Hurricane Irene deployment, both of which were quite memorable. Dr. Bluestein provided a great foundation for my education, serving as an instructor in four different courses (perhaps setting a record). Watching videos of Dr. Bluestein's research groups collecting radar data also motivated my interest in radar and mesoscale studies. I am grateful to Dr. Pamela Heinselman for her mentoring,

and her willingness to provide career advice and insight. I benefited greatly from working with her during my Master's degree, and continued to enjoy our collaborations and discussions throughout the Ph.D. I have enjoyed sharing an office corridor with Dr. Mark Yeary. He has always given useful advice for research or career-related questions, for which I am grateful.

The SoM faculty provided a great undergraduate and graduate education, and I would like to thank the SoM staff for their hard work. I am grateful to Dr. Petra Klein for giving me an opportunity to conduct research with her as an undergraduate, which helped cultivate my research skills and accelerate my progress as a graduate student. Dr. Alan Shapiro has been a great resource for advice, an excellent instructor, and a terrific liaison and advocate for the students. Dr. Mark Laufersweiler was a great resource for both computing help and interesting discussions on a variety of topics. I would like to thank Celia Jones, Marcia Pallutto, Becky Steely, Nancy Campbell, and Christie Upchurch for their assistance throughout my time at OU, and for many enjoyable conversations.

I would like to thank several ARRC scientists, engineers and staff for their efforts, which have facilitated the research activities conducted in this Dissertation. Dr. Boon Leng Cheong has been a great resource throughout my graduate education for helpful discussions about polarimetric radar, numerical simulations and computing issues. Redmond Kelley and John Meier are thanked for their tremendous efforts in maintaining the ARRC radars, allowing us to collect great data sets with OU-PRIME and the AIR. Finally, I appreciate the assistance of

ARRC staff, Krysta Bruehl, Jo Ann Mehl, and Lauren White, for their great effort and patience, which has made life as an ARRC student much easier.

I would like to thank Dr. Takashi Maruyama for supervising my six-month stay at Kyoto University, and enabling a great educational, professional, and personal experience. I appreciate his effort in helping me understand the numerical simulation process for LES, and the time he devoted to making arrangements for my stay. I also enjoyed the lunches and dinners with Professor Maruyama, his insights into Japanese culture, and the lab trip to Kyushu. I enjoyed getting to know the Japanese students in Professor Maruyama's lab, Junya Okazaki, Mayuko Hanatani, and Naoko Tamura. I am grateful for the opportunity to meet several international students as well. I look forward to continuing my collaborations with Professor Maruyama in the future.

Discussions with Jim Kurdzo, Chris Schwarz, Dr. Matt Kumjian, Dr. Brad Isom, Feng Nai, Dr. Qing Cao, Gabe Garfield, Dan Betten, Dr. Jeff Snyder, Dr. Robin Tanamachi, and many others have been helpful and enjoyable. In particular, I have enjoyed sharing an office with Jim Kurdzo and having an excellent scientist with whom I can discuss various science and engineering topics. Discussions with Dr. Kim Elmore on statistics and Dr. Alexander Ryzhkov on polarimetric radar were helpful and enlightening.

Funding for this research was provided by NSF grants ATM-0750790, AGS-1303685, and IIA-1209444. OU-PRIME was maintained by Redmond Kelley,

John Meier, Dr. Boon Leng Cheong, and several other engineers, whose efforts contributed to providing high-quality data. The National Weather Service Weather Forecast Office is also thanked (Doug Speheger and Greg Stumpf, in particular) for providing high-resolution damage surveys which were critical to many analyses herein.

I thank my roommates Pat, Darrel and Boomer for putting up with me for four years, and for many great late-night ice cream trips to Braum's. I also thank my girlfriend, Christina Tippy, for her support and understanding throughout the Dissertation writing process. Bruce Thomas has been a great mentor and friend, and provided an internship in high school that was a turning point for my education and career path.

Finally, I am grateful to my family for their support over the past decade. They enabled me pursue my dream of studying meteorology at OU and obtain a Ph.D., and rarely complained about me watching the Weather Channel too much as a child. I thank my parents, Tom and Ellen Bodine, for their endless love, support and encouragement, and for being the best parents anyone could hope to have.

Table of Contents

List Of Tables

List Of Figures

Abstract

Tornadic debris are critical aspects of tornado studies because airborne debris pose significant threats to life and property, and debris often dominate backscattered radar signals, causing biased Doppler velocity measurements. Polarimetric radar offers new research opportunities because debris produce a unique polarimetric radar signature called the tornadic debris signature (TDS). In this study, new applications of TDSs are examined using Transmission (T) matrix calculations, polarimetric radar observations, and numerical simulations. To illuminate electromagnetic scattering characteristics of different debris types, T-matrix calculations are presented. While most TDS studies have focused on tornado detection, this study conducts a detailed analysis of 14 TDS cases to determine relationships between TDS parameters and EF-rating. As tornado EF-rating increases, 90th percentile radar reflectivity factor, TDS height, and TDS volume increase, and 10th percentile co-polar cross-correlation coefficient and differential reflectivity decrease. While the TDS parameter analysis focuses on a single radar frequency, debris scattering characteristics vary depending on radar frequency, and thus multiple frequency polarimetric radar observations may provide new information about debris. In a statistical analysis of dual-wavelength TDSs, higher radar reflectivity factor and lower co-polar cross-correlation coefficient are observed at S band compared to C band, and negative differential reflectivity is sometimes observed simultaneously at both frequencies.

Multiple frequency radar observations have additional utility in determining debris concentrations to assess debris loading impacts. To simulate polarimetric radar signatures, tornado vortices are simulated in a Large-Eddy Simulation (LES) model with a drag force coupling parameterization based on debris trajectories, enabling momentum exchange between air and debris. As debris loading increases, simulations reveal decreasing near-surface radial, tangential and vertical velocities in the lowest grid cell. Further increases in debris loading cause greater reductions in near-surface velocities and reduced tornado core tangential and vertical velocities. Using T-matrix calculations and LES model runs, equivalent radar reflectivity factor and two-way attenuation rates are calculated to determine if equivalent radar reflectivity factor or attenuation provide useful upper-bounds on debris loading. These simulations reveal that if sufficient amounts of debris loading are present to affect tornado dynamics, significant attenuation will occur at W band, in many cases fully attenuating the transmitted radar signal.

Chapter 1

Introduction

Tornadic debris are a critical part of tornado studies because they have significant societal impacts and greatly affect radar measurements of tornadoes. Airborne debris cause most tornado-related fatalities (Bohonos and Hogan 1999), and can increase damage caused by tornadoes. Debris puncturing windows or walls can increase damage by changing the structure's internal pressure leading to greater damage (Minor et al. 1977). The damage potential of extreme wind events is therefore a function of both wind speed and debris loading (Wills et al. 2002). Finally, tornadoes can transport low terminal fall speed debris long distances (Anderson 1985a,b; Snow et al. 1995; Magsig and Snow 1998), in some cases as far as 300 km. Such long-distance debris transport could result in widespread dispersion of hazardous materials if such materials are lofted by tornadoes.

Radar resolution volumes within a tornado may contain a variety of scatterers of varying size, shape, orientation, and composition. Scatterers could be small such as sand particles or rain drops, or large objects such as plywood boards, roof tiles, or tree branches. A photograph of lofted wood boards and other debris in the 19 May 2013 tornado is provided in Fig. 1.1. Because Doppler radars measure the velocity of the scatterers rather than the actual wind speed,

errors are introduced into these Doppler velocity measurements when air-debris velocity differences arise. In tornadoes, debris or hydrometeors are centrifuged radially outward, and have lower tangential and vertical velocities compared to the air velocities (Snow 1984; Dowell et al. 2005). The magnitudes of air-debris velocity differences increase as centrifugal forces on debris increase. For example, centrifugal forces increase for higher wind speeds or smaller tornado diameters, or for higher particle densities and larger diameters (Dowell et al. 2005). These air-debris velocity differences can easily exceed common errors in Doppler velocity data, and can be tens of m s^{-1} for larger debris (Dowell et al. 2005). Debris centrifuging effects increase when velocity retrievals are used to examine flow in secondary circulations in tornadoes (radial-vertical wind components). When integrating the continuity equation in three-dimensional wind retrievals for tornadoes, such as the Ground-Based Velocity Tracking Display (GBVTD; Lee et al. 1999), debris centrifuging effects create velocity retrievals that are excessively divergent and have stronger central downdrafts (Nolan 2013). Thus, air-debris velocity differences must be understood and corrected to accurately interpret Doppler velocity data and obtain accurate three-dimensional velocity retrievals in tornadoes.

Polarimetric radar offers an improved capability to differentiate between meteorological and non-meteorological scatterers (Zrnić and Ryzhkov 1999). Lofted debris from tornadoes are an important subset of non-meteorological scatterers that can be detected using polarimetric radar. Using polarimetric radar data

Figure 1.1: Still frame image from video of the 19 May 2013 Shawnee, Oklahoma EF-4 tornado (image courtesy of Brandon Sullivan). The tornado lofted several large wood boards after passing through a residential area.

from the 3 May 1999 tornado outbreak, Ryzhkov et al. (2002) and Ryzhkov et al. (2005) noted a polarimetric radar signature associated with lofted tornadic debris called the tornadic debris signature (TDS). Tornadic debris have wide distributions of sizes, shapes, compositions, and orientations, which produce electromagnetic scattering characteristics that are markedly different than hydrometeors. Within the TDS, Ryzhkov et al. (2002) and Ryzhkov et al. (2005) observed relatively high horizontal radar reflectivity factor (Z_{HH}), low differential reflectivity (Z_{DR}), and extremely low copolar cross-correlation coefficient (ρ_{HV}). They formulated an initial criteria for tornado detection based on a TDS with $Z_{HH} > 45$ dBZ, $Z_{DR} < 0.5$ dB, and $\rho_{HV} < 0.8$.

Tornado detection was the first application of TDSs (Ryzhkov et al. 2002, 2005), and forecasters have used TDSs to confirm tornadoes (Scharfenberg et al. 2005; Schultz and co-authors 2012a). Because a tornado must be producing damage to cause a TDS, the TDS does not provide any predictive capability of tornadogenesis. However, TDSs at relatively close ranges typically appear within the first volume scan after tornado formation (Ryzhkov et al. 2005; Bodine et al. 2013). Because the radar beam height increases with range, tornado detection at greater ranges becomes more difficult. Bodine et al. (2013) noted several cases of EF-0 and EF-1 tornadoes at ranges of 100 km or greater that did not produce TDSs, likely because insufficient debris was lofted to the 0.5° elevation scan. False TDS detections based on polarimetric debris signatures may also

occur after tornado dissipation because debris continues to fall out (Ryzhkov et al. 2005; Schultz and co-authors 2012b; Bodine et al. 2013).

TDSs have been documented at a wide range of radar wavelengths. Bluestein et al. (2007) investigated polarimetric TDSs using an X-band mobile radar. They observed an increase in Z_{DR} associated with precipitation entrainment in the TDS, and suggested that ρ_{HV} was a better indicator of the TDS compared to Z_{DR}. Kumjian and Ryzhkov (2008) examined nine TDSs associated with tornadoes rated EF-1 or greater, revealing that TDSs did occur with weak tornadoes (although they note that some weak tornadoes may not loft sufficient amounts of debris to produce a TDS). Although video observations of large debris indicate that debris orientations are random, studies have also revealed negative Z_{DR} signatures in TDSs at S, C, and X bands, suggesting the possibility of some degree of common alignment of scatterers (Ryzhkov et al. 2005; Bluestein et al. 2007; Bodine et al. 2011).

In addition to tornado detection, TDSs may also provide useful information about damage characteristics of tornadoes. Ryzhkov et al. (2005) examined three tornado cases from the 3 May 1999 tornado outbreak and found that the maximum TDS area and minimum ρ_{HV} and Z_{DR} occurred during the period of maximum damage. Given the limited sample size of these comparisons, detailed comparisons of TDS parameters with damage surveys are needed for a larger number of cases. In the present study, modified TDS parameters from Ryzhkov

et al. (2005) and new TDS parameters are compared to damage surveys to examine the relationship between surface damage characteristics and the TDS. These new TDS parameters focus on volumetric distributions of debris in tornadoes and the parent thunderstorm. Past studies of long-distance debris transport indicate that debris are transported farther in tornadoes with higher EF-ratings (e.g., Snow et al. 1995), suggesting that debris column volume or height may be related to tornado EF-rating.

While TDS observations have illuminated polarimetric characteristics of tornadic debris, the relationships between debris characteristics (e.g., size, type, or concentration) and polarimetric variables are unknown. If a relationship between debris characteristics and polarimetric radar variables can be developed, it may be possible to develop a debris classification algorithm, which could be used to correct debris centrifuging effects on Doppler velocity data, improve estimates of damage severity using polarimetric radar, and provide measurements of debris loading in tornadoes. To develop a debris classification system, it may be useful to incorporate polarimetric radar observations at multiple frequencies. In this study, an examination of S- and C-band polarimetric radar data from volume scans with close spatial and temporal matching are presented to explore similarities and differences between TDSs at S and C bands.

To simulate polarimetric radar signatures, debris trajectories within a realistic tornado-scale flow are required. In this study, debris trajectories are calculated in a Large-Eddy Simulation (LES) model with a trajectory-based drag

force model parameterization to allow momentum exchange between the air and debris. Gong (2006) and Lewellen et al. (2008) found that large concentrations of sand-sized particles in the corner flow region reduced near-surface radial, tangential and vertical velocities in tornadoes, and reduced tornado core velocities to a lesser extent. In the present study, debris loading experiments are conducted for sand-sized particles using monodispersive particle distributions, and larger debris such as large wood boards. Based on these simulations, Transmission matrix (T-matrix; Waterman 1969, 1971) calculations are performed for sand and wood debris, and equivalent radar reflectivity factor and attenuation patterns at different radar frequencies are calculated for different LES model runs.

In Chapter 2, an overview of electromagnetic scattering and polarimetric radar is presented, including discussions of theoretical values of polarimetric variables for both hydrometeors and debris. The polarimetric radar discussion is followed by a brief overview of aerodynamic characteristics of debris. Chapter 3 examines the application of using TDS parameters to estimate surface damage characteristics. In Chapter 4, S- and C-band polarimetric radar observations from the 10 May 2010 Norman-Moore-Oklahoma City EF-4 tornado are investigated to illuminate similarities and differences between wavelengths. Chapter 5 presents LES model studies of tornadic debris using a trajectory-based drag force feedback parameterization. Equivalent radar reflectivity factor and attenuation

rates are calculated for different sand and soil particle size distributions to develop practical methods for estimating small particle debris loading in tornadoes. Conclusions and recommendations for future work are presented in Chapter 6.

Chapter 2

Background

In this chapter, an overview of electromagnetic scattering is presented and polarimetric radar variables from T-matrix calculations are discussed for hydrometeors and debris. Then, aerodynamic characteristics of different debris types are discussed.

2.1 Polarimetric radar

2.1.1 Electromagnetic scattering of single particles

This section includes a discussion of electromagnetic scattering of individual particles. An overview of the electromagnetic backscattering matrices is presented, followed by a discussion of the scattering characteristics of particles interacting with electromagnetic (EM) waves. A fundamental concept of polarimetric radar is the interaction of EM waves with particles (e.g., hydrometeors or non-meteorological scatterers). Particles can scatter or absorb energy from incident EM waves. For monostatic radar measurements, scattering in the opposite direction of the incident EM wave is particularly important, and is referred to as backscattering.

2.1.1.1 Radar cross-sections

Radar cross-sections describe the scattering and absorption characteristics of individual particles. The general definition of a radar cross-section, σ, is an apparent area that depends on physical characteristics of the scatterer (e.g., size, shape, orientation, composition) and radar properties (e.g., frequency), and describes the amount of energy scattered or absorbed by an object. If the incident power density on the scatterer is S_i, then the power incident on the scatter is σS_i (Doviak and Zrnić 1993). The received power density, S_r, at some radius, r, from the object is,

$$S_r = \frac{S_i \sigma(\hat{s}, \hat{i})}{4\pi r^2}, \tag{2.1}$$

where $\hat{i}$ and $\hat{s}$ denote the unit vector in the direction of the incident and scattered EM wave, respectively (using the vector convention from Bringi and Chandrasekar (2001)). In the isotropic scattering case, the radar cross section is independent of the direction of the incident and scattered EM wave. A classic type of isotropic scattering, called Rayleigh scattering, occurs for scatterers with small diameters, D, compared to the radar wavelength, λ, such that $D < \frac{\lambda}{16}$. For scatterers exhibiting Rayleigh scattering, their scattering cross-section, σ_s, is:

$$\sigma_s = \frac{2}{3}\frac{\pi^5}{\lambda^4} |K_m|^2 D^6, \tag{2.2}$$

where K_m is a function of the complex refractive index $m = n' - jn''$,

$$K_m = \frac{m^2 - 1}{m^2 + 2}. \tag{2.3}$$

The absorption cross-section, σ_a, is expressed as,

$$\sigma_a = \frac{\pi^2}{\lambda} \operatorname{Im}(-K_m) D^3. \tag{2.4}$$

Multiplying (2.2) and (2.4) by the incident power energy S_i, the incident power scattered or absorbed is obtained. Comparing (2.2) and (2.4), it is evident that within the Rayleigh scattering regime $\sigma_a > \sigma_s$. Thus, more incident energy is absorbed than scattered by Rayleigh scatterers.

The prevalence of monostatic radars (i.e., radars with a single antenna for transmitting and receiving) for meteorological observations makes the backscatter cross-section, σ_b, particularly important. The backscatter cross-section has a similar definition to the radar cross-section, except that the scattering direction is specified as the direction opposite of the incident EM wave, so that

$$\sigma_b = \sigma(-\hat{i}, \hat{i}). \tag{2.5}$$

For Rayleigh scatterers, the backscatter cross-section is:

$$\sigma_b = \frac{\pi^5}{\lambda^4} |K_m|^2 D^6. \tag{2.6}$$

Combining (2.1), (2.5), and (2.6), it becomes apparent that received power density changes as a function of D^6 for Rayleigh scatterers. Fig. 2.1 shows the backscatter cross-section of liquid spheres, calculated using (2.6) and Mie scattering calculation codes for homogeneous spheres (Matzler 2002). The Rayleigh approximation and Mie solution for the backscatter cross-section exhibits close agreement for $D < \frac{\lambda}{16}$. The range of sizes where diameters are greater than $\frac{\lambda}{16}$ is called the Mie scattering region, where σ_b and D do not exhibit a monotonic

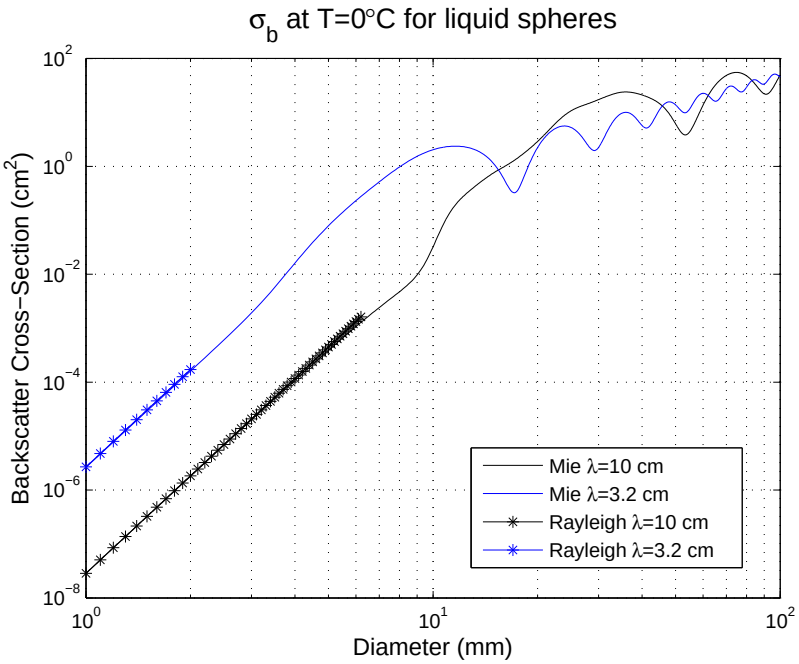

Figure 2.1: Backscatter cross-section (cm^2) at S and X band (black and blue lines, respectively) for liquid spheres at 0°C. The solid lines and solid lines with asterisks show backscatter cross-sections from Mie and Rayleigh scattering calculations, respectively.

relationship, particularly when $D > \lambda$. The oscillating behavior of σ_b occurs because EM waves creep along the surface of the scatterer, and constructively or destructively interfere with EM waves backscattered along the original incidence angle of the transmitted EM wave (often called specular waves), causing higher and lower backscatter cross-sections.

2.1.1.2 Backscattering matrix and complex scattering amplitudes

The backscattering matrix, $\mathbf{S}$, provides another method of determining the scattering characteristics of objects. The elements of the backscattering matrix, S_{ij}, are the complex scattering amplitudes for a given polarization, which relate the incident ($\mathbf{E^i}$) and backscattered ($\mathbf{E^b}$) electric fields (Bickel 1965; McCormick and Hendry 1975, 1985; Doviak and Zrnić 1993). Using the notation from Doviak and Zrnić (1993) for an arbitrary orthogonal polarization, $\mathbf{S}$ is related to the incident ($\mathbf{E^i}$) and backscattered electric fields ($\mathbf{E^b}$) by,

$$\begin{bmatrix} E_1 \\ E_2 \end{bmatrix}^b = \begin{bmatrix} S_{11} & S_{12} \\ S_{21} & S_{22} \end{bmatrix} \begin{bmatrix} E_1 \\ E_2 \end{bmatrix}^i \frac{e^{-jkr}}{r}. \tag{2.7}$$

Linear polarizations are commonly used for weather radar, and are implemented on the Weather Surveillance Radar 1988 Doppler (WSR-88D) radar network (Doviak et al. 2000). For a linearly polarized EM wave,

$$\begin{bmatrix} E_h \\ E_v \end{bmatrix}^b = \begin{bmatrix} S_{hh} & S_{hv} \\ S_{vh} & S_{vv} \end{bmatrix} \begin{bmatrix} E_h \\ E_v \end{bmatrix}^i \frac{e^{-jkr}}{r}, \tag{2.8}$$

where r is the range of the scatterer from the radar antenna and k is the wavenumber of the EM wave. The first (second) subscript in each element of $\mathbf{S}$

corresponds to the polarization of the backscattered (incident) EM waves. The co-polar (diagonal) elements of **S** refer to the complex scattering amplitude along the same direction as the incident wave, whereas the cross-polar elements (off-diagonal) of **S** correspond to complex scattering amplitudes along the orthogonal direction of the incident waves.

Given that hydrometeors and non-meteorological scatterers have varied orientations, the scattering matrix must account for the angle of the scatterer relative to the incident EM wave (Holt 1984; Bringi and Chandrasekar 2001). Fig. 2.2 shows the scattering angles for an oriented spheroid with a symmetry axis along the line OS. β is the canting angle of the spheroid in the polarization plane, and ϕ is the angle between the incident EM wave and the symmetry axis of the spheroid. To illustrate the geometry, consider a simple case of scattering with an oblate spheroid where the incident EM wave is propagating along the x-axis, with $\hat{h_i}$ and $\hat{v_i}$ oriented along the y- and z-axes, and with OS oriented in the +z direction. In this case, ϕ=90°, which corresponds to a case of a 0° elevation angle with the major axis of the spheroid oriented horizontally. As β increases (or decreases), the major axis now has components in both the horizontal and vertical polarizations, and the magnitude of cross-polar scattering elements increase. The scattering matrix (2.8) can be expressed in terms of β and ϕ to account for scatterer orientation (Holt 1984; Bringi and Chandrasekar 2001), as follows:

$$\begin{bmatrix} E_h \\ E_v \end{bmatrix}^b = \begin{bmatrix} S_{11}(\phi)\cos^2\beta + S_{22}(\phi)\sin^2\beta & \frac{1}{2}(S_{22}(\phi) - S_{11}(\phi))\sin^2 2\beta \\ \frac{1}{2}(S_{22}(\phi) - S_{11}(\phi))\sin^2 2\beta & S_{11}(\phi)\sin^2\beta + S_{22}(\phi)\cos^2\beta \end{bmatrix} \begin{bmatrix} E_h \\ E_v \end{bmatrix}^i \frac{e^{-jkr}}{r}. \tag{2.9}$$

Weather radars can also transmit electromagnetic waves with circular polarization (e.g., McCormick and Hendry 1975). The unit vectors for a linear

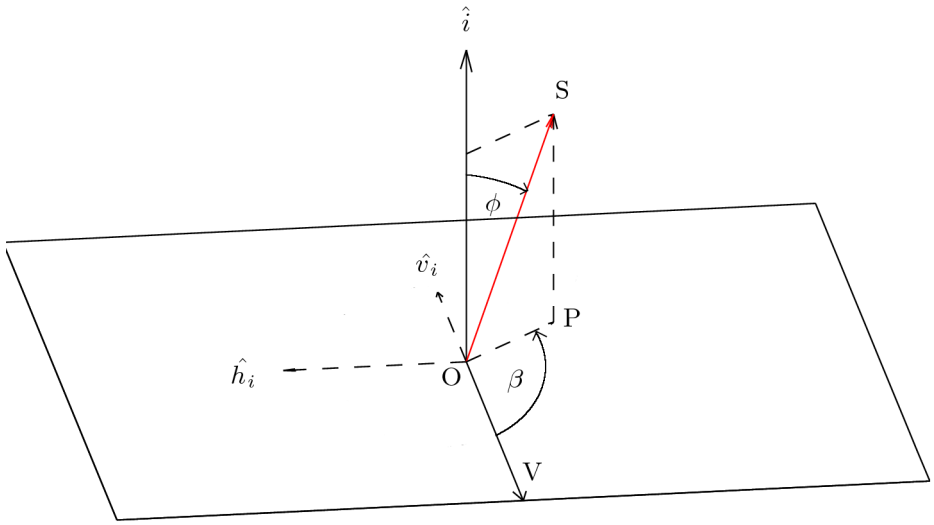

Figure 2.2: Figure showing the scattering angles for an oriented spheroid (adapted from Bringi and Chandrasekar (2001)). OS indicates the symmetry axis of the spheroid. $\hat{i}$ indicates the direction of incident EM wave propagation, and $\hat{v}_i$ and $\hat{h}_i$ are the vertical and horizontal polarization unit vectors. β measures the canting angle in the polarization plane, and ϕ measures the angle between the direction of incident EM wave propagation and the spheroid symmetry axis.

polarized EM wave and a circularly polarized EM wave can be related through the following matrix transformation:

$$\begin{bmatrix} \hat{r} \\ \hat{l} \end{bmatrix} = \frac{\sqrt{2}}{2} [G] \begin{bmatrix} \hat{h} \\ \hat{v} \end{bmatrix}, \tag{2.10}$$

where $\hat{r}$ and $\hat{l}$ are unit vectors in the direction of the right- and left-hand circular polarizations and the **G** is:

$$\frac{\sqrt{2}}{2} \begin{bmatrix} -i & 1 \\ i & 1 \end{bmatrix}. \tag{2.11}$$

By multiplying the incident linearly polarized electric field by **G**, Bringi and Hendry (1990) show that the incident electric fields for a linearly and circularly polarized EM wave are related by:

$$\begin{bmatrix} E_r \\ E_l \end{bmatrix}^i = [G] \begin{bmatrix} E_h \\ E_v \end{bmatrix}^i, \tag{2.12}$$

where E_r and E_l are the incident electric field components in the right-hand and left-hand circular polarizations. The scattering matrix for a circularly polarized EM wave, $\mathbf{S_c}$, becomes:

$$[S_c] = [G]^*[S][G]^{-1}. \tag{2.13}$$

The components of the circularly polarized scattering matrix are related to the linear scattering matrix as follows:

$$\begin{aligned} S_{ll} &= \tfrac{1}{2}\left(S_{vv} - S_{hh} + i2S_{vh}\right) \\ S_{rr} &= \tfrac{1}{2}\left(S_{vv} - S_{hh} - i2S_{vh}\right) \\ S_{rl} &= \tfrac{1}{2}\left(S_{vv} + S_{hh}\right) \\ S_{lr} &= \tfrac{1}{2}\left(S_{vv} + S_{hh}\right) \end{aligned} \tag{2.14}$$

where S_{ll} and S_{rr} are backscattered returns of the same handedness as the incident EM wave, and S_{rl} (S_{lr}) is right-hand (left-hand) circular backscattered returns from a transmitted left-hand (right-hand) circular EM wave. Some intriguing properties of circular polarization radar are evident from (2.14). For a spherical scatterer, which has equal diagonal components of the linear scattering matrix (i.e., S_{hh} and S_{vv} are equal) and off-diagonal components equal to zero, the scattering matrix elements for the circular polarization with transmitted and received EM waves of the same handedness (i.e., S_{ll} and S_{rr}) are zero. In other words, no return power would be measured for a circularly-polarized radar transmitting and receiving only right-handed circular polarization EM waves. Because backscattered returns for spherical scatterers can be mitigated, circular polarization is commonly used to mitigate precipitation clutter for aviation (Bringi and Chandrasekar 2001).

2.1.2 Polarimetric radar measurements

Polarimetric radar variables are derived from second-order moments of the complex received radar signals. Complex received radar signals, V_{ij}, are the sum of the signals of the individual scatterers, as given by:

$$V_{ij} = \sum_{n=1}^{N} S_{ij}(n) \exp(-j2kr) F(r) \tag{2.15}$$

where N is the number of scatterers, $F(r)$ is a variable which accounts for range dependence, attenuation, and various radar parameters, and k is the wavenumber (e.g., Doviak and Zrnić 1993). By calculating second-order moments of the

complex received radar signals, polarimetric radar variables can be estimated. The covariance matrix **C** is computed by calculating second-order moments of combinations of the complex received radar signals (e.g., $< S_{hv}S_{hh}^{*} >$ or $< S_{hh}S_{hh}^{*} >$). The covariance matrix, C, is expressed as,

$$C = \begin{bmatrix} < |S_{hh}|^2 > & < S_{hv}S_{hh}^{*} > & < S_{vv}S_{hh}^{*} > \\ < S_{hh}S_{hv}^{*} > & < |S_{hv}|^2 > & < S_{vv}S_{hv}^{*} > \\ < S_{hh}S_{vv}^{*} > & < S_{hv}S_{vv}^{*} > & < |S_{vv}|^2 > \end{bmatrix}. \tag{2.16}$$

Although there are 16 second-order moments, there are only 9 unique moments due to reciprocity ($S_{hv} = S_{vh}$).

Polarimetric radars operate different configurations of transmitting and receiving pulses (Doviak et al. 2000). The configuration of transmitting and receiving pulses affects which covariance matrix elements are measured. In simultaneous transmit, simultaneous receive (STSR) configuration, the radar transmits and receives both horizontal and vertical polarizations. Consequently, because both horizontal and vertical polarizations are transmitted simultaneously, it is not possible to discriminate between backscattered returns caused by horizontal or vertical incident radiation. In other words, for the vertical channel receiver, cross-polar backscattered energy from a horizontally polarized incident EM wave cannot be separated from co-polar backscattered energy from a vertically polarized incident EM wave. However, in an alternating pulse transmission configuration (e.g., alternating transmit simultaneous receive, or ATSR), it becomes possible to distinguish backscattered radiation from horizontal and vertical incident radiation, and thus all elements in the covariance matrix can be measured.

2.1.2.1 Radar reflectivity factor

Z_{hh} and Z_{vv} are the horizontal and vertical radar reflectivity factors, respectively, as shown in (2.17) and (2.18), where N is the number of scatterers per cubic meter.

$$Z_{hh} = \frac{4\lambda^4}{\pi^4 |K_m|^2} < |NS_{hh}|^2 > \tag{2.17}$$

$$Z_{vv} = \frac{4\lambda^4}{\pi^4 |K_m|^2} < |NS_{vv}|^2 > \tag{2.18}$$

For Rayleigh scatterers, radar reflectivity factors are particularly sensitive to scatterer sizes. In the case of a sphere, S_{hh} and S_{vv} can be written as,

$$S_{hh,vv} = \left(\frac{2\pi}{\lambda}\right)^2 C_m D^3, \tag{2.19}$$

where C_m (2.20) is a constant value (Oguchi 1983; Doviak and Zrnić 1993).

$$C_m = \frac{m^2 - 1}{\frac{1}{3}(m^2 - 1) + 1} \tag{2.20}$$

Combining (2.17) and (2.19), it becomes evident that Z_{hh} and Z_{vv} are a function of D^6. While radar reflectivity factor is strongly dependent on size, N can vary over several orders of magnitude (e.g., Marshall and Palmer 1948; Ulbrich 1983), and thus affect radar reflectivity factor.

Radar reflectivity factor and other polarimetric variables for different precipitation types is shown in Table 2.1. Rain encompasses a relatively large range of radar reflectivity factors because drop-size distributions (DSDs) are highly varied and rain possesses a high refractive index compared to dry snow or ice crystals. Wet hail exhibits high radar reflectivity factors as a consequence of its

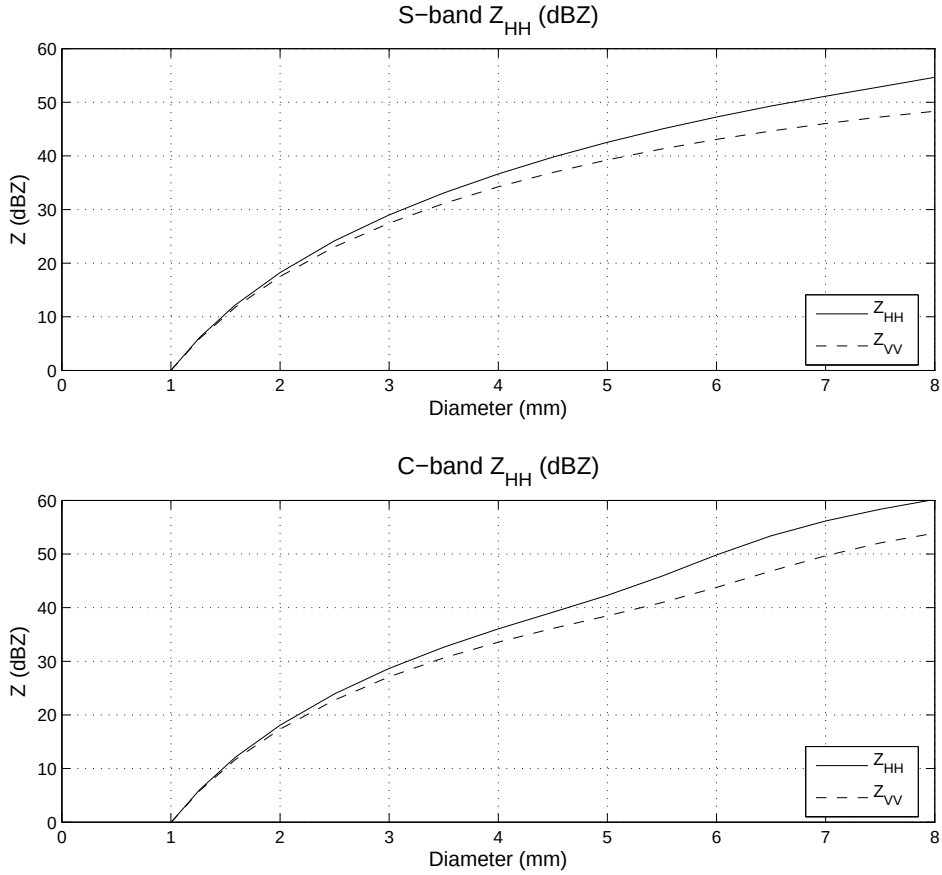

Figure 2.3: Horizontal and vertical radar reflectivity factor for rain (solid and dashed lines) for a concentration of 1 drop per m^{-3} at S and C bands (top and bottom plots). Differences between horizontal and vertical radar reflectivity factor increase as drop diameter increases.

water coating and large size, which cause greater backscattered energy. Polarimetric radar variables can be calculated using T-matrix codes, which provide scattering amplitudes for different hydrometeor sizes or orientations. Horizontal and vertical radar reflectivity factors for rain are computed using T-matrix codes for spheroids with fixed orientations (Waterman 1971; Mischenko et al. 1996; Mischenko 2000). Fig. 2.3 shows horizontal and vertical radar reflectivity factors for rain at S and C bands at a concentration of 1 drop per m^{-3} using drop axis ratios from Thurai and Bringi (2005) and Thurai et al. (2007). Owing to the oblateness of larger drops, the difference between Z_{HH} and Z_{VV} increases with increasing drop size, which provides useful information to discriminate rain drop size.

Table 2.1: Common values of polarimetric variables for different precipitation types at S band (adapted from Doviak and Zrnić (1993)).

Precipitation Type	Z_{HH} (dBZ)	Z_{DR} (dB)	$\lvert\rho_{HV}(0)\rvert$	LDR (dB)
Rain	25 – 60	0.5 – 4	> 0.97	-27 – -34
Dry snow	< 35	0 – 0.5	> 0.99	$<$ -34
Melting snow	< 45	0 – 3	0.8 – 0.95	-13 – -18
Small, wet hail	50 – 60	-0.5 – 0.5	> 0.95	$<$ -20
Large, wet hail	55 – 70	$<$ -0.5	> 0.96	-10 – -15

2.1.2.2 Differential reflectivity

The ratio of horizontal to vertical radar reflectivity factor, called differential reflectivity or Z_{DR} (Seliga and Bringi 1976, 1978), provides useful information about the shapes and sizes of scatterers. Z_{DR} is defined as:

$$Z_{DR} = 10 \log_{10} \left(\frac{< |S_{hh}|^2 >}{< |S_{vv}|^2 >} \right). \tag{2.21}$$

The axis ratio of a scatterer is typically defined as $\frac{b}{a}$, where a and b are the horizontal and vertical axes, respectively. For an oblate (prolate) spheroid, the horizontal (vertical) axis is greater than the vertical (horizontal) axis which results in positive (negative) Z_{DR}. For Rayleigh scatterers, Z_{DR} measurements are particularly useful in discriminating rain drop size because rain drops become increasing oblate (i.e., lower axis ratio) as drop diameter increases (Fig. 2.4). By making assumptions about the DSD (assuming an exponential DSD), Seliga and Bringi (1976) found that Z_{DR} is related to median drop diameter.

Drop axis ratios have been extensively studied in wind tunnel studies, numerical simulations, and disdrometer observations. Empirical equations have been formulated to represent the axis ratio as a function of drop diameter. Pruppacher and Pitter (1971) applied a linear fit to laboratory observations of drop axis ratio in a wind tunnel, and obtained the following linear relationship between axis ratio and drop diameter,

$$\frac{b}{a} = 1.03 - 0.062D. \tag{2.22}$$

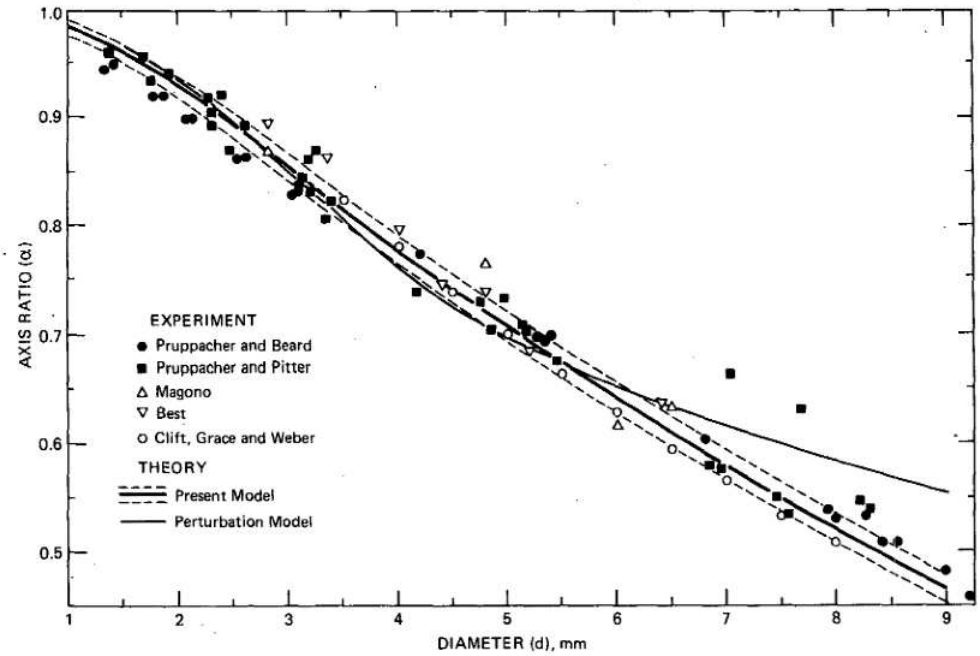

FIG. 8. Experimental and model results for axis ratio (α) as a function of drop size (d). The dashed lines show present model results for upper and lower bounds.

Figure 2.4: Rain drop axis ratio as a function of diameter (adapted from Beard and Chuang (1987)) computed from laboratory experiments and models. Rain drop axis ratio decreases as drop diameter increases.

Using model simulations, Beard and Chuang (1987) obtained the following equation for drop axis ratio as a function of diameter, valid for drop diameters less than 7 mm:

$$\frac{b}{a} = 1.0048 + 5.7 \times 10^{-4} D - 2.628 \times 10^{-2} D^2 + 3.682 \times 10^{-3} D^3 - 1.677 \times 10^{-4} D^4. \tag{2.23}$$

More recent studies have found that the Beard and Chuang (1987) equation tends to create axis ratios that are too small at larger diameters (Andsager et al. 1999). Axis ratios have also been estimated from 2D video disdrometers observations (e.g., Thurai and Bringi 2005). Thurai and Bringi (2005) and Thurai et al. (2007) obtained the following axis ratios,

$$\frac{b}{a} = 1.065 - 0.0625D - 0.00399D^2 + 0.000766D^3 - 0.00004095D^4. \tag{2.24}$$

Differential reflectivity measurements for rain exhibit significant differences depending on radar frequency, particularly for larger drop sizes at higher frequencies. At S band, rain drops satisfy the Rayleigh condition and Z_{HH}, Z_{VV} and Z_{DR} increase as a function of diameter (Figs. 2.3, 2.5). At C band, however, the Rayleigh size criteria is not satisfied for rain drop diameters exceeding $\approx$ 3.4 mm, and Mie scattering effects are observed. For example, Z_{DR} exhibits a peak between 6 – 7 dB and then decreases due to an oscillation of the backscatter cross-section of rain drops in the Mie scattering region. Rain drop canting angle distributions (e.g., Beard and Jameson 1983) also affect Z_{DR} measurements by reducing alignment between the incident horizontal and vertical electromagnetic waves and rain drop major and minor axes, resulting in lower Z_{DR} values.

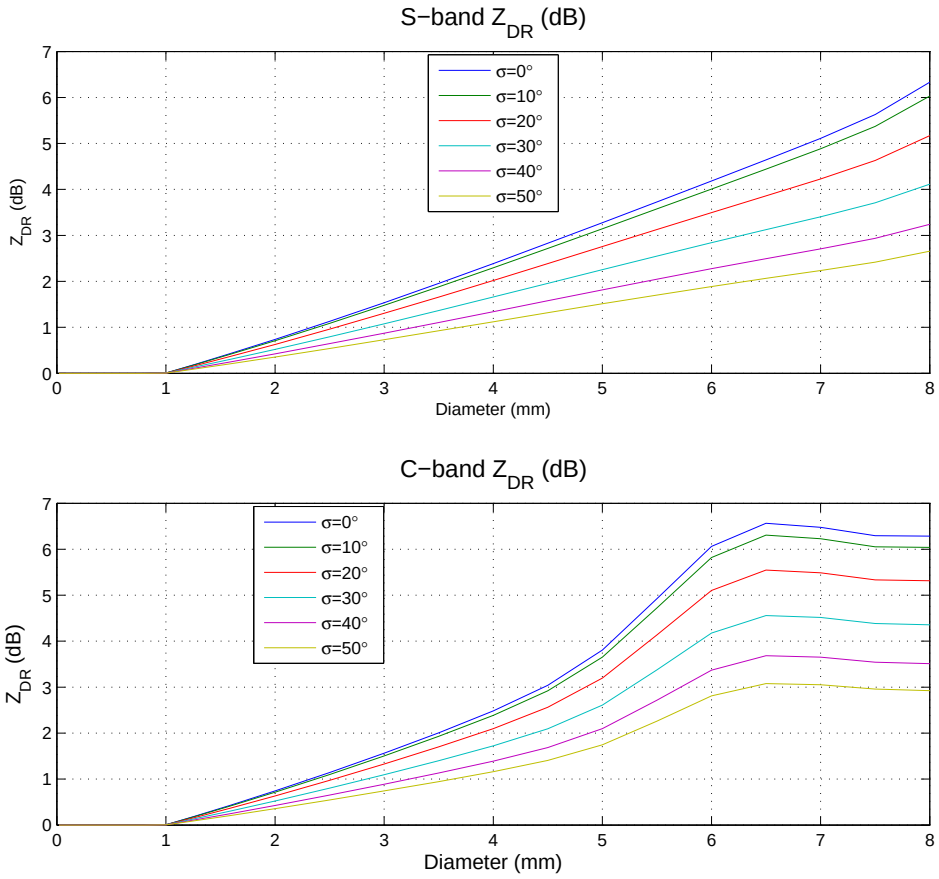

Figure 2.5: Differential reflectivity or Z_{DR} (dB) for rain (solid and dashed lines) for a concentration of 1 drop per m^{-3} at S and C bands (top and bottom plots), shown for canting angle distributions represented by a Gaussian probability density function with σ=0°, 10°, 20°, 30°, 40°, and 50°. As the variability of drop canting angle increases, Z_{DR} decreases because the drop major axis has horizontal and vertical components.

2.1.2.3 Co-polar cross-correlation coefficient and backscatter differential phase

Co-polar cross-correlation coefficient, ρ_{HV}, measures the correlation between the vertical and horizontal co-polar received signals (Sachidananda and Zrnić 1985; Jameson 1987; Balakrishnan and Zrnić 1990), and is related to the covariance matrix elements as follows,

$$\rho_{hv} = \frac{< S_{vv} S_{hh}^{*} >}{< |S_{hh}|^2 >^{\frac{1}{2}} < |S_{vv}|^2 >^{\frac{1}{2}}}. \tag{2.25}$$

The covariance matrix element $< S_{vv} S_{hh}^{*} >$ can be expressed in terms of magnitude and phase as follows:

$$< S_{vv} S_{hh}^{*} > = < |S_{vv} S_{hh}^{*}| \exp(-j(\delta_{hh} - \delta_{vv})) > . \tag{2.26}$$

The magnitude and phase of ρ_{HV} are commonly referred to as correlation coefficient and backscatter differential phase, δ_{dp}. Typically, the magnitude of ρ_{HV} is estimated at zero-lag, $|\rho_{HV}(0)|$. However, estimation using multiple lags can mitigate errors in ρ_{HV} and other polarimetric radar variables at lower signal-to-noise ratios (SNRs) (Lei et al. 2012).

Co-polar cross-correlation coefficient decreases as the diversity of scatterer shapes and orientations increase (Jameson 1987; Balakrishnan and Zrnić 1990; Ryzhkov et al. 2005). For rain, lower values of ρ_{HV} can result from broader DSDs which create a greater variety of rain drop shapes, and larger variances in drop canting angles (Jameson 1987; Jameson and Davé 1988). For hail, polarimetric radar measurements exhibit lower ρ_{HV} compared to rain as a consequence of

resonance scattering effects (i.e., a larger δ_{DP}), a lower degree of common orientation due to tumbling, and non-spherical shapes of hailstones. Balakrishnan and Zrnić (1990) show that for wet hail ρ_{HV} decreases for increasingly random orientation (Fig. 2.6). Fig. 2.6 shows that ρ_{HV} for wet hail diameters greater than 50 mm decreases below 0.6 for completely random orientations of hail. Given that such low values are not observed for hail, one might suspect that hail possesses some degree of common alignment. Balakrishnan and Zrnić (1990) also calculated ρ_{HV} as a function of protuberance-to-diameter ratio, $\frac{\sigma_D}{D}$, and found that increasing protuberance-to-diameter ratios lead to lower ρ_{HV}. ρ_{HV} can be calculated for Rayleigh scatterers for different protuberance-to-diameter ratios as follows:

$$|\rho_{HV}(0)| = \frac{\left(1 + 3\frac{\sigma_D^2}{D^2}\right)^2}{1 + 15\frac{\sigma_D^2}{D^2} + 45\frac{\sigma_D^4}{D^4} + 15\frac{\sigma_D^6}{D^6}}. \tag{2.27}$$

2.1.2.4 Linear and circular depolarization ratio

Linear depolarization ratio, or L_{DR}, is the ratio of cross-polar power, $< |S_{hv}|^2 >$, to co-polar power, $< |S_{vv}|^2 >$:

$$L_{DR} = 10 \log_{10} \left(\frac{< |S_{hv}|^2 >}{< |S_{vv}|^2 >} \right). \tag{2.28}$$

Either S_{hv} or S_{vh} can be used in the numerator of (2.28) to estimate L_{DR}, and will yield equivalent results for reciprocal media. For a spheroid, cross-polar signals are generated when the major and minor axes are not aligned with the horizontal and vertical polarized electromagnetic waves. For a spheroid with no

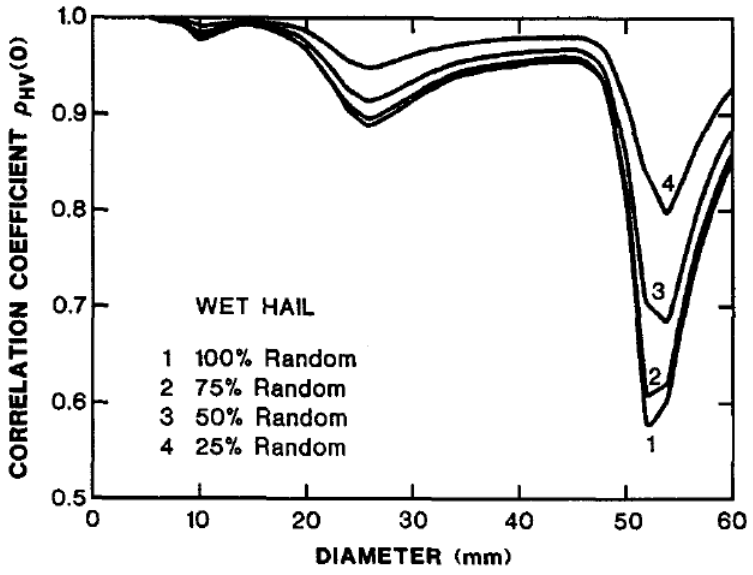

Figure 2.6: Co-polar cross-correlation coefficient (ρ_{HV}) for wet hail as a function of diameter and randomness of orientation (figure adapted from Balakrishnan and Zrnić (1990)). As the common alignment of particles decreases, ρ_{HV} decreases.

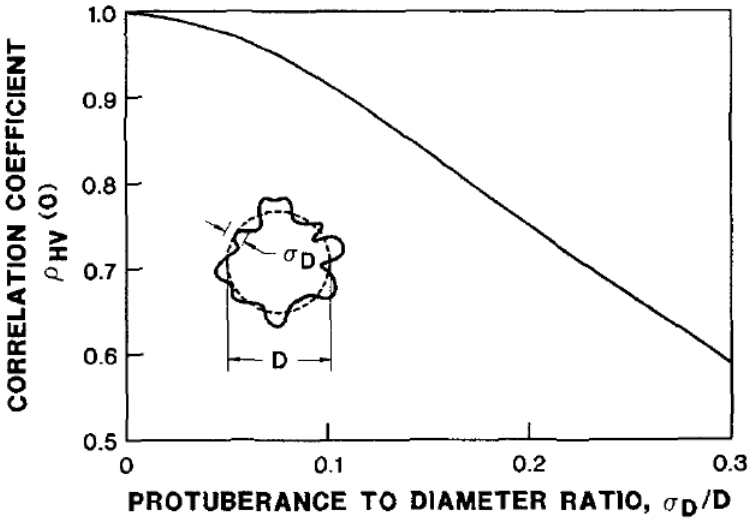

Figure 2.7: Co-polar cross-correlation coefficient (ρ_{HV}) for wet hail as a function of diameter and protuberance to diameter ratio, σ_D/D (figure adapted from Balakrishnan and Zrnić (1990)). As particles become increasingly non-spherical, ρ_{HV} decreases.

canting, such as $\beta = 0°$ or 90° in (2.9), L_{DR} approaches a theoretical limit of -∞ dB (Doviak and Zrnić 1993). Because some degree of canting occurs with rain drops, L_{DR} values for rain typically range between -27 – -34 dB (Table 2.1). For larger, wet ice crystals, larger cross-polar signals and higher L_{DR} values are generated because the ice crystal has a liquid water coat and a higher refractive index.

Circular depolarization ratio (CDR; McCormick and Hendry 1975; Holt 1984; Seliga et al. 1984) is the ratio of the power from the parallel polarization (same handedness as the transmitted EM wave) to the orthogonal polarization (opposite handedness as the transmitted EM wave). For a radar transmitting right-hand circular polarization, CDR is:

$$CDR = 10 \log_{10} \frac{|S_{rr}|^2}{|S_{lr}|^2}. \tag{2.29}$$

For spherical objects, CDR is -∞ dB and increases as scatterer eccentricity increases. For rain drops, Seliga et al. (1984) found that Z_{DR} and CDR are related as follows:

$$CDR = \left(\frac{1 - {Z_{DR}}^{\frac{1}{2}}}{1 + {Z_{DR}}^{\frac{1}{2}}} \right)^2. \tag{2.30}$$

A comparison of CDR calculated using T-matrix code and (2.30) is shown in Fig. 2.8. In general, close agreement is observed except at large diameters due to slight differences in the equations for axis ratio. CDR increases as rain drop size increases due to increasing eccentricity of the drop.

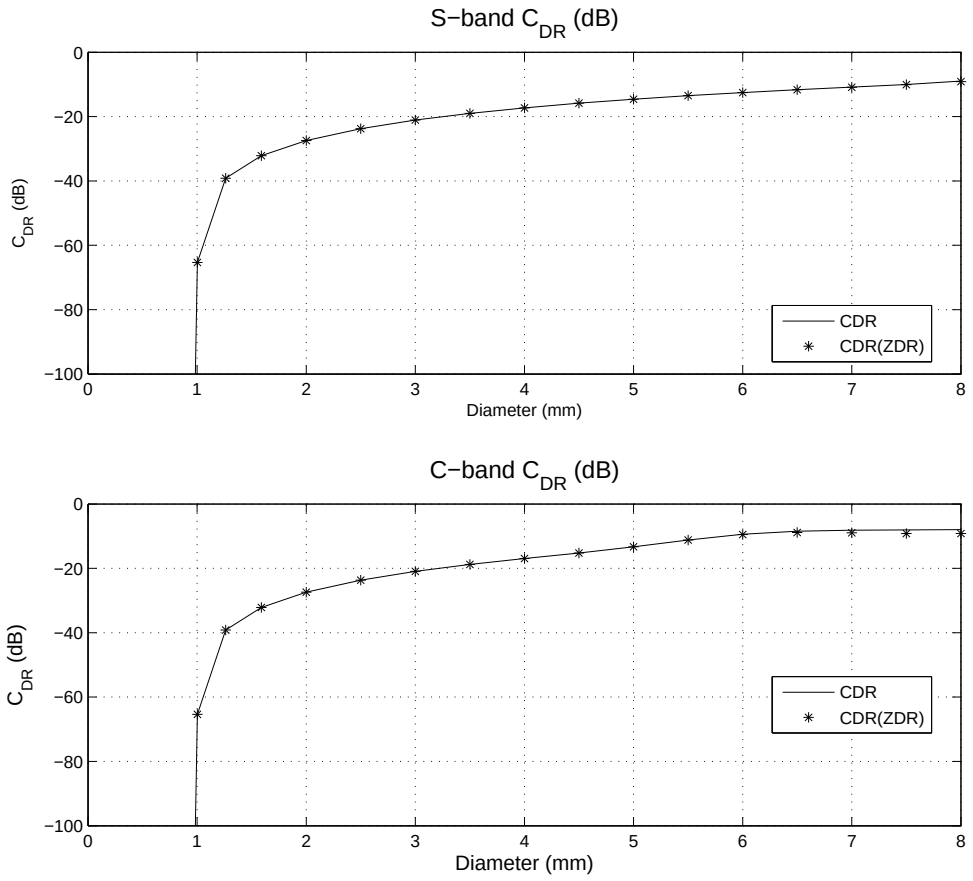

Figure 2.8: Circular depolarization ratio or C_{DR} (dB) for rain with a concentration of 1 drop per m^{-3} at S and C bands (top and bottom plots). The T-matrix calculated CDR is shown by the solid black line, and CDR calculated from (2.30) is shown by the black asterisks. Circular depolarization ratio increases with increasing drop diameter.

2.1.3 Polarimetric radar variables for tornadic debris

In this section, polarimetric radar variables are calculated for scatterers that have similar physical sizes and shapes as common debris types. T-matrix calculations can become ill-conditioned for spheroids with large aspect ratios or high refractive indices, which limits the types of debris simulated in this study. Moreover, irregular shapes (e.g., corners of a wood board) cannot be calculated using T-matrix calculations, which makes it difficult to simulate many debris types. Nonetheless, T-matrix calculations may illuminate some general electromagnetic scattering characteristics of debris and their relationships to polarimetric variables. In the future, more sophisticated methods for determining the complex backscatter cross-sections will be conducted, including anechoic chamber measurements and High Frequency Structural Simulator (HFSS) calculations, which are better suited to determine how well the T-matrix calculations for basic shapes simulated herein compare to actual debris.

The material composition of scatterers affects its electromagnetic scattering characteristics. The scatterer's complex relative permittivity, ϵ_r, is a relative measure of a scatterer's ability to store electrical charge, and therefore indicates its potential to backscatter EM waves. ϵ_r is often written in terms of its real and complex components as $\epsilon_r = \epsilon^{'} + i\epsilon^{''}$. The complex relative permittivity often changes as a function of frequency and temperature (Ray 1972). For water, the real part of the complex relative permittivity increases as wavelength increases while the imaginary part of ϵ_r exhibits a maximum value at approximately a

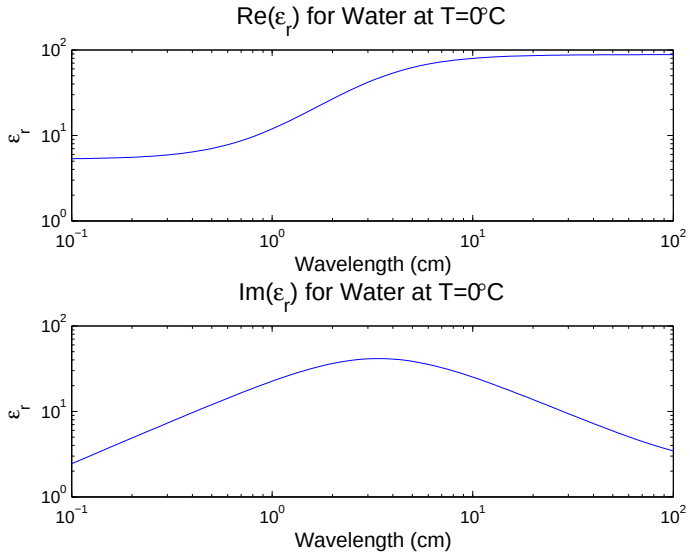

Figure 2.9: Complex relative permittivity (ϵ_r) of water at T=0°C as a function of wavelength (cm). The real part of ϵ_r increases as wavelength increases, while the imaginary part of ϵ_r has a maximum value for about a 3-cm wavelength.

3-cm wavelength (Fig. 2.9). The real and imaginary components of the relative permittivity are related to the complex refractive index by:

$$\epsilon^{'} = n'^2 - n''^2, \tag{2.31}$$

and

$$\epsilon^{''} = 2n'n''. \tag{2.32}$$

2.1.3.1 Dust and Sand

Dust and sand particles lofted in tornadoes are often quite prominent, forming a large rotating particle cloud around the tornado that varies considerably in spatial extent. Dust and sand debris clouds often provide the first confirmation

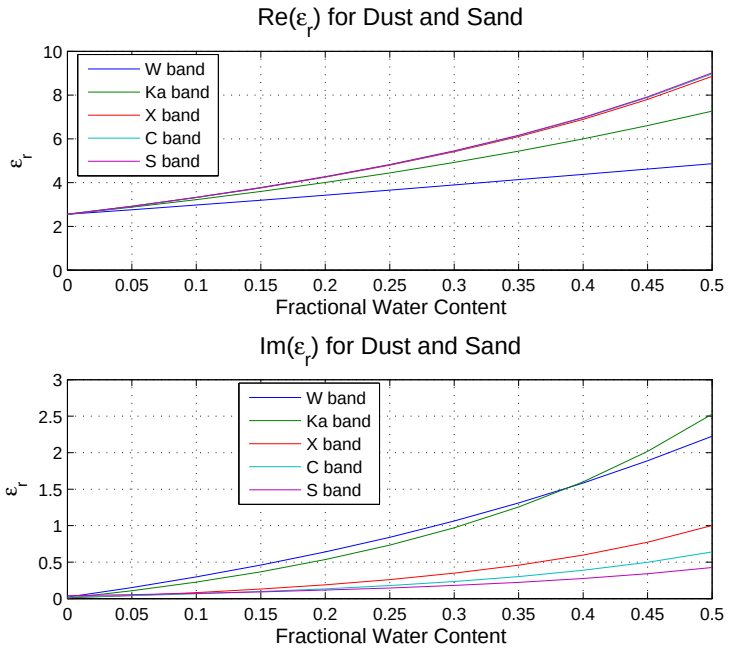

Figure 2.10: Complex relative permittivity (ϵ_r) of sand as a function of fractional water content at Ka, X, C, and S bands. As fractional water content increases, both real and imaginary parts of ϵ_r increase.

of a vortex in contact with the surface before the condensation funnel extends to the surface. In some cases, dust and sand particles lofted by tornadoes may be the only visible debris. Given that dust and sand particles are frequently lofted by tornadoes, it is crucial to determine their electromagnetic scattering characteristics.

Several studies have examined the relative permittivity of dust and sands at different locations at a wide range of frequencies. In this study, the relative permittivity measurements of Matzler (1998) are chosen because they encompass a broad range of frequencies used in weather radar measurements (3 – 10 GHz).

Their measurements exhibit good agreement with other complex relative permittivity measurements in the 0.1 – 10 GHz range (e.g., Wang and Schmugge 1980; Dobson et al. 1985; Ulaby et al. 1990). Measurements by Gatesman et al. (2005) are used to examine polarimetric radar signatures of dust and sand at frequencies exceeding 10 GHz. Given that soils can have significantly different compositions, a more comprehensive investigation of complex relative permittivity across the common range of weather radar frequencies is needed, but is beyond the scope of the present study.

To examine scattering characteristics of wet dust and sand, relative permittivities for different fractional volumes, f_v, are computed using the Maxwell-Garnett mixing formula:

$$\epsilon_e = \frac{1 + 2f_v y}{1 - f_v y}\epsilon_1, \tag{2.33}$$

where

$$y = \frac{\epsilon_2 - \epsilon_1}{\epsilon_2 + 2\epsilon_1}. \tag{2.34}$$

ϵ_1 and ϵ_2 are the complex relative permittivities of dry sand and water, respectively. Fig. 2.10 shows the complex relative permittivities for dust and sand for common weather radar frequency bands for different fractional water contents. The real and imaginary components of the complex relative permittivity increase as fractional water content increases, leading to higher refractive indices for wet dust or sand. Matzler (1998) showed that the dielectric loss for dry sand decreases as a function of frequency between 3 – 10 GHz, which is the opposite behavior in dielectric loss for water.

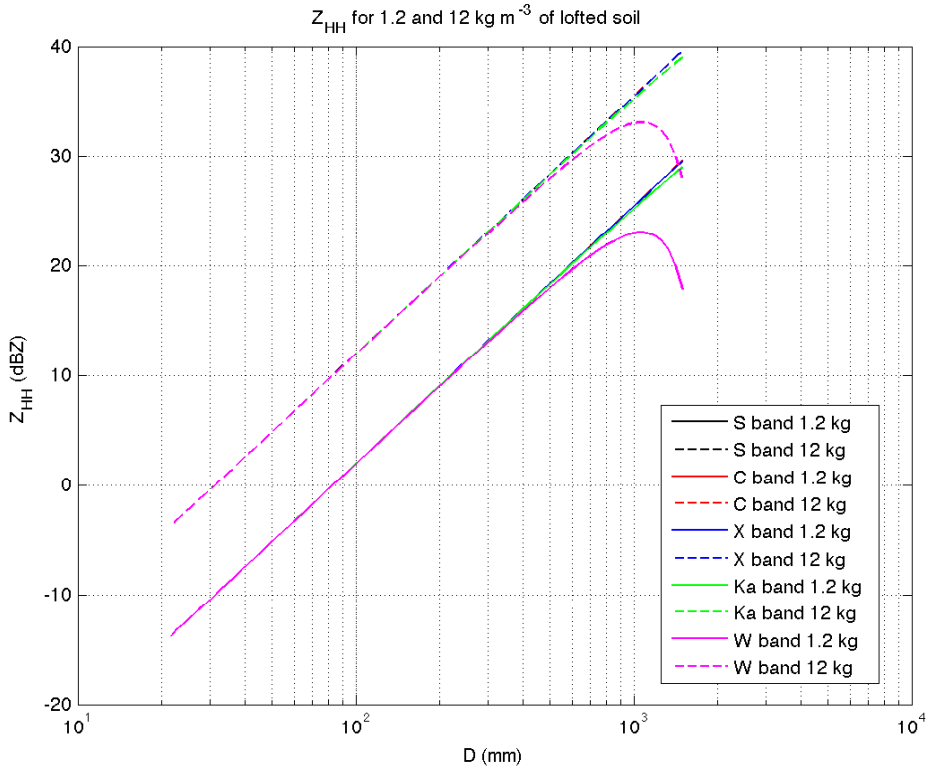

Figure 2.11: Equivalent radar reflectivity factor (Z_{HH}) at S, C, X, Ka, and W bands for dry dust as a function of diameter (mm). Differences between S, C, and X bands are small over the range of sizes computed. Mie scattering effects are prominent at W band with Z_{HH} oscillations evident and much lower Z_{HH} compared to other longer radar wavelengths, particularly for D $>$ 1 mm.

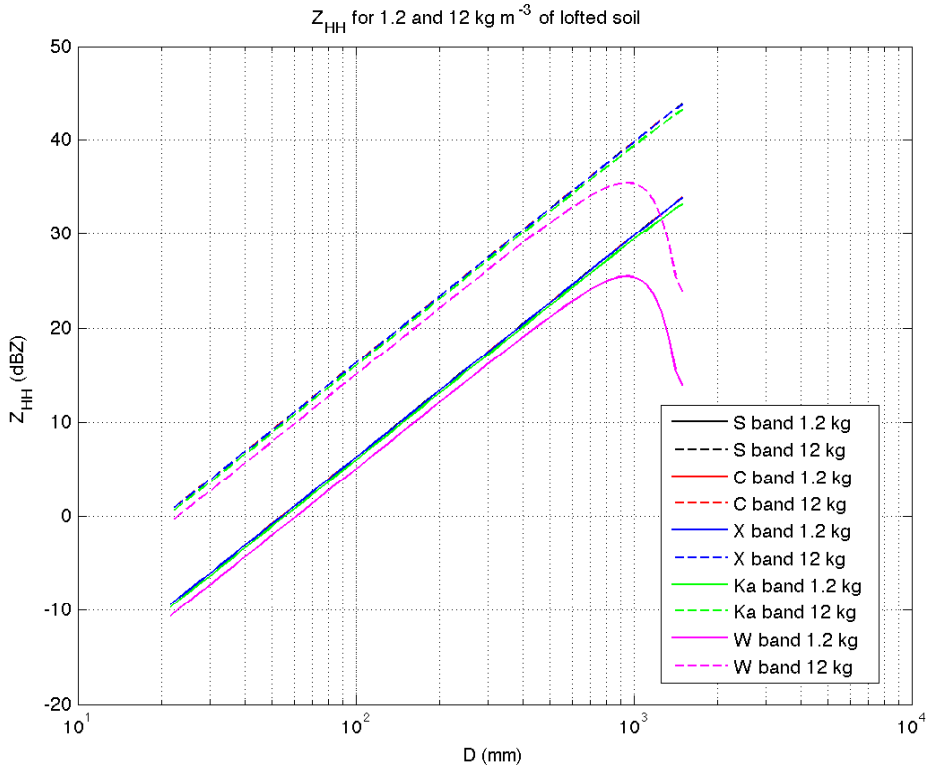

Figure 2.12: Equivalent radar reflectivity factor (Z_{HH}) at S, C, X, Ka, and W bands for wet dust as a function of diameter (mm). Equivalent radar reflectivity factor for wet dust is generally higher than dry dust.

Using complex refractive indices computed from the complex relative permittivity, equivalent radar reflectivity factor is computed from T-matrix calculations as shown in Figs. 2.11 and 2.12. T-matrix calculations are performed for a particle concentration of 1 m^{-3} for dry and wet (20% fractional water content) dust and sands. Equivalent radar reflectivity factor exhibits close agreement among longer radar wavelengths, and differences among S, C, and X band are less than 0.02 dB. For sand particles with D > 0.1 mm, Ka band exhibits lower Z_{HH} compared to the other wavelengths due to Mie scattering effects, resulting in differences of 0.1 – 1 dB. W-band Z_{HH} exhibits much larger differences for larger sand particles, particularly for increasing wetness. The dual-wavelength Z_{HH} difference between S and W bands are 2.4 and 12.1 dB (4.3 and 25.7 dB) for 0.5-mm and 1-mm radius dry (wet) sand particles.

Several studies have obtained particle size distributions of soils for geological and agricultural studies (e.g., Tyler and Wheatcraft 1989, 1992), which may be useful for determining the amount of lofted dust or soil particle as a function of particle size. With a realistic soil distribution, polarimetric radar variables can be computed for different soil types. Soil particles follow fractal behavior (Turcotte 1986), which allows soil particle distributions to be expressed in the following form:

$$N_s r_s^p = const., \tag{2.35}$$

where N_s is the number of soil particles greater than radius, r_s. For larger values of p, soil particle size distributions exhibit larger numbers of smaller particles.

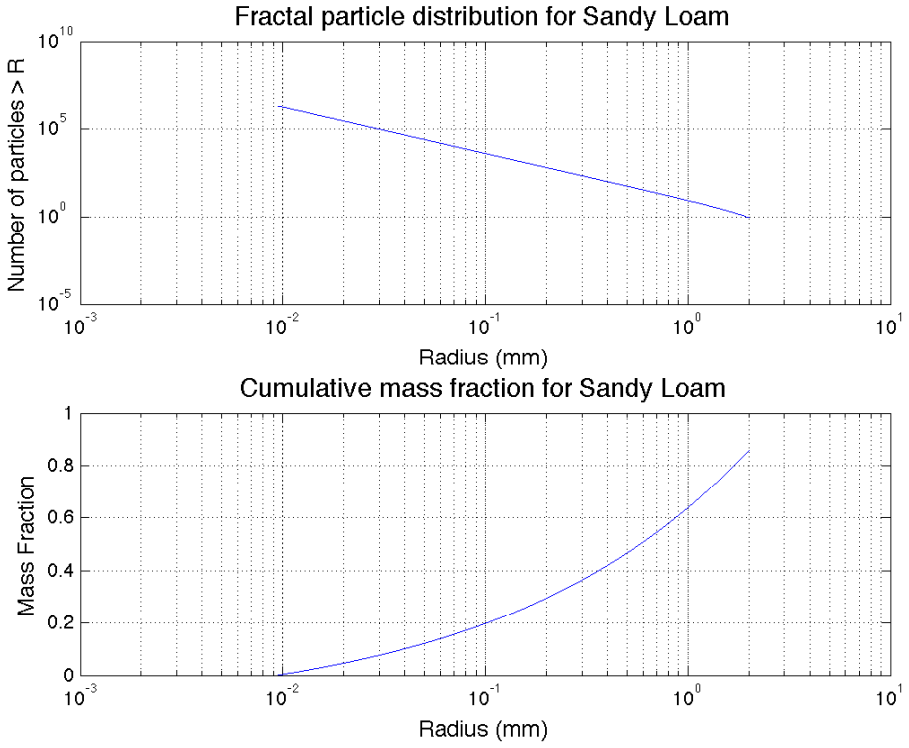

Figure 2.13: Fractal particle distribution and cumulative mass fraction for sandy loam soil. Compared to the clay loam soil, sandy loam soil contains a higher concentration of large particle sizes.

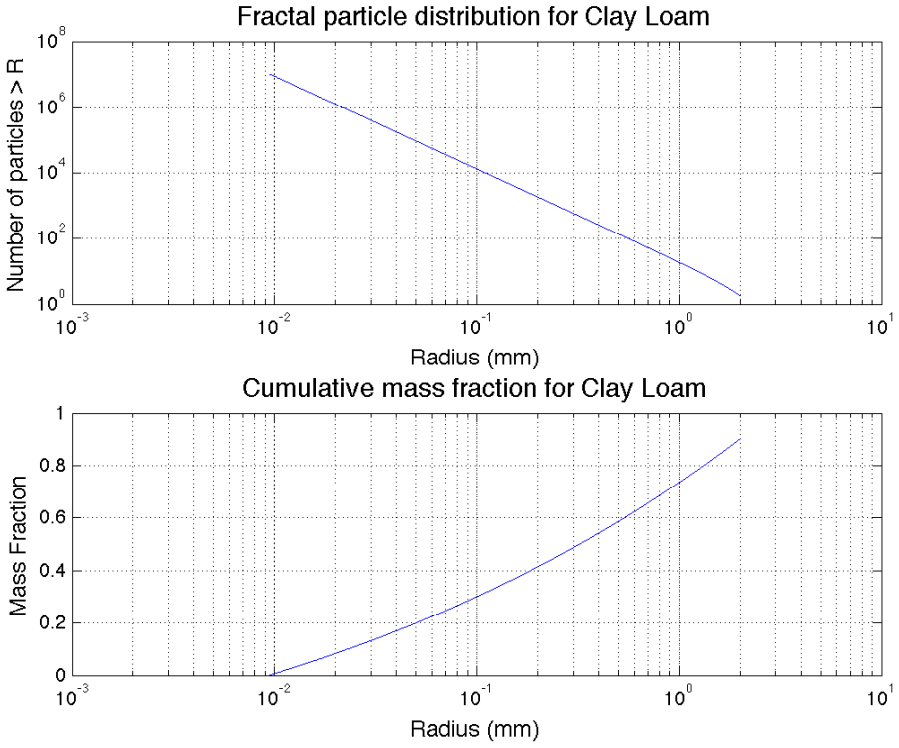

Figure 2.14: Fractal particle distribution and cumulative mass fraction for clay loam soil. Compared to the sandy soil, clay exhibits a larger mass fraction for smaller particle sizes.

For sandy loam and clay loam soils (Tyler and Wheatcraft 1992), the exponent p has values of 2.646 and 2.832, respectively. Figs. 2.13 and 2.14 show the fractal particle distribution and cumulative mass fraction for sandy loam and clay soils, respectively. For the same amount of mass, the sandy loam soil will have a greater proportion of larger particles.

T-matrix calculations of equivalent radar reflectivity factor were performed for sandy and clay loam soil distributions. Equivalent radar reflectivity factors for 1.2 kg of dry and wet sandy loam soils and dry and wet clay loam soils are shown in Table 2.2. In the following analysis, 1.2 kg of soil is used because this mass is the same as the mass of air at sea level (in later discussions, debris loading calculations are normalized by air density). Equivalent radar reflectivity factor differences among S, C, and X bands are small because scatterers exhibit Rayleigh scattering, and slight differences on the order of hundredths of a dB result from small differences ϵ_r. At Ka and W bands, resonance effects reduce equivalent radar reflectivity factor contributions of larger sand particles.

Contributions of 1.2 and 12 kg of dry and wet sand particles to Z_{HH} as a function of diameter are shown in Fig. 2.15 and 2.16. For wet sand particles (20% fractional water content), Z_{HH} is $2-4$ dB greater compared to dry sand particles. For the smaller scatterers at longer wavelengths, equivalent radar reflectivity factor contributions of larger sand particles is greater than the smaller particles even though the concentration of particles decreases on the order of 10^6 as the radius increases from 10^{-2} to 1 mm. At W band, the contribution of Z_{HH} for

Table 2.2: Equivalent radar reflectivity factor for 1.2 kg of dry and wet sandy and clay loam soils.

Soil Type	S-band Z_{HH} (dBZ)	C-band Z_{HH} (dBZ)	X-band Z_{HH} (dBZ)	Ka-band Z_{HH} (dBZ)	W-band Z_{HH} (dBZ)
Dry sand	40.9	40.9	40.9	40.3	35.2
Dry clay	38.6	38.6	38.5	38.0	33.3
Wet sand	45.2	45.2	45.2	44.5	37.4
Wet clay	42.9	42.9	42.9	42.2	35.5

particles greater than 1 mm in diameter decreases as a consequence of resonance effects.

2.1.3.2 Rocks

Rocks exhibit some differences in complex relative permittivity depending on rock type (Ulaby et al. 1990). However, the real component of the complex relative permittivity is approximately constant throughout the frequency range of weather radars. For simplicity, the rocks are assumed to be spherical, and the complex relative permittivities are chosen for sedimentary rocks (e.g., a common rock type).

Equivalent radar reflectivity factor exhibits large variations among common weather radar wavelengths for rocks, as shown in Fig. 2.17 with a concentration of 1 m^3. Mie scattering effects on radar reflectivity are clearly evident at each wavelength, commencing at a greater diameter for larger wavelengths. The highest Z_{HH} values are observed with larger radar wavelengths because

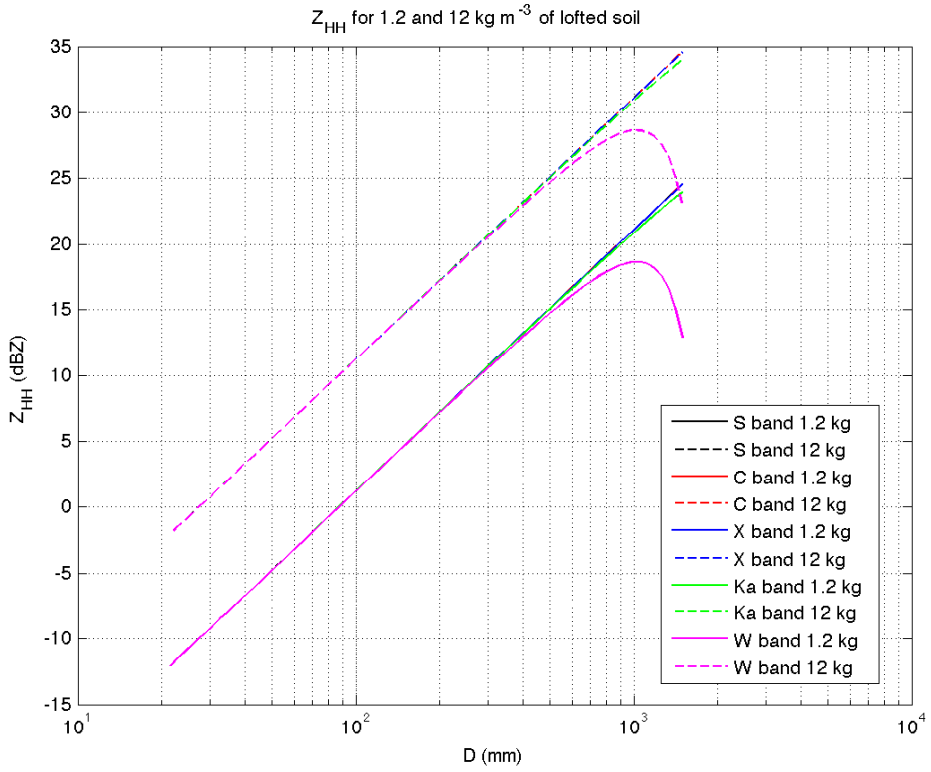

Figure 2.15: Equivalent radar reflectivity factor (Z_{HH}) as a function of size for 1.2 and 12 kg of dry sandy loam soil at S, C, X, Ka, and W bands. Even though soil particle concentrations decrease with increasing size, larger particle sizes have greater contributions to equivalent radar reflectivity factor except for the range of sizes where resonance are important.

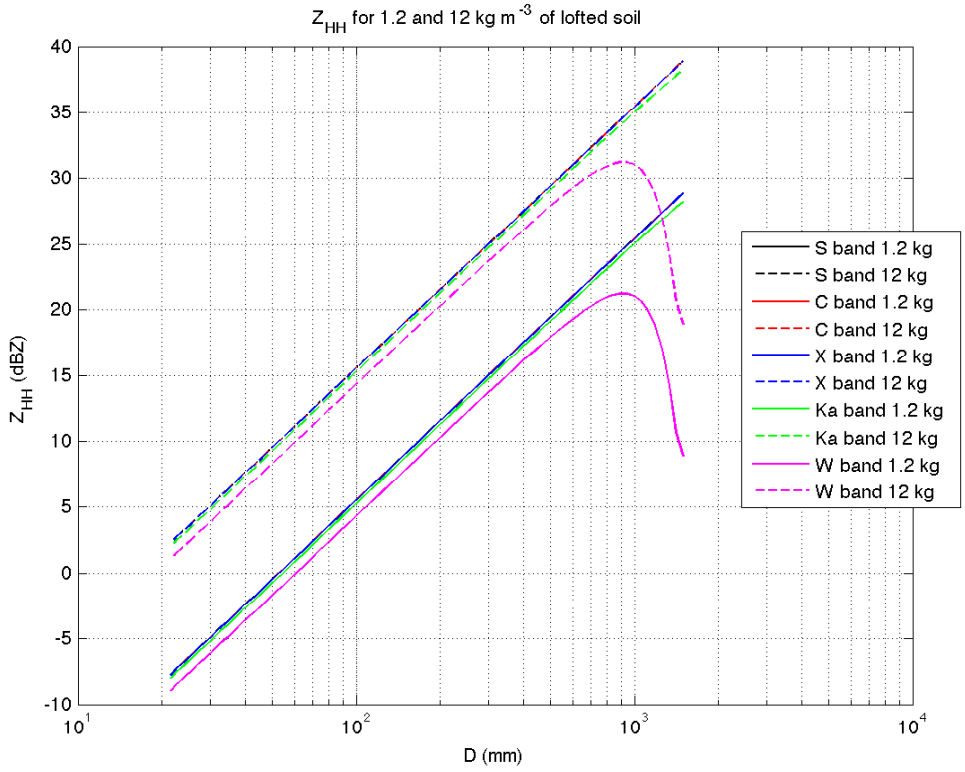

Figure 2.16: Equivalent reflectivity factor (Z_{HH}) as a function of size for 1.2 and 12 kg of dry clay loam soil at S, C, X, Ka, and W bands. Even though soil particle concentrations decrease with increasing size, larger particle sizes have greater contributions to equivalent radar reflectivity factor except for the range of sizes where resonance are important.

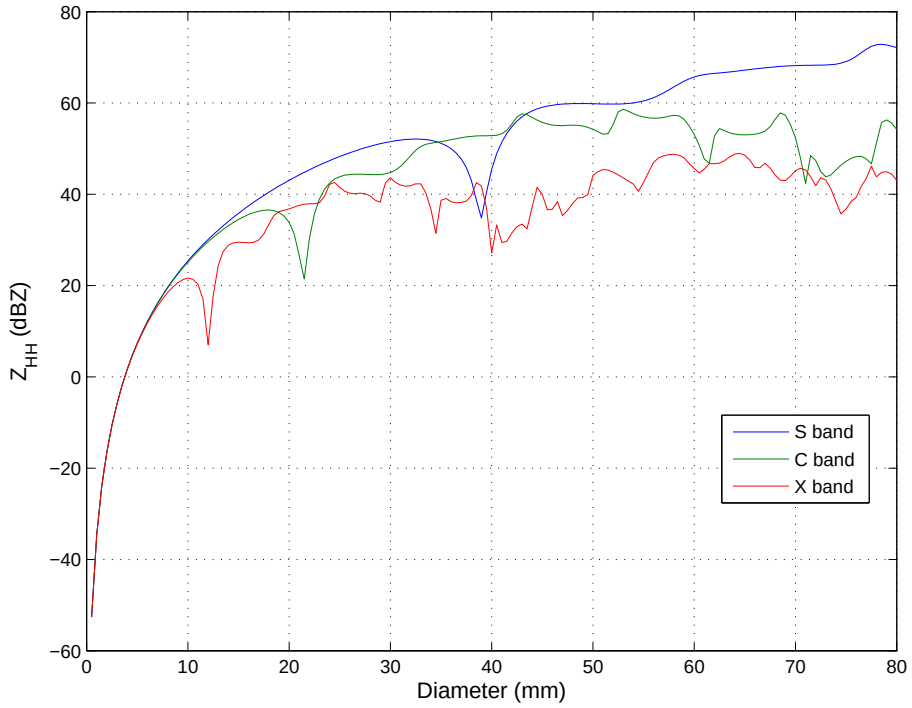

Figure 2.17: Equivalent reflectivity factor (Z_{HH}) at S, C, and X bands for rocks as a function of diameter (mm) with a concentration of 1 m^3. For rocks with diameters $> \frac{\lambda}{16}$, equivalent radar reflectivity factor has a complex relationship with rock diameter due to constructive and destructive interference associated with Mie scattering effects.

the backscatter cross-section increases proportionally to D^6 for a greater range of diameters prior to oscillating in the Mie scattering region. S- and X-band Z_{HH} clearly demonstrate this effect, as X-band Z_{HH} remains nearly constant over a large diameter range where S-band Z_{HH} increases.

Rocks exhibit Z_{HH} differences among wavelengths which could be exploited to ascertain rock size. While S-band Z_{HH} is well-correlated with rock size, the dependence of Z_{HH} on number concentration creates a challenge for relating

Z_{HH} directly to scatterer size. However, if a small number of dominant scatterers of similar type are present in a resolution volume, size classification may be more feasible using dual-wavelength differences because the number concentration is the same at both wavelengths and thus number concentration cancels out in a ratio of Z_{HH} at two different frequencies. Correlation coefficients between different dual-wavelength Z_{HH} differences and rock diameter are presented in Table 2.3. The highest correlation coefficients occur with combinations of S band and other frequencies, with the highest correlation occurring for the S – X band Z_{HH} difference.

Table 2.3: Correlation coefficient between rock diameter and dual-wavelength Z_{HH} differences for different radar wavelength combinations.

Wavelengths	Correlation Coefficient
S – C	0.66
S – X	0.87
C – X	0.33

2.1.3.3 Wood

Wood debris is commonly lofted in tornadoes passing over residential areas or areas with dense tree cover. In photographs and videos of tornadoes, wood debris is sometimes visible, and thus wood pieces may be among the largest scatterers in tornadoes (when present). Wood debris from buildings may include elongated

boards, such as a "2 X 4", with one dimension significantly longer than the other two dimensions. Plywood sheets with two similar dimensions and a small thickness are also common debris types, as well as fragmented pieces of wood. Wood debris could also result from lofted tree branches. In this section, both oblate and prolate spheroids are modeled to encompass both elongated debris similar to a "2 X 4" and oblate spheroids to examine more "plate-like" debris.

A complex relative permittivity, ϵ_r, of 2 - $0.2j$ is used at each wavelength, based on measurements at S band (Daian et al. 2006) and X band (Jebbor et al. 2011). Owing to the lack of studies of wood's complex relative permittivity, the variation of ϵ_r over different frequencies or wood types is unknown, and thus is assumed to be constant. To examine debris wetting effects on wood, the Maxwell-Garnet mixing formula is used (2.33) to compute ϵ_r.

For dry wood spheroids, equivalent radar reflectivity factor for wood prolate and oblate spheroids exhibits reduced dependence on size compared to the rock case. Equivalent radar reflectivity factors of prolate and oblate spheroids with axis ratios of 3 and $\frac{1}{3}$ at S, C, and X bands are shown in Figs. 2.18 and 2.19. For the prolate spheroids, Z_{HH} generally increases as a function of diameter, however, constructive and destructive interference due to resonance effects create large amplitude Z_{HH} oscillations. Z_{HH} oscillations due to resonance effects are more prominent at C and X bands, and oscillation frequency increases as radar frequency decreases. For oblate spheroids, Z_{HH} generally increases as a function of diameter at S band, however, Z_{HH} at C and X bands actually decreases for

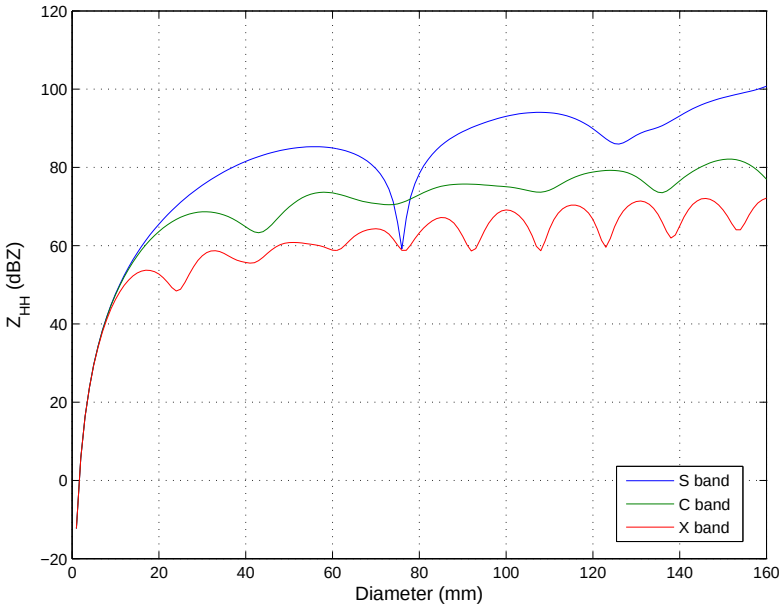

Figure 2.18: Equivalent radar reflectivity factor for a dry prolate wood spheroid with an axis ratio of 3 and a vertically oriented symmetry axis at S, C, and X bands. Equivalent radar reflectivity factor oscillates for wood spheroids with diameters greater than $\frac{\lambda}{16}$. In general, for the same diameter range equivalent radar reflectivity factor for prolate spheroids increases as radar wavelength increases.

large diameters. Given the complexity of Z_{HH} for prolate and oblate spheroids, debris size could not be uniquely determined from Z_{HH}.

Dual-wavelength Z_{HH} differences are prominent between S, C, and X, with the largest magnitude differences occurring between S and X band (Figs. 2.20 and 2.21). Hail exhibits similar behavior for large hailstones with greater Z_{HH} differences between S and X bands compared to S and C bands (e.g., Atlas and Ludlam 1961; Snyder et al. 2010; Picca and Ryzhkov 2012). For the prolate spheroid case, resonance scattering effects for horizontal, linearly polarized EM

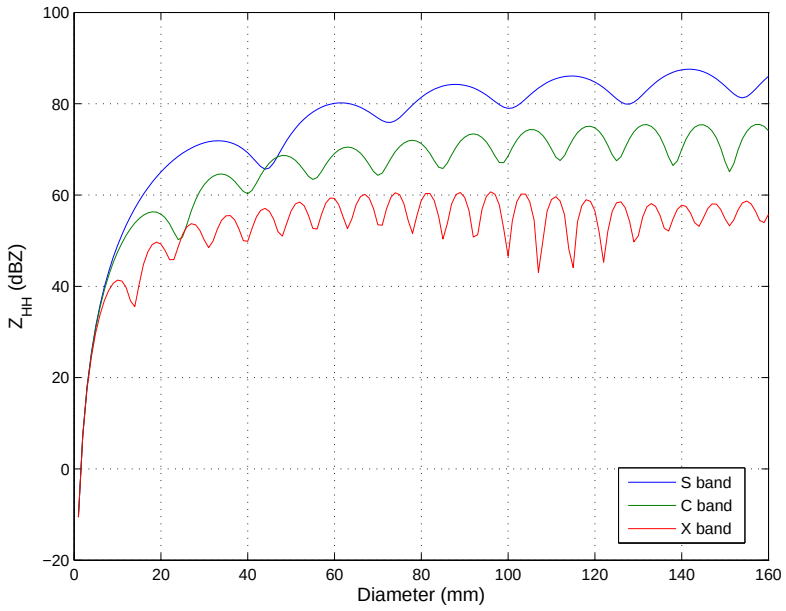

Figure 2.19: Equivalent radar reflectivity factor for a dry oblate wood spheroid with an axis ratio of $\frac{1}{3}$ and a vertically oriented symmetry axis at S, C, and X bands. Similar to prolate wood spheroids, equivalent radar reflectivity factor oscillates for wood oblate spheroids with diameters greater than $\frac{\lambda}{16}$. In general, for the same diameter range equivalent radar reflectivity factor for oblate spheroids increases as radar wavelength increases.

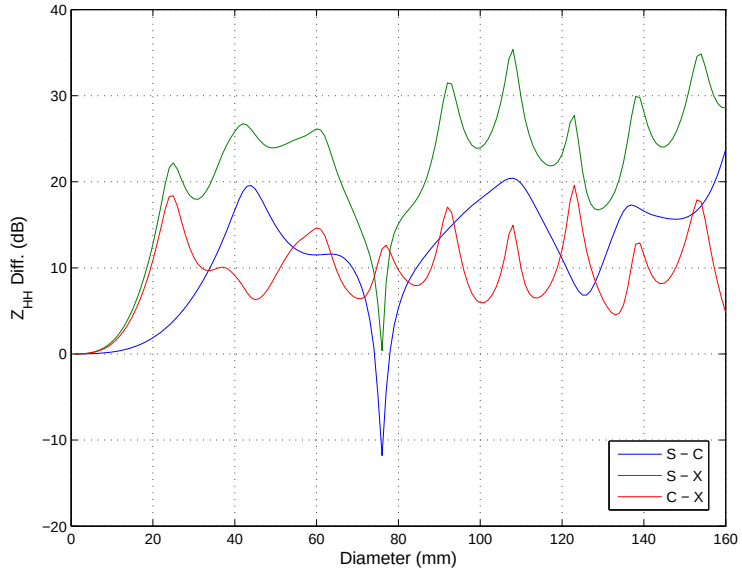

Figure 2.20: Equivalent radar reflectivity factor dual-wavelength differences for a dry prolate wood spheroid with an axis ratio of 3 at S, C, and X bands as a function of diameter (mm). Dual-wavelength differences exhibit complex relationships with debris size, particularly for diameters greater than $\frac{\lambda}{16}$.

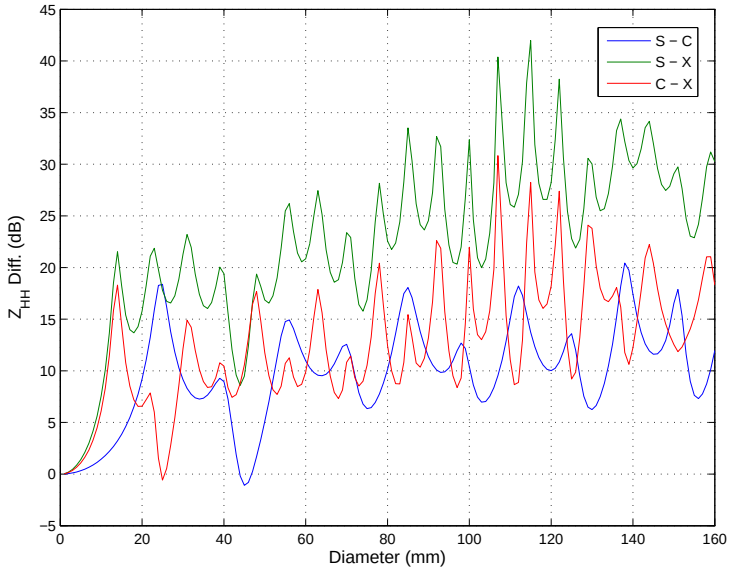

Figure 2.21: Equivalent radar reflectivity factor dual-wavelength differences for a dry oblate wood spheroid with an axis ratio of $\frac{1}{3}$ at S, C, and X bands as a function of diameter (mm). As observed for prolate wood spheroids, dual-wavelength differences exhibit complex relationships with debris size, particularly for diameters greater than $\frac{\lambda}{16}$.

Table 2.4: Correlation coefficient between dry prolate spheroid diameter and dual-wavelength Z_{HH} differences for different radar wavelength combinations.

Wavelengths	Correlation Coefficient
S – C	0.62
S – X	0.63
C – X	0.29

waves occur at a larger equivolume diameter compared to the oblate spheroid case because the prolate spheroid's horizontal dimension is smaller than the vertical dimension. As a result, large dual-wavelength differences for the prolate spheroid start at a greater equivolume diameter compared to the oblate spheroid case.

Dual-wavelength differences monotonically increase until the start of the first Z_{HH} oscillation at the shorter wavelength. Accordingly, S- and C-band Z_{HH} differences increase monotonically to a greater diameter than S- and X-band Z_{HH} differences. After the first Z_{HH} oscillation, however, large oscillations occur in the dual-wavelength Z_{HH} differences which become more complicated than Z_{HH} at a single frequency due to the superposition of two different resonance patterns. Dual-wavelength Z_{HH} differences exhibit modest positive correlations, with the highest correlation for both prolate and oblate spheroids occurring for S and X-band Z_{HH} differences (Tables 2.4 and 2.5).

Table 2.5: Correlation coefficient between dry oblate spheroid diameter and dual-wavelength Z_{HH} differences for different radar wavelength combinations.

Wavelengths	Correlation Coefficient
S – C	0.51
S – X	0.78
C – X	0.65

To examine debris wetting effects, T-matrix calculations are performed for wet prolate and oblate spheroids with axis ratios of 3 and $\frac{1}{3}$ using a fractional water content of 20%. Equivalent radar reflectivity factor for wet prolate and oblate spheroids are shown in Figs. 2.22 and 2.23. Depending on debris size, debris wetting can cause higher or lower equivalent radar reflectivity factor because resonance scattering effects change. However, mean equivalent radar reflectivity factor for wet debris is 3.8, 4.8, and 4.6 dB greater than dry debris for wet prolate spheroids at S, C, and X bands, respectively. For wet oblate spheroids, mean equivalent radar reflectivity factor is 5.4, 1.7, and 2.5 dB greater than dry oblate spheroids at S, C, and X bands, respectively. Thus, wetting effects on wood debris tend to increase backscattered power compared to dry debris.

2.2 Aerodynamic characteristics of debris

The diverse physical properties of debris that lead to complex electromagnetic scattering characteristics also lead to complex aerodynamic properties of debris.

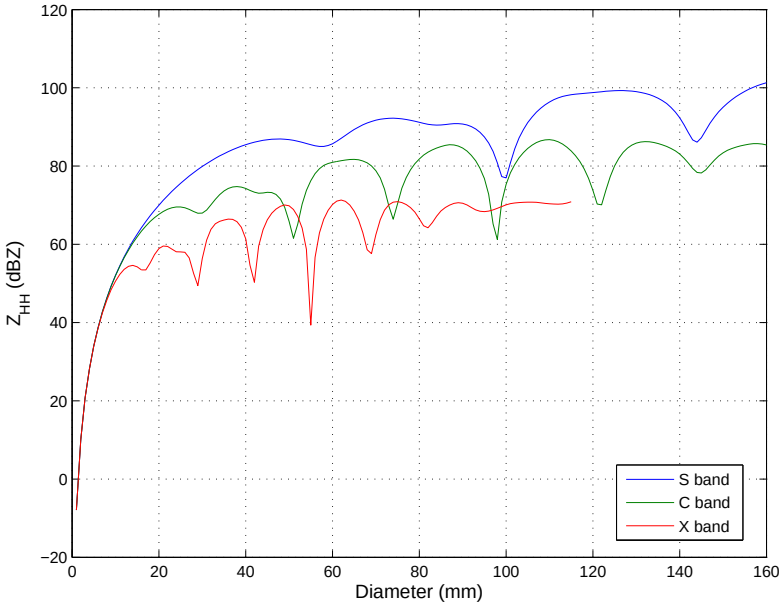

Figure 2.22: Equivalent radar reflectivity factor for a wet prolate wood spheroid with an axis ratio of 3 and a vertically oriented symmetry axis at S, C, and X bands. Equivalent radar reflectivity factor for wet prolate wood spheroids is generally higher than dry prolate spheroids.

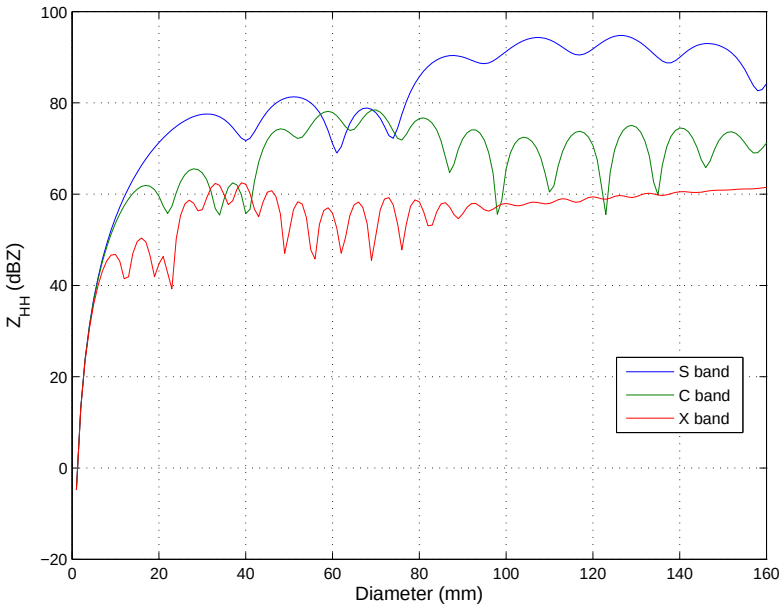

Figure 2.23: Equivalent radar reflectivity factor for a wet oblate wood spheroid with an axis ratio of $\frac{1}{3}$ and a vertically oriented symmetry axis at S, C, and X bands. Equivalent radar reflectivity factor for wet oblate wood spheroids is generally higher than dry oblate spheroids.

Debris aerodynamics can change as a function of the orientation of the debris relative to the wind. Moreover, aerodynamic properties of debris not only depend on physical characteristics of debris, but often vary significantly depending on characteristics of the wind flow (e.g., mean speed or turbulence). In this section, the aerodynamic properties of different airborne debris types are discussed, including a discussion of the effects of the surrounding flow. An understanding of debris aerodynamics is required to accurately calculate the three-dimensional motion of debris.

2.2.1 Aerodynamic forces

Aerodynamics literature discusses two types of objects: bluff and streamlined bodies (Simiu and Scanlan 1996; Holmes 2001; Flay 2013). Flow over the streamlined body exhibits parallel flow to a body (Fig. 2.24). In contrast, bluff bodies exhibit a separation of the flow at the upstream corner(s) of an object (Fig. 2.25), which creates a pressure minimum (wake low) downstream from the object. At the interface of the uniform flow surrounding the object and the downstream wake region, a shear layer develops with enhanced vortex generation. Vortices entrain air from the wake region, reducing pressure in the wake region. Note that if flow separation did not occur and streamlines remained parallel to the object, pressure would increase downstream as flow decelerates around the body.

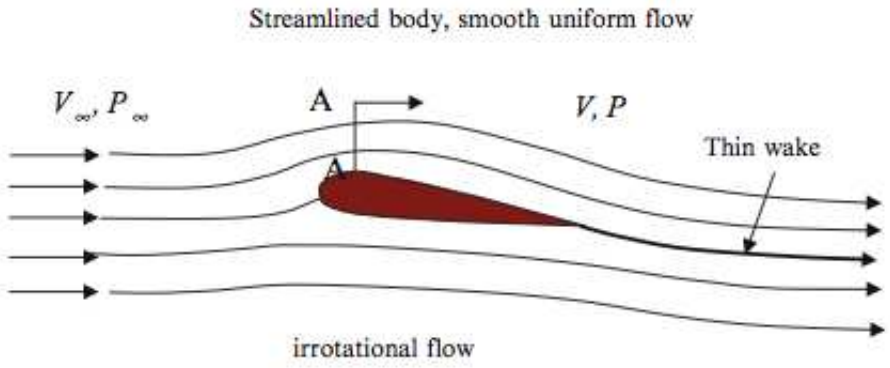

Figure 2.24: Example of uniform flow around a streamlined body (adapted from Flay (2013)). The streamlines are parallel to the object.

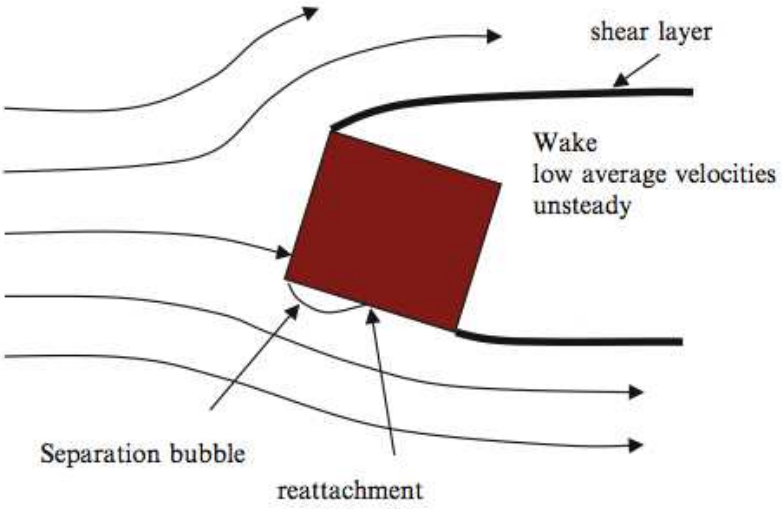

Figure 2.25: Example of uniform flow around a bluff body (adapted from Flay (2013)). The streamlines downstream from the object are not parallel, and a low pressure area develops on the downstream side of the object. A shear layer also develops at the interface between the uniform, outer flow and the downstream wake region.

Bernoulli's equation can illuminate some properties of the flow at the upstream stagnation point, and is used to derive the expression for a non-dimensional pressure coefficient. Bernoulli's equation (2.36) states that the static and dynamic pressure (first and second terms on the left-hand side of the equation) are constant along a streamline. In order for Bernoulli's equation to be valid, the flow must be inviscid and not rotating. Hence, Bernoulli's equation would not be valid in the wake region of the bluff body.

$$p + \frac{1}{2}\rho U^2 = Const. \tag{2.36}$$

The pressure difference between the ambient flow and the upstream stagnation point can be expressed as

$$p - p_o = \frac{1}{2}\rho \left(U_o^2 - U^2\right), \tag{2.37}$$

where the ambient flow velocity and pressure are expressed as U_o and p_o, respectively. To obtain a pressure coefficient, C_p, the right-hand side of (2.37) is divided by the dynamic pressure of the ambient flow. Thus, the pressure coefficient is,

$$C_p = \frac{\frac{1}{2}\rho \left(U_o^2 - U^2\right)}{\frac{1}{2}\rho U_o^2}. \tag{2.38}$$

To obtain a non-dimensional representation of aerodynamic forces (Holmes 2001), force coefficients (C_F), are obtained by dividing the aerodynamic force (F_A) by the product of the dynamic pressure and the object's area, A:

$$C_F = \frac{F_A}{\frac{1}{2}\rho U_o^2 A}. \tag{2.39}$$

Drag (lift) forces represents the aerodynamic force acting along (normal to) the direction of the wind. Hence, aerodynamic force coefficients are often represented in terms of the drag (C_D) and lift (C_L) coefficients. Aerodynamic drag forces can also be expressed in Cartesian coordinates, C_{dx}, C_{dy}, and C_{dz}. This representation of aerodynamics force coefficients is typical for wind tunnel measurements, which enable more sophisticated debris trajectory calculations by incorporating three-dimensional variations in aerodynamic forces (e.g., Richards et al. 2008).

2.2.2 Debris classification and wind speed thresholds for flight

A general classification of debris types based on aerodynamic properties was developed by Wills et al. (2002), who classified debris types into three categories: compact, plate and rod (Fig. 2.26). Compact debris possess similar spatial dimensions in all three dimensions, including debris such as rocks. Plate or sheet-type debris exhibit two similar spatial dimensions and one comparatively smaller dimension. Examples of plate-type debris include plywood sheets or roof-tiles. Finally, rod-type debris exhibit a particular length and diameter, and could represent debris with one dimension that is much longer than the other two dimensions, such as "2x4"s or fence posts.

The aerodynamic force, F_a, for different debris types is given by,

$$F_a = \frac{1}{2}\rho U_r^2 A C_F, \tag{2.40}$$

where ρ is the air density, U_r is the air-debris relative velocity, A is the cross-sectional area of the debris, and C_F is the aerodynamic force coefficient. For

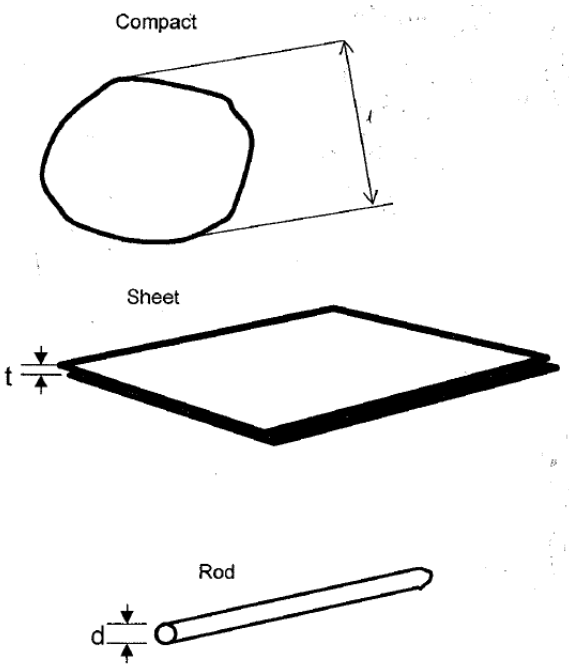

Figure 2.26: Compact, sheet, and rod type debris with characteristic dimensions (adapted from Wills et al. (2002)). Characteristic dimensions for the compact, sheet, and rod debris types are length (l), thickness (t), and diameter (d).

simplified estimates of compact debris motion, Wills et al. (2002) assumed that the aerodynamic force coefficient is independent of object orientation, or an average value over all orientations.

A critical component of debris studies involves determining the necessary criteria for the initial debris launch. The Wills et al. (2002) model provides a simplified physical model for understanding characteristics of debris flight for different debris types. For loose debris, debris flight occurs when the aerodynamic force acting on the debris exceeds its weight (i.e., $F_a > mg$). For debris attached to the surface, the force required to dislodge debris and enable flight exceeds its weight. Wills et al. (2002) define the fixing integrity parameter, I, as the ratio of the force required to dislodge the debris to its mass. Incorporating the fixing integrity parameter, a general equation for the criteria for debris flight is,

$$\frac{1}{2}\rho U_r^2 l^2 C_F > mgI. \tag{2.41}$$

Using the masses for compact (2.42), plate (2.43), and rod type debris (2.44), where t is the thickness of the plate, d is the diameter of the rod, and ρ_d is the debris density, the wind speed thresholds for debris flight is obtained for compact (2.45), sheet (2.46), and rod (2.47) debris.

$$m = \rho_d l^3 \tag{2.42}$$

$$m = \rho_d t l^2 \tag{2.43}$$

$$m = \rho_d \pi \left(\frac{d}{2}\right)^2 l \tag{2.44}$$

$$U_r^2 = 2\frac{\rho_d}{\rho}\frac{I}{C_F}lg \tag{2.45}$$

$$U_r^2 = 2\frac{\rho_d}{\rho}\frac{I}{C_F}tg \tag{2.46}$$

$$U_r^2 = \frac{\pi}{2}\frac{\rho_d}{\rho}\frac{I}{C_F}dg \tag{2.47}$$

The debris flight initiation equations above illuminate basic characteristics of debris flight initiation for different debris types. In particular, for a given debris type the wind speed required for debris to become airborne can be determined (although U_r is the air-debris relative velocity, U is the air speed before debris movement initiates). For plate- and rod-type debris, plate thickness and rod diameter affect the wind speed flight threshold, whereas the horizontal plate dimensions and rod length have no effect.

Although the basic formulation above provides a relationship between debris flight initiation and wind speed, the arbitrary fixing integrity parameter could vary widely for natural and man-made structures. Moreover, the complexities of aerodynamic force coefficients likely create more complicated behavior in debris flight characteristics. In particular, non-spherical debris exhibit varying aerodynamic force coefficients depending on their orientation (discussed later). Finally, other factors could lead to a time-dependent behavior of the fixing integrity parameter, such as debris impacts loosening a fixed object on the surface.

2.2.3 Measured aerodynamic force and moment coefficients

In this section, a brief discussion of drag force coefficients for different objects is discussed, including spherical, plate, and rod debris.

2.2.3.1 Spherical debris

Spherical debris represent the simplest case for drag force coefficients because their drag force coefficient is independent of orientation. Even though the drag force coefficient exhibits isotropic behavior, spherical debris drag force coefficients exhibit large variations as a function of the particle Reynolds number, Re_p,

$$Re_p = \frac{|u_i - u_{di}|\, D}{\nu}, \tag{2.48}$$

where u_i and u_{di} are the air and debris velocities in tensor notation, D is the particle diameter, and ν is the kinematic viscosity ($\nu = \frac{\mu}{\rho}$, where μ is the air viscosity). This Reynolds number formulation differs from the common form in fluid dynamics ($Re = uL/\nu$) because a particle-relative velocity is used and the particle diameter is used as a length scale. Laboratory measurements of C_D show that C_D decreases as Re_p increases (Fig. 2.27). White (2006) presents the following empirical formulation of C_D as a function of Re_p:

$$C_D = \frac{24}{Re_p} + \frac{6}{1 + \sqrt{Re_p}} + 0.4 \qquad 0 \leq Re_p \leq 2 \times 10^5 \tag{2.49}$$

which fits the data to within an accuracy of $\pm 10\%$.

For Re_p greater than 2×10^5, the flow around the sphere becomes "supercritical", and the flow around the sphere's surface becomes turbulent farther upstream (White 2006). A pressure gradient acts against the flow around the sphere on the downstream half because a pressure minimum exists at the midpoint (according to Bernoulli's law, the flow accelerates around the sphere and

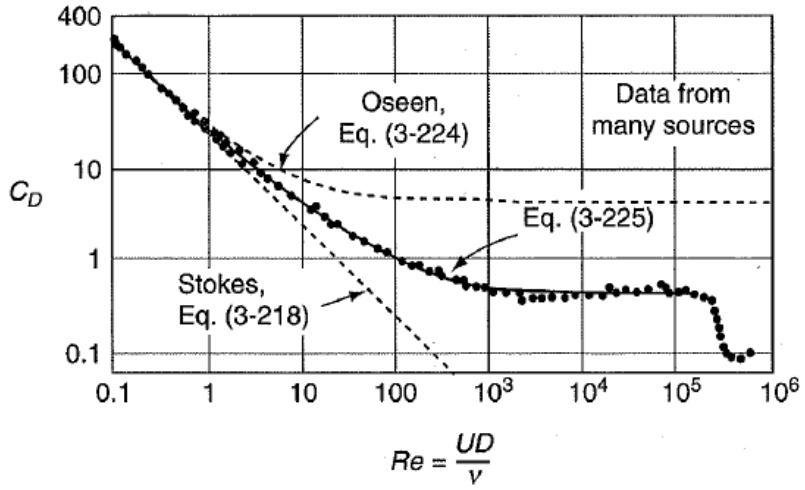

Figure 2.27: Drag force coefficient (C_D) as a function of the particle Reynolds number (Re_p) (adapted from White (2006)). C_D generally decreases as the particle Reynolds number increases.

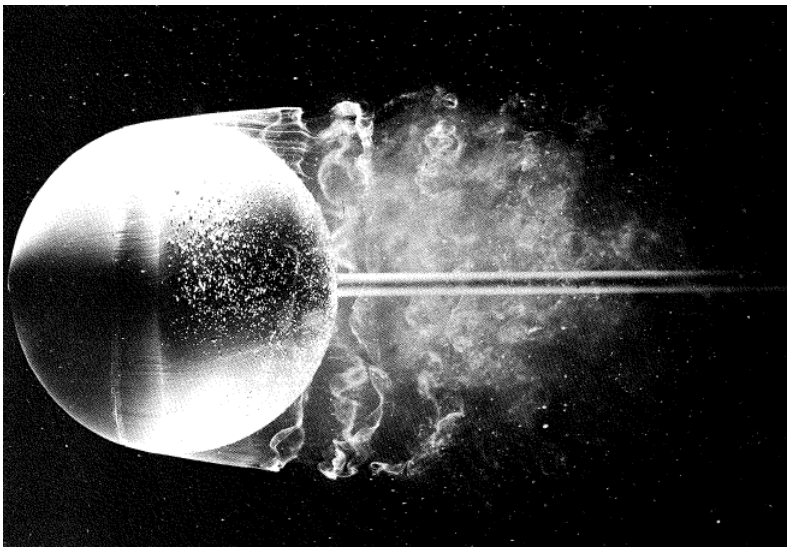

Figure 2.28: Example of a lower Reynolds number flow in which the wake forms on the upstream half of the sphere. A large wake develops on the downstream half of the sphere (adapted from Van Dyke (1982)).

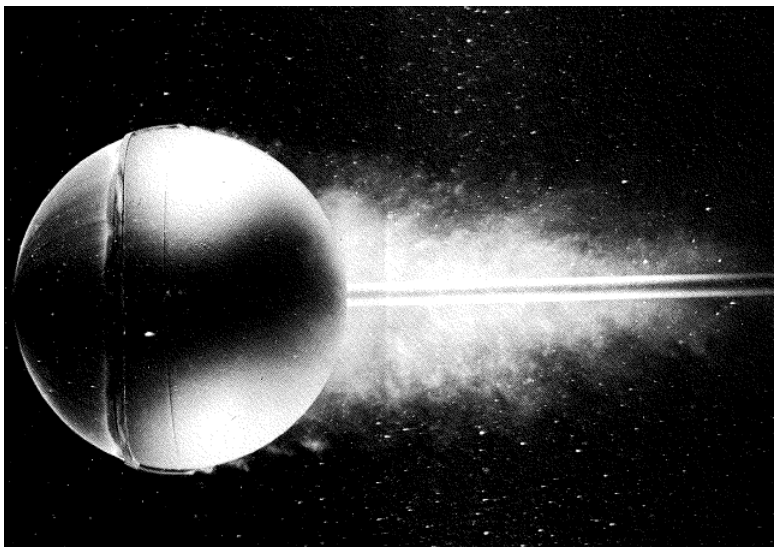

Figure 2.29: "Supercritical" flow in which wake formation occurs on the downstream half of the sphere. A trip wire is placed on the sphere to induce turbulence because much higher Reynolds number flow simulations are not feasible (adapted from Van Dyke (1982)).

therefore pressure must decrease). In the presence of turbulence, however, momentum transfer inhibits the near-surface flow reversal which causes the wake to form. As a result, increased turbulence leads to the wake forming further downstream and creates a smaller wake and reduced drag (White 2006; Flay 2013). Examples of laminar and turbulent flows are shown in Figs. 2.28 and 2.29.

2.2.3.2 Plate- and rod-type debris

In contrast to spherical debris, non-spherical debris pose unique challenges due to anisotropic variations in drag force coefficients. However, the sharp edges of debris cause flow separation and wake formation, even at low values of Re_p, which significantly reduces the dependence of the drag force coefficient on Re_p (Scruton 1981). Thus, measurements of drag force coefficients of non-spherical debris made at lower Re_p (e.g., in wind tunnels) can be extended to higher Re_p flows (Flay 2013).

Numerous wind tunnel measurements have been conducted to determine the normal force coefficients, C_N, for square plates in two-dimensional flows (Hoerner 1965; Tachikawa 1983; Lin et al. 2006; Holmes et al. 2006). C_N represents the aerodynamic force coefficient perpendicular to the plate, and the plate is assumed

to rotate only in the direction of the flow. Holmes et al. (2006) created a model for C_N based on these wind tunnel measurements (Fig. 2.30), as follows:

$$C_N = \left\{ \begin{array}{ll} 1.7(\theta/40^\circ) & \theta < 40^\circ \\ 1.15 & 40^\circ \leq \theta < 140^\circ \\ 1.7(180^\circ - \theta)/40^\circ & \theta \geq 140^\circ \end{array} \right\} \tag{2.50}$$

where θ is the attack angle of the square plate, or the angle between the wind vector and the square plate. In their model, the normal force coefficient increases with increasing plate inclination relative to the wind and a larger wake is produced behind the plate up to a 40° inclination angle. Using the normal force coefficients, the drag and lift force coefficients can be calculated using (2.51) and (2.52).

$$C_D = 0.1 + C_N \sin(\theta) \tag{2.51}$$

$$C_L = C_N \cos(\theta) \tag{2.52}$$

The aerodynamic moments, sometimes called pitching moments, describe the aerodynamic force acting on debris at its aerodynamic center. The aerodynamic center represents the point where the pitching moment does not depend on the inclination angle of debris (Flandro et al. 2011). The aerodynamic moment coefficients, C_M, determine the rotational characteristics of non-spherical debris. Holmes et al. (2006) developed a model for C_M based on wind tunnel data as

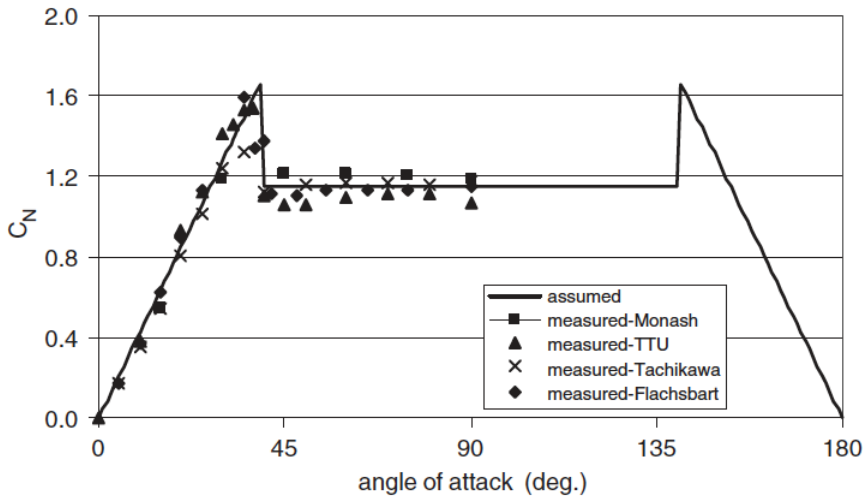

Figure 2.30: Wind tunnel measurements of the normal force coefficient, C_N, for square plates compared to the model by Holmes et al. (2006) (adapted from Holmes et al. (2006)). Normal force coefficients increase up to a 38° angle of a attack, and remain constant up to 90°.

a function of inclination angle where $C_M = C_N\left(\frac{d_{pc}}{l}\right)$, and $\frac{d_{pc}}{l}$ is computed as follows:

$$\frac{d_{pc}}{l} = \left\{ \begin{array}{ll} 0.3 - 0.22(\theta/38) & \theta \leq 38^\circ \\ 0.08\cos(2(\theta - 38)) & 38^\circ \leq \theta < 82.5^\circ \\ 0 & 82.5^\circ \leq \theta < 97.5^\circ \\ -0.08\cos(2(142 - \theta)) & 97.5^\circ \leq \theta < 142^\circ \\ -0.3 + 0.22((180 - \theta)/38) & \theta \geq 142^\circ \end{array} \right\} \tag{2.53}$$

where d_{pc} is the distance from the center of the plate to the location where the maximum pressure is exerted on the plate.

Surprisingly few studies have documented rotationally varying aerodynamic force and moment coefficients for rod-type debris. Aerodynamic force and moment coefficient measurements for rod-type debris are expected in the near future at the Environmental Wind Engineering Laboratory at Kyoto University. Lin et al. (2007) obtained mean and standard deviations of drag force coefficients for rod-type debris. The mean and standard deviation of C_D is 0.809 and 0.0203, respectively. Richards (2012) also show aerodynamic force and moment coefficients for rod-type debris with three different thicknesses.

Chapter 3

Tornado Damage Estimation Using Polarimetric Radar

This chapter discusses the potential of tornadic debris signature parameters for near real-time damage estimation using data from a polarimetric WSR-88D radar. TDS parameters are calculated and compared to detailed damage surveys provided by the National Weather Service (NWS). In addition to this study, an analysis of TDS parameters compared to damage surveys at C band is presented in Bodine et al. (2011).

3.1 Introduction

Although previous studies have shown the capability to use polarimetric radar to detect tornadoes, the application of the TDS to estimate near-real-time tornado damage severity has not yet been thoroughly examined. In this chapter, modified versions of the Ryzhkov et al. (2005) TDS parameters and new TDS parameters are examined using KOUN S-band polarimetric WSR-88D (Doviak et al. 2000) radar data. TDS parameters are compared to detailed damage surveys provided by the NWS Weather Forecast Office (WFO) in Norman, Oklahoma. TDS parameters are tested on the 14 tornado cases from the 10 May 2010 and 24 May 2011 tornado outbreaks, providing an analysis of the performance of TDS parameters for varied tornado intensities and sizes, distances from the

radar, and different storm-scale environments. In addition to these 14 tornado cases, seven tornado cases that did not produce TDSs are also documented.

Section 3.2 presents a description of the data from the Norman, Oklahoma (KOUN) polarimetric WSR-88D, a brief overview of the tornado outbreaks and tornado damage surveys, and a description of the TDS parameters evaluated in the study. In Section 3.3, detailed comparisons between two NWS damage surveys and TDS parameters are presented. Section 3.4 compares the highest and lowest values of TDS parameters for 14 tornado cases with the EF-rating of each tornado. A discussion of potential factors impacting the TDS and the strengths and limitations of each TDS parameter is presented in Section 3.5, followed by the conclusions from the study in Section 3.6.

3.2 Data and TDS parameter design

3.2.1 Data and damage survey overview

Data from the KOUN radar located in Norman, Oklahoma are analyzed in this study. KOUN is a prototype WSR-88D polarimetric (dual-pol) S-band radar with a 0.9° beamwidth and 250-m range resolution. Raw, Level-II KOUN data from the 10 May 2010 and 24 May 2011 tornado outbreaks are examined in this study (different from the gridded data used in Ryzhkov et al. 2005). During both events, KOUN operated volume coverage pattern (VCP) 12 (Brown et al. 2005b), which includes the following elevation angles: 0.5°, 0.9°, 1.3°, 1.8°, 2.4°, 3.1°, 4.0°, 5.1°, 6.4°, 8.0°, 10.0°, 12.5°, 15.6°, and 19.5°. The 0.5°, 0.9°, and 1.3°

elevation angles are oversampled at 0.5° resolution (Brown et al. 2005a), and the VCP requires 4 min 18 s to complete.

On 10 May 2010, 55 tornadoes struck portions of central and eastern Oklahoma. The two strongest tornadoes were rated EF-4 and occurred near Norman, Oklahoma. For a detailed discussion about the 10 May 2010 tornado outbreak and C-band observations of TDSs, the reader is referred to Palmer et al. (2011). On 24 May 2011, 12 tornadoes struck western and central Oklahoma, including 2 EF-4 tornadoes and 1 EF-5 tornado. Fig. 3.1 shows the tornado damage paths on 10 May 2010 and 24 May 2011, which were plotted using data provided by the Norman NWS WFO. Of the tornadoes shown in Fig. 3.1, only the tornadoes occurring within 120 km of KOUN are investigated.

Damage surveys based on the EF-scale are compared to TDS parameters. The EF-rating depends on the type of damage indicators along the damage path and the degree of damage (WSEC 2006). An important note is that the EF-scale underestimates tornado wind speeds when the highest degree of damage for the damage indicators is observed. In rural areas, the upper bound of wind speed that can be established from tree damage, farm buildings, or manufactured homes, is much lower than engineered structures, sometimes resulting in underestimated maximum wind speeds. Accordingly, some discrepancies between the along-path EF-scale rating and TDS parameters may be expected, even though both are dependent upon tornado damage. For example, consider a tornado producing isolated, EF-4 damage to a well-constructed home and an identical

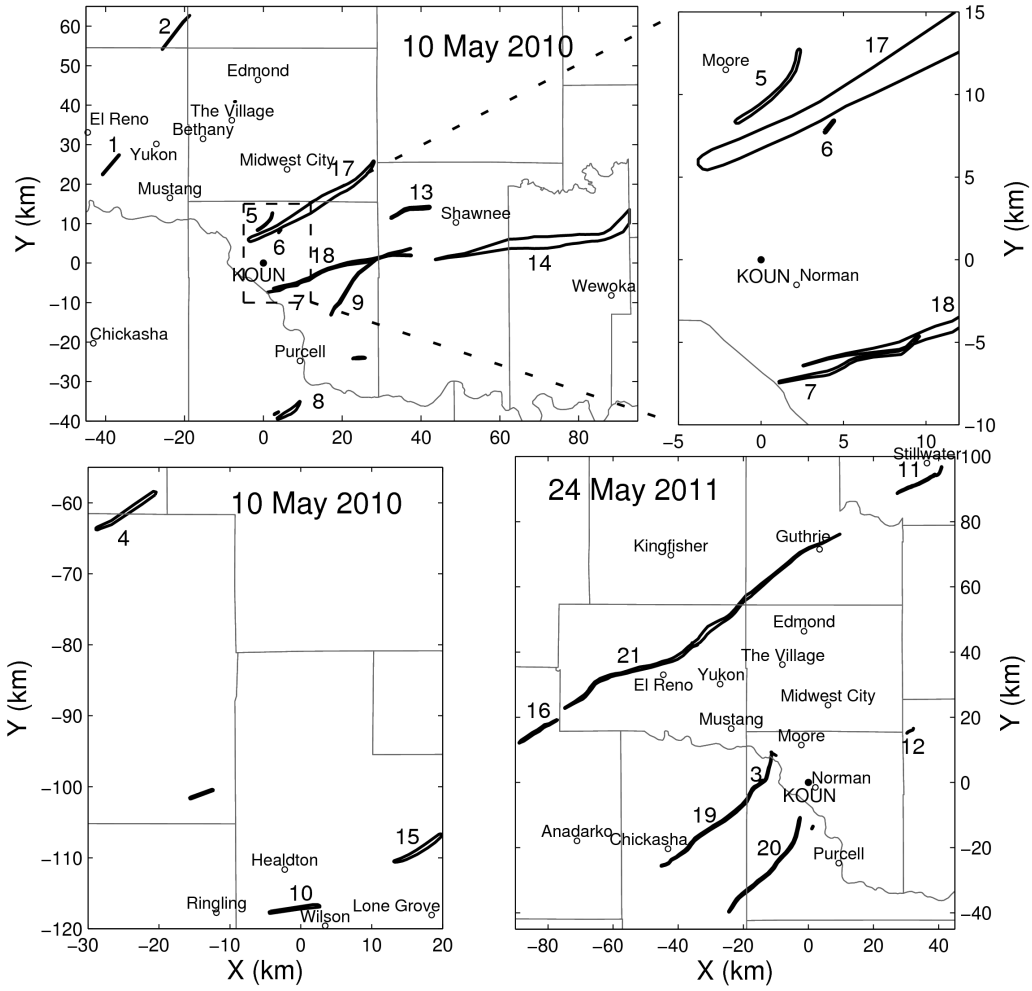

Figure 3.1: Damage tracks for tornadoes 1 – 21 discussed in this study from 10 May 2010 and 24 May 2011. The dashed box on the upper left panel indicates the location of the inset panel on the top right. The bottom left panel shows the tornadoes in south central Oklahoma on 10 May 2010 and the bottom right panel shows the damage survey from 24 May 2011. The X and Y coordinates indicate the zonal and meridional distance from KOUN.

tornado that remains in a rural area with no engineered structures. The TDS for a tornado producing EF-4 damage to the residence may not differ significantly from the same tornado in a rural area with no engineered structures unless the debris lofted from the residence substantially changes the TDS. Moreover, the contribution of debris from the isolated residence may only affect a small portion of the TDS for a large diameter tornado. Given that the differences in TDSs resulting from engineered structures and vegetation are not well understood, the differences in TDSs resulting from man-made structures and vegetation are unknown.

A reasonable hypothesis is that a more intense tornado may loft more tornadic debris than a weaker tornado. Nonetheless, complex relationships between damage characteristics and spatial distributions of tornado wind speeds may emerge. For example, damage caused by rapidly translating suction vortices may differ from damage associated with tornadoes characterized by nearly axisymmetric velocity distributions acting over longer periods of time (Snyder and Bluestein 2014). In the absence of engineered structures, the TDS may reflect changes in tornado intensity that cannot be deduced by the EF-scale in the absence of engineered structures (e.g., a violent tornado lofting more vegetation than a weak tornado). Nonetheless, because near-surface, tornado-scale wind measurements were not available along the damage path, the focus of this study is to compare EF-rating and damage path width to TDS parameters, not tornado intensity.

3.2.2 Threshold determination

Before TDS parameters are introduced, the determination of thresholds is discussed. Given that the data set encompasses a relatively small number of cases, the presented thresholds may not be optimal for all tornado cases. Moreover, differences in population density or vegetation type may result in variations of lofted debris type, size, and concentration, and could affect what TDS threshold is optimal.

The purpose of the thresholds is to identify resolution volumes containing tornadic debris. To identify possible thresholds, all of the 0.5° KOUN data within 2 km for the 21 tornado cases were aggregated to examine the distributions of Z_{HH}, Z_{DR}, and ρ_{HV} within 2 km of these tornadoes. Bivariate histograms of Z_{DR} and ρ_{HV}, and Z_{HH} and ρ_{HV} were produced using these data (Fig. 3.2). Bivariate histograms of Z_{DR} and ρ_{HV} reveal a wide range of Z_{DR} values for lower ρ_{HV} values, but a shift toward positive values for higher ρ_{HV} (Fig. 3.2a). The increase in Z_{DR} as ρ_{HV} increases is likely due to an increasing contribution of precipitation within the resolution volume (Bluestein et al. 2007; Schwarz and Burgess 2011; Bodine et al. 2011). To determine an appropriate ρ_{HV} threshold (hereafter, $\hat{\rho}_{HV}$), the median Z_{DR} was computed for all 0.5° KOUN data used in the study. The median Z_{DR} remains below 0.5 dB for ρ_{HV} values between 0.2 – 0.82. However, median Z_{DR} increases as ρ_{HV} increases for $\rho_{HV} > 0.82$, likely due to an increasing contribution of rain drops within the resolution volume. So, the $\hat{\rho}_{HV}$ used in this study is 0.82. At S-band, this $\hat{\rho}_{HV}$ also excludes very

large hail (Picca and Ryzhkov 2012). The median Z_{HH} for resolution volumes with $\rho_{HV} <$ below 0.82 was 43 dBZ. The median Z_{HH} value is used as the threshold for Z_{HH} (hereafter, $\hat{Z}_{HH}$). The first set of thresholds, $\hat{\rho}_{HV}$= 0.82 and $\hat{Z}_{HH}$= 43 dBZ, will be called T1. For comparison, a second set of thresholds is presented for comparison. A second $\hat{Z}_{HH}$ value of 51 dBZ is based on the 75th percentile Z_{HH} value for all of 0.5° KOUN data described above satisfying $\rho_{HV} <$ 0.82. A second $\hat{\rho}_{HV}$ of 0.72 is used, based on the 25th percentile ρ_{HV} value for all of the 0.5° KOUN data described above. The second set of thresholds will be called T2.

3.2.3 TDS parameters

This study investigates two categories of TDS parameters: lowest elevation angle and spatial TDS parameters. Lowest elevation angle TDS parameters examine 10th or 90th percentiles of polarimetric variables at the lowest available elevation angle (0.5° herein). The 10th percentile ρ_{HV} value, $q_{0.1}\{\rho_{HV}\}$, is defined as the 10th percentile of ρ_{HV} values where $Z_{HH} > \hat{Z}_{HH}$. The 10th percentile Z_{DR} parameter, $q_{0.1}\{Z_{DR}\}$, is computed using all resolution volumes with $Z_{HH} > \hat{Z}_{HH}$ and $\rho_{HV} < \hat{\rho}_{HV}$. $q_{0.9}\{Z_{HH}\}$ is defined as the 90th percentile Z_{HH} value where $\rho_{HV} < \hat{\rho}_{HV}$. Lowest elevation angle TDS parameters were only calculated if at least 10 resolution volumes satisfied the aforementioned thresholds.

A spatial resampling was applied to the lowest elevation angle TDS parameters using a nonparametric ordinary bootstrap resampling procedure (Efron

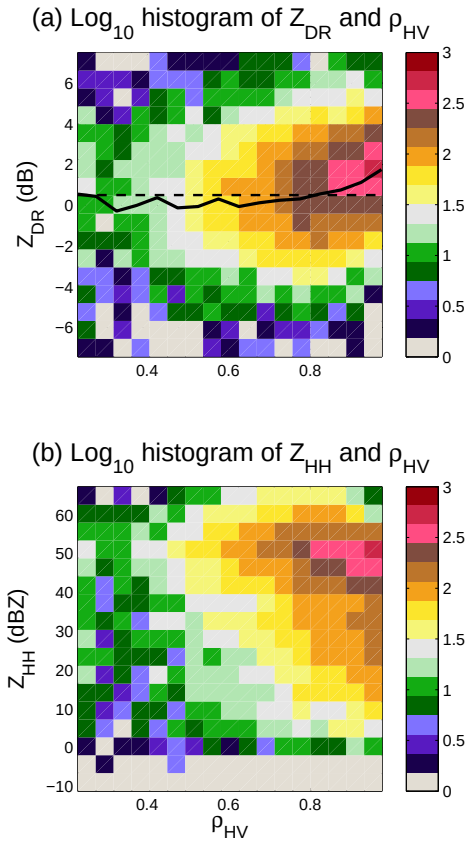

Figure 3.2: Log_{10} bivariate histograms showing (a) Z_{DR} and ρ_{HV}, and (b) Z_{HH} and ρ_{HV}. The solid black line on (a) shows the median value of Z_{DR} as a function of ρ_{HV}. The median Z_{DR} increases above 0.5 dB (black, dashed line) at $\rho_{HV} = 0.82$.

1979). The term bootstrap originated from the phrase, "to lift himself up by his bootstrap", and refers to doing something seemingly impossible. In statistics, bootstrapping involves resampling from the same population multiple times to improve statistical estimates. For statistics herein, 1000 bootstrap resamples were taken to estimate the 95% confidence interval (CI). An important note is that the spatial correlation of polarimetric radar variables may result in an underestimate of CI. While a moving-tile resampling procedure was considered (e.g., Davison and Hinkley 1997), it was not possible to obtain a sufficiently large number of tiles to produce enough resamples for analysis times with smaller TDSs.

Modeling studies suggest that large debris concentrations decrease as a function of height (Dowell et al. 2005), so temporal changes in lowest elevation angle TDS parameters could reflect changes in sampling height rather than temporal evolution of the tornado. Tornado observations at close ranges have observed that Z_{HH} often decreases with height in tornadoes (e.g., Wurman et al. 1996; Wurman and Gill 2000; Bluestein et al. 2004; Wakimoto et al. 2011), so changes in range must be considered when applying the lowest elevation angle TDS parameters, particularly for tornadoes at close ranges. Nonetheless, because the highest concentration of debris elements is near the surface and lofted debris reaches the lowest elevation angle faster than higher elevation angles, the lowest elevation angle may yield the most important information about lofted tornadic debris and the severity of tornado damage.

Spatial TDS parameters provide a method of estimating the amount of resolution volumes containing tornadic debris. These parameters are based on the areal or volumetric coverage of the TDS, defined using $\hat{Z}_{HH}$ and $\hat{\rho}_{HV}$. The areal coverage of the TDS, A^i_{TDS}, is the total area of resolution volumes where $Z_{HH} > \hat{Z}_{HH}$ and $\rho_{HV} < \hat{\rho}_{HV}$, and provides an estimate of the total area of resolution volumes containing debris at a particular elevation angle, i. Quantization effects are possible for smaller tornadoes where only a few resolution volumes contain a TDS. For the time series of TDS parameter presented later, however, typical numbers of resolution volumes ranged from 30 – 200. A^i_{TDS} is computed at multiple elevations to estimate the TDS volume, V_{TDS}. V_{TDS} (3.1) is obtained by summing the areal coverage through all elevation angles in the volume (N total elevation angles) after computing the representative depth of each elevation angle, Δh_i. If a TDS is observed between two consecutive elevation angles, it is assumed to be continuous between the two elevation angles.

$$V_{TDS} = \sum_{i=1}^{N} A^i_{TDS} \Delta h_i. \tag{3.1}$$

To compute Δh_i, the midpoint between the adjacent upper and lower elevation angles must be computed. The lower midpoint, z_L, is determined by averaging the beam height at the current elevation angle, i, and the previous elevation angle, $i-1$. The upper midpoint, z_U, is determined by averaging the beam height of the current elevation angle and next elevation angle, $i+1$. Then, Δh_i is z_U - z_L.

The final TDS parameter is the maximum TDS height, h_{max}, which is the maximum height where $Z_{HH} > \hat{Z}_{HH}$ and $\rho_{HV} < \hat{\rho}_{HV}$ during a volume scan. As a check for vertical continuity of the TDS, the TDS must be also observed at the next lowest elevation angle (except at the lowest elevation angle).

3.3 Detailed comparisons with damage surveys

3.3.1 Chickasha-Newcastle EF-4 tornado

The 24 May 2011 Chickasha-Newcastle EF-4 tornado forms in the southern part of Chickasha, Oklahoma at 2206 UTC. At 2208 UTC, the tornado produces EF-0 to EF-1 damage (Fig. 3.3). Two resolution volumes with Z_{HH} between 30 – 40 dBZ and $\rho_{HV} < 0.85$ are observed at 0.5° (about 580 m AGL), perhaps indicating some lofted light debris by the tornado (not shown). At 2212 UTC, the tornado produces EF-1 and EF-2 damage on the east side of Chickasha (Fig. 3.3, 3.4). Fig. 3.5 shows the 0.5° elevation Z_{HH}, v_r, ρ_{HV}, and a TDS is seen at X = -41 km, Y = -23 km. The changes in TDS parameters correspond to an increase in tornado EF-rating during this period (Fig. 3.6). $q_{0.9}\{Z_{HH}\}$ increases (Fig. 3.6a,b), and $q_{0.1}\{\rho_{HV}\}$ and $q_{0.1}\{Z_{DR}\}$ decrease for thresholds T1 (Fig. 3.6c,e). The higher $\hat{Z}_{HH}$ imposed for T2 prevents a TDS parameter calculation for $q_{0.1}\{\rho_{HV}\}$ and $q_{0.1}\{Z_{DR}\}$ until 2216 UTC (Fig. 3.6d,f). The areal coverage of the TDS at the lowest elevation angle, A^1_{TDS}, TDS volume, and TDS height increase for T1, but A^1_{TDS} and the TDS height do not change for T2

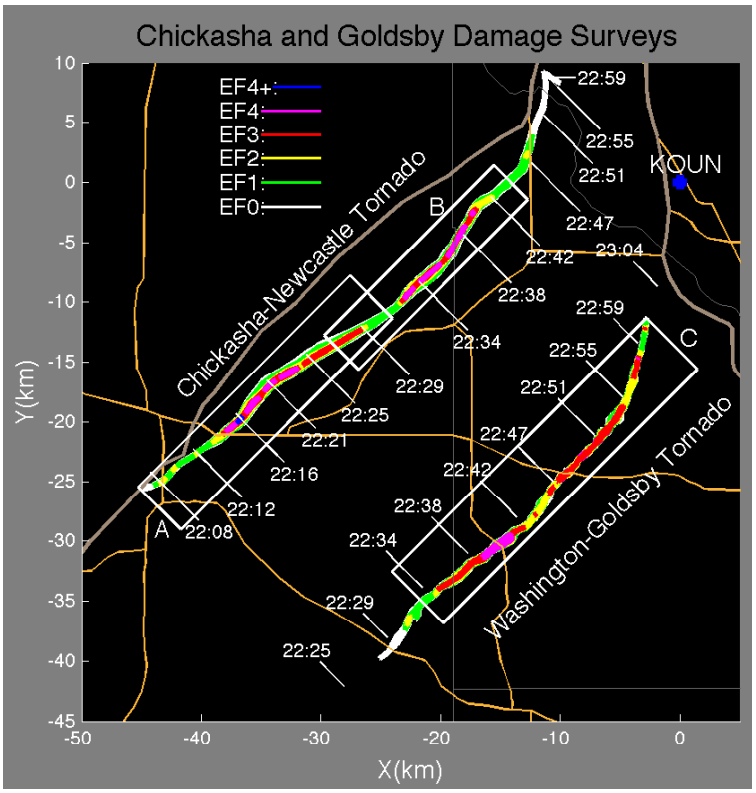

Figure 3.3: Damage surveys complied by the Norman, Oklahoma NWS WFO for the Chickasha-Newcastle and Washington-Goldsby tornadoes on 24 May 2011. The EF-rating along the damage path is contoured, and the times and locations of the center of tornado vortex signature at 0.5° are shown by the white text and lines, respectively. The blue circle shows the location of KOUN. The boxes A, B, and C denote parts of the damage path shown in more detail in Fig. 3.4.

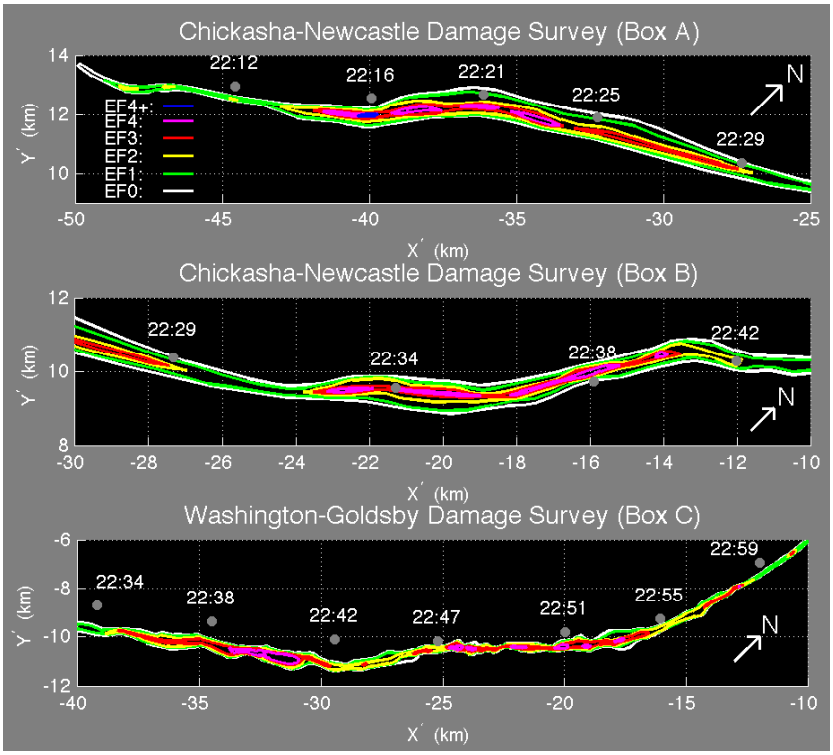

Figure 3.4: Zoomed and rotated images of the Chickasha-Newcastle tornado damage path (A and B), and the Washington-Goldsby tornado damage path (C) on 24 May 2011. The image has been rotated so that the x-axis is oriented southwest to northeast, the y-axis is oriented from southeast to northwest. The EF-rating along the damage path is contoured, and the times and locations of the center of tornado vortex signature at 0.5° are shown by the white text and gray dots, respectively. The white arrow points north.

(Fig. 3.7). During this period, the width of the damage path remains between 150 – 250 m (Fig. 3.4).

The tornado EF-rating increases to EF-4 and the damage path widens from 250 – 650 m between 2212 and 2216 UTC (Fig. 3.4). For thresholds T1 and T2, $q_{0.9}\{Z_{HH}\}$ increases (no CI overlap), and $q_{0.1}\{Z_{DR}\}$ and $q_{0.1}\{\rho_{HV}\}$ values decrease to their lowest values observed for the tornado (Fig. 3.6). While the CIs at 2212 and 2216 UTC overlap for $q_{0.1}\{\rho_{HV}\}$ and $q_{0.1}\{Z_{DR}\}$, the CIs do not overlap the mean over all resamples. Hence, a statistically significant difference remains likely. For both thresholds, A^1_{TDS}, TDS volume, and TDS height increase (Fig. 3.7). The volumetric TDS parameters exhibit a more substantial change than the lowest elevation angle TDS parameters. Because spatial TDS parameters are based on the spatial coverage of resolution volumes with tornadic debris, these parameters may provide a better estimate of the total amount of damage occurring. Moreover, TDS volume and height increase due to the vertical advection of tornadic debris through the updraft.

The tornado produces EF-3 to EF-4 damage over a 700 – 1000 m path between 2221 – 2229 UTC (Fig. 3.4). During this period, $q_{0.9}\{Z_{HH}\}$ exhibits statistically significant increases for both T1 and T2 (Fig. 3.6a,b). $q_{0.1}\{\rho_{HV}\}$ and $q_{0.1}\{Z_{DR}\}$ remain very low for both T1 and T2, and statistically significant changes are not observed (Fig. 3.6c,d,e,f). The brief increase in $q_{0.1}\{Z_{DR}\}$ occurs as a band of large drops wraps around the vortex at 2221 UTC (not shown), and may have increased Z_{DR} values. At 2225 and 2229 UTC, a TDS based on

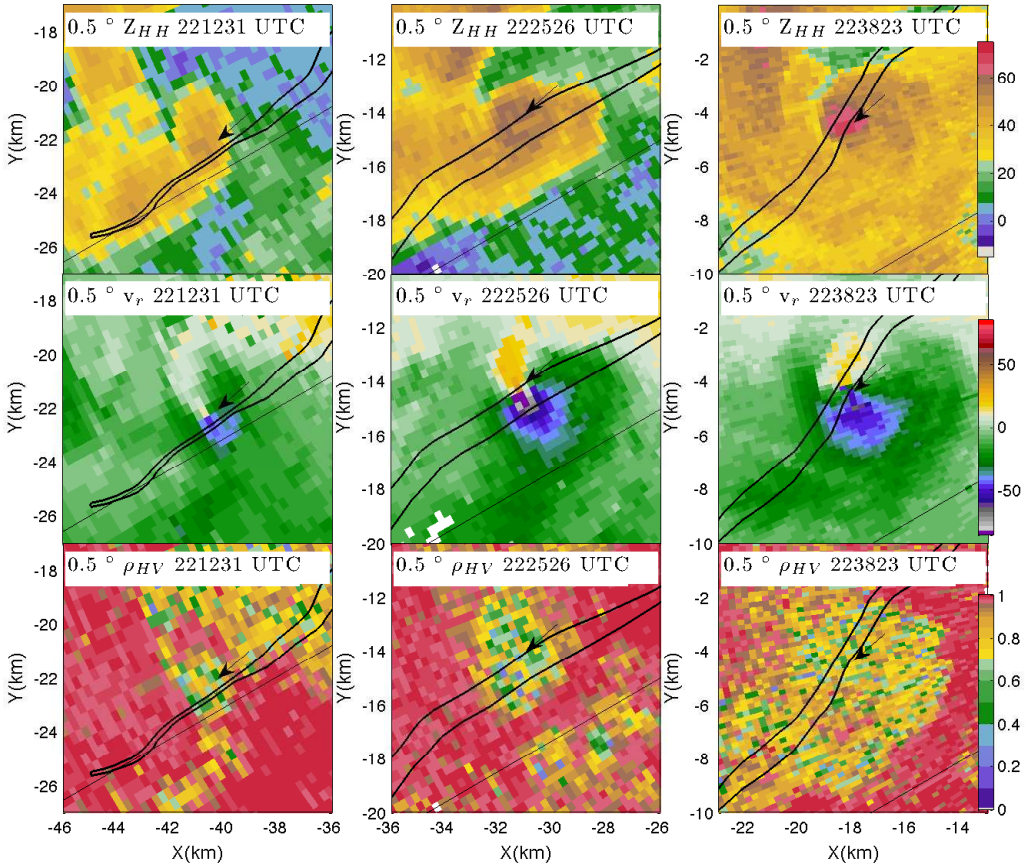

Figure 3.5: 0.5° elevation Z_{HH}, v_r, ρ_{HV} at 2212, 2225, and 2238 UTC for the Chickasha-Newcastle, Oklahoma tornado. The solid black line shows the Chickasha, Oklahoma damage path and the thin black line is the radial at a 240° azimuth. The black arrow indicates the location of the TDS.

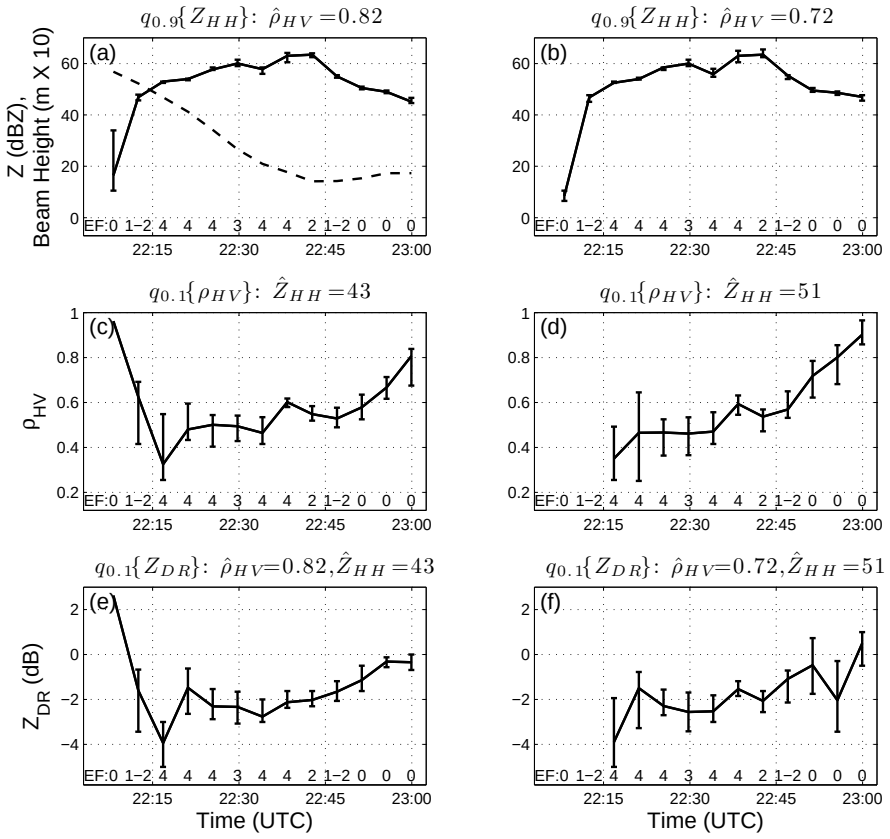

Figure 3.6: TDS parameters $q_{0.9}\{Z_{HH}\}$ for (a) T1 and (b) T2, $q_{0.1}\{\rho_{HV}\}$ for (c) T1 and (d) T2, and $q_{0.1}\{Z_{DR}\}$ for (e) T1 and (f) T2, shown for the Chickasha, Oklahoma EF-4 tornado. The error bars show the 95% CI for each parameter based on 1000 bootstrap resamples. The black dash dotted line on (a) shows the height of the beam at the 0.5° elevation (in m times 10).

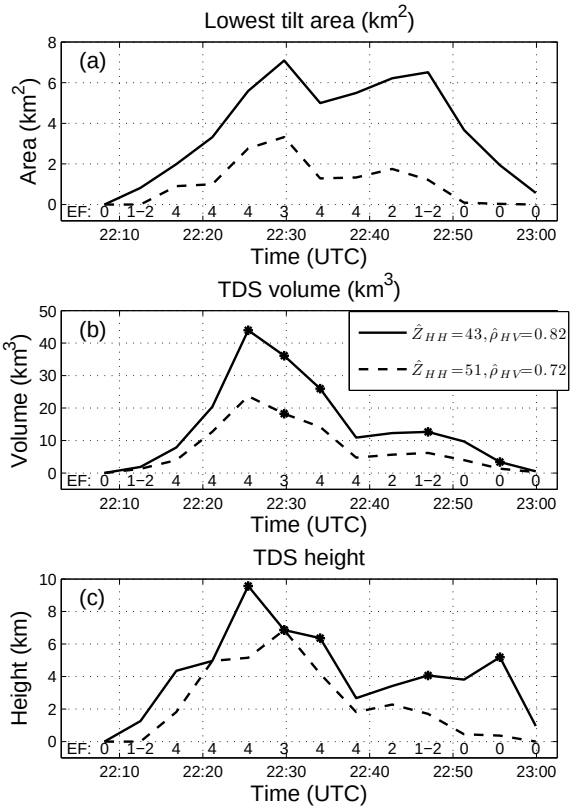

Figure 3.7: (a) A^1_{TDS} for T1 and T2, (b) TDS volume for T1 and T2, (c) h_{max} for T1 and T2, shown for the Chickasha, Oklahoma EF-4 tornado. For h_{max} and TDS volume, the black dots indicate where a TDS occurs at the highest elevation angle, so the TDS may extend higher and the TDS height and volume may be underestimated. For each plot, the solid and dashed lines show the values for T1 and T2, respectively.

threshold T1 is identified at the highest elevation angle, so the TDS volume and height shown are likely underestimated (Fig. 3.7b). At 2225 UTC, the maximum TDS height and volume for T1 are observed, 9.6 km and 44 km^3, respectively. Figs. 3.5 and 3.8 show Z_{HH}, v_r, and ρ_{HV} at 0.5°, 3.2°, 8.1°, and 15.6° elevation angles. A TDS occurs at each elevation angle, although the areal extent of the TDS decreases at the higher elevation angles. Using thresholds T2, the TDS volume reaches a maximum of 24 km^3 (Fig. 3.7b). While the TDS extends through the highest elevation angle at 2229 UTC, the TDS volume of 19 km^3 is likely a good estimate because the areal coverage of debris resolution volumes at 19.5° elevation angle is quite small compared to the lower elevation angles.

Between 2229 – 2234 UTC, the damage survey indicates a 3-km swath where the damage path narrowed to 300 – 400 m and primarily EF-1 damage is observed (Box B in Fig. 3.4). Between 2229 – 2234 UTC, the TDS height and volume for T2 both decrease, while the TDS height and volume for T1 remain unbounded (Fig. 3.6c,d). For this particular case, the less stringent thresholds T1 are less useful because they do not constrain the TDS height within the VCP. The 0.5° elevation scans occur at 2229 and 2234 UTC, so KOUN did not have observations at the 0.5° elevation during the brief period of reduced damage severity and extent. A statistically significant reduction in $q_{0.9}\{Z_{HH}\}$ is observed at 2234 UTC compared to 2229 and 2238 UTC. Hence, a slight reduction in the $q_{0.9}\{Z_{HH}\}$ at 2234 UTC could correspond to less debris lofted at 0.5° elevation (Fig. 3.6a,b).

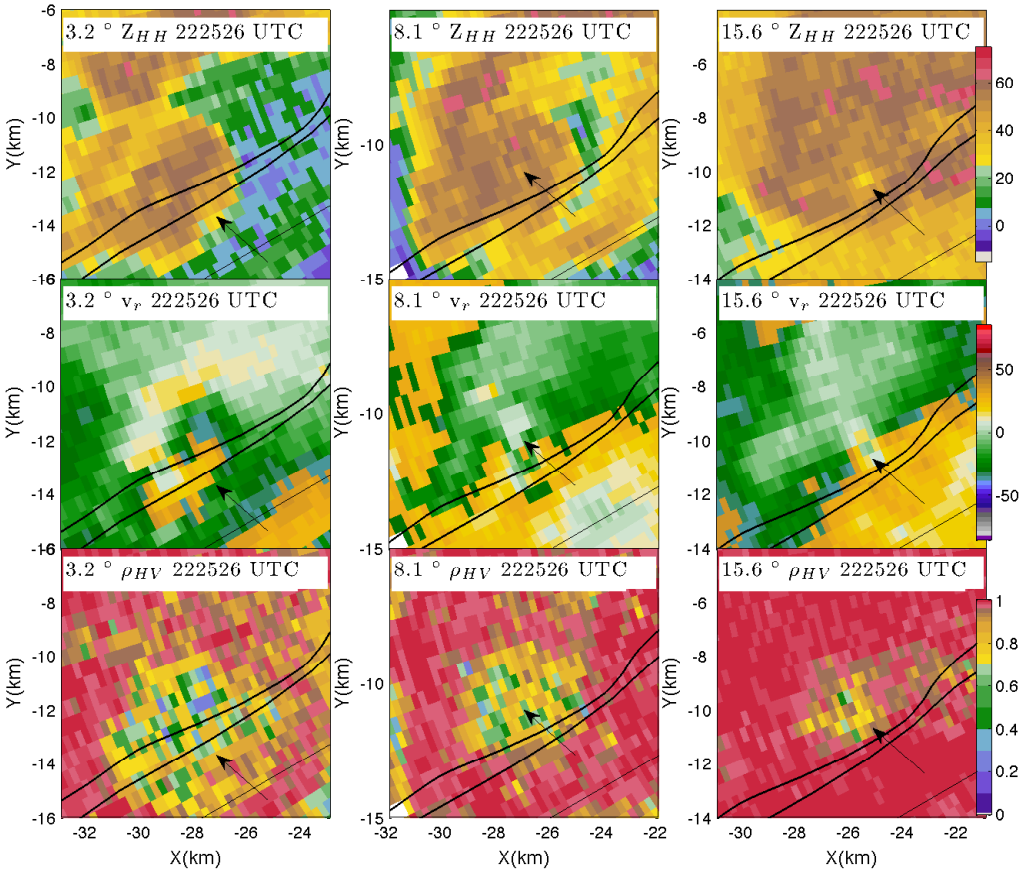

Figure 3.8: 3.2°, 8.1°, and 15.6° elevation Z_{HH}, v_r, ρ_{HV} at 2225 UTC for the Chickasha, Oklahoma tornado, which correspond to an altitude of 1.9, 4.6, and 7.8 km AGL at the center of the image. The thin black line is the radial at a 240° azimuth, and the black arrow indicates the location of the TDS.

The period of reduced damage severity and extent corresponds to a more pronounced decrease in TDS height and volume compared to $q_{0.9}\{Z_{HH}\}$. The TDS volume and height remain relatively low between 2234 – 2238 UTC (although still lofting debris above 2 km) after the tornado EF rating increases to 3 and 4 (Fig. 3.4). However, the reduced TDS height and volume may be attributed to the brief decrease in damage severity and extent and consequently less lofted debris through the storm, or a decrease in updraft intensity which would decrease the vertical velocities of debris elements. Given that debris must be lofted to 5 km to affect the maximum height of the TDS, we suspect that decreased updraft intensity may play a role in lowering the TDS height and perhaps reducing the TDS volume.

The EF-rating decreases from 4 to 1 between 2238 – 2247 UTC (Fig. 3.3). $q_{0.9}\{Z_{HH}\}$ decreases (Fig. 3.6a,b) while $q_{0.1}\{\rho_{HV}\}$ and $q_{0.1}\{Z_{DR}\}$ do not exhibit statistically significant changes. The spatial TDS parameters remain relatively constant or even increase in some cases (Fig. 3.7). During the 2238 UTC volume scan, debris fallout away from the tornado occurs within the rear-flank downdraft (RFD) with high Z_{HH} (40 – 55 dBZ) and low ρ_{HV} (< 0.8) (Fig. 3.5). The increased amount of debris at the lower elevation angles causes the areal coverage parameter to increase or remain constant (Fig. 3.7a), even though the severity of damage and amount of damage decrease. The large region of debris fallout may indicate a weakening of the updraft, as previously suggested. For thresholds T1 and T2, TDS volume and h_{max} exhibits a secondary maximum during the 2242

and 2247 UTC scans, although h_{max} is lower than the 6+ km maximum observed earlier (Fig. 3.7b,c). In this case, the vertical advection of lofted tornadic debris during the reintensification of the tornado and widening of the damage path between 2234 – 2238 UTC may cause this maximum in TDS height 5 – 10 min later. However, a weaker updraft could explain why the TDS height and volume remain lower than the previous period of EF-3 and EF-4 damage.

As the tornado dissipates between 2251 – 2259 UTC, most of the TDS parameters indicate a decrease in the amount of lofted tornadic debris. A^1_{TDS}, and TDS volume decrease throughout this period for both T1 and T2. The TDS height for T2 decreases, while the TDS height for T1 fluctuates considerably. At 2259 UTC, the TDS parameters indicate a decrease in the amount of tornadic debris lofted, and the tornado dissipates at 2301 UTC according to the NWS damage survey (Fig. 3.3). By 2259 UTC, $q_{0.9}\{Z_{HH}\}$ falls below 50 dBZ, and $q_{0.1}\{\rho_{HV}\}$ and $q_{0.1}\{Z_{DR}\}$ both increase to their highest values since the tornado formed (Fig. 3.6). The CIs reveal statistically significant increases in $q_{0.9}\{Z_{HH}\}$ and decreases in $q_{0.1}\{\rho_{HV}\}$ and $q_{0.1}\{Z_{DR}\}$ between 2251 – 2259 UTC. A^1_{TDS} and TDS volume decrease to their lowest values since the tornado formed, and TDS is only detected when using thresholds T1 within the lowest 1 km (Fig. 3.6). Some of the remaining areas of high Z_{HH} and low ρ_{HV} could result from debris fallout from the weakening tornado and updraft and/or debris with small terminal fall speeds (e.g., leaves, insulation).

3.3.2 Washington-Goldsby EF-4 tornado

The 24 May 2011 Washington-Goldsby EF-4 tornado forms two miles west of Bradley, Oklahoma at 2226 UTC (Fig. 3.3). At 2225 UTC, while a TDS is not observed, ρ_{HV} values fall below the thresholds for T1 and T2 in the TVS (not shown) where Z_{HH} is between 20 – 25 dBZ (Fig. 3.9a,b). While lower ρ_{HV} could result from a lower signal-to-noise ratio (SNR), much higher ρ_{HV} values (0.97 – 0.98) are observed at 20–25 dBZ within the hook echo (in regions with small drops). So, the lower ρ_{HV} values within the TVS could indicate some light debris being lofted at the onset of tornadogenesis.

The tornado produces EF-0 damage at 2229 UTC consisting of small and large branch damage to hardwood trees (Fig. 3.3). Fig. 3.11 shows the 0.5° Z_{HH}, v_r, and ρ_{HV} at 2229, 2238, and 2259 UTC. At 2229 UTC, a TDS can be seen by high Z_{HH} ($>$ 50 dBZ) and low ρ_{HV}. $q_{0.9}\{Z_{HH}\}$ increases to 48 and 50 dBZ, respectively for T1 and T2 (Fig. 3.9a,b), and $q_{0.1}\{\rho_{HV}\}$ and $q_{0.1}\{Z_{DR}\}$ indicate low ρ_{HV} and Z_{DR} values that were not present in the previous volume scan (Fig. 3.9c-f). The spatial TDS parameters increase between 2225 – 2229 UTC (Fig. 3.10). Between 2229 – 2234 UTC, the tornado produces EF-1 and EF-2 damage and the width of the damage path is between 300 – 400 m (Figs. 3.3, 3.4). At 2234 UTC, $q_{0.9}\{Z_{HH}\}$ exhibits a statistically significant increase and $q_{0.1}\{\rho_{HV}\}$ and $q_{0.1}\{Z_{DR}\}$ remain low but do not exhibit statistically significant changes (Fig. 3.9). A^1_{TDS}, TDS volume, and TDS height increase between 2229 – 2234 UTC, except for TDS height using thresholds T1 (Fig. 3.10).

To this point, the tornado has passed through rural areas and the damage survey does not indicate any damage to residences. Nonetheless, the tornado lofts enough tree limbs, leaves, and other light debris to produce a substantial, deep TDS.

The tornado EF-rating increases to 3 by 2238 UTC (Fig. 3.4). Between 2234 – 2238 UTC, statistically significant changes in the lowest elevation angle TDS parameters (Fig. 3.9) were not observed, and the TDS height and volume increase (Fig. 3.10b,c). Between 2238 – 2242 UTC, the tornado destroys a well-constructed residence leaving only the concrete slab (EF-4 damage), and the damage path widens to 500 – 700 m (Fig. 3.4). $q_{0.9}\{Z_{HH}\}$ exhibits a statistically significant increase (Fig. 3.9a) and the TDS height and volume reach their maximum values throughout the tornado (Fig. 3.10). For thresholds T1 a TDS occurs at the highest elevation angle, so the TDS parameters may underestimate the TDS volume and height (in this case, $\geq$ 32 km^3 and $\geq$ 8.3 km). For thresholds T2, the TDS volume and height are 16 km^3 and 6.7 km, and maximum TDS height is below the highest elevation angle.

Tornado damage severity and damage path width decrease between 2242 – 2247 UTC (Fig. 3.4). The tornado primarily produces EF-1 and EF-2 damage with some small regions of EF-3 damage, and the width of the damage path narrows to 250 – 400 m. By 2247 UTC, the TDS height for threshold T1 remains unbounded, but the TDS height for threshold T2 falls from 8.3 to 3.2 km and the TDS volume decreases from 16 to 5 km^3 (Fig. 3.11). The decrease in TDS

height and volume could reflect the reduction in tornadic debris lofted and/or a weakening of the updraft. By the start of the 2247 UTC scan, the tornado reintensifies and produces EF-4 damage. The CIs for $q_{0.9}\{Z_{HH}\}$ overlap for T1 (but do not overlap the mean over all replicates) while the CIs for T2 do not overlap. Hence, a statistically significant decrease in $q_{0.9}\{Z_{HH}\}$ is likely observed between 2242 – 2247 UTC (Fig. 3.9a,b).

The tornado produces primarily EF-3 damage between 2247 – 2251 UTC with some small regions of EF-4 damage (Fig. 3.4). The width of the damage path fluctuates considerably, ranging from 150 – 600 m. During this period, the TDS volume (for T2) increases slightly (Fig. 3.10b,c). The $q_{0.9}\{Z_{HH}\}$ parameter increases slightly to 66 dBZ for both T1 and T2 (Fig. 3.9a,b) while statistically significant changes in the other lowest elevation angle TDS parameters are not observed.

Between 2251 – 2255 UTC, a broader region of EF-3 damage is observed and the damage path width ranges from 400 – 900 m (Fig. 3.4). The tornado was approaching KOUN from the south, and was located 13–18 km from KOUN between 2251–2255 UTC. Using threshold T1, the TDS height cannot be determined beginning at 2242 UTC through tornado dissipation. However, the more stringent threshold resolves that the TDS height decreases from 6 km to 3 km between 2251 – 2259 UTC. During this same period, the TDS volume remains approximately constant while the tornado continues to produce EF-2 to 4 damage. The decrease in TDS height with a constant TDS volume suggests that the

debris is more concentrated at lower levels. This could result from a weakening storm-scale updraft, which would reduce the updraft's ability to loft and suspend debris at the mid- and upper-levels of the storm.

As the tornado weakens, $q_{0.9}\{Z_{HH}\}$ decreases to 53 dBZ by 2259 UTC for T1 and T2 (Fig. 3.9a). However, $q_{0.1}\{\rho_{HV}\}$ shows statistically significant decreasing values for T1 (Fig. 3.9b,c,d). Just prior to dissipating, the tornado produces EF-4 damage, which may account for the low ρ_{HV} and Z_{DR} values. As the tornado dissipates, a broad large region of lofted debris descends from the weakening storm. Scientists at the National Weather Center observed pieces of insulation and leaves falling after the tornado dissipated. A broad region of lower ρ_{HV} and high Z_{HH} (Fig. 3.11) over a 3.5 km^2 region is observed between 2259 – 2304 UTC, causing increase in A^1_{TDS}. Using thresholds T2, however, A^1_{TDS} decreases during this period.

3.4 Evaluation of TDS parameters as tornado damage metrics

Table 3.1 lists 21 tornado cases investigated in this study, including 14 that produced a TDS and 7 missed detections (labelled ND). TDS parameters are computed for the 14 tornadoes that produced TDSs throughout the duration of the tornado, using the times provided by the National Weather Service damage surveys. In some cases, fewer than 10 resolution volumes met the specified thresholds. $q_{0.1}\{\rho_{HV}\}$ and $q_{0.1}\{Z_{DR}\}$ have 13 and 11 cases for thresholds T1 and

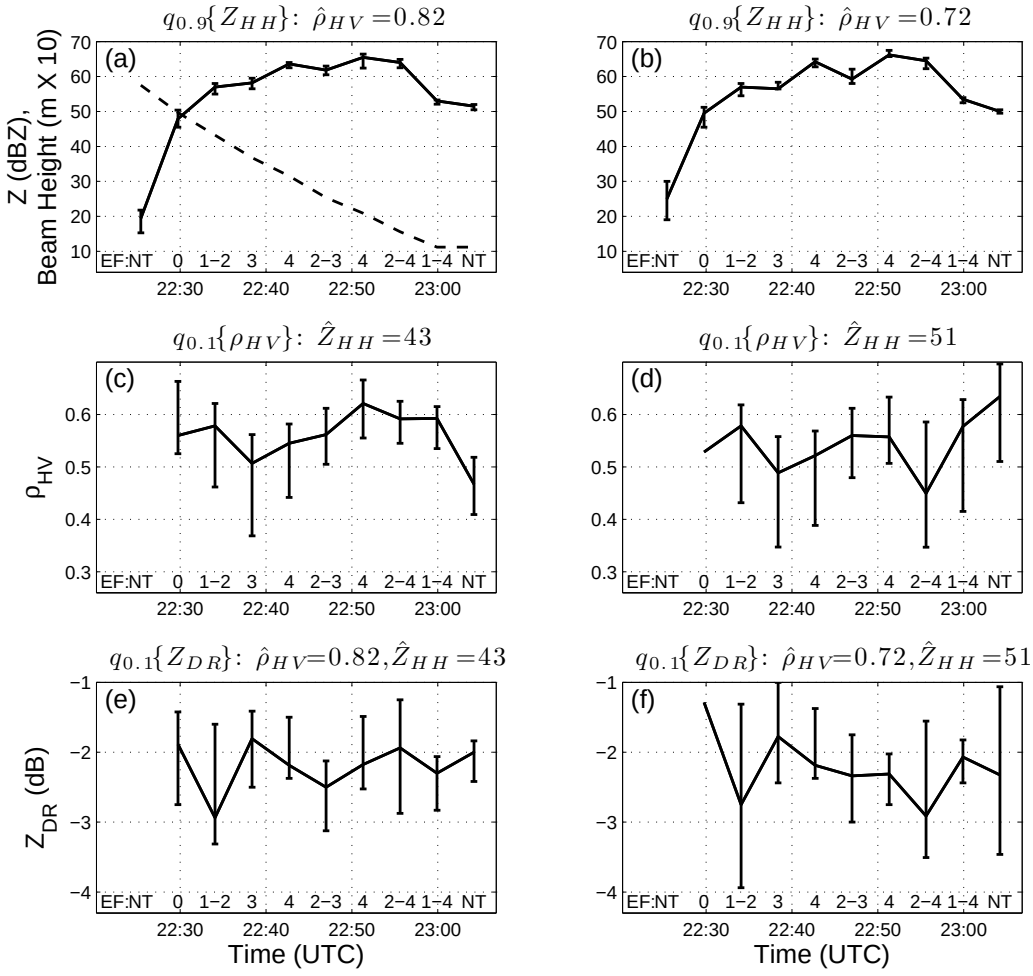

Figure 3.9: Same as Figure 3.6, except for the Goldsby EF-4 tornado. NT indicates that a tornado was not observed.

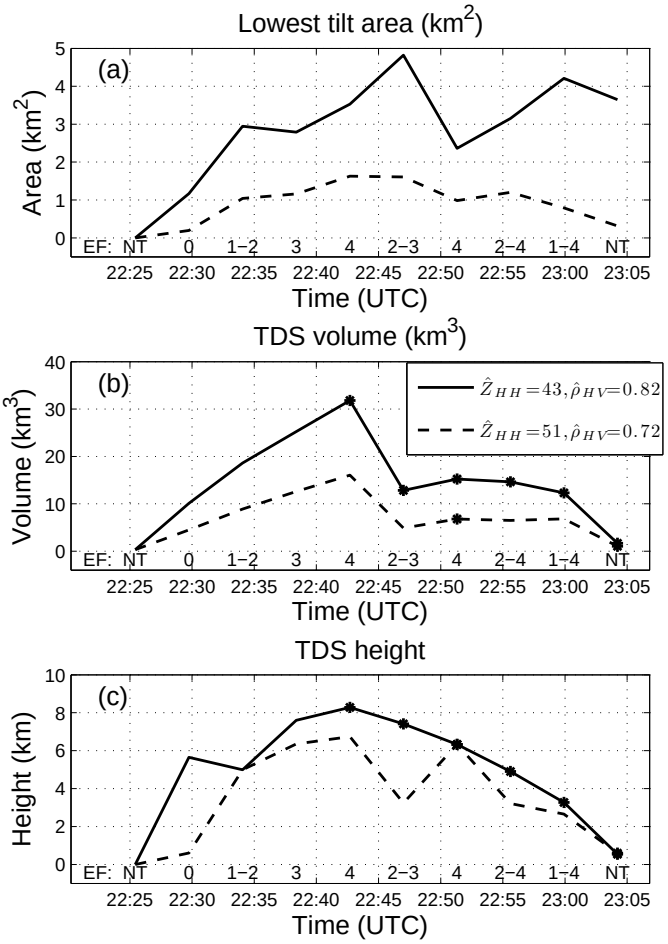

Figure 3.10: Same as Figure 3.7, except for the Goldsby EF-4 tornado. NT indicates that a tornado was not observed.

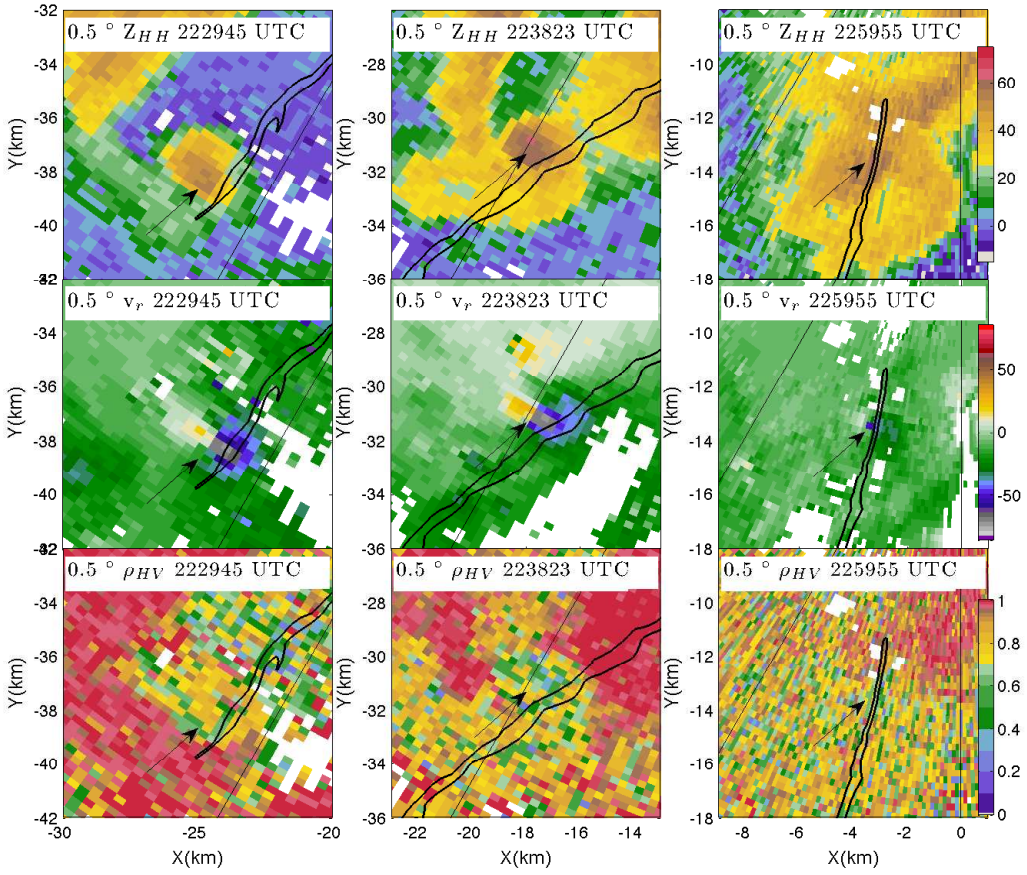

Figure 3.11: 0.5° elevation Z_{HH}, v_r, ρ_{HV} at 2229, 2238, and 2259 UTC for the Washington-Goldsby, Oklahoma tornado. The solid black line shows the Washington-Goldsby, Oklahoma damage path and the thin black line is the radial at a 210° azimuth. The black arrow indicates the location of the TDS.

T2, respectively, whereas $q_{0.9}\{Z_{HH}\}$ has 14 cases for both thresholds. The table shows the location, date, EF-rating, tornado times, and the range from KOUN. Tables 3.2 and 3.3 show the maximum or minimum values of TDS parameters for thresholds T1 and T2, respectively.

Two tornadoes were excluded owing to difficulties in either separating the TDS from another tornado or temporal sampling limitations. The parent storm of the Chickaska-Newcastle EF-4 tornado (tornado 19) produces a satellite tornado (tornado 3), which occurs within the TDS of the EF-4 tornado. The southern Moore EF-1 tornado (tornado 6) lasts only 1 min according the NWS damage survey, and radar scans remain above 2.4° elevation during this period. A TDS and TVS are not observed, so tornado 6 is excluded from the analysis.

In several cases, a TDS is not detected (Table 3.1). No TDSs are detected in EF-0 cases, likely because the tornado must loft sufficient amounts of debris and the EF-0 tornadoes were over 45 km from KOUN (tornadoes 1–2 in Fig. 3.1). The Healdton, Oklahoma EF-2 tornado (tornado 10) does not produce a TDS, although an EF-3 tornado that occurred 12 min later produces a substantial TDS (tornado 13). Both tornadoes are located over 100 km from the radar, so lofted debris must reach at least 2 km to be sampled by the 0.5° elevation scan.

The maximum and minimum values of lowest elevation angle TDS parameters reveal some interesting trends. For thresholds T1, the maximum $q_{0.9}\{Z_{HH}\}$ for weak tornadoes are between 38 – 46 dBZ (Fig. 3.12a). Most strong tornadoes $q_{0.9}\{Z_{HH}\}$ values between 45 – 60 dBZ, and $q_{0.9}\{Z_{HH}\}$ values exceed 55 dBZ

for the 5 violent tornadoes. In stronger tornadoes, higher $q_{0.9}\{Z_{HH}\}$ could result from the tornado lofting a greater number of debris elements, larger debris element sizes, or debris elements with high dielectric constants. The outlier case is the McLoud EF-2 tornado (tornado 12). While $q_{0.9}\{Z_{HH}\}$ was quite low (25.5 dBZ), higher Z_{HH} values (> 40 dBZ) satisfying T1 were observed at higher elevation angles. Because the tornado was relatively brief (4 min), the lowest elevation angle may not have observed the tornado's debris field when the most severe damage was occurring.

For the minimum $q_{0.1}\{\rho_{HV}\}$, decreasing minimum values are observed as tornado EF-rating increases (Fig. 3.12b). Weak tornadoes had minimum values of $q_{0.1}\{\rho_{HV}\}$ above 0.8, while strong and violent tornadoes had minimum $q_{0.1}\{\rho_{HV}\}$ below 0.8. For the five violent tornado cases, minimum $q_{0.1}\{\rho_{HV}\}$ was below 0.5. For minimum $q_{0.1}\{Z_{DR}\}$, only two weak tornado cases met the threshold T1, but values were near-zero or positive (Fig. 3.12c). For strong and violent tornadoes, the minimum $q_{0.1}\{Z_{DR}\}$ values were primarily below 0 dB, and violent tornadoes were below -2 dB. Similar results are seen for threshold T2 (Fig. 3.13b,c). For extremely low ρ_{HV} values observed in violent tornadoes, the variance of Z_{DR} appears to cause negative Z_{DR} values. However, Ryzhkov et al. (2005) and Bluestein et al. (2007) observed regions of negative Z_{DR} at S- and X-band, and Bodine et al. (2011) observed a coherent region of negative Z_{DR} in the outer debris ring of an EF-4 tornado.

The maximum values of the spatial TDS parameters also reveal interesting trends as tornado damage severity increases. For thresholds T1 and T2, an increase in EF-rating corresponds to higher TDS heights (Fig. 3.14a,c) and greater TDS volumes (Fig. 3.14b,d). The more stringent threshold T2 reduces the TDS height and TDS volume, decreasing the spread of values. For both thresholds, violent tornadoes exhibit much larger spread of TDS heights and volumes compared to weak and strong tornadoes, and in a few cases the TDS height and volume may be underestimated because the TDS extends to the highest elevation angle (Tables 3.2, 3.3). In violent tornado cases, the maximum TDS height for T1 ranges from 4.8 – 12.4 km, and the TDS volume ranges from 11 – 51 km^3. The 12.4-km TDS height and 51-km^3 TDS volume occurs after an EF-5 tornado struck Piedmont, Oklahoma producing a large region of EF-4 damage with numerous homes were destroyed and unfortunately two fatalities (Table 3.2). As noted previously, the maximum in TDS height and volume for the Chickasha and Goldsby tornadoes occurs about 5 – 10 min after periods of sustained, widespread EF-3 or 4 damage.

3.5 Discussion

3.5.1 Storm-scale influences on TDS parameters

Precipitation and associated downdrafts may affect the TDS. When precipitation is entrained into the TDS, ρ_{HV} values within the TDS increase (Schwarz and Burgess 2011; Bodine et al. 2011). An increase in ρ_{HV} would occur if the debris

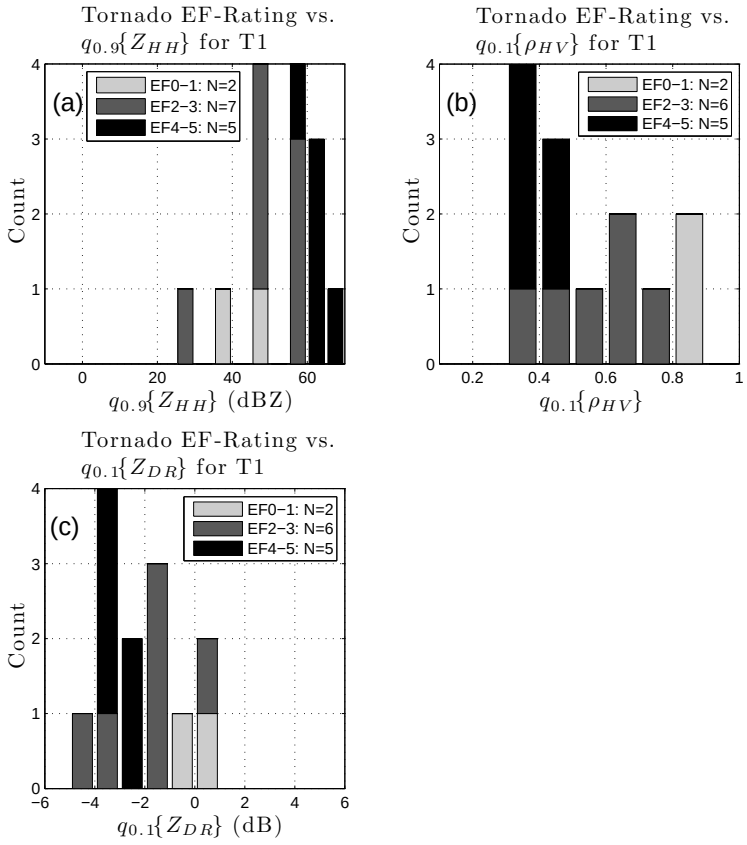

Figure 3.12: Stacked bar graph of (a) $q_{0.9}\{Z_{HH}\}$, (b) $q_{0.1}\{\rho_{HV}\}$, and (c) $q_{0.1}\{Z_{DR}\}$ for thresholds T1. The number, N, indicates the number of cases meeting the required thresholds for each parameter. The light gray, dark gray, and black shadings indicate EF-0 or 1, EF-2 or 3, and EF-4 or 5 tornadoes, respectively. Note that while all 14 cases met the threshold T2 for $\hat{\rho}_{HV}$, only 13 cases met the threshold T2 for $\hat{Z}_{HH}$.

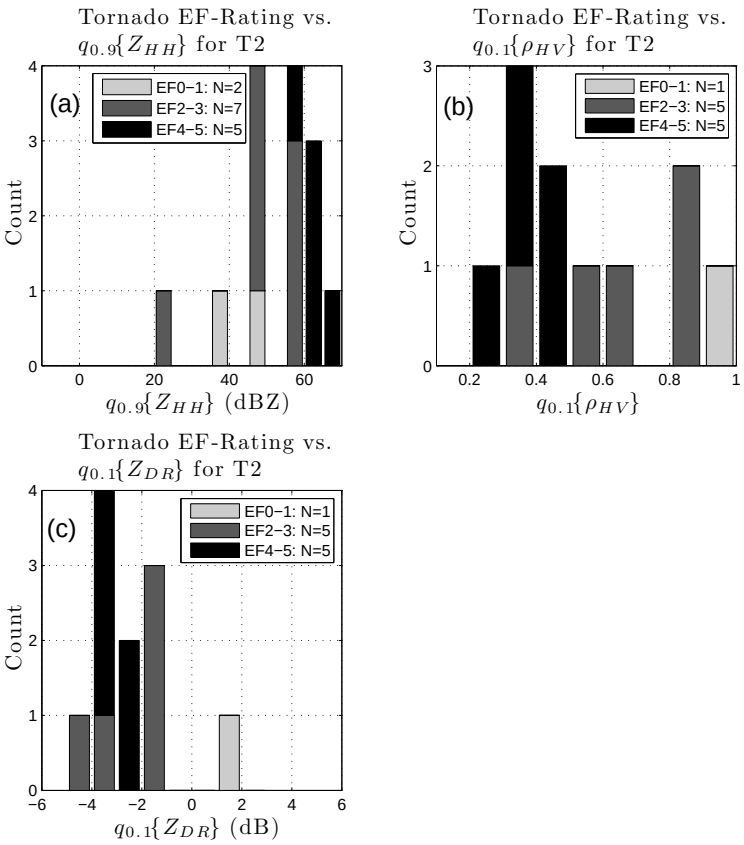

Figure 3.13: Same as Fig. 3.12 except for thresholds T2. Note that while all 14 cases met the threshold T2 for $\hat{\rho}_{HV}$, only 11 cases met the threshold T2 for $\hat{Z}_{HH}$.

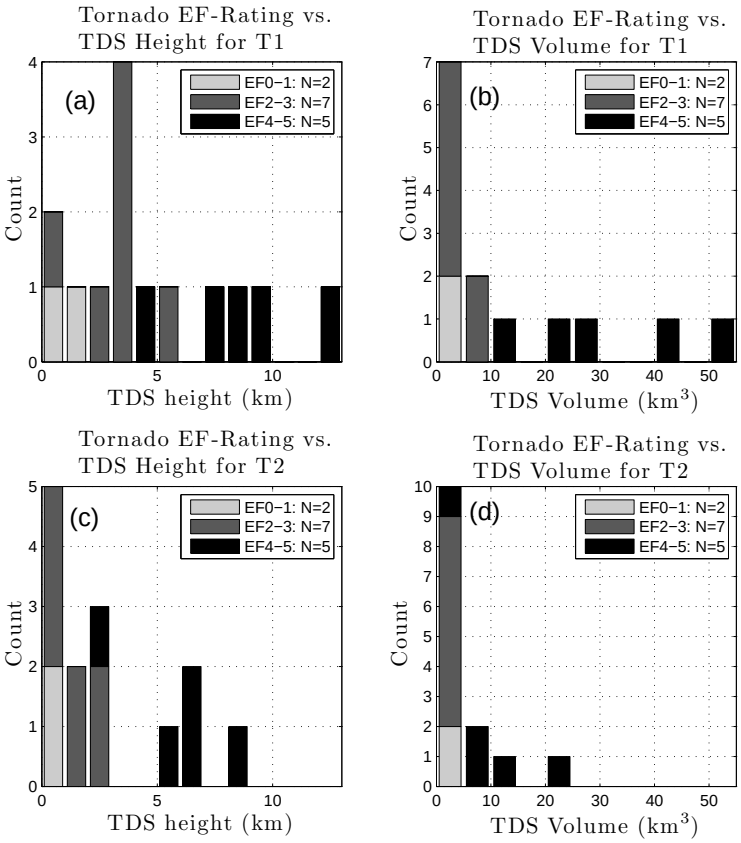

Figure 3.14: Stacked bar graph of (a) TDS height and (b) TDS volume for thresholds T1, and (c) TDS height and (d) TDS volume for thresholds T2. The light gray, dark gray, and black shadings indicate EF-0 or 1, EF-2 or 3, and EF-4 or 5 tornadoes, respectively.

Table 3.1: The locations, tornado number, date, EF-rating, times, range from KOUN for the 21 tornado cases.

Location	Tornado Number	Date	EF Rating	Time (UTC)	Range (km)
Union City	1	10 May 2010	EF-0	2146–2152	45 – 47
Piedmont	2	10 May 2010	EF-0	2146–2154	59 – 65
Newcastle	3	24 May 2011	EF-0	2245	15
Bray	4	10 May 2010	EF-1	2220–2227	57 – 63
Moore	5	10 May 2010	EF-1	2222–2227	9 – 14
Moore	6	10 May 2010	EF-1	2227	9
Norman	7	10 May 2010	EF-1	2234–2240	10
Wayne	8	10 May 2010	EF-1	2236–2243	38
Noble/East Norman	9	10 May 2010	EF-2	2239–2259	30
Healdton	10	10 May 2010	EF-2	2304–2310	114 – 116
Stillwater	11	24 May 2011	EF-2	2250–2305	102 – 105
McLoud	12	24 May 2011	EF-2	2336–2339	39
Dale	13	10 May 2010	EF-3	2248–2302	38 – 48
Tecumseh	14	10 May 2010	EF-3	2256–2347	57 – 95
Lone Grove	15	10 May 2010	EF-3	2322–2334	105 – 109
Lookeba	16	24 May 2011	EF-3	2031–2046	82 – 86
Oklahoma City	17	10 May 2010	EF-4	2220–2251	14 – 55
Lake Thunderbird	18	10 May 2010	EF-4	2232–2259	11 – 41
Chickasha	19	24 May 2011	EF-4	2206–2301	13 – 45
Goldsby	20	24 May 2011	EF-4	2226–2305	9 – 45
El Reno	21	24 May 2011	EF-5	2050–2235	55 – 89

Table 3.2: The locations, tornado number, EF-rating, $q_{0.9}\{Z_{HH}\}$, $q_{0.1}\{\rho_{HV}\}$, $q_{0.1}\{Z_{DR}\}$, h_{max}, V_{max} for 21 tornado cases for thresholds T1. ND indicates that a TDS was not detected. BT indicates that an insufficient number of resolution volumes met the threshold criteria so the lowest elevation angle TDS parameter could not be computed. The asterisk next to the TDS height and volume indicates that a TDS was observed at the highest elevation angle (19.5°), and thus are a minimum bound.

Location	Tornado Number	EF Rating	$q_{0.9}\{Z_{HH}\}$ (dBZ)	$q_{0.1}\{\rho_{HV}\}$	$q_{0.1}\{Z_{DR}\}$ (dB)	h_{max} (km)	V_{max} (km^3)
Union City	1	EF-0	ND	ND	ND	ND	ND
Piedmont	2	EF-0	ND	ND	ND	ND	ND
Newcastle	3	EF-0	ND	ND	ND	ND	ND
Bray	4	EF-1	46.1	0.84	-0.4	1.1	0.3
Moore	5	EF-1	ND	ND	ND	ND	ND
Moore	6	EF-1	ND	ND	ND	ND	ND
Norman	7	EF-1	39.3	0.82	BT	0	0
Wayne	8	EF-1	ND	ND	ND	ND	ND
Noble	9	EF-2	48	0.48	-3.9	5.4	5
Healdton	10	EF-2	ND	ND	ND	ND	ND
Stillwater	11	EF-2	55.3	0.63	-1.0	3.1	3
McLoud	12	EF-2	25.5	BT	BT	1.0	0
Dale	13	EF-3	58.5	0.75	0.1	2.1	1
Tecumseh	14	EF-3	55.5	0.58	-1.2	3.7	9
Lone Grove	15	EF-3	48.7	0.39	-4.5	3.5	3
Lookeba	16	EF-3	47.0	0.66	-1.0	3.2	3
Oklahoma City	17	EF-4	60.5	0.30	-3.2	4.8	11
Lake Thunderbird	18	EF-4	57.4	0.49	-3.3	7.3*	21*
Chickasha	19	EF-4	63.5	0.33	-3.9	9.6*	40*
Goldsby	20	EF-4	65.5	0.47	-2.9	8.3*	27*
El Reno	21	EF-5	62.4	0.40	-2.44	12.4*	51*

Table 3.3: The locations, tornado number, EF-rating, $q_{0.9}\{Z_{HH}\}$, $q_{0.1}\{\rho_{HV}\}$, $q_{0.1}\{Z_{DR}\}$, h_{max}, V_{max} for 21 tornado cases for thresholds T2. BT indicates that an insufficient number of resolution volumes met the threshold criteria so the lowest elevation angle TDS parameter could not be computed. The asterisk next to the TDS height and volume indicates that a TDS was observed at the highest elevation angle (19.5°), and thus are a minimum bound.

Location	Tornado Number	EF Rating	$q_{0.9}\{Z_{HH}\}$ (dBZ)	$q_{0.1}\{\rho_{HV}\}$	$q_{0.1}\{Z_{DR}\}$ (dB)	h_{max} (km)	V_{max} (km^3)
Union City	1	EF-0	ND	ND	ND	ND	ND
Piedmont	2	EF-0	ND	ND	ND	ND	ND
Newcastle	3	EF-0	ND	ND	ND	ND	ND
Bray	4	EF-1	46	0.99	1.9	0	0
Moore	5	EF-1	ND	ND	ND	ND	ND
Moore	6	EF-1	ND	ND	ND	ND	ND
Norman	7	EF-1	38.3	BT	BT	0	0
Wayne	8	EF-1	ND	ND	ND	ND	ND
Noble	9	EF-2	47.5	0.39	-4.1	1.4	0.1
Healdton	10	EF-2	ND	ND	ND	ND	ND
Stillwater	11	EF-2	55.2	0.59	-1.5	2.2	1
McLoud	12	EF-2	22	BT	BT	0	0
Dale	13	EF-3	55.0	0.82	-3.7	1.1	0.1
Tecumseh	14	EF-3	55.6	0.62	-3.2	2.1	1
Lone Grove	15	EF-3	47.3	0.83	-1.5	0	0
Lookeba	16	EF-3	45.9	BT	BT	0	0
Oklahoma City	17	EF-4	61.0	0.30	-3.0	2.7	1
Lake Thunderbird	18	EF-4	57.0	0.48	-3.3	5.9	6
Chickasha	19	EF-4	63.5	0.35	-3.9	6.9*	14*
Goldsby	20	EF-4	66.2	0.45	-2.9	6.7*	8*
El Reno	21	EF-5	63.2	0.26	-3.3	8.1	22

concentration remained the same but the concentration of raindrops increased in the resolution volume. If resolution volume initially possessed a ρ_{HV} value at or just below the $\hat{\rho}_{HV}$, then an increase in raindrop size or concentration could increase ρ_{HV} above the $\hat{\rho}_{HV}$ and the resolution volume would no longer meet the TDS criteria. When the tornado is surrounded by downdraft, a reduced number of debris elements may be transported vertically because the downdraft enhances debris fallout. Hence, a reduced TDS height and volume in tornadic supercells with greater precipitation entrainment may result from storm-scale differences in the intensity and areal extent of updrafts and downdrafts surrounding the tornado.

This study reveals that in some cases large amounts of tornadic debris are transported quite high into the storm. As suggested by Dowell et al. (2005), centrifuged tornadic debris may be recycled by the storm-scale updraft. As expected, the TDS is much wider than the actual damage path at the surface in the Chickasha and Goldsby tornadoes due to debris centrifuging (e.g., Snow 1984; Dowell et al. 2005). For the Chickasha and Goldsby tornadoes, the most significant tornado damage occurs along the right side of the tornado relative to its motion, where ground-relative wind speeds are enhanced by storm motion. Lofted debris is centrifuged and advected cyclonically, producing a broader and more uniform TDS. Even though debris has been centrifuged from the tornado, centrifuged debris remain beneath the low-level mesocyclone and sufficiently small

and low terminal velocity debris are "recycled" and transported vertically into the updraft.

3.5.2 TDS parameter utility

Given that the TDS parameters incorporate data from different elevation angles, the time required to loft debris to the height of different elevation angles will vary (depending on updraft strength and debris fall speeds). Hence, the TDS parameters will exhibit some delay between when damage occurs and when a change in the TDS parameters are observed. The lowest elevation angle TDS parameters should have the smallest lag times. For example, debris lofted at 20 m s^{-1} would reach a typical 0.5° beam height of 200 – 600 m in 10 – 30 s. Accordingly, debris will take longer to reach the higher elevation angles. Thus, the delay for the TDS height and volume may be greater compared to the lowest elevation angle TDS parameters.

An important limitation of the lowest elevation angle TDS parameters is that these parameters could reflect changes in sampling height (due to changes in range) rather than changes in tornadic debris. However, the two cases presented (both tornadoes approaching the radar) show good correlation between the damage surveys and changes in $q_{0.9}\{Z_{HH}\}$ during tornado intensification and dissipation. In a case with the tornado moving away from the radar, the Norman-Lake Thunderbird tornado (tornado 18) exhibits increasing $q_{0.9}\{Z_{HH}\}$ values during tornado intensification and maximum values during the period of EF-4

damage east of Lake Thunderbird (not shown). Hence, for these cases, changes in the debris field appear to be more important than changes in sampling height. Nonetheless, more cases are needed to better understand how changes in beam height affect the lowest elevation angle TDS parameters.

Spatial TDS parameters provide an indication of the amount of tornado damage occurring and updraft intensity. Given that the TDS volume depends on the spatial coverage of the TDS throughout the storm, it provides a diagnostic tool for examining the amount of debris lofted by the tornado. The Chickasha EF-4 tornado exhibits higher maximum TDS volumes compared to Goldsby EF-4 tornado, which could result from the wider damage path of the Chickasha EF-4 tornado and consequently, more lofted debris. Nonetheless, the TDS volume also depends on the strength of the storm-scale updraft and whether or not the updraft can suspend tornadic debris. The maximum TDS height may possess a greater sensitivity to the intensity of the storm-scale updraft than the TDS volume because the areal coverage of the TDS decreases with height (see Fig. 3.8). The primary limitation of the TDS volume and height parameters is the lag time between when tornadic debris is lofted and when tornadic debris reach the TDS height. In this study, the maximum TDS volume or height occur about 5 – 10 min after the most significant damage occurs at the surface. Hence, these parameters should be viewed as a cumulative measure of tornadic debris over the preceding 5 – 10 min period.

3.5.3 Discrepancies between damage survey and TDS parameters

Interesting differences are evident between the Goldsby EF-rating and the TDS parameters during its intensification. At 2229 UTC, the damage survey indicate only EF-0 damage while $q_{0.9}\{Z_{HH}\}$, and $q_{0.1}\{\rho_{HV}\}$ are 48 dBZ and 0.56, respectively (Fig. 3.9). Comparing these values to the maximum or minimum values for other tornadoes (Fig. 3.12), such values are characteristic of higher EF-rated tornado cases presented herein. Moreover, for other EF-0 tornadoes no TDS is observed (Tables 3.2, 3.3), suggesting not enough debris is lofted to produce a TDS. A possible explanation for this discrepancy is that the EF-scale underestimated tornado intensity, and a more intense tornado was present and lofted more tornadic debris. By 2234 UTC, the threshold T1 TDS height and volume are 5 km and 10 km^3, respectively (Fig. 3.10). These values are more consistent with the TDS height and volumes observed for other violent tornado cases rather than a tornado producing EF-1 or 2 damage (Fig. 3.13). Thus, the EF-scale may still underestimate tornado intensity at 2234 UTC. The first engineered structure listed as a damage indicator in the survey is at 2234 UTC, so an underestimation of tornado intensity is certainly possible. Moreover, the differences in TDS height and volume may reflect a stronger low-level updraft present, resulting in more rapid vertical transport of debris.

The Chickasha and Goldsby tornadoes primarily affected rural areas with some small to medium-sized towns. However, the primary source of scatterers in

rural areas appears to be vegetation. Along the Chickasha and Goldsby tornado damage paths, hardwood trees provided a source of debris elements. Importantly, in regions with little vegetation or few man-made structures, tornadoes may have lower Z_{HH} and higher ρ_{HV} values than areas with higher population density or more vegetation cover. Hence, TDS parameters may not perform as well in areas with little vegetation or engineered structures.

3.6 Conclusions

This study investigates the potential of using polarimetric radar to estimate tornado damage severity and spatial extent. The study uses modified TDS parameters developed by Ryzhkov et al. (2005) and develops other new TDS parameters for estimating tornado damage. Using two detailed damage surveys conducted by the Norman NWS WFO, comparisons between TDS parameters and damage surveys are presented. Then, TDS parameters are computed for 14 tornado cases in central Oklahoma and the EF-rating is compared to maximum or minimum TDS parameter values.

The TDS parameters tend to be correlated with the damage surveys. During tornado intensification, $q_{0.9}\{Z_{HH}\}$ and spatial TDS parameters increase and $q_{0.1}\{\rho_{HV}\}$ and $q_{0.1}\{Z_{DR}\}$ decrease. During tornado dissipation, $q_{0.9}\{Z_{HH}\}$ decreases while the other lowest elevation angle TDS parameters sometimes show a trend. The application of TDS parameters during tornado dissipation is complicated by debris fallout, which may increase the areal coverage of the TDS

at the lowest elevation angle. The maxima or minima of TDS parameter values also show potential for assessing the amount and severity of tornado damage. Maximum $q_{0.9}\{Z_{HH}\}$, TDS height, and TDS volume increase and minimum $q_{0.1}\{Z_{DR}\}$ and $q_{0.1}\{\rho_{HV}\}$ decrease as tornado damage severity increases. Because the damage surveys from the other cases were not as detailed, it is unknown if the maximum or minimum TDS parameter values coincide with the peak damage intensity for most cases. The peak values of the TDS volume and height tend to occur after significant amounts of tornadic debris have been lofted over a 5 – 10 min period.

This paper illustrates the potential for estimating tornado damage using polarimetric radar. The information provided by the TDS parameters could help forecasters identify changing trends in tornado damage severity, and estimate the severity and extent of tornado damage in near real-time. This new information could allow forecasters to issue more specific statements about tornado damage severity through special weather statements or tornado emergencies, and disseminate this information to the public, emergency managers, and the media. The TDS parameters are not intended to predict when a violent tornado will occur and the TDS should not be relied on for issuing tornado warnings. However, they could enable forecasters to gauge tornado damage severity, particularly when spotter reports are unavailable (e.g., for rain-wrapped tornadoes or at night) or when low-level velocity data are not available (e.g., at long ranges). The TDS parameters can provide near real-time information about the severity

of tornado damage to emergency managers and first responders to ensure that their efforts are immediately directed to the most severely affected areas.

The study also raises several intriguing scientific questions about tornadic debris and supercell dynamics. Numerous studies have documented tornadic debris sedimentation in the RFD, forward-flank downdraft, and also observed tornadic debris fallout over 100 km from the storm (e.g., Snow et al. 1995; Magsig and Snow 1998). In the present study, a broad region of tornadic debris fallout is observed within the RFD, possibly caused by debris fallout after updraft weakening or small fall speeds of light debris (e.g., leaves, insulation). If the updraft weakened, was the weaker updraft caused by storm-scale processes or could tornadic debris loading throughout the updraft be a contributing factor? We speculate that both factors could be important in the present case. Finally, the rapid, vertical advection of tornadic debris in violent tornado cases suggests the presence of a very strong, low-level updraft (also Oklahoma City and Lake Thunderbird EF-4 tornadoes, tornadoes 17 and 18, not shown) compared to weaker tornadoes. If so, how does a strong, low-level updraft contribute to tornado intensification and maintenance?

To further investigate the potential for nowcasting tornado damage using TDS parameters, future studies should examine more tornado cases, including cases in different geographic areas and cases with detailed damage surveys. More cases are needed to determine if a near real-time classification of tornado damage severity can be developed. To better understand the relationship

between the amount of lofted debris and tornado intensity, studies combining polarimetric WSR-88D data with mobile radar observations should be pursued. Future studies could also investigate the relationship between TDS height and volume and storm-scale updraft intensity using polarimetric radar and rapid-scan, dual-Doppler data. The current upgrade to the WSR-88D network with dual-polarization will provide the opportunity to expand this research to a much larger data set, different geographic areas, and would allow the implementation of TDS parameters as a tool for providing near real-time information tornado damage and severity.

Chapter 4

Dual-Wavelength Observations of Tornadic Debris Signatures

In this chapter, statistical TDS analyses are presented using dual-wavelength polarimetric radar observations from KOUN and the University of Oklahoma Polarimetric Radar for Innovations in Meteorology and Engineering (OU-PRIME) at S and C bands, respectively.

4.1 Introduction

Although TDSs have been documented at different wavelengths, comparisons of dual-wavelength TDSs have not yet been presented. Moreover, statistical properties of TDSs have not been thoroughly investigated, particularly as a function of height. A better characterization of statistical properties of TDSs could improve tornado detection and damage severity estimates. Thus, this study examines statistical properties of TDSs from two radars operating at S and C bands to ascertain similarities and differences between S- and C-band TDSs. Close proximity of an EF-4 tornado on 10 May 2010 to OU-PRIME and KOUN provide unique opportunities for close-range, dual-wavelength comparisons. This study also relates statistical analyses to surface damage characteristics to ascertain relationships between debris characteristics and polarimetric

variables. Finally, polarimetric radar observations are compared to axisymmetric velocity retrievals to investigate relationships between three-dimensional TDS structure and tornado dynamics.

Section 4.2 describes OU-PRIME and KOUN, permutation tests used in statistical radar comparisons, and T-matrix calculations for simplified debris. Dual-wavelength polarimetric radar analyses of TDSs are presented in Section 4.3. Finally, conclusions from the study are presented in Section 4.4.

4.2 Data and methods

This study investigates TDS statistics using OU-PRIME and KOUN polarimetric radar data. Detailed comparisons of the radars' specifications can be found in Palmer et al. (2011), as well as an overview of the 10 May 2010 tornado outbreak. OU-PRIME is a C-band, polarimetric radar with a 0.45° 3-dB beamwidth and a peak transmit power of 1 MW. On 10 May 2010, OU-PRIME operated a pulse length and range resolution of 125 m and maximum unambiguous velocity of 16 m s^{-1}. KOUN has a 0.9° 3-dB beamwidth, range resolution of 250 m, a peak transmit power of 750 kW, and operated a maximum unambiguous velocity of 27.5 m s^{-1}. KOUN and OU-PRIME data are gridded and plotted in Cartesian coordinates, and dual-wavelength comparison plots are shown using zonal and meridional distance from KOUN. Radial velocity data were edited and dealiased using SOLOII software (Oye et al. 1995).

On 10 May 2010, OU-PRIME operated volumetric sector scans with update times between 2 min 20 s and 2 min 40 s. Volumetric sector scans included the following elevation angles: 1.0°, 2.0°, 3.0°, 4.0°, 5.0°, 6.5°, and 9.0°. KOUN operated VCP 12 (Brown et al. 2005b) for the volume scans presented in this study. VCP 12 requires 4 min 18 s to complete, and includes the following elevation angles: 0.5°, 0.9°, 1.3°, 1.8°, 2.4°, 3.1°, 4.0°, 5.1°, 6.4°, 8.0°, 10.0°, 12.5°, 15.6°, and 19.5°. KOUN data at the lowest three elevation angles are oversampled at 0.5° resolution (Brown et al. 2005a).

KOUN and OU-PRIME scans exhibited serendipitously close temporal and spatial matching from 2230 – 2232 UTC. Table 4.1 shows beam heights at the center of the TVS, and scan times for the three comparisons of KOUN and OU-PRIME data. Differences in beam center heights for KOUN and OU-PRIME range from ± 20 – 90 m, and scan times are nearly synchronous at the lowest level comparison and differences in scan times approach 55 s at the highest tilt comparison. A notable difference is that KOUN's resolution volumes are 2 – 2.5 times larger than OU-PRIME. Consequently, KOUN's larger beamwidth illuminates debris at higher and lower altitudes compared to OU-PRIME. While some differences in resolution volumes exist, close temporal and spatial matching suggest that debris types within the tornado at a given height are likely similar. It is therefore assumed that statistical, dual-wavelength comparisons represents similar debris distributions.

Table 4.1: Scan times (UTC), elevation angles (°), beam height in m and resolution volume size in km^3 (at the center of the tornado) during dual-wavelength comparisons between OU-PRIME and KOUN.

Radar	OU-PRIME	KOUN
Scan Time	22:30:59 – 22:31:14	22:30:56 – 22:31:13
Elevation Angle	1.0°	1.4°
Beam Height	360 m	340 m
Resolution Volume Size	0.008 km^3	0.016 km^3
Scan Time	22:31:14 – 22:31:31	22:31:44 – 22:31:57
Elevation Angle	2.0°	2.4°
Beam Height	720 m	630 m
Resolution Volume Size	0.008 km^3	0.018 km^3
Scan Time	22:31:31 – 22:31:47	22:32:13 – 22:32:26
Elevation Angle	3.0°	4.0°
Beam Height	1110 m	1090 m
Resolution Volume Size	0.008 km^3	0.019 km^3

A basic thresholding procedure is implemented to identify the debris field of the tornado. Some S-band resolution volumes within the tornado exhibit relatively high ρ_{HV} (0.8 – 0.95) while C-band ρ_{HV} is much lower. If thresholds imposed by previous studies are used to identify TDSs (e.g., Ryzhkov et al. 2005; Bodine et al. 2013), these high ρ_{HV} regions would be excluded from the analysis. Another issue arises from using high Z_{HH} thresholds, which remove resolution volumes with small or low concentrations of debris (e.g., within the weak-echo hole). To avoid removing high ρ_{HV} or low Z_{HH} resolution volumes at S-band, all resolution volumes within the radius of maximum wind (RMW) of the tornado or low-level mesocyclone are included in the analysis. Between the RMW and 1.5 $\times$ RMW, the ρ_{HV} threshold of 0.82 used by Bodine et al. (2013) is imposed but no threshold on Z_{HH} is imposed. The extended region allows centrifuged debris outside of the RMW to be included in analyses, while excluding resolution volumes where hydrometeors are the dominant scatterers.

Nonparametric resampling techniques, such as the bootstrap or permutation tests, resample data without assumptions about the type of distribution that fits the data (Efron and Tibshirani 1993). Because underlying distributions of polarimetric variables in TDSs are unknown, nonparametric tests are applicable to this study. Permutation tests are used to determine statistical significance of two samples with a null hypothesis that the two samples have the same parent distributions. The two sample permutation tests herein involve different radar elevation angles to investigate changes in polarimetric variable statistics with

height, and different wavelengths to examine dual-wavelength similarities and differences. For each permutation test, 5000 permutations are performed, and then 5000 test statistics are computed for the permutated data.

T-matrix calculations use electromagnetic scattering theory to characterize electromagnetic wave scattering by different objects (e.g., hydrometeors, debris). The T-matrix method can determine scattering characteristics of objects in the Mie scattering region (i.e., where $D \geq \frac{\lambda}{16}$), and also applies to non-spherical or two-layer scatterers such as water-coated hail (Bringi and Seliga 1977). Using the backscatter and forward scattering amplitudes from the T-matrix calculation, polarimetric radar variables can be obtained for different types of hydrometeors (e.g., Vivekanandan et al. 1991; Zhang et al. 2001).

In this study, T-matrix calculations are presented for elongated debris to develop a basic understanding of polarimetric variables for two simplified debris types. Variations in debris sizes, irregularities in debris shapes, and varied compositions likely limit the applicability of these T-matrix calculations to other debris types. T-matrix calculations are performed using an axis ratio of 0.2 and 5 (i.e., oblate and prolate spheroids) for dry and wet debris. Wet debris is given a fractional water content of 50%, and complex relative permittivities for dry and wet debris are $1.9\text{-}0.01j$ and $15.9\text{-}4.6j$, respectively. The effective dielectric factor for wet "debris" is computed using the Maxwell-Garnet formula with water as the background. These complex relative permittivities are based on measurements for leaves (Ulaby et al. 1987), and are similar to values presented earlier

for wood. Figs. 4.1 and 4.2 show Z_{HH}, Z_{DR}, and δ_{DP} for dry and wet elongated "debris" with axis ratios of 0.2 and 5. Z_{HH} is computed for a monodispersed size distribution with a debris concentration of 0.01 m^{-3}.

4.3 Statistical analysis of TDSs

4.3.1 2229 UTC KOUN low-altitude TDSs

During the 22:29:51 UTC volume scan, KOUN collected three levels of polarimetric radar data in the lowest 350 m of the tornado. Using these data, changes in polarimetric variables with height are investigated. 0.5° elevation KOUN velocity data indicate that the tornado was located southwest of the intersection of 119th Street and Douglas Boulevard. Satellite imagery indicates that the tornado passed through a densely wooded area west of Lake Stanley Draper with a low population density and a small number of manmade structures (Fig. 4.3). An interesting observation is that the 2229 UTC TVS is offset from the center of the damage path by 590 m. One explanation for the offset is that the most severe damage occurred on the southeast side of the tornado where storm motion increased ground-relative wind speeds. Vortex tilt can also cause separation between the TVS and the damage path. Given the low beam height of 110 m, however, an offset of 590 m would require vortex tilt of about 80°.

Low-altitude KOUN scans show distinct TDSs with concentric regions of high Z_{HH} collocated with the TVSs and low ρ_{HV} (Fig. 4.4). 13% of the Z_{HH} values inside the TDS exceed 60 dBZ at 0.5° elevation compared to only 1% at

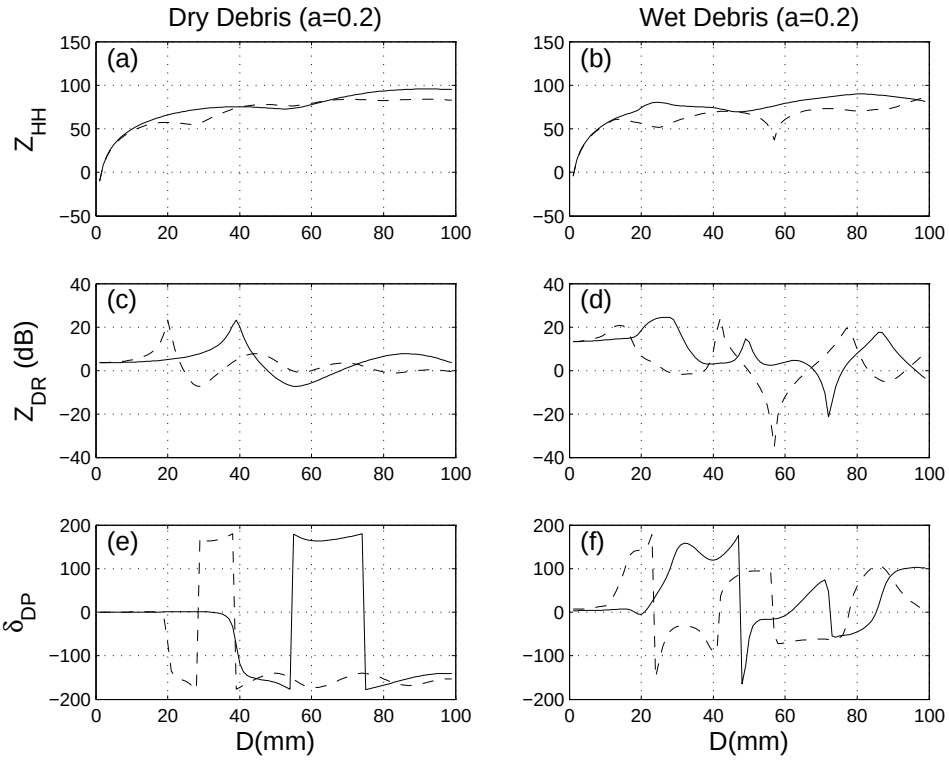

Figure 4.1: Z_{HH} calculated for (a) dry and (b) wet debris (fractional water content = 50%), Z_{DR} calculated for (c) dry and (d) wet debris, and δ_{DP} calculated for (e) dry and (f) wet debris. S-band (C-band) values for Z_{HH}, Z_{DR} and δ_{DP} are shown using solid (dashed) lines. Polarimetric variables are calculated using backscatter amplitudes from a T-matrix calculation using a spheroid with an axis ratio of 0.2.

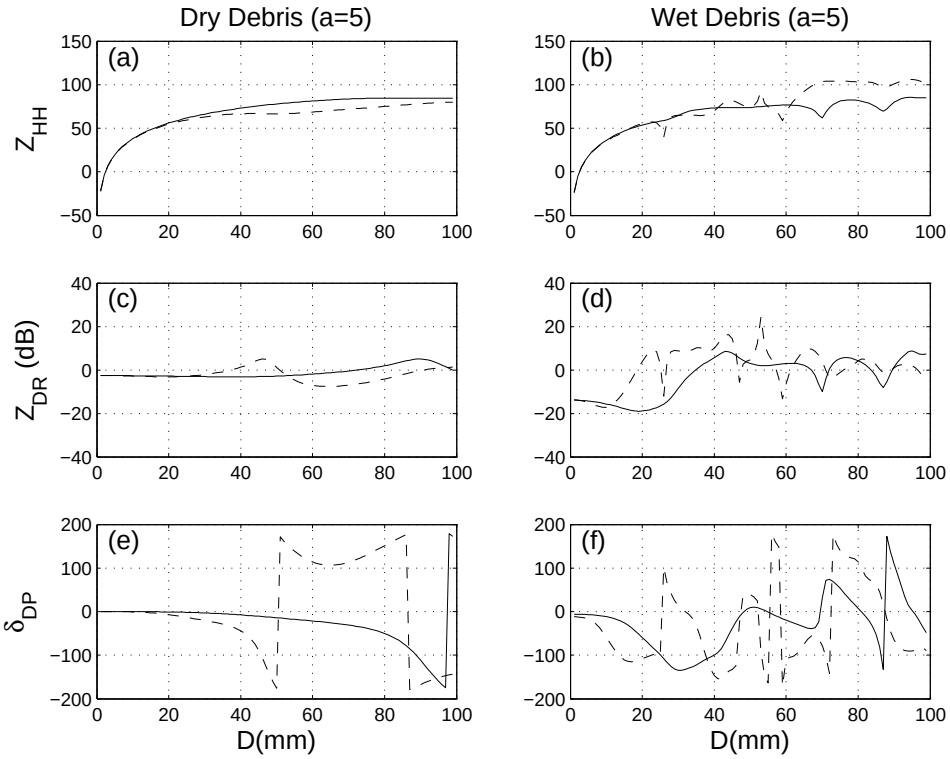

Figure 4.2: Same as Fig. 4.1, except for an axis ratio of 5.

Figure 4.3: Satellite imagery with an overlay of the NWS damage path (white line) and locations of the 0.5° elevation TVS (yellow pins) at 22:29:51 (top) and 22:38:27 UTC (bottom). Images were created using Google Earth and satellite imagery from 8 April 2010.

Table 4.2: 90th percentile Z_{HH} (dBZ), median ρ_{HV}, median Z_{DR} (dB), and 90th percentile Z_{DR} (dB) for the 0.5° and 1.4° KOUN elevation scans at 22:29:51 UTC. P-values are determined through hypothesis testing using a permutation test with 5000 permutations.

Statistic	KOUN 0.5°	KOUN 1.4°	Difference	P-value
90th percentile Z_{HH}	60.8	56.5	4.3	0.001
Median ρ_{HV}	0.70	0.75	-0.05	0.014
Median Z_{DR}	-0.1	-0.3	0.2	0.206
90th percentile Z_{DR}	2.7	2.0	0.7	0.020

1.4° elevation (Fig. 4.5). 90th percentile Z_{HH} exhibits a statistically significant decrease between the 0.5° and 1.4° elevation with a permutation test p-value of 0.001 (Table 4.2). Decreasing Z_{HH} with height occurs frequently in tornadoes (e.g., Wurman et al. 1996; Wurman and Gill 2000; Bluestein et al. 2004; Dowell et al. 2005) as a consequence of debris centrifuging and fallout (Snow 1984; Dowell et al. 2005).

An increase in ρ_{HV} is evident between 0.5° and 1.4° elevation angles. Examination of the histogram of 1.4° ρ_{HV} reveals a higher frequency of $\rho_{HV} > 0.85$ compared to the 0.5° ρ_{HV} histogram (Fig. 4.5). Median ρ_{HV} exhibits a statistically significant increase in ρ_{HV} with a permutation test p-value of 0.014. The increase in ρ_{HV} with height may be attributed to a reduction in non-Rayleigh scattering as debris size decreases with height. Because debris distributions likely

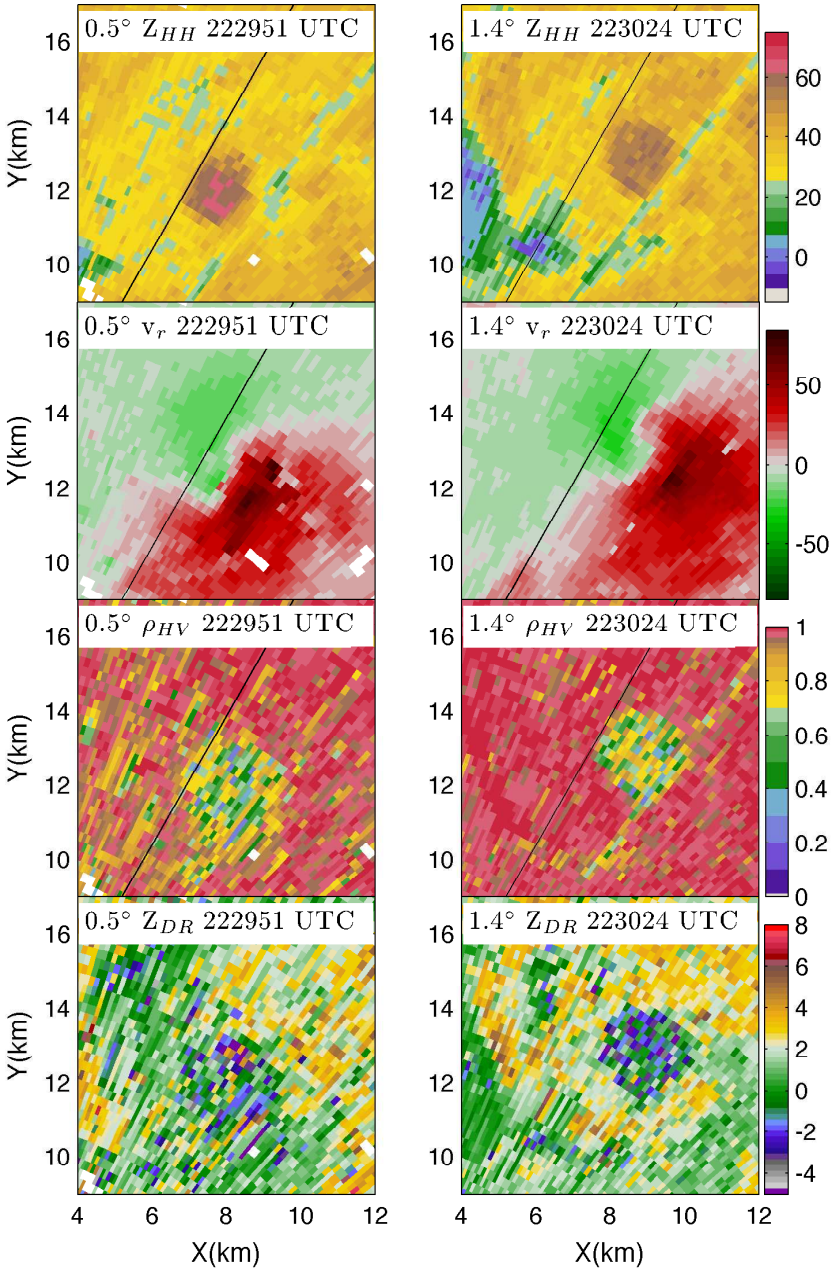

Figure 4.4: KOUN Z_{HH} (dBZ), radial velocity, ρ_{HV}, and Z_{DR} at 0.5° and 1.4° elevation at 22:29:51 and 22:30:24 UTC, respectively. TDSs are evident with high Z_{HH} and low ρ_{HV} collocated with the TVS.

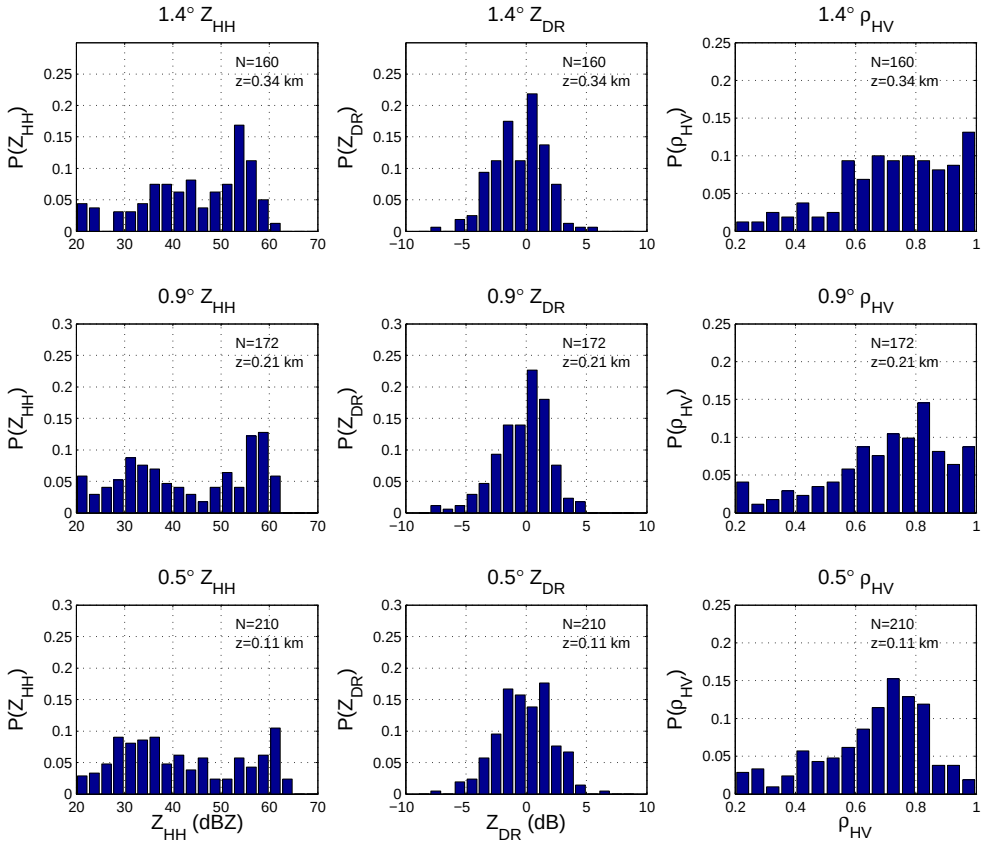

Figure 4.5: Histograms of KOUN Z_{HH}, Z_{DR}, and ρ_{HV} at 0.5°, 0.9°, and 1.4° elevation during the 22:29:51 UTC volume scan. 90th percentile Z_{HH} decreases with height, and median ρ_{HV} increases with height.

exhibit a range of debris sizes and shapes, some Rayleigh and non-Rayleigh scatterers contribute to the TDS. As larger debris are centrifuged and fall out, concentrations of non-Rayleigh scatterers will decrease, increasing ρ_{HV}. Moreover, given the strong Z_{HH} dependence on size, decreasing debris size increases the relative power-weighted contributions of Rayleigh scatterers (e.g., rain drops or smaller debris) compared to non-Rayleigh scatterers, which also increases ρ_{HV}.

Studies have discussed negative Z_{DR} in tornadoes, indicating some common degree of debris alignment and/or non-Rayleigh scattering. At 0.5° and 1.4° elevation, median Z_{DR} is -0.1 and -0.3 dB, respectively. Permutation tests indicate a p-value of 0.206, indicating that a statistically significant change in median Z_{DR} is not likely. 90th percentile Z_{DR} indicates a statistically significant reduction in large positive values of Z_{DR} at 1.4° compared to 0.5° (Table 4.2). Fig. 4.4 shows this reduction in positive Z_{DR} values and a higher frequency of negative Z_{DR} at 1.4° elevation compared to the 0.5° elevation. A discussion of possible causes of negative Z_{DR} and decreasing Z_{DR} with height are presented later.

High spatial Z_{DR} variability is evident within the TDS (Fig. 4.4). The 0.5° elevation Z_{DR} histogram (Fig. 4.5) indicates a roughly symmetric distribution centered near 0 dB with some positive and negative Z_{DR} values. Spatial variability of Z_{DR} may depend on several factors. Errors in Z_{DR} estimates and other polarimetric variables increase as ρ_{HV} and signal-to-noise ratio (SNR) decrease (Bringi and Chandrasekar 2001). Thus, greater Z_{DR} variability in TDSs may occur due to low ρ_{HV}, although high SNR in tornadoes containing large or numerous debris may mitigate this effect. Many debris exhibit large aspect ratios and may possess inherently large ranges of Z_{DR} depending on their orientation. Random orientations of large debris, however, could cause near-zero Z_{DR} if numerous debris are present. As the number of scatterers decrease, large magnitude Z_{DR} of a few scatterers may contribute to higher variability of Z_{DR}.

4.3.2 2230 – 2232 UTC dual-wavelength analyses

Dual-wavelength analyses of OU-PRIME and KOUN data are presented in this section, exploiting close temporal and spatial matching of radar scans between 2230 – 2232 UTC. For clarity, pairs of elevation angles at the approximately matching heights and times are abbreviated using C and S to refer to C-band and S-band, as follows:

- Comparison level 1: C_1 and S_1 for 1.0° OU-PRIME and 1.4° KOUN data
- Comparison level 2: C_2 and S_2 for 2.0° OU-PRIME and 2.4° KOUN data
- Comparison level 3: C_3 and S_3 for 3.0° OU-PRIME and 4.0° KOUN data

4.3.2.1 Radar reflectivity factor

S-band Z_{HH} exceeds C-band Z_{HH} within the TDS. 90th percentile Z_{HH} at S-band is 9.0 – 11.0 dB higher than C-band at each comparison height, and median Z_{HH} at S-band is 4.8 – 7.2 dB higher than C-band (Tables 4.3 – 4.5). Higher Z_{HH} at S-band has been observed for hail compared to X-band (Atlas and Ludlam 1961; Snyder et al. 2010) and C-band (Picca and Ryzhkov 2012) due to resonance effects. Likewise, resonance effects in TDSs may contribute to large Z_{HH} differences at S- and C-band. Given that 90th percentile Z_{HH} represents the highest radar reflectivity factors in the TDS and larger dual-wavelength Z_{HH} differences are observed for 90th percentile Z_{HH} compared to median Z_{HH}, larger dual-wavelength differences may indicate larger debris sizes.

Table 4.3: Median and 90th percentile Z_{HH} (dBZ), median ρ_{HV}, median Z_{DR} (dB), 90th percentile Z_{DR} (dB), Z_{DR} median absolute deviation (MAD), and median Φ_{DP} (°) in the TDS and surrounding areas of rain, for the 1.0° OU-PRIME and 1.4° KOUN elevation. Center beam heights for OU-PRIME and KOUN are 360 and 340 m AGL, respectively. OU-PRIME and KOUN scan times are 22:30:59 – 22:31:14 UTC and 22:30:56 – 22:31:13 UTC, respectively. For median Φ_{DP} in the TDS and rain, p-values are only calculated for Φ_{DP} differences between the TDS and rain, so the dual-wavelength differences are not calculated (NC).

Statistic	OU-PRIME 1.0°	KOUN 1.4°	Difference	P-value
Median Z_{HH}	42.0	47.0	-5.0	$\leq$ 0.0002
90th percentile Z_{HH}	47.5	56.5	-9.0	$\leq$ 0.0002
Median ρ_{HV}	0.60	0.75	-0.15	$\leq$ 0.0002
Median Z_{DR}	0.2	-0.3	0.5	0.005
90th percentile Z_{DR}	3.5	2.0	1.5	0.001
Z_{DR} MAD	1.1	1.5	-0.4	0.199
Median Φ_{DP} (TDS)	-8.2	9.6	-17.8	NC
Median Φ_{DP} (Rain)	4.4	3.9	0.5	NC

Table 4.4: Same as Table 4.3, except for the 2.0° OU-PRIME and 2.4° KOUN elevation. Center beam heights for OU-PRIME and KOUN are 720 and 630 m AGL, respectively. OU-PRIME and KOUN scan times are 22:31:14 – 22:31:31 UTC and 22:31:44 – 22:31:57 UTC, respectively.

Statistic	OU-PRIME 2.0°	KOUN 2.4°	Difference	P-value
Median Z_{HH}	41.5	46.3	-4.8	≤ 0.0002
90th percentile Z_{HH}	45.3	53.9	-8.6	≤ 0.0002
Median ρ_{HV}	0.61	0.76	-0.15	≤ 0.0002
Median Z_{DR}	-0.2	-0.7	0.5	0.011
90th percentile Z_{DR}	1.9	2.2	-0.3	0.194
Z_{DR} MAD	1.1	1.5	-0.4	0.199
Median Φ_{DP} (TDS)	-7.2	11.8	-19.0	NC
Median Φ_{DP} (Rain)	6.2	4.6	1.6	NC

Table 4.5: Same as Table 4.3, except for the 3.0° OU-PRIME and 4.0° KOUN elevation. Center beam heights for OU-PRIME and KOUN are 1110 and 1090 m AGL, respectively. OU-PRIME and KOUN scan times are 22:31:31 – 22:31:47 UTC and 22:32:13 – 22:32:26 UTC, respectively.

Statistic	OU-PRIME 3.0°	KOUN 4.0°	Difference	P-value
Median Z_{HH}	39.8	47.0	-7.2	≤ 0.0002
90th percentile Z_{HH}	43.5	54.5	-11.0	≤ 0.0002
Median ρ_{HV}	0.66	0.80	-0.14	≤ 0.0002
Median Z_{DR}	0.1	-0.1	0.2	0.325
90th percentile Z_{DR}	1.8	2.5	-0.7	0.006
Z_{DR} MAD	1.0	1.8	-0.8	0.200
Median Φ_{DP} (TDS)	2.0	13.1	-11.1	NC
Median Φ_{DP} (Rain)	11.4	6.7	4.7	NC

T-matrix calculations reveal that S-band Z_{HH} is often higher than C-band Z_{HH}. Dual-wavelength Z_{HH} differences exhibit significant differences depending on "debris" aspect ratio or wetness (Figs. 4.1,4.2). With the exception of wet, prolate spheroids, S-band Z_{HH} is generally greater than or equal to C-band Z_{HH}. Several diameter ranges of dry and wet oblate spheroids and dry prolate spheroids could produce a TDS with 10 dB differences in S-band and C-band Z_{HH}, such as dry, oblate spheroids with diameters between 22 – 32 mm.

4.3.2.2 Co-polar cross-correlation coefficient

Comparisons of OU-PRIME and KOUN data from 2230 – 2232 UTC reveal differences in ρ_{HV}. S_1 and C_1 ρ_{HV}, Z_{DR}, and Φ_{DP} are shown in Fig. 4.6. Higher ρ_{HV} values are generally observed at S_1 compared to C_1 (Fig. 4.7). At the three comparison levels, median ρ_{HV} at S-band is 0.14 – 0.15 higher than C-band, and permutation tests reveal statistically significant differences between S- and C-band (Tables 4.3 – 4.5).

An increase in both S- and C-band ρ_{HV} is observed from 350 m to 1100 m (Fig. 4.7). Permutation tests are conducted for S_1 and S_3, and C_1 and C_3 to determine if statistically significant changes in ρ_{HV} occur with height. The difference in S_1 and S_3 median ρ_{HV} is -0.05 and the p-value is 0.044, indicating a statistically significant increase in S-band median ρ_{HV} with height. Similar increases are observed in C-band median ρ_{HV} with a difference of -0.05 and a p-value of 0.006. The increase in ρ_{HV} corresponds to a decrease in Z_{HH}, which

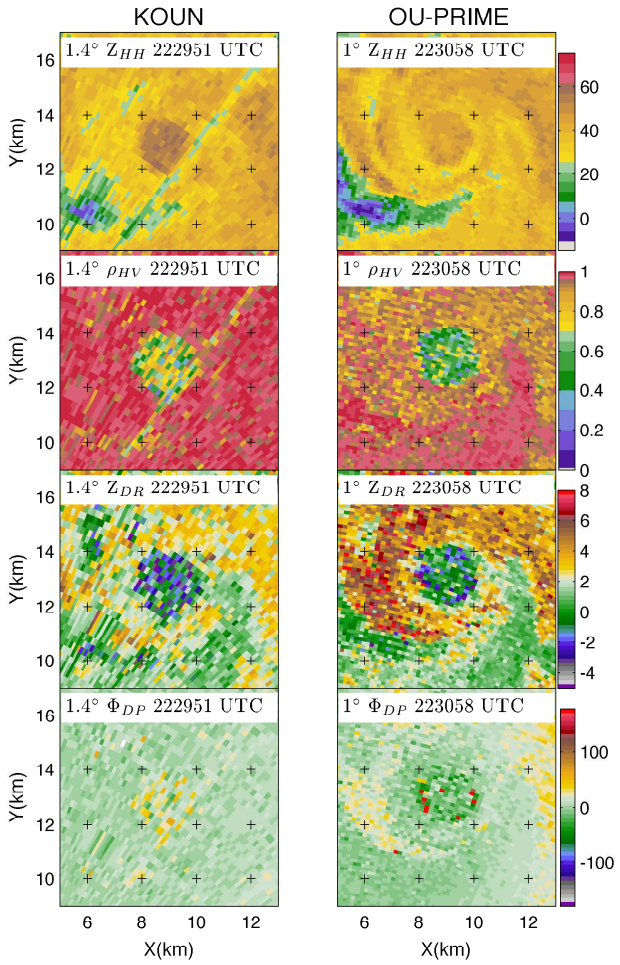

Figure 4.6: 1.4° KOUN (left column) and 1° OU-PRIME (right column) Z_{HH}, ρ_{HV}, Z_{DR} (dB), and Φ_{DP} (°) at 22:30:56 and 22:30:59 UTC, respectively. The x and y coordinates show the distance from KOUN (in km). ρ_{HV} is generally higher at S-band compared to C-band. Within the TDS, ρ_{HV} at C-band is typically below 0.7 while S-band ρ_{HV} is above 0.7 in the same regions. Both KOUN and OU-PRIME exhibit considerable variability in Z_{DR}, and regions of negative Z_{DR}. S-band (C-band) Φ_{DP} exhibits a positive (negative) shift within the TDS.

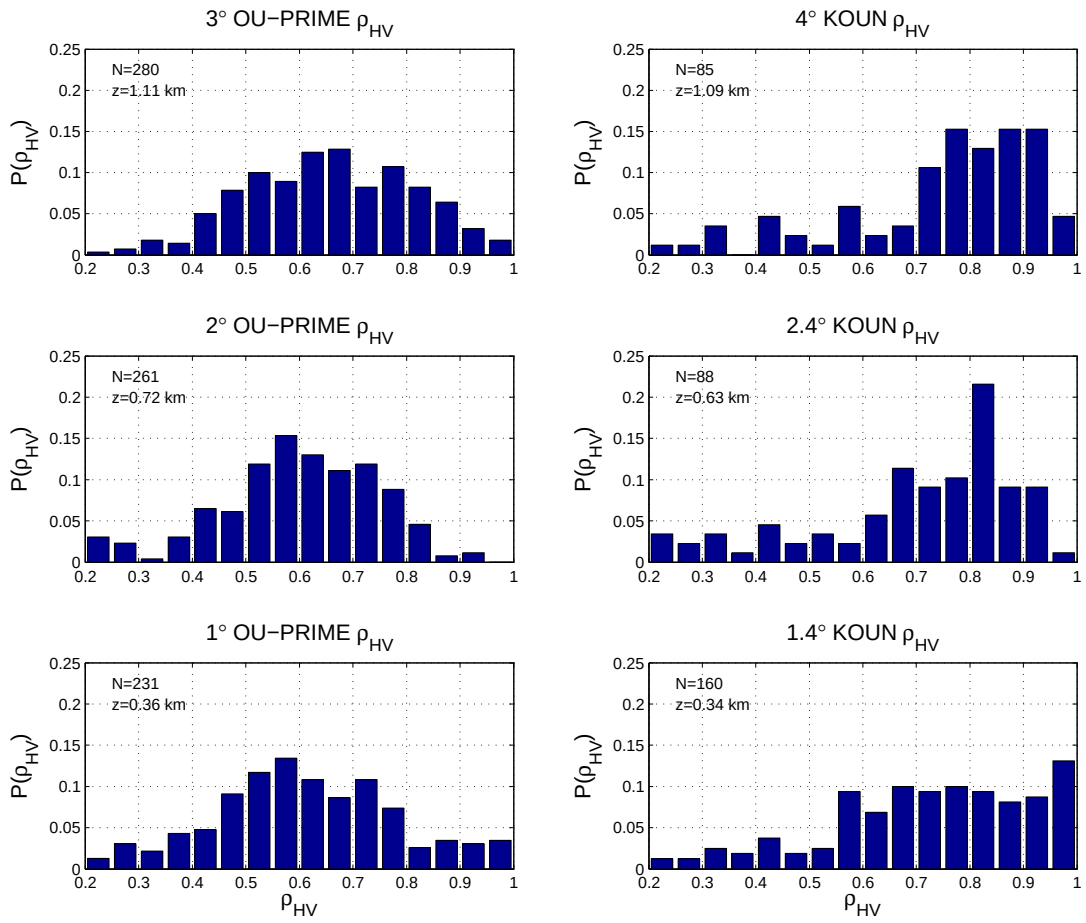

Figure 4.7: Histograms of OU-PRIME and KOUN ρ_{HV} at comparable beam heights. As height increases, ρ_{HV} increases at both S-band and C-band.

suggests a decrease in debris size and/or concentration. Differences between S_1 and S_3 90th percentile Z_{HH}, and C_1 and C_3 90th percentile Z_{HH} are 2.0 and 4.0 dB, respectively, with p-values of 0.099 and 0.

Differences in non-Rayleigh scattering characteristics at S- and C-band may explain differences in ρ_{HV}. If debris exhibit a sufficiently large range of sizes, larger scatterers may exhibit non-Rayleigh scattering while the smaller scatterers exhibit Rayleigh scattering. Because non-Rayleigh scattering occurs for larger debris sizes at S-band compared to C-band, a large size distribution of debris would contain fewer non-Rayleigh scatterers at S-band compared to C-band. Thus, the impact of resonance effects on ρ_{HV} would be greater at C-band compared to S-band, causing lower ρ_{HV} at C-band. Moreover, C-band has a greater sensitivity to deviations from a spherical shape compared to S-band, resulting in lower ρ_{HV} (Balakrishnan and Zrnić 1990). Large variations in debris shapes, sizes, and orientations may be a contributing factor to the large variability of ρ_{HV} in TDSs. The increase in ρ_{HV} with height at both S- and C-band may result from a smaller ratio of non-Rayleigh scatterers to total scatterers due to debris fallout and centrifuging.

4.3.2.3 Differential reflectivity

OU-PRIME and KOUN data exhibit similarities and differences in Z_{DR}. Contiguous regions of negative Z_{DR} are observed at both S_1 and C_1, respectively (Fig. 4.6). Mean values of S_1 and C_1 median Z_{DR} are -0.3 and 0.2 dB,

respectively, indicating lower Z_{DR} at S-band (Table 4.3). Higher 90th percentile Z_{DR} is observed at C-band, with a greater dual-wavelength difference in 90th percentile Z_{DR} compared to median Z_{DR}.

An intriguing observation of TDS studies is that coherent regions of negative Z_{DR} are observed while positive Z_{DR} regions are only observed in regions of higher ρ_{HV} where precipitation entrainment is suspected. If no common debris alignment occurs, individual debris would produce both large positive and negative Z_{DR}, which could average to near-zero values for a resolution volume. Bluestein et al. (2007) suggest that a small number of commonly aligned debris in a resolution volume could cause negative Z_{DR}. In such cases, distinct peaks in the Doppler spectra would likely be evident. In the present case, C-band Doppler spectra in negative Z_{DR} regions are generally flat or exhibit broad peaks, suggesting that a large number of debris contribute to negative Z_{DR} measurements.

The negative Z_{DR} signature occurs when the tornado is passing over a heavily vegetated area with few manmade structures near Lake Stanley Draper (Fig. 4.3), and the NWS damage survey notes extensive tree damage in this area. Although some larger debris from structures could be lofted, numerical modeling simulations have shown that most large, dense debris fall out in the lowest 300 m AGL (Snow 1984; Dowell et al. 2005). Based on satellite imagery and the damage survey, it is speculated that vegetation, such as leaves or small tree branches, are the dominant scatterers in the TDS during this dual-wavelength comparison

at 340 – 360 m AGL. A second explanation is that a small concentration of large debris remains above 300 m AGL, and produce negative Z_{DR}.

The presence of both very low ρ_{HV} and negative Z_{DR} creates an interesting conundrum. Given low ρ_{HV} collocated with the negative Z_{DR} signature, scatterers likely exhibit non-Rayleigh scattering and/or a low common degree of scatterer alignment. Balakrishnan and Zrnić (1990) found that as the degree of common alignment of wet hail decreases, ρ_{HV} decreases. Hence, very low ρ_{HV} may suggest a low degree of common alignment. However, given that debris scattering characteristics are complex due to their unusual shapes, sizes, and compositions, we speculate that the wide range of scatterer characteristics within a resolution volume could still produce very low ρ_{HV} even if some degree of common scatterer alignment exists. Given the large instrinic Z_{DR} values of debris (Fig. 4.1c,f), even a small degree of common alignment could produce the slightly negative Z_{DR} values observed herein. We speculate that observations of increasingly negative Z_{DR} with height could result from a greater tendency of smaller, less-dense debris to exhibit a greater degree of common alignment whereas larger debris near the surface are exhibit a lower degree of common alignment.

Z_{DR} exhibits large spatial variability within the TDS at both S-band and C-band (Fig. 4.6). Errors in Z_{DR} measurements increase as ρ_{HV} decreases (Bringi and Chandrasekar 2001), which may account for some variability in Z_{DR}. Histograms of Z_{DR} at each comparison level (Fig. 4.8) also reveal high variability

of Z_{DR} at each elevation angle. Although S-band Z_{DR} MAD is higher at each elevation angle compared to C-band, the permutation test p-value is 0.198 – 0.200. Thus, the permutation test does not yield statistical significance for dual-wavelength Z_{DR} MAD differences.

4.3.2.4 Differential propagation phase

Within the TDS, differential propagation phase, Φ_{DP}, exhibits high variability and different offsets at S- and C-band compared to surrounding areas of rain (Fig. 4.6). Non-Rayleigh scattering effects of numerous debris within resolution volumes likely contributes to high variability of δ_{DP}, leading to high variability of Φ_{DP}. An interesting observation is that Φ_{DP} differ from Φ_{DP} values outside of the TDS. To investigate these differences, median Φ_{DP} inside and outside of the TDS are calculated to illuminate the differences in Φ_{DP}. The same thresholding procedure discussed in Section 4.2 is used to identify the TDS. To provide a comparison in areas of rain, resolution volumes with ρ_{HV} above 0.98 and 0.93 at S-band and C-band, respectively, are identified within an annulus between the radius of maximum wind and a 4-km radius from the vortex center.

Higher (lower) median Φ_{DP} is observed within the TDS at S-band (C-band) compared to surrounding areas of rain. Tables 4.3 – 4.5 present median S- and C-band Φ_{DP} in rain and in the TDS. A permutation test is performed at S- and C-band comparing median Φ_{DP} in the TDS and rain. P-values for S_1 – S_3

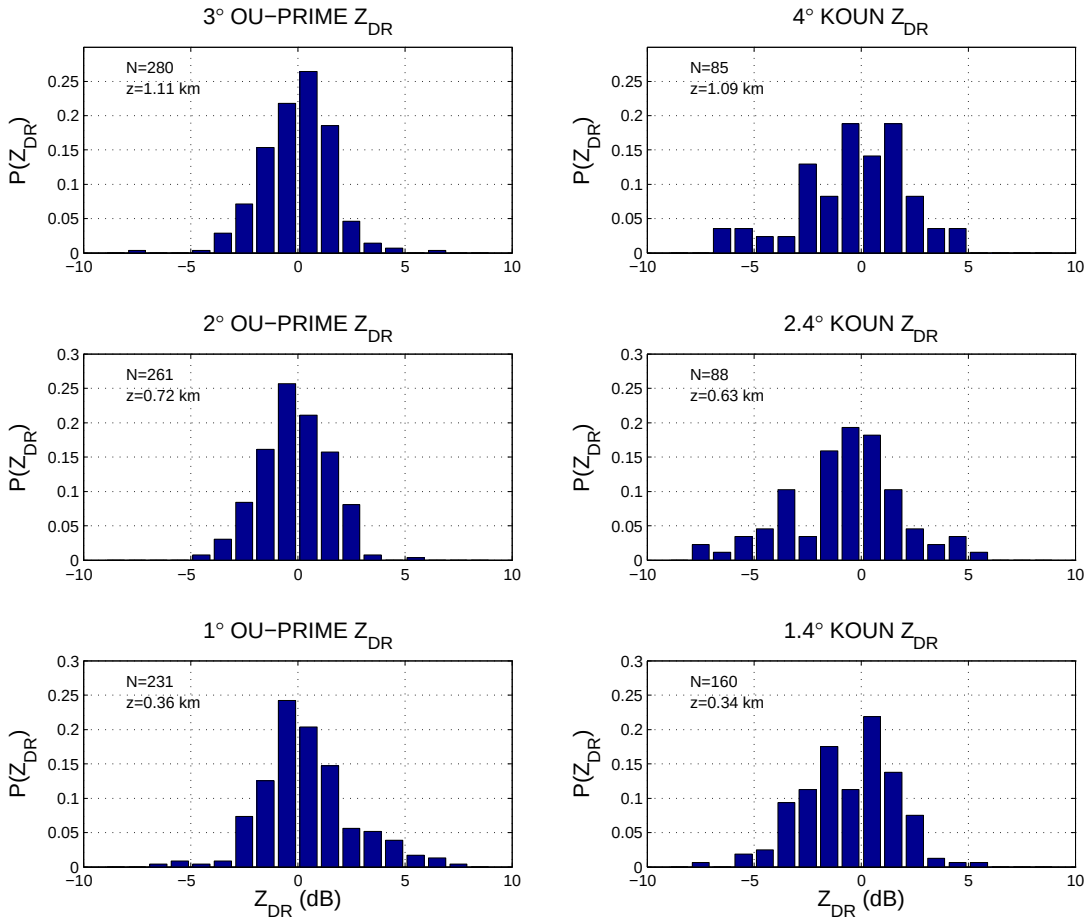

Figure 4.8: Histograms of OU-PRIME and KOUN Z_{DR} at comparable beam heights. Higher variability of Z_{DR} is observed at S-band compared to C-band, although statistically significant differences are not observed.

and C_1 – C_3 are ≤ 0.0002, indicating a statistically significant offset in median Φ_{DP} within the TDS at both S- and C-band.

δ_{DP} folding may account for the observations of a slightly positive (negative) shift in Φ_{DP} at S-band (C-band). δ_{DP} folding occurs where δ_{DP} changes from -180° to 180°, or from 180° to -180° (Figs. 4.1,4.2). Due to the larger electrical sizes of scatterers at C-band compared to S-band, the first δ_{DP} fold at C-band occurs at a smaller diameter compared to S-band. For example, in the case of wet, oblate debris (Fig. 4.1f), the first δ_{DP} fold at S- and C-band occur at 47 and 23 mm, respectively. Based on KOUN and OU-PRIME observations, positive (negative) δ_{DP} at S-band (C-band) could result for diameter ranges of 24 – 41 mm or 62 – 72 mm.

Based on T-matrix calculations, if a large range of scatterer diameters are present, a δ_{DP} offset is less likely because multiple folds average out large positive and negative δ_{DP}. On the other hand, if a small range of scatterer diameters are present, or a few similarly sized debris dominant the backscattered radar signal, then a distinct δ_{DP} offset is more likely. Hence, δ_{DP} offsets could provide some qualitative information about debris size distributions. However, using δ_{DP} to estimate debris size might not be feasible because δ_{DP} depends on poorly known variables such as debris composition, orientation, and water coating.

4.3.3 2238 UTC volume scans

The 2238 UTC KOUN volume scan encompasses the period of most severe tornado damage. At 2238 UTC, examination of 0.5° KOUN velocity data reveals that the tornado had just passed over 1-40 near Choctaw Road (Fig. 4.3). The NWS damage survey found EF-4 tornado damage to houses in the Deerfield West subdivision just west of I-40, and a gas station and restaurant sustained up to EF-3 damage as the tornado passed over I-40 (NOAA National Climatic Data Center 2010).

Decreasing Z_{HH} with height is observed at 2238 UTC (Fig. 4.9), indicating a decrease in debris size or concentration with height. 90th percentile Z_{HH} exhibits a statistically significant decrease in height with a permutation test p-value of 0.001. Given differences in damage severity and terrain characteristics between the 2229 and 2238 UTC volume scans, polarimetric variables might be expected to exhibit some differences. To compare similar altitudes between the 2229 and 2238 UTC scans, 0.9° KOUN data at 2229 UTC (z=210 m) and 0.5° KOUN data at 2238 UTC (z=200 m AGL) are selected. 2238 UTC 0.5° elevation median and 90th percentile Z_{HH} are 7.3 and 3.0 dB higher, respectively, compared to 2229 UTC 0.5° elevation KOUN data. Permutation tests yield p-values of $\leq$ 0.0002 for both statistics, indicating statistically significant differences.

Higher ρ_{HV} is observed in the TDS at 2238 UTC compared to 2229 UTC. 2238 UTC 0.5° median ρ_{HV} is 0.04 higher than 0.9° 2229 UTC ρ_{HV}. Permutation

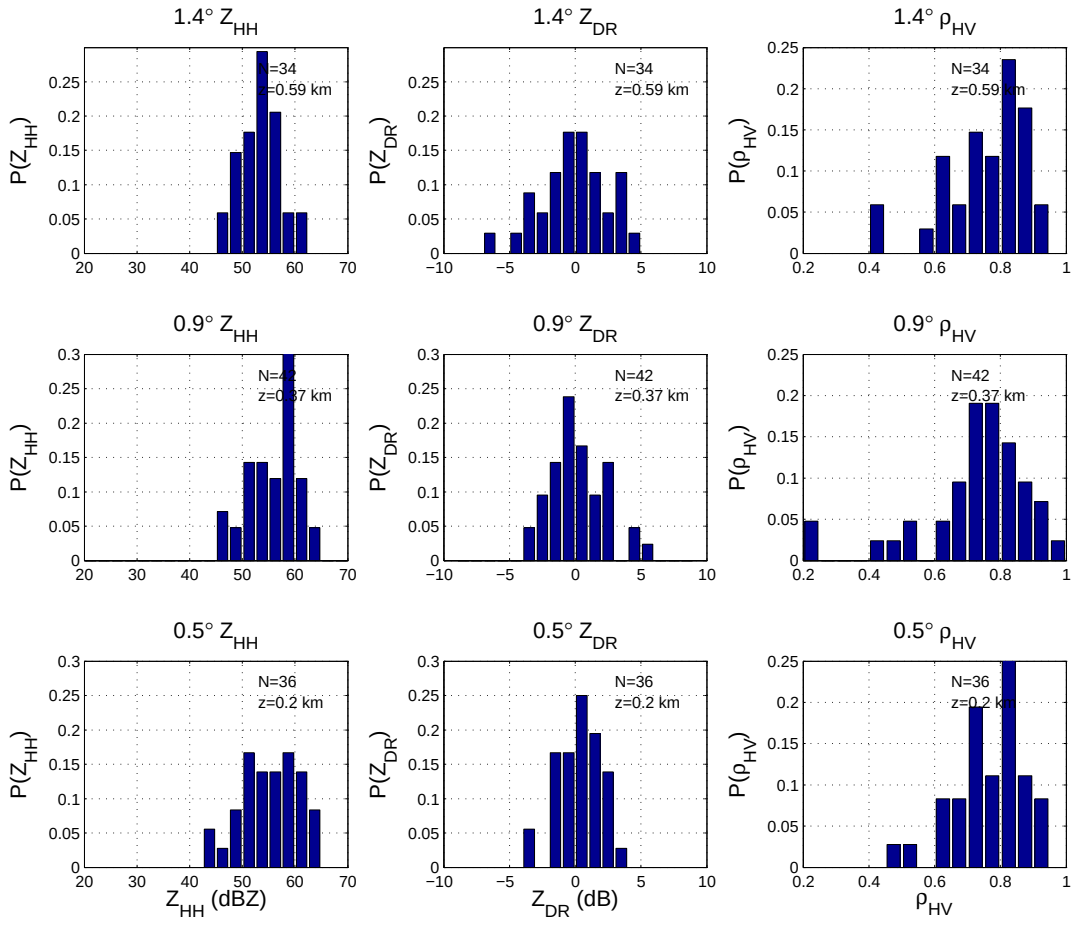

Figure 4.9: Histograms of KOUN Z_{HH}, Z_{DR}, and ρ_{HV} at 0.5°, 0.9°, and 1.4° elevation during the 22:38:27 UTC volume scan.

Table 4.6: 90th percentile Z_{HH} (dBZ), median ρ_{HV}, and median and 90th percentile Z_{DR} (dB) for the 0.5° and 1.4° KOUN elevation scans at 22:38:27 UTC. P-values are determined through hypothesis testing using a permutation test with 5000 permutations.

Statistic	KOUN 0.5°	KOUN 1.4°	Difference	P-value
90th percentile Z_{HH}	62.5	58.2	4.3	0.001
Median ρ_{HV}	0.78	0.79	-0.01	0.435
Median Z_{DR}	0.5	0.0	0.5	0.165
90th percentile Z_{DR}	2.5	3.4	-0.9	0.130

tests indicate that the median ρ_{HV} difference is statistically significant at a p-value of 0.029. A possible cause of higher ρ_{HV} in tornadoes is precipitation entrainment. Higher ρ_{HV} and increases in Z_{DR} have been observed when rain bands wrap around tornadoes (Schwarz and Burgess 2011; Bodine et al. 2011). In the present case, permutation tests indicate that changes in median and 90th percentile Z_{DR} are not statistically significant, for this case.

Similarities are observed in the 2238 – 2239 UTC dual-wavelength analyses compared to the earlier dual-wavelength analyses. For the 1.4° KOUN and 1° OU-PRIME elevation angles, S-band median and 90th percentile Z_{HH} are higher compared to C-band Z_{HH} (Table 4.7) with p-values of ≤ 0.0002 for median and 90th percentile Z_{HH}, indicating statistically significant differences in Z_{HH}. ρ_{HV} is higher in the TDS at S-band compared to C-band (Fig. 4.10), with

Table 4.7: 90th percentile and median Z_{HH} (dBZ), median ρ_{HV}, median Z_{DR} (dB), 90th percentile Z_{DR} (dB), Z_{DR} MAD (dB), and median Φ_{DP} (°) in the TDS and surrounding areas of rain, for 1.0° OU-PRIME and 1.4° KOUN elevation. Center beam heights for OU-PRIME and KOUN are 484 and 595 m AGL, respectively, and resolution volume sizes for OU-PRIME and KOUN are 0.014 and 0.059 km^3, respectively. OU-PRIME and KOUN scan times are 22:38:13 – 22:38:31 UTC and 22:39:31 – 22:39:48 UTC, respectively.

Statistic	OU-PRIME 1.0°	KOUN 1.4°	Difference	P-value
Median Z_{HH}	44.5	54.0	-9.5	≤ 0.0002
90th percentile Z_{HH}	47.7	58.2	-10.5	≤ 0.0002
Median ρ_{HV}	0.67	0.79	-0.12	≤ 0.0002
Median Z_{DR}	-0.2	0.0	-0.2	0.37
90th percentile Z_{DR}	1.1	3.8	-2.7	0.001
Z_{DR} MAD	0.7	1.5	-0.8	0.200
Median Φ_{DP} (TDS)	1.8	7.6	-5.8	NC
Median Φ_{DP} (Rain)	13.9	7.8	6.1	NC

a difference of -0.12. The permutation test p-value of ≤ 0.0002 indicates a statistically significant difference in median ρ_{HV} at S- and C-band.

Some interesting differences are observed during the 2238 – 2239 UTC dual-wavelength comparison compared to the earlier dual-wavelength analyses. Median and 90th percentile Z_{HH} are 9.8 and 9.7 dB higher at S-band compared to C-band. In contrast to the 2231 UTC dual-wavelength comparison, median Z_{HH} does not exhibit a smaller dual-wavelength difference compared to 90th percentile Z_{HH}. This result indicates a greater number of resolution volumes containing large dual-wavelength Z_{HH} differences during the 2238 – 2239 UTC comparison, and may suggest greater amounts of large debris lofted compared to 2230 – 2232 UTC comparison. Given increased damage severity at 2238 UTC indicated by the damage survey and higher density of manmade structures (Fig. 4.3), an increase in lofted debris size is consistent with the damage survey. Differences are also noted in Φ_{DP} compared to the earlier dual-wavelength comparison. For median Φ_{DP}, a negative shift is observed at C-band while a statistically significant shift in S-band Φ_{DP} is not observed in the TDS.

4.3.4 Range profiles of polarimetric radar data and axisymmetric velocity

Axisymmetric velocity retrieval techniques have been applied to high-resolution radar data to retrieve three-dimensional tornado wind fields (e.g., Lee et al. 1999; Lee and Wurman 2005; Dowell et al. 2005). Range profiles of axisymmetric radial

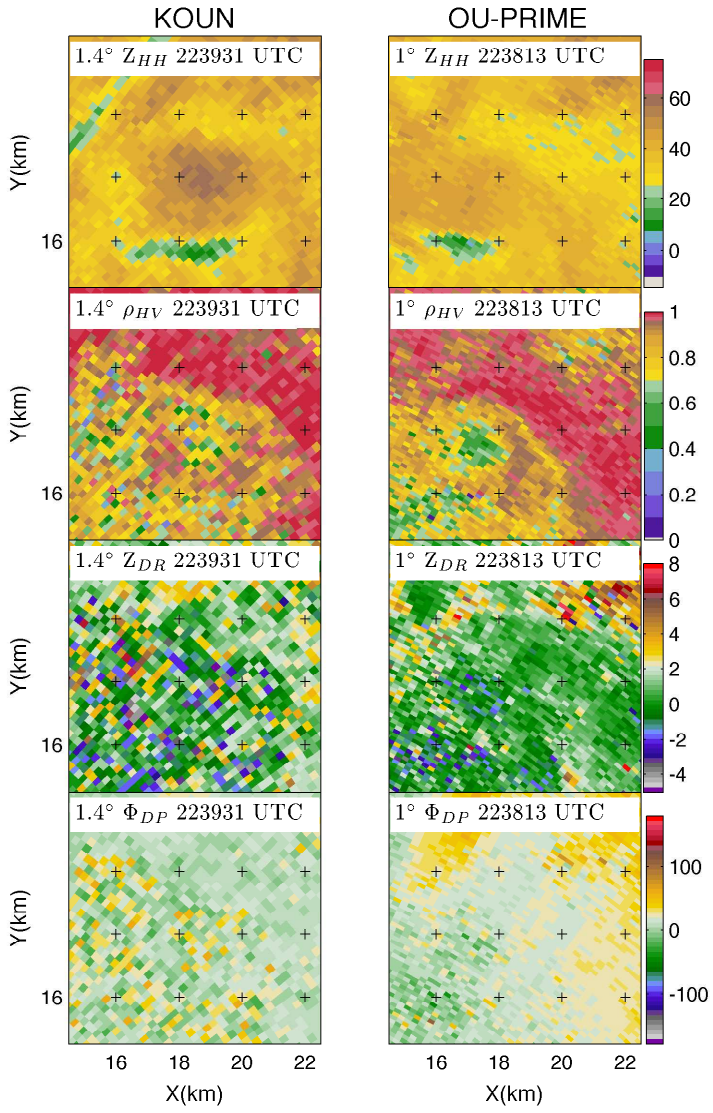

Figure 4.10: 1.4° KOUN (left column) and 1° OU-PRIME (right column) Z_{HH} (dBZ), ρ_{HV}, Z_{DR} (dB), and Φ_{DP} (°) at 22:39:31 and 22:38:13 UTC, respectively. The x and y coordinates show the distance from KOUN (in km). TDSs are evident at both S- and C-band, and the TDS is further east for the KOUN scan due to the time difference between scans. As observed during the earlier dual-wavelength comparison, ρ_{HV} is higher at S-band compared to C-band.

and tangential velocities, $u_p(r)$ and $v_p(r)$, are retrieved using a method developed by Dowell et al. (2005), which uses a least squares fit for Doppler radial velocity data. To avoid confusion between axisymmetric radial velocities and Doppler radial velocity, the latter will be referred to as Doppler velocity hereafter. For KOUN and OU-PRIME, $u_p(r)$ and $v_p(r)$ are computed for 250-m wide annuli, at 125-m intervals, respectively. Velocity retrievals are obtained for the 2229 UTC KOUN and 2230 UTC OU-PRIME volume scans at low elevation angles.

A comparison of KOUN and OU-PRIME data at similar altitudes show close agreement between retrieved velocity profiles from the two radars. Fig. 4.11a–d shows range profiles of radial and tangential winds, and Fig. 4.11e–h shows range profiles of Z_{HH} and ρ_{HV}. Maximum tangential wind speeds from 1.4° KOUN and 1.0° OU-PRIME are 46 and 50 m s^{-1}, respectively (Fig. 4.11b). Although the radar comparison yields relatively close agreement, some differences may result from different resolution volume geometries and spatial resolutions. Larger resolution volume sizes from KOUN may not fully sample the azimuthal Doppler velocity profile, which may result in an underestimate of the maximum tangential wind speed (e.g., Carbone et al. 1985). Errors in KOUN least squares fit velocity estimates may also be higher because fewer resolution volumes are available within each annuli, and the sensitivity of errors to the number of available resolution volumes could be quantified in future work.

Comparisons of polarimetric variables and the wind retrievals suggest possible effects of debris centrifuging on retrieved velocity profiles. A consistent trend

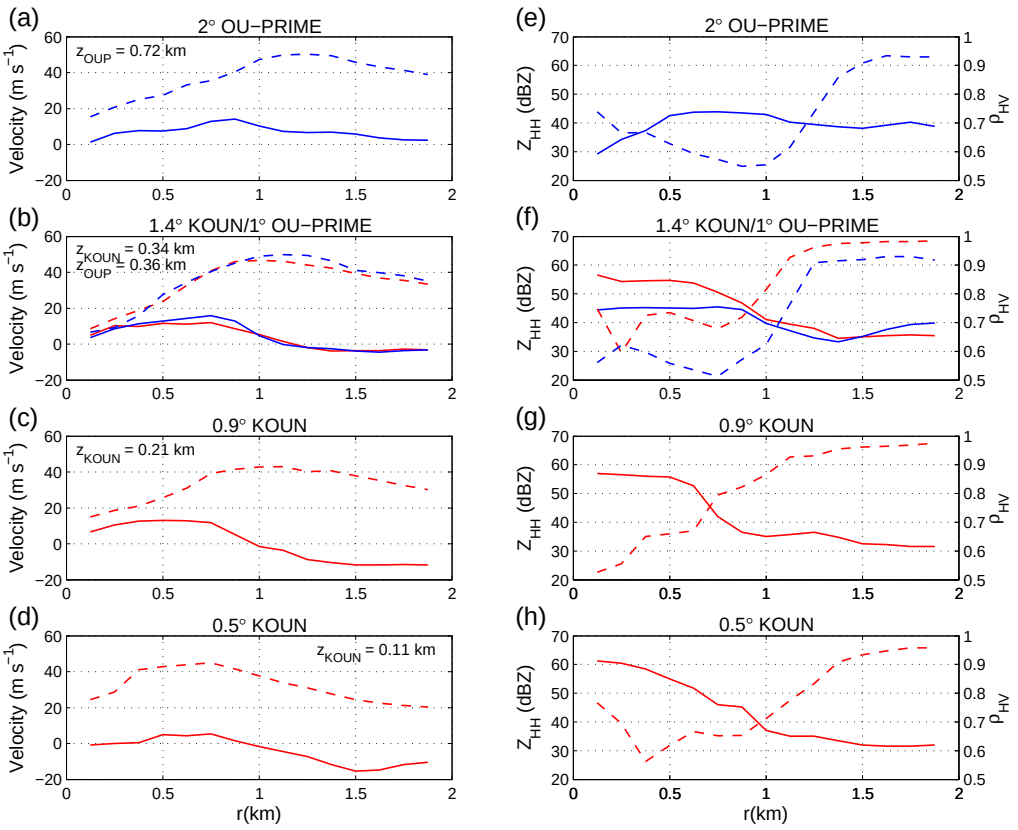

Figure 4.11: Range profiles of radial and tangential velocity from the 2229 UTC KOUN and 2230 UTC OU-PRIME volume scans, showing (a) 2.0° OU-PRIME (z=0.72 km), (b) 1.0° OU-PRIME (z=0.36 km), and 1.4° KOUN (z=0.34 km), (c) 0.9° KOUN (z=0.21 km), and (d) 0.5° KOUN (z=0.11 km). Range profiles of Z_{HH} (dBZ) and ρ_{HV} are shown in plots (e) – (h), and are arranged in the same order as (a) – (d). Red and blue lines are used to show range profiles of KOUN and OU-PRIME data, respectively. For (a) – (d), the solid (dashed) lines indicate range profiles of radial (tangential) wind speeds. For (e) – (h), the solid (dashed) lines indicate range profiles of Z_{HH} and ρ_{HV}. Beam heights at the center of the tornado are labelled on each figure.

in range profiles of radial velocity from 100 m to 720 m AGL (Fig. 4.11a–d) is radial divergence ($\frac{d(ru_p)}{dr} > 0$) from the vortex center to radii of 0.5 – 0.75 km, and radial convergence ($\frac{d(ru_p)}{dr} < 0$) beyond these radii. If air-scatterer velocity differences are neglected, integration of the continuity equation would reveal a two-cell vortex with a central downdraft surrounded by an annulus of updraft. In the region of largest u_p, median Z_{HH} exceeds 45 dBZ and median ρ_{HV} is below 0.8 (Fig. 4.11e–h). Thus, dominant scatterers in the region of radial divergence and positive u_p are tornadic debris. Because scatterer properties, such as size or density, must be known to estimate debris centrifuging effects, contributions of debris centrifuging to the radial wind component cannot be accurately determined.

Range profiles near the surface exhibit decreasing Z_{HH} as a function of range. 0.5° KOUN Z_{HH} profile (Fig. 4.11a, z=110 m) reveals a maximum in Z_{HH} at the center of the tornado, suggesting that the vortex center contains the largest debris, highest concentration of debris, or both. One explanation for this observation is that inflow may inhibit debris centrifuging at low levels. Range profiles of radial winds indicate inflow at r > 1 km, with maximum inflow velocities of -15 m s^{-1}. At closer radii, debris centrifuging or debris falling into the inflow layer may mask inflow winds (e.g., Dowell et al. 2005). A second explanation is that a smaller scale vortex is present within the 1-km scale vortex, which could enhance debris generation and lofting. 0.5° Doppler velocity data indicate that a smaller scale vortex may be embedded within the 1-km scale radius vortex.

However, the smaller scale vortex is not adequately resolved by KOUN, so the maximum tangential wind speed within the smaller scale vortex is unknown.

At 350 m AGL, Z_{HH} remains approximately constant with range inside the TDS (Fig. 4.11f). The highest value of u_p within the tornado of 15.7 m s^{-1} is observed at a range of 750 m AGL. Positive u_p at 0.21 km and 0.34 km indicates outward motion of scatterers from r=0 to 750 m. Compared to 0.5° elevation (z=110 m), lower Z_{HH} at 1.4° elevation is observed near the center of the tornado, and higher Z_{HH} is observed closer to the maximum u_p (Fig. 4.11f). The shift of higher Z_{HH} toward greater ranges likely arises from debris centrifuging, radially outward debris motion caused by a two-cell vortex (divergence within core flow), or both. At 2° elevation (z=720 m AGL), OU-PRIME data reveal a weak-echo hole (WEH; Fujita 1981; Wurman et al. 1996; Wurman and Gill 2000; Bluestein et al. 2004; Dowell et al. 2005). Within the WEH, median ρ_{HV} exhibits a relative maximum within the RMW even though a minimum in Z_{HH} is observed. The increase in ρ_{HV} in the center of the tornado may result from a decrease in the mean size of scatterers due to centrifuging, and therefore reduce the proportion of scatterers exhibiting non-Rayleigh scattering (Fig. 4.11e, z=720 m).

4.4 Conclusions

Statistical analyses of dual-wavelength polarimetric TDSs are presented with comparisons to damage surveys. Low-altitude KOUN radar measurements are examined to investigate changes in polarimetric TDSs with height. While the

tornado passed through a region of dense vegetation, KOUN Z_{HH} decreases with height, ρ_{HV} increases with height, and Z_{DR} became increasing negative. Debris centrifuging and fallout likely results in a reduction in larger scatterers, which decreases Z_{HH}. If a large number of non-Rayleigh scatterers fallout, an increase in ρ_{HV} should occur with height.

As the tornado passed through an urban area where EF-3 and EF-4 damage was observed, KOUN Z_{HH} decreases with height while statistically significant changes in other polarimetric variable statistics are not observed. Higher 90th percentile Z_{HH} is observed compared to the earlier observations at similar beam heights over a vegetated area. Curiously, higher median ρ_{HV} is also observed. It is speculated that higher ρ_{HV} is attributed to precipitation entrainment, although differences in debris scattering characteristics or larger resolution volume sizes cannot be ruled out.

Significant differences are observed in TDSs at S- and C-band. S-band exhibits higher Z_{HH} and ρ_{HV} values compared to C-band, likely a consequence of non-Rayleigh scattering. 90th percentile Z_{HH} dual-wavelength differences of 10 dB are observed. A larger dual-wavelength difference in median Z_{HH} occurs while the tornado caused greater amounts of damage, which suggests a greater amount of lofted large debris. Dual-wavelength comparisons reveal that S-band median ρ_{HV} is 0.12 – 0.15 higher than C-band ρ_{HV}. Non-Rayleigh scattering effects may account for lower ρ_{HV} at C-band as a consequence of a larger proportion of non-Rayleigh scatterers and greater sensitivity to deviations from

spherical shapes at C-band. Increasing ρ_{HV} is observed with increasing height above 350 m AGL, which could indicate a smaller proportion of non-Rayleigh scatterers resulting from fallout of larger debris.

A conceptual diagram of the polarimetric TDS at different altitudes is presented in Fig. 4.12. At lower altitudes, a Z_{HH} maximum occurs in the center of the vortex and low ρ_{HV} is observed throughout the TDS. At 350 m, relatively uniform Z_{HH} and low ρ_{HV} are observed, indicating an outward centrifuging of debris from the vortex center compared to lower altitudes. At 720 m, a weak-echo hole and a ρ_{HV} maximum are observed in the vortex center, implying higher concentrations of Rayleigh scatterers, reduced concentrations of debris, or both. Tanamachi et al. (2012) present a conceptual model of the TDS with a WEH aloft. In their observations, however, they observe low ρ_{HV} in the WEH, perhaps resulting from very low SNR due to low scatterer concentrations. Houser (2013) also observed both low and high ρ_{HV} aloft in WEHs at X band.

Range profiles of polarimetric variables and axisymmetric velocity retrievals suggest debris centrifuging effects on velocity retrievals. Higher Z_{HH} and low ρ_{HV} are observed in regions of positive u_p, indicating an outward motion of scatterers within the TDS. Using range profiles, polarimetric radar observations and velocity retrievals may help identify areas where debris centrifuging may contaminate Doppler velocity measurements. Unfortunately, contributions of debris centrifuging to velocity retrievals cannot be determined without substantial speculation about debris scattering characteristics.

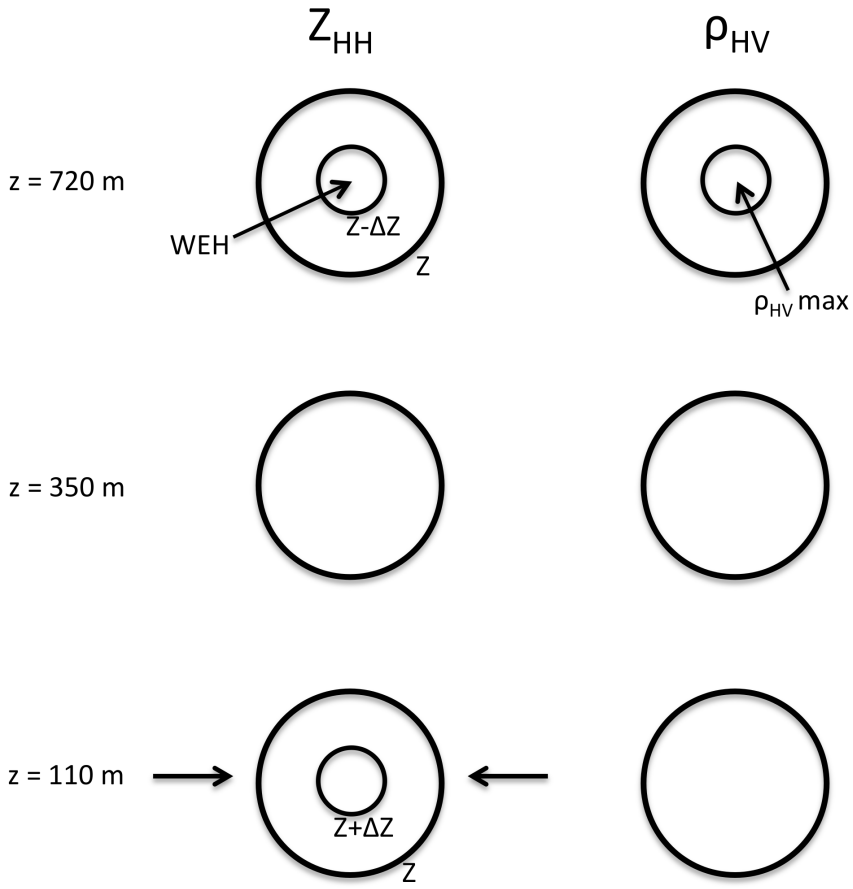

Figure 4.12: Schematic of polarimetric TDS as a function of height. Near the surface, Z_{HH} decreases with range, as shown by the Z+ΔZ contour inside the Z contour. Strong inflow (black arrows) observed at low altitudes may concentrate debris in the vortex center. At 350 m, Z_{HH} is constant with range and ρ_{HV} exhibits low values. At higher altitudes, a WEH (area inside the Z-ΔZ contour) forms, collocated with a ρ_{HV} maximum. A minimum in Z_{HH} and maximum in ρ_{HV} suggests a reduction in scatterer sizes in the vortex center and/or increased contributions from Rayleigh scatterers (e.g., rain drops).

This study addresses the need for statistical analyses of TDSs and dual-wavelength polarimetric radar comparisons of TDSs with good spatial and temporal matching. Dual-wavelength comparisons of TDSs illuminate some general characteristics of debris scattering, which may help interpret TDSs. Although dual-wavelength polarimetric radar measurements are uncommon in an operational setting, dual-wavelength Z_{HH} observations of TDSs are possible using the WSR-88D network with C-band Terminal Doppler Weather Radars or television station radars. Moreover, future radar networks could include polarimetric radars with operating different frequencies, including closely spaced X-band radars (McLaughlin and co-authors 2009).

Some intriguing differences are noted in TDS structure with height and at different wavelengths, indicating some potential for debris size estimation using polarimetric radar. A debris size estimation technique could help estimate and correct debris centrifuging effects on Doppler radial velocity fields and three-dimensional wind field retrievals. Wakimoto et al. (2012) proposed a method of correcting debris centrifuging effects using radar reflectivity factor under the assumption that scatterers within the tornado were similar to rain drops, and estimated centrifuging effects based on drop diameters retrieved from a Marshall-Palmer drop-size distribution. They noted large differences in ground-based velocity tracking display (GBVTD; Lee et al. 1999) vertical velocity fields for corrected and uncorrected radial velocities. Common observations of low ρ_{HV} in tornadoes suggest that tornadic debris exhibit resonance effects and are larger

than rain drops. Accordingly, applying this method may result in an underestimation of debris diameter and centrifuging effects. To correct radial velocity for debris centrifuging, a quantitative retrieval of debris distribution characteristics (e.g., size, concentration, type) would be needed, and would require a fundamental investigation of debris scattering characteristics to understand the relationship between debris characteristics and polarimetric radar variables.

Chapter 5

Numerical Simulations of Tornadic Debris Using A Large-Eddy Simulation Model

In this chapter, LESs of tornado-like vortices are presented with a drag force feedback parameterization that allows momentum exchange between air and debris. Sensitivity tests are conducted to examine what debris concentrations are required to affect tornado dynamics, and methods for determining maximum bounds on debris concentrations in tornadoes are developed.

5.1 Overview of the LES model and debris trajectory calculation

In this section, overviews of the LES model setup and debris trajectory calculation are presented. Boundary conditions used to create different types of vortex flows are discussed, and the procedure for calculating debris trajectories is presented, including a drag force coupling model to incorporate momentum exchange between the air and debris.

5.1.1 LES model configuration

The present study uses an LES model to investigate debris effects on tornado dynamics. The LES model is based on RIAM-COMPACT developed at Kyushu University (Uchida and Ohya 2003), and details about the numerical calculation scheme are provided in Appendix A. Maruyama (2011) discuss modifications of the LES model for tornado simulations and debris trajectory calculations for spherical debris. In this study, LES model runs employ 155, 155, and 89 grid points in the x-, y-, and z-dimensions, respectively. A fine grid is employed within the updraft region to provide maximum resolution within the tornado, with non-dimensional grid spacing of 0.003 in the x- and y-dimensions and 0.006 in the z-dimension. Outside of this region, a staggered grid is used with grid spacings in the x- and y-dimensions varying from 0.003 – 0.03 and varying from 0.006 – 0.016 in the z-dimension. The governing equations of the LES model are non-dimensional, so results can be dimensionalized by choosing a characteristic velocity, V_0. For example, for $V_0 = 150$ and 250 m s^{-1}, the smallest horizontal grid spacings are 6.9 and 19.1 m, respectively.

The LES model boundary conditions create similar flow conditions to tornado vortex chambers, using a convergence and convection region (e.g., Ward 1972; Church et al. 1979; Church and Snow 1993). The LES model configuration for a vortex breakdown simulation is shown in Fig. 5.1, and an example of a Ward-type vortex chamber is shown in Fig. 5.2 for comparison. Inflow and low-level vorticity are provided through four inlet regions, with dimensions of

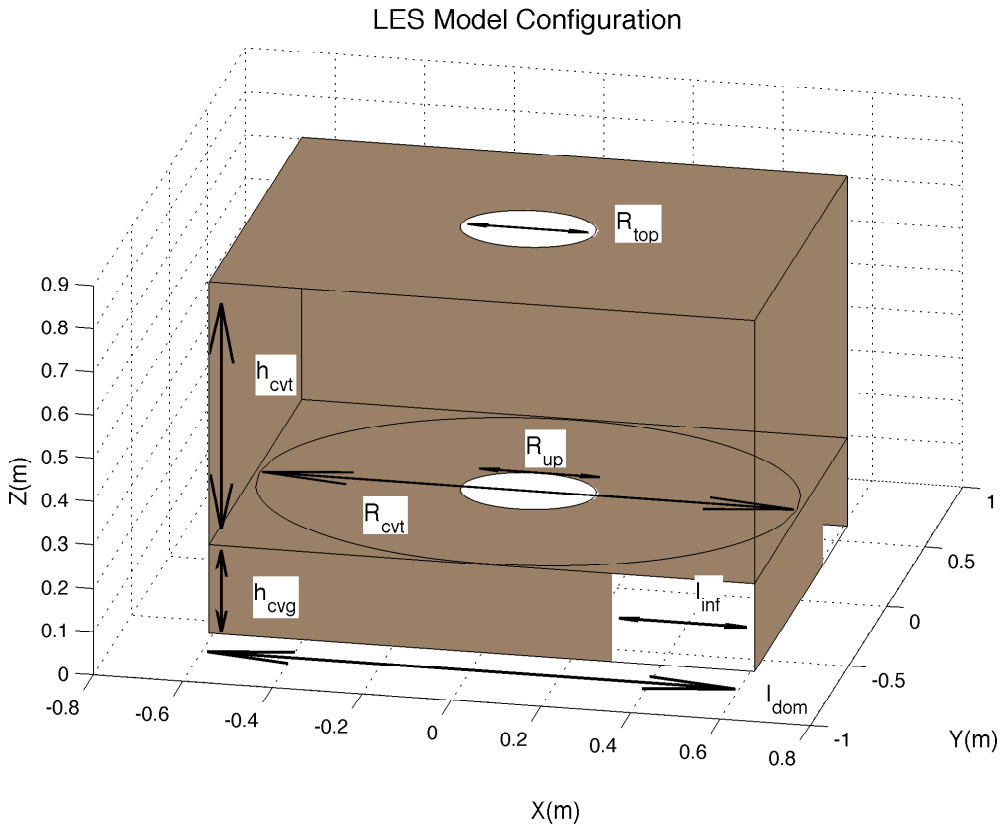

Figure 5.1: Configuration of the LES model for a vortex breakdown simulation. Flow into the convergence region enters through 4 inlets on the side walls of the convergence region, which have length l_{inf} and height h_{cvg}. Flow exits the model domain through the outlet at the top with radius, r_{top}.

length l_{inf}, and the height h_{cvg}, where h_{cvg} is the height of the convergence (or inflow) region. Within each inlet, Dirichlet boundary conditions are used with unidirectional flow perpendicular to the opening and a velocity specified by a log-wind profile with a roughness length, z_0, of 0.1 m, and a maximum velocity of v_{in}. No-slip boundary conditions are employed at the surface and on the side walls of the convergence region except in the inlet regions. A circular opening separates the convergence and convection regions with a fixed radius, r_{up}, similar to the Ward-type vortex chamber. Above the convergence region, the convection region has a height and radius given by h_{cvt} and r_{cvt}, respectively. At the top of the convection region, Dirichlet boundary conditions are specified for a fixed radius, r_{top}, with an updraft velocity, w_{top}.

By changing the dimensions of different simulation parameters (e.g., convergence region height), a variety of vortex flows can be simulated. Table 5.1 provides a summary of simulation parameters used to create different vortex flows herein. The three simulations include vortex flows with a vortex breakdown, two-cell vortex, and suction vortices. Davies-Jones (1973) and Church et al. (1979) discuss the geometric and dynamical similarities between tornado-like vortices in vortex chambers and actual thunderstorms and associated tornadoes. They define three non-dimensional parameters to describe the vortex chamber's flow geometry: ratio of the inflow height to updraft hole radius (h_{cvg}/r_{up}), ratio of the convection region height to the convergence region height (h_{cvt}/h_{cvg}), and ratio

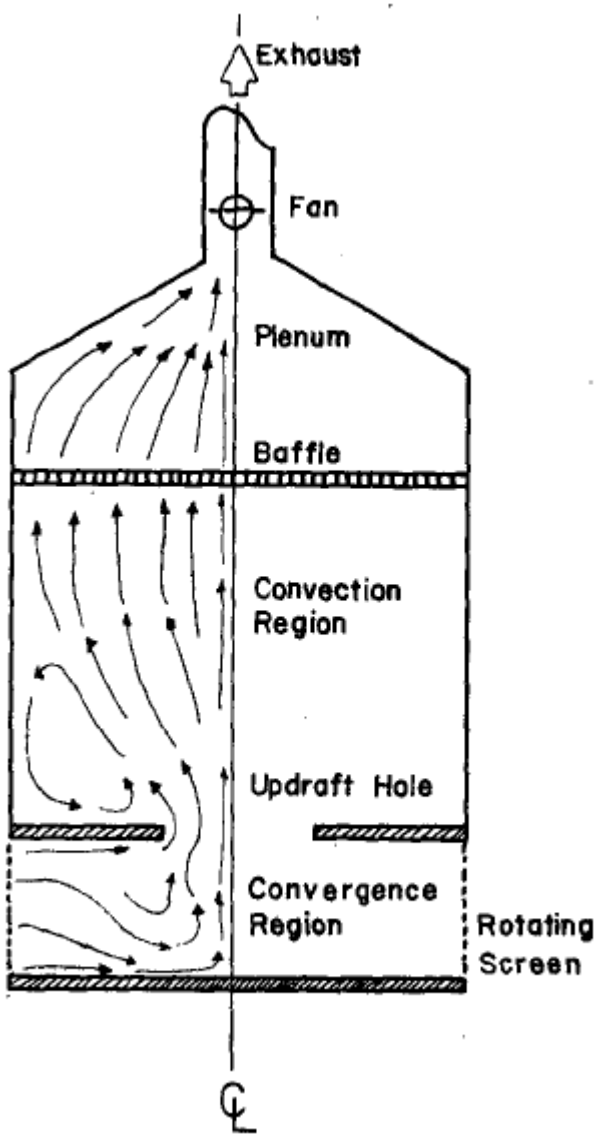

Figure 5.2: Configuration of a Ward-type vortex chamber (adapted from Church et al. (1979)). Similar to the LES configuration, the vortex chamber has a convergence and convection region separated by an updraft hole. Flow exits the vortex chamber through an exhaust fan at the top of the chamber.

Table 5.1: List of LES model configuration parameters for the vortex breakdown, two-cell vortex, and suction vortex simulations.

	Vortex Breakdown	Two-Cell Vortex	Suction Vortex
Inflow region leng. (l_{inf})	0.29 m	0.29 m	0.52 m
Convergence region hgt. (h_{cvg})	0.2 m	0.2 m	0.03 m
Inflow boundary velocity (v_{in})	0.04 m s^{-1}	0.05 m s^{-1}	0.13 m s^{-1}
Horizontal domain leng. (l_{dom})	1.28 m	1.28 m	1.28 m
Convection region rad. (r_{cvt})	0.6 m	0.6 m	0.6 m
Updraft opening rad. (r_{up})	0.17 m	0.20 m	0.15 m
Top outlet rad. (r_{top})	0.06 m	0.06 m	0.05 m
Convection region hgt.(h_{cvt})	0.6 m	0.6 m	0.8 m
Top outlet velocity (w_{top})	1 m s^{-1}	1 m s^{-1}	1 m s^{-1}
h_{cvg}/r_{up}	1.18	1	0.2
h_{cvt}/h_{cvg}	3	3	27
l_{inf}/r_{up}	3.76	3.20	4.27

of the outer confluence region to the updraft hole region (l_{inf}/r_{up}). In a supercell thunderstorm, the inflow depth and mesocyclone (updraft hole radius) have similar spatial scales (e.g., 1 – 3 km), thus values close to unity are expected, consistent with the LES configurations for the vortex breakdown and two-cell vortex simulations (Table 5.1). In the suction vortex LES configuration, inflow occurs through a smaller depth, producing a higher swirl ratio, S:

$$S = \frac{r_{up}\Gamma}{2Qh_{cvg}} \tag{5.1}$$

where Γ is the circulation at the radius of the updraft opening, and Q is the volume flow rate through the vortex chamber. In the atmosphere, typical depths of supercell storms range from 8 – 15 km. Accordingly, h_{cvt}/h_{cvg} may vary from 2.7 – 15 (values toward the middle portion of this range may be favored because deeper convection probably has deeper inflow layers). The value of h_{cvt}/h_{cvg} for the suction vortex configuration may be too large for a supercell flow, however, the increased depth of the convection region facilitates the development of the central downdraft.

5.1.2 LES model experiments

The first set of simulations involves a vortex breakdown (Benjamin 1962; Wilson 1986). In a vortex breakdown, a transition point occurs between supercritical and subcritical flow along the central axis. The supercritical (subcritical) flow region is defined as the region in which inertial waves move vertically slower (faster) than the air, and is located below (above) the vortex breakdown. The

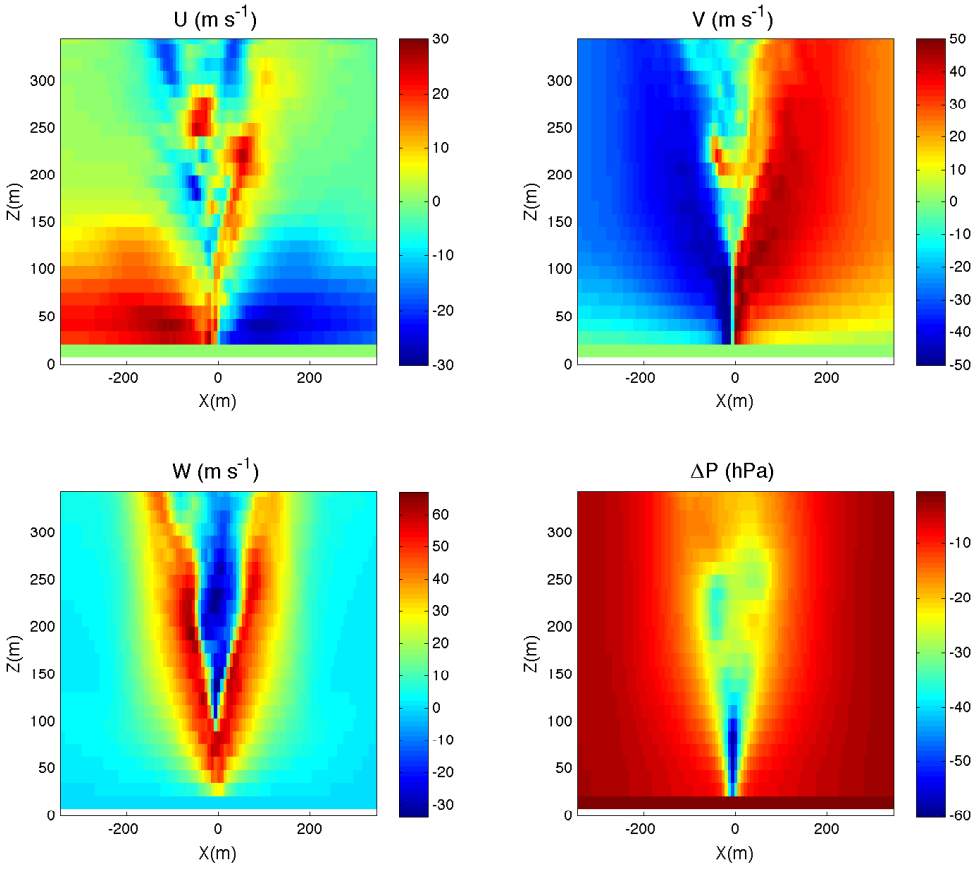

Figure 5.3: Vertical cross-sections of zonal (u), meridional (v), vertical (w) velocities (m s^{-1}) and pressure change (ΔP; hPa) for a vortex breakdown simulation averaged over 1 s for ($V_0 = 150$ m s^{-1}). The vortex breakdown occurs at a height of 100 m AGL along the tornado's central axis.

supercritical region consists of a narrow vortex (often called an end-wall vortex) and large vertical velocities along the central axis while the subcritical region exhibits a larger core diameter, greater turbulence, and near-zero or negative vertical velocities (Church et al. 1979).

The LES model reproduces the expected flow characteristics for a vortex breakdown. Vertical cross-sections of zonal, meridional, vertical wind speeds,

and pressure in the x-z plane are shown in Fig. 5.3 for the LES vortex breakdown case. The inflow layer extends to a height of 150 m, with the largest inflow velocities in the lowest 50 m (i.e., corner flow region). Along the central axis of the tornado, this strong radial flow is diverted upward along the central axis, creating an intense jet extending up to the vortex breakdown. Compared to above the vortex breakdown, tangential velocities are greater and the vortex diameter is smaller below the vortex breakdown. The minimum pressure change also occurs below the vortex breakdown, with values as low as -55 – -60 hPa between z = 35 – 75 m.

As the swirl ratio increases from the vortex breakdown case, the vortex breakdown location decreases in altitude until it reaches the surface. Once the downdraft reaches the surface, the tornado becomes a two-cell vortex characterized by a central downdraft surrounded by an annulus of updraft. Vertical cross-sections of zonal, meridional, vertical wind speeds, and pressure in the x-z plane are shown for the two-cell vortex simulation in Fig. 5.4. In contrast to the vortex breakdown case, the corner flow turns upward prior to reaching the central axis of the tornado, and the vortex diameter is comparatively larger.

For very high swirl ratios, the vortex flow can develop two or more smaller scale vortices (called suction vortices) which rotate around the central axis, and increase wind speeds compared to the surrounding vortex flow. Evidence for suction vortices was first noted by Fujita (1967, 1970), who observed cycloidal

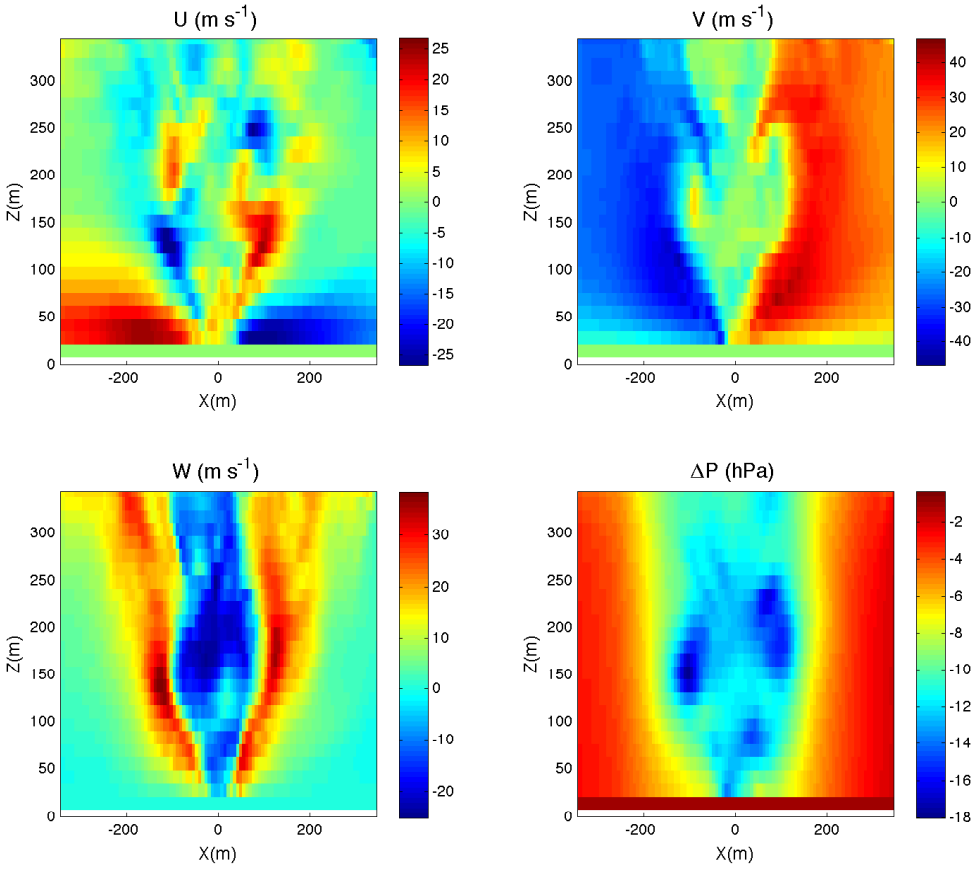

Figure 5.4: Vertical cross-sections of zonal (u), meridional (v), vertical (w) velocities (m s^{-1}) and pressure change (ΔP; hPa) for a two-cell vortex averaged over 1 s (V_0 = 150 m s^{-1}). In the two-cell vortex simulation, the central downdraft extends to the surface.

marks in a corn field. Mobile radar observations have also revealed multiple-vortex structure in tornadoes (e.g., Wurman 2002; Lee and Wurman 2005). The vortex flow conditions required for suction vortex formation have been investigated using tornado vortex chambers, analytical stability analyses, and numerical simulations. Tornado vortex simulators produce multiple vortices for high swirl ratios, with numbers of suction vortices ranging between 2 – 6 (e.g., Ward 1972; Church et al. 1979; Church and Snow 1993). Vortex sheet instability caused by strong radial gradients of tangential velocity is believed to allow growth of larger wavenumber modes at higher swirl ratios (Snow 1978; Rotunno 1978; Walko and Gall 1984).

The configuration for the suction vortex simulation (Table 5.1) produces three suction vortices in a very high swirl ratio flow. Horizontal cross-sections of zonal, meridional, and vertical velocities, and pressure at a height of 77 m are shown in Fig. 5.5. The suction vortices are located inside of the azimuthally averaged radius of maximum wind and along the axis of strong radial shear in vertical velocity created by the transition from downdraft to updraft, similar to other LES model simulations of tornadoes with suction vortices (Lewellen et al. 2000, cf. Fig. 2). Suction vortices also create locally intense vertical velocity gradients ($\frac{\partial w}{\partial r} > 0$) and contain the largest vertical velocities in the vortex flow, similar to the simulations of Lewellen et al. (2000).

The three simulations exhibit similar dynamical quantities when compared to previous numerical simulations of tornadoes. Common parameters for examining

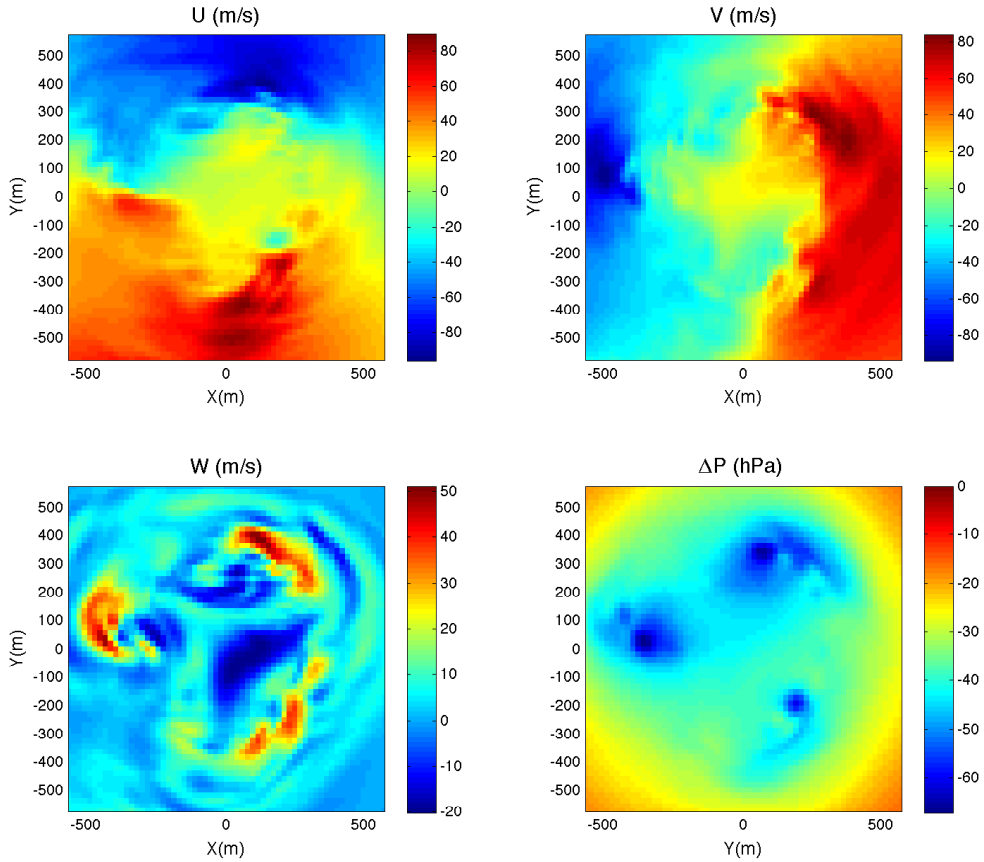

Figure 5.5: Horizontal cross-sections of zonal (u), meridional (v), vertical (w) velocities (m s^{-1}) and pressure change (ΔP; hPa) for a suction vortex simulation averaged over 1 s for ($V_0 = 250$ m s^{-1}) at a height of 77 m. Three intense suction vortices are evident with enhanced tangential velocities and reduced pressure, and large radial gradients in vertical velocity.

tornado dynamics are shown in Table 5.2 for the vortex breakdown, two-cell vortex, and suction vortex simulations. Lewellen et al. (2000) define vortex intensification as:

$$I_v = \frac{v_{max}}{v_c} \tag{5.2}$$

where v_{max} and v_c are the maximum and core tangential velocities, respectively. The corner flow swirl ratio (Sc; Lewellen et al. 2000; Lewellen and Lewellen 2007a,b) is defined as:

$$S_c = \frac{r_c \Gamma_\infty^2}{\gamma} \tag{5.3}$$

where r_c is the vortex core diameter, Γ_∞ is the angular momentum far from the vortex center, and γ is the depleted angular momentum:

$$\gamma = -\int_0^{z_{top}} 2\pi r u \left(\Gamma_\infty - \Gamma\right) dz, \tag{5.4}$$

where z_{top} is the top of inflow layer. Depleted angular momentum is a measure of the vertically integrated reduction of angular momentum in the inward radial jet of the vortex. The corner flow swirl ratio, S_c, becomes a measure of the efficiency of the vortex flow to transport depleted angular momentum air into the vortex core.

As near-surface angular momentum of the air is reduced (i.e., $\Gamma_\infty - \Gamma$ increases), the inward radial jet penetrates to a smaller radius before centrifugal forces increase sufficiently to inhibit the parcel's radial inward acceleration and divert the air parcel upward. Lewellen et al. (2000) found that greater vortex intensification occurs when the radial inward jet can overshoot the radial distance

where the angular momentum in the corner flow is equal to the angular momentum in the core. However, if too much angular momentum is depleted, significant vortex intensification may not occur. In the LES vortex breakdown simulation, near-surface angular momentum depletion and radial inward jet overshooting occurs in the vortex breakdown simulation, leading to greater near-surface intensification of the vortex compared to the two-cell vortex and suction vortex simulations.

5.1.3 Debris trajectory calculation and drag force feedback model

The implementation of tornadic debris in the LES model herein differs from the "two-fluid" approach used by Gong (2006) and Lewellen et al. (2008) in that Lagrangian debris trajectories are calculated, and a body force term is added to the Navier-Stokes Equations to model the two-way air-debris coupling. In the "two-fluid" approach, two Navier-Stokes Equations are formulated for both air and debris and are solved simultaneously, with debris treated as a fluid with much higher density. The momentum equations for air and debris are similar except that the debris equation is treated as pressureless and a gravitational acceleration term is added. The debris continuity equation also allows for changes in debris fluid density with time, and incorporates subgrid turbulence.

An advantage of the Lagrangian approach is that a large number of trajectories are provided in each grid cell within the tornado vortex, allowing for variability of debris velocity in each grid cell. Moreover, debris trajectories can be

Table 5.2: Non-dimensional parameters characterizing tornado dynamics for the LES model runs with V_0 = 150 m s^{-1}, including the corner flow swirl ratio (S_c), intensification parameter (I_p), maximum near-surface and core tangential velocities (v_{max} and v_c), ratio of maximum inflow speed to core tangential velocity (u_{min}/v_c), ratio of minimum vertical velocity to core tangential velocity (w_{min}/v_c), and ratio of maximum vertical velocity to core tangential velocity (w_{max}/v_c).

	Vortex Breakdown	Two-Cell Vortex	Suction Vortex
Corner flow swirl ratio (S_c)	2.09	2.87	26.0
Intensification parameter (I_v)	1.39	1.29	1.06
Max. core tang. velocity (v_c)	29.9 m s^{-1}	28.8 m s^{-1}	40.9 m s^{-1}
Max. tang. velocity (v_{max})	41.4 m s^{-1}	37.0 m s^{-1}	43.6 m s^{-1}
u_{min}/v_c	-0.67	-0.91	-0.25
w_{min}/v_c	-0.14	-0.69	-0.37
w_{max}/v_c	0.84	0.96	0.13

calculated for non-spherical debris (e.g., "2 X 4s", roof tiles) using a six-degree-of-freedom drag coefficient model with three-dimensional drag force coefficients. A limitation to this approach is that computational resources constrain the number of trajectories, so the number of debris in a given simulation is limited to the order of 10^6. Moreover, a sufficiently small time step must be used to obtain accurate trajectories for large velocities. To ensure that accurate trajectories were obtained, the time step was decreased until debris distributions remained unchanged for further reductions in the time step.

Non-dimensional debris trajectories are calculated using the following equation, as described in Maruyama (2011):

$$\frac{du_{di}}{dt} = C_D T_a \left(u_i - u_{di}\right) \left|u_i - u_{di}\right| - \delta_{i,3}, \tag{5.5}$$

where C_D is the drag force coefficient, and u_i and u_{di} are the air and debris velocities, respectively. T_a is the Tachikawa number (Holmes et al. 2006),

$$T_a = \frac{\rho A V_0^2}{2mg}, \tag{5.6}$$

where ρ is air density, A is debris area, m is debris mass, and g is gravitational acceleration. T_a is a ratio of the aerodynamic and gravitational forces acting on debris. Spherical debris considered herein are assumed to have isotropic drag coefficients as specified in (2.49). For wood debris, a mean value of C_D of 1.2 is used (Hoerner 1965). Using (5.5), debris trajectories are calculated using 2nd-order Runge-Kutta integration with a non-dimensional time step of 10^{-3}.

The drag force model implemented in the present study is based on Newton's third law, and assumes that if a drag force is exerted on a particle, a reaction

force of equal magnitude and opposite direction must be exerted on the air. Shapiro (2005) use similar physical reasoning to model two-way drag force coupling to examine horizontal momentum exchange between air and rain drops. The aerodynamic force exerted on one debris element is given by,

$$f_{xi} = \frac{1}{2}\rho C_D A \left(u_i - u_{di}\right) \left|u_i - u_{di}\right|. \tag{5.7}$$

For each grid cell, the aerodynamic force per unit mass, F_{xi}, is computed by summing the aerodynamic forces, $f_{xi,n}$, in the grid cell over the total number of debris elements, N, and dividing by the product of ρ and the grid volume, V_{grid}:

$$F_{xi} = \frac{1}{\rho V_{grid}} \sum_{n=1}^{N} f_{xi,n}. \tag{5.8}$$

Because the reaction force to the aerodynamic force is in the opposite direction, F_{xi} is then subtracted from the spatially averaged Navier-Stokes equation, as shown in (5.9), where $\nu = \frac{\mu}{\rho}$ and S is a scaling factor.

$$\frac{\partial \overline{u}_i}{\partial t} + \frac{\partial}{\partial x_j}\left(\overline{u}_i \overline{u}_j\right) = -\frac{1}{\rho}\frac{\partial \overline{p}}{\partial x_i} + 2\frac{\partial \left(\nu + \nu_{SGS}\right) D}{\partial u_i} - SF_{xi}. \tag{5.9}$$

In some cases, the number of debris required for a realistic simulation exceeds the number of computationally feasible trajectories. In such cases, the drag force is multiplied by S to increase the number of debris by a factor of S. This scaling assumes that enough trajectories are simulated to accurately represent the mean characteristics of the debris in the grid cell (i.e., relative velocity). In the simulations presented herein, most grid cells in the corner flow region contain hundreds or thousands of debris per grid cell.

The relationship between surface debris lofting characteristics and wind speeds in tornadoes is poorly understood. The primary measure of tornado intensity is the Fujita or Enhanced Fujita scale, which proposes that increased damage severity is correlated with wind speed (McDonald et al. 2004; WSEC 2006), although this relationship is largely unvalidated by actual wind speed measurements (Wurman et al. 2013). For example, no measurements of the mass flux of dust or debris into a tornado as a function of wind speed exist. However, measurements of soil particle fluxes in dust devils and laboratory vortices have been made. Neakrase and Greeley (2010) found that soil particle fluxes in laboratory vortices with similar characteristics to dust devils varied from 10^{-5} – 1 kg m^{-2}, with smaller fluxes occurring over surfaces with greater surface roughness. Measurements of dust and sand fluxes in dust devils, however, suggest that fluxes are much smaller than 1 kg m^{-2}. Metzger et al. (2011) found that total particle fluxes were on the order of 10^{-3} kg m^{-2}.

Given the poorly understood relationship between debris lofting and tornado wind speeds, sensitivity tests are conducted with fixed amounts of debris in the domain, N_{deb}. For each simulation, N_{deb} is gradually increased to allow the wind field to adjust to the debris until the total number reaches N_{deb}, and then N_{deb} remains constant (i.e., debris trajectories are reinitialized at the surface after exiting the domain). Given that regions with higher wind speeds are expected to exhibit greater debris lofting, a basic model is employed to determine the horizontal distribution of debris lofting. Batt et al. (1999) found that the surface

fluxes of sand particles were proportional to $u^{\frac{3}{2}}$, and Gong (2006) and Lewellen et al. (2008) employed this power-law relationship in their LES debris studies. In the present study, surface debris fluxes are specified using

$$N_{flux} = c_{deb} e^{\frac{3}{2}}, \tag{5.10}$$

where e is turbulent kinetic energy (TKE),

$$e = u'^2 + v'^2 + w'^2, \tag{5.11}$$

and c_{deb} is a constant of proportionality that allows for variations in surface debris fluxes while preserving the $\frac{3}{2}$ power-law relationship. Different c_{deb} values reflect differences in the availability of particles or debris from the surface, which account for different surface types. For the case of soil fluxes, high values of c_{deb} could occur over a bare soil surface whereas low values could occur over a heavily vegetated or rough surface. The simulations use TKE instead of horizontal wind speed because experiments with horizontal wind speed had comparatively larger surface debris fluxes away from the vortex, which generally contradicts observations (although corner flow winds can cause damage in some cases).

To provide a comparison with previous debris centrifuging research, relative velocities from one-dimensional simulations by Dowell et al. (2005) are compared to values obtained in this study using the trajectory-based method (5.5) in a vortex flow described by a Fiedler vortex (Fiedler 1989, 1994). The Fiedler

Table 5.3: Rain drop and debris velocities from Dowell et al. (2005) for different vortex flows.

Vortex Flow Parameters	Particle Type	Max. u_d (m s^{-1})	Max. v_d (m s^{-1})	Max. w_d (m s^{-1})
v_{max} = 50 m s^{-1}, r_{max} = 100 m	Drop, D=0.5 mm	3.5	49.8	-1.1
v_{max} = 100 m s^{-1}, r_{max} = 100 m	Drop, D=0.5 mm	7.2	99.6	-0.6
v_{max} = 100 m s^{-1}, r_{max} = 200 m	Drop, D=0.5 mm	5.1	99.8	-0.8
v_{max} = 50 m s^{-1}, r_{max} = 100 m	Drop, D=5 mm	13.8	45.9	-6.1
v_{max} = 100 m s^{-1}, r_{max} = 100 m	Drop, D=5 mm	28.3	91.2	-3.2
v_{max} = 100 m s^{-1}, r_{max} = 200 m	Drop, D=5 mm	22.1	95.4	-4.3
v_{max} = 50 m s^{-1}, r_{max} = 100 m	Plywood sheet	18.9	38.8	-14.7
v_{max} = 100 m s^{-1}, r_{max} = 100 m	Plywood sheet	35.2	68.1	-10.0
v_{max} = 100 m s^{-1}, r_{max} = 200 m	Plywood sheet	34.0	84.8	-9.9
v_{max} = 50 m s^{-1}, r_{max} = 100 m	Brick	20.4	29.7	-35.3
v_{max} = 100 m s^{-1}, r_{max} = 100 m	Brick	41.2	52.3	-26.0
v_{max} = 100 m s^{-1}, r_{max} = 200 m	Brick	40.9	65.1	-27.1

Table 5.4: Rain drop and debris velocities calculated using the trajectory-based approach for different vortex flows.

Vortex Flow Parameters	Particle Type	Max. u_p (m s^{-1})	Max. v_p (m s^{-1})	Max. w_p (m s^{-1})
v_{max} = 50 m s^{-1}, r_{max} = 100 m	Drop, D=0.5 mm	4.1	49.7	-1.2
v_{max} = 100 m s^{-1}, r_{max} = 100 m	Drop, D=0.5 mm	9.8	99.3	-0.7
v_{max} = 100 m s^{-1}, r_{max} = 200 m	Drop, D=0.5 mm	6.5	99.7	-1.0
v_{max} = 50 m s^{-1}, r_{max} = 100 m	Drop, D=5 mm	14.4	45.5	-6.5
v_{max} = 100 m s^{-1}, r_{max} = 100 m	Drop, D=5 mm	30.0	89.8	-3.6
v_{max} = 100 m s^{-1}, r_{max} = 200 m	Drop, D=5 mm	23.6	94.6	–4.5
v_{max} = 50 m s^{-1}, r_{max} = 100 m	Plywood	19.0	38.2	-15.5
v_{max} = 100 m s^{-1}, r_{max} = 100 m	Plywood	39.0	73.5	-8.7
v_{max} = 100 m s^{-1}, r_{max} = 200 m	Plywood	34.0	84.0	-10.5
v_{max} = 50 m s^{-1}, r_{max} = 100 m	Brick	19.8	31.0	-29.0
v_{max} = 100 m s^{-1}, r_{max} = 100 m	Brick	41.0	55.5	-21.0
v_{max} = 100 m s^{-1}, r_{max} = 200 m	Brick	40.2	68.8	-22.2

vortex has no radial or vertical wind velocities, and tangential velocities are expressed as:

$$v = \frac{2v_{max}r_{max}r}{r_{max}^2 + r^2}, \tag{5.12}$$

where r_{max} is radius of maximum wind and v_{max} is the maximum tangential velocity. An advantage of the Fiedler vortex is that it eliminates the unnatural cusp exhibited by the Rankine vortex tangential wind profile. Comparisons of maximum radial (u_d), tangential (v_d), and vertical (w_d) speeds for 0.5-mm, 5-mm diameter drops, 4'x8' plywood sheets and bricks are shown for the Dowell et al. (2005) study and the present study in Tables 5.3 and 5.4, respectively. In general, both methods produce similar values for rain drop and debris velocities in different vortex flows. For example, both methods show that the peak radial debris velocity approximately increases by a factor of 2 when the maximum tangential wind speeds increase by a factor of 2. Differences between the two methods result from differences in drag force coefficients, and uncertainty in the sizes of the plywood sheet and brick used in their study. Dowell et al. (2005) also assume the drag force is proportional to the value achieved at terminal fall speed whereas the value in the present study depends on particle Reynolds number for rain drops and constant values for non-spherical debris.

5.2 Three-dimensional LES debris simulations

In this section, debris loading effects for sand particles and wood boards are examined using LES with a drag force feedback parameterization. Then,

methods for determining maximum bounds on debris loading using equivalent radar reflectivity factor and attenuation are presented.

5.2.1 Debris loading effects on tornado dynamics

Given that tornadoes loft significant amounts of debris, debris loading may affect tornado dynamics through momentum transfer between the air and debris. Lewellen et al. (2008) examined debris loading effects of sand-sized debris particles using LES, and defined debris loading, D_L, as:

$$D_L = \frac{\overline{m_d}/V}{\rho}, \tag{5.13}$$

where m_d is the mass of debris within volume V. In some simulations, their simulations revealed values of D_L ranging from 1 – 10 in the corner flow region, and observed reductions in near-surface radial, tangential and vertical wind speeds up to 30%. While these results suggest that tornado dynamics may be significantly altered by debris loading, amounts of debris loading in tornadoes remains unverified by observations. As discussed previously, sand fluxes may vary by orders of magnitude depending on surface characteristics. Hence, the goal of the present study is to examine what amounts of debris loading are required to affect tornado dynamics. Debris loading simulations will encompass different sand-sized particles and wood boards. Then, to ascertain what values of debris loading are realistic, radar simulated equivalent radar reflectivity factor and attenuation are calculated from the model simulations.

5.2.1.1 Sand particles

Momentum exchange through drag forces tends to reduce differences between air and debris velocities. For example, consider sand particles initially at rest that are lofted by inflow of 20 m s^{-1}. In (5.7), the aerodynamic force (acting on the debris) in the x-direction, f_x, is negative and causes u_d to decrease. In response, the air exhibits a positive acceleration in the x-direction because f_x and thus F_x are negative, resulting in $\frac{\partial u}{\partial t} > 0$ (5.9). Similarly, debris lofted into an updraft are accelerated vertically because the aerodynamic force in the z-direction, f_z, is positive. Accordingly, the reaction force acting on the air results in a negative vertical acceleration ($\frac{\partial w}{\partial t} < 0$).

Simulations are performed for 10^{11} 1-mm sand particles for the vortex breakdown case using a debris density, ρ_d, of 2650 kg m^{-3} for 306 s. Simulations for the debris and no-debris case (Control) are initialized using the same three-dimensional velocity fields from a steady-state vortex breakdown simulation. Mean aerodynamic reaction forces, debris loading, air-debris relative velocities (hereafter, called relative velocities), and equivalent radar reflectivity factor are shown in Fig. 5.6. Mean radial, tangential, and vertical velocities, and pressure, and the change in the aforementioned variables from the control simulation are presented in Fig. 5.7. The largest radial acceleration of the air occurs within the lowest grid cell within a radius of 100 m. In this region, a maximum debris loading occurs due to increased debris lofting caused by higher velocities in the

tornado vortex. In the lowest non-zero grid cell, the sand particles' radial velocities decrease at the expense of inward radial momentum of the air, as described in the previous example.

In addition to radial momentum transfer, outward radial accelerations of the air are caused by debris centrifuging. In the lowest grid cell, sand particles are quickly accelerated, resulting in the greatest depletion of inward radial momentum of the air. Above this region, centrifugal acceleration of debris creates larger radial relative velocity differences (Fig. 5.6). Drag forces acting on the debris during centrifuging acceleration are radially inward (5.7) because u_d exceeds u, resulting in a radially outward reaction force acting on the air. Radial relative velocities increase with increasing radius and height, however, the radial outward accelerations become smaller because the sand particles are present in much smaller concentrations above the corner flow region.

While aerodynamic forces acting on debris and reaction forces acting on the air are relatively easy to understand, the resulting changes to corner flow structure are complicated by feedback mechanisms. The velocity change experienced by an air parcel is a function of both the acceleration (forces) acting on the air parcel and the time an air parcel resides within a particular volume. Initially, as debris loading occurs in the lowest grid cell, radial velocities increase and vertical velocities decrease, increasing the amount of time an air parcel resides in the lower corner flow. As a result, air parcels experience greater accelerations

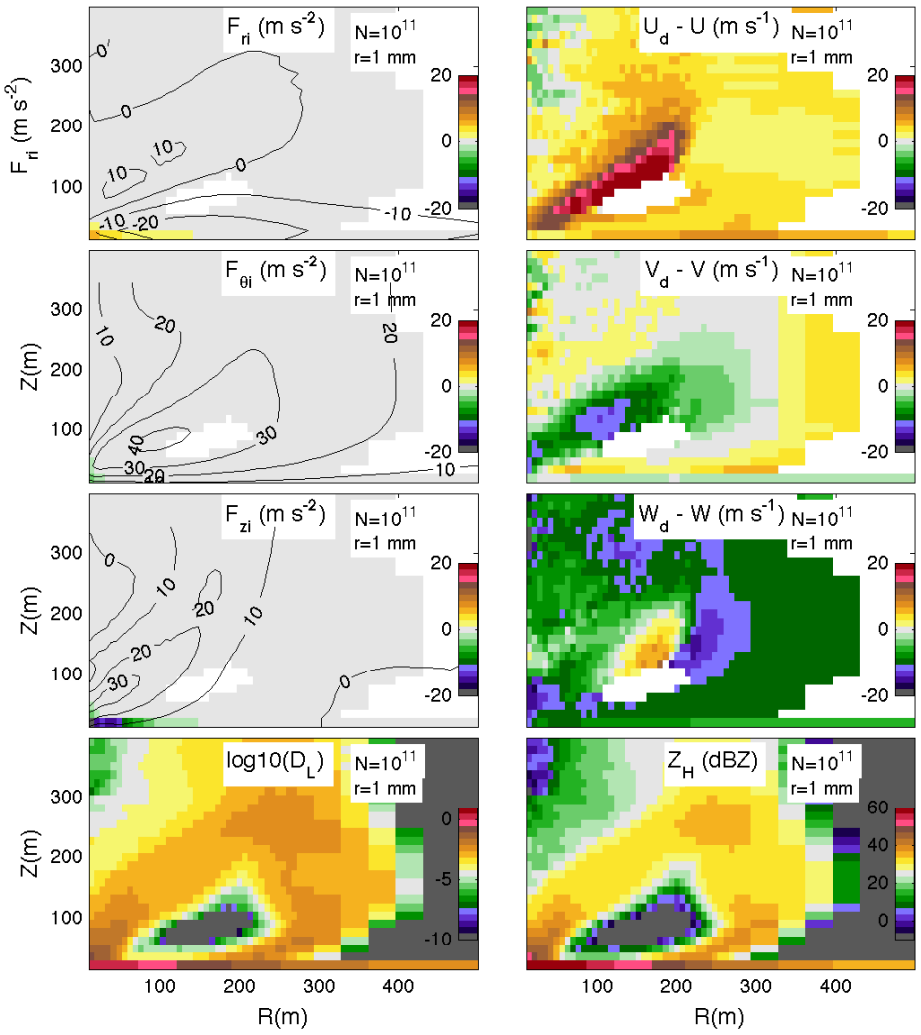

Figure 5.6: Aerodynamic forces and relative velocities are shown for the 10^{11} 1-mm sand particle simulation. The left column shows mean radial (F_{ri}), tangential ($F_{\theta i}$), and vertical accelerations (F_{zi}) in m s^{-2}, and $\log_{10}$ of debris loading (D_L), and the right column shows radial, tangential and vertical velocity differences between air and debris (m s^{-1}) and S-band equivalent radar reflectivity factor (dBZ) computed from T-matrix calculations. Radial, tangential and vertical velocities are also contoured onto the F_{ri}, $F_{\theta i}$, and F_{zi} plots at intervals of 10 m s^{-1}, respectively.

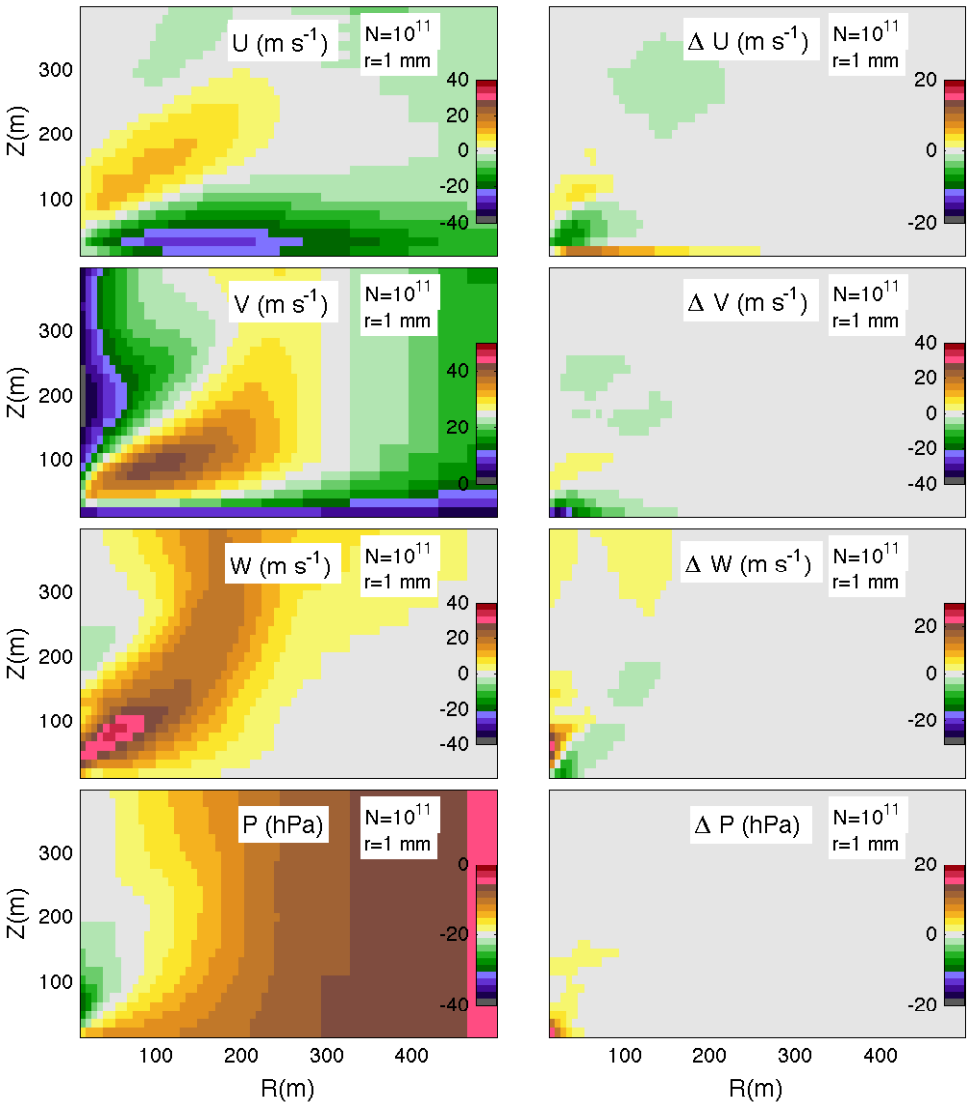

Figure 5.7: The left column shows radial, tangential, and vertical velocities (m s^{-1}) and pressure (hPa) from the 10^{11} 1-mm sand particle simulation, and the right column shows the change in radial, tangential, and vertical velocities, and pressure, from the control (no-debris) simulation.

in the lowest grid cells, resulting in higher radial velocities and lower tangential and vertical velocities (i.e., a positive feedback). At higher altitudes in the corner flow, this feedback is reduced because the air possesses relatively high angular momentum (e.g., $\frac{\partial v}{\partial z} > 0$), and therefore the air is deflected upwards at a larger radius compared to the reduced angular momentum air near the surface (Lewellen et al. 2000), resulting in smaller reductions in tangential velocities. While this explanation explains the tangential velocity changes, pressure gradient changes and mass continuity constraints further complicate the secondary circulation flow.

In response to the reduction in near-surface tangential velocities, surface pressure increases in the vortex center at the surface (Fig. 5.7), creating additional feedbacks on the initial momentum exchange forcing. The reduction in radial pressure gradient force near the surface acts to decrease inflow velocities. In the present simulation, buoyancy (i.e., vertical velocity specified by the upper boundary condition) is fixed, so an increase in surface pressure results in a negative vertical dynamic perturbation pressure gradient force, and therefore increases vertical velocities along the central axis. Because significant radial momentum is depleted in the lowest model grid level and the mass continuity equation must still be satisfied, increased inflow velocities are observed above the lowest model grid level near the vortex core. The impact of debris loading on tornado dynamics results in significant changes in the near-surface wind speeds for the 10^{11} 1-mm sand particle simulation. In the lowest grid level, inflow, tangential and

vertical velocities are reduced up to 10.4, 35.9, and 10.6 m s^{-1}, respectively. The maximum tangential wind speeds in the lowest grid level are reduced from 39.5 to 9.4 m s^{-1}.

While the preceding simulation shows that debris loading can affect tornado dynamics, the amount of debris loading that actually occurs in tornadoes remains unknown and has not been measured directly. Peak debris loading values in the preceding simulation were 3.9, which is similar to peak debris loading values in Lewellen et al. (2008). To constrain the maximum amount of debris loading possible, equivalent radar reflectivity factor can provide an upper-bound on the amount of debris contained in a TDS. Tornadoes contain a wide range of potential scatterer types, which could potentially make significant contributions to the received radar signal. For this case, the maximum bound is created by assuming that radar reflectivity factor is created by a single type of debris. An important caveat is that even a few small scatterers can produce large Z_{HH} values which are orders of magnitude larger than even a high concentration of smaller scatterers, such as sand particles. Observations of low ρ_{HV} in TDSs suggest that Mie scatterers are the dominant scatterers in tornadoes (e.g., scatterers with diameters exceeding $\frac{\lambda}{16}$). Therefore, the contribution of sand particles to a tornadic debris signature may contribute some fraction (perhaps orders of magnitude smaller than larger debris) of the total Z_{HH}. For example, in rain/hail mixtures, small

concentrations of hail produce much higher Z_{HH} than comparatively high concentrations of rain drops. Thus, other methods that are less dependent on debris size are needed to estimate debris concentrations, and will be discussed later.

Mean S-band equivalent radar reflectivity factor is shown for the 10^{11} sand particle simulation (Fig. 5.6), and is computed using T-matrix calculations (assuming dry sand). Due to the small differences in equivalent radar reflectivity factor for the sand particles in this section, similar equivalent radar reflectivity factor would be observed at C, X, and Ka-band. As expected, the largest equivalent radar reflectivity factor values are observed near the surface and equivalent radar reflectivity factor decreases with height. A minimum in Z_{HH} in the vortex center aloft, or weak-echo hole (WEH; e.g., Fujita 1981; Wurman et al. 1996; Wurman and Gill 2000; Bluestein et al. 2004; Dowell et al. 2005) forms due to debris centrifuging and radial outward motion above the vortex breakdown.

Radar reflectivity factors vary greatly in tornadic debris signatures from 20 – 70 dBZ (e.g., Ryzhkov et al. 2005; Bluestein et al. 2007; Bunkers and Baxter 2011; Bodine et al. 2013). Equivalent radar reflectivity factor exhibits a maximum value of 65.3 dBZ in the corner flow region where most debris are lofted, which is within observed Z_{HH} values for TDSs. Given that radar measurements in the corner flow region are quite rare (i.e., where debris loading exhibits a maximum), equivalent radar reflectivity at heights of 50 and 100 m are also discussed. Maximum equivalent radar reflectivity at 50 and 100 m AGL are 46.4

and 37.0 dBZ, respectively. These equivalent radar reflectivity values are plausible Z_{HH} values for tornadoes, although better methods for constraining debris loading based on radar measurements will be discussed later.

By decreasing the amount of debris in the simulation by an order of magnitude to 10^{10} sand particles, debris loading effects on tornado dynamics become minimal. Radial accelerations, and tangential and vertical decelerations are smaller compared to the 10^{11} particle simulation (Fig. 5.8). Although the 10^{10} and 10^{11} simulations exhibit some differences in relative velocities (particularly in the lowest grid cell), reduced debris loading is primarily responsible for the smaller accelerations. The maximum value of debris loading for the 10^{10} and 10^{11} simulations is 0.06 and 3.93, respectively. Consequently, air parcels passing through these regions exhibit smaller magnitude accelerations compared to the 10^{11} sand particle simulation, and thus changes in velocity in the corner flow region are small (Fig. 5.9). Moreover, the feedback mechanisms described for the 10^{11} simulation do not occur because the initial forcing from momentum transfer is too small, and thus less debris accumulates in the corner flow. Examining equivalent radar reflectivity factor for the 10^{10} simulation, the maximum value is 46.6 dBZ for the entire simulation domain, and 40.5 and 33.4 dBZ at 50 and 100 m, respectively.

Sensitivity tests are also performed for 0.25-mm radius sand particles to assess effects of smaller sand particles on vortex dynamics. Radial, tangential, and vertical accelerations and air-debris relative velocity differences, debris loading,

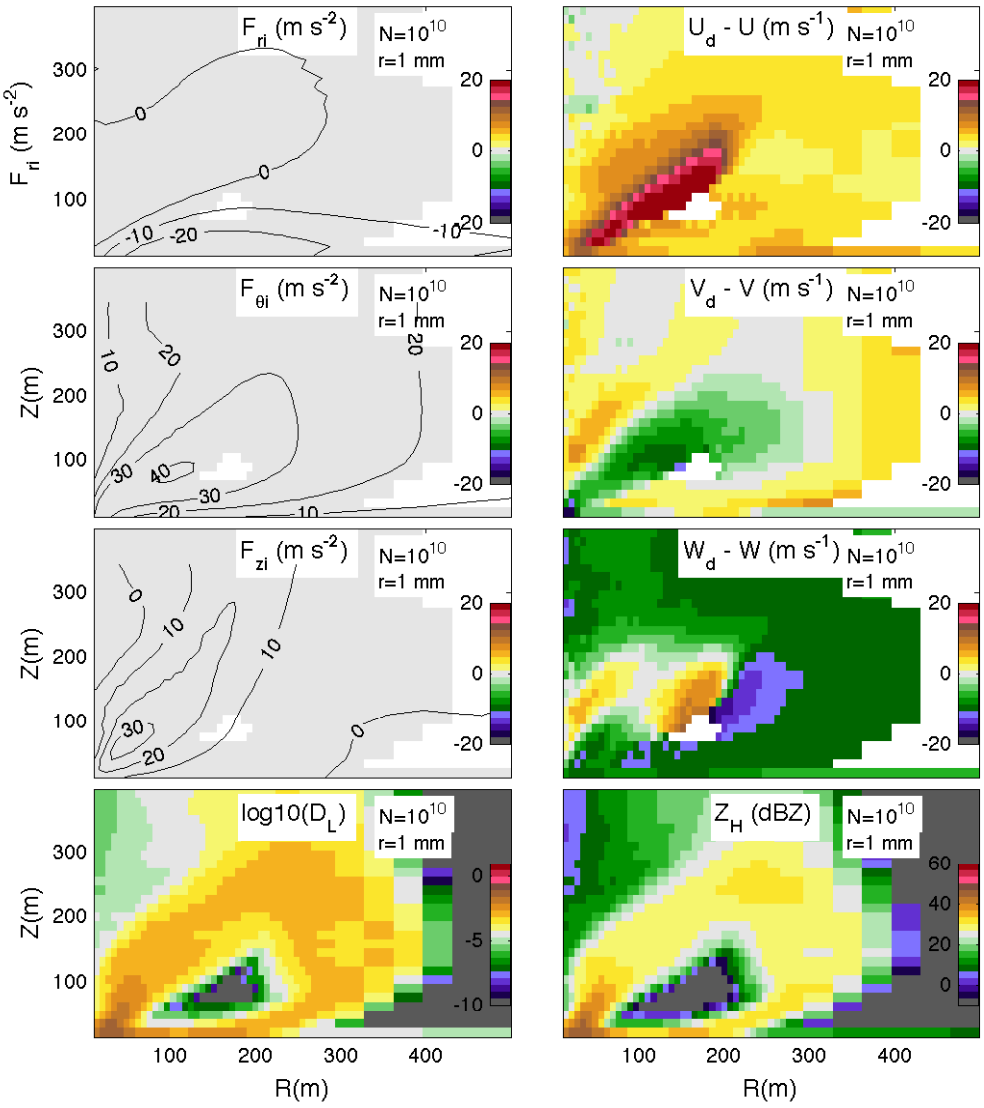

Figure 5.8: Same as Fig. 5.6, except for 10^{10} 1-mm radius sand particles. Compared to the 10^{11} 1-mm radius sand particle simulation, accelerations and decelerations are much smaller because debris loading values in the corner flow region are much smaller.

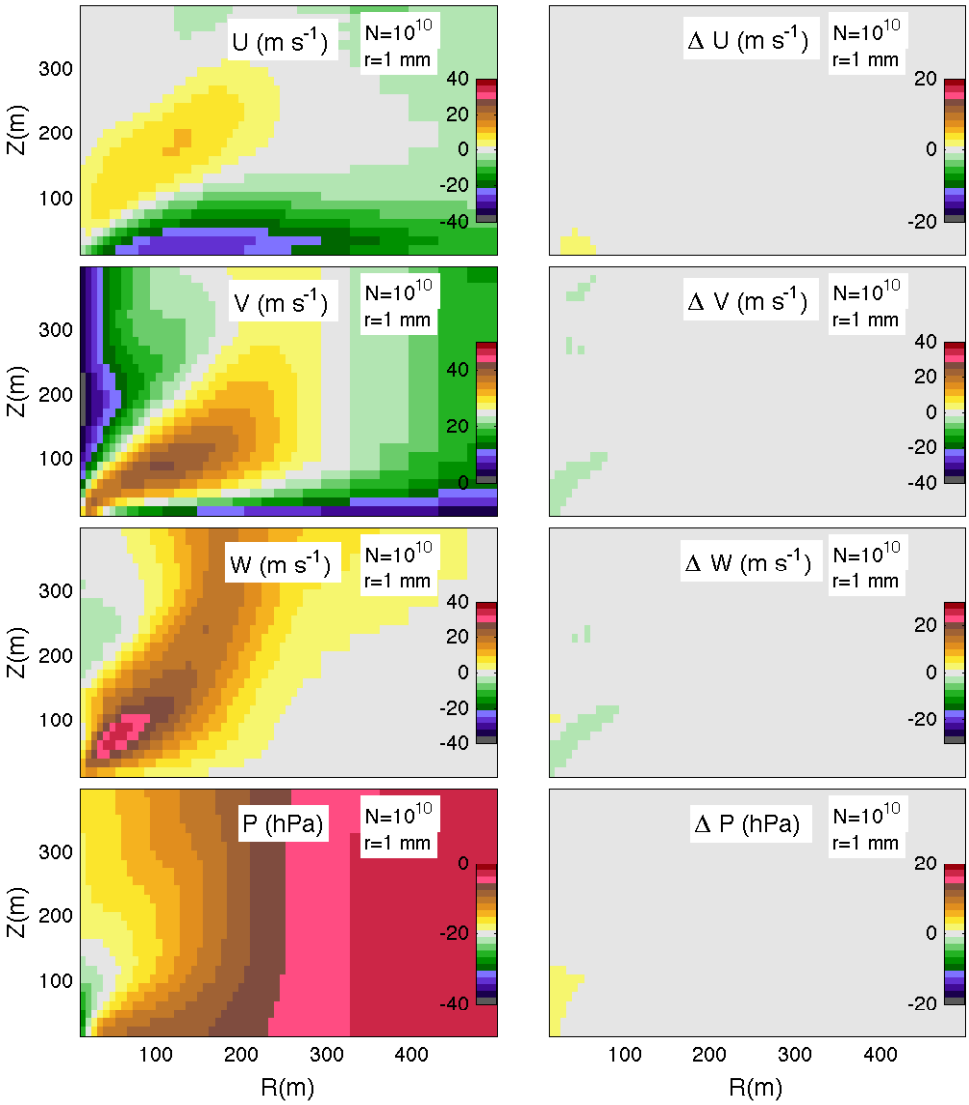

Figure 5.9: Same as Fig. 5.7, except for 10^{10} 1-mm radius sand particles. Compared to the 10^{11} 1-mm radius sand particle simulation, smaller magnitude changes in radial, tangential, and vertical velocities, and pressure are observed due to reduced debris loading.

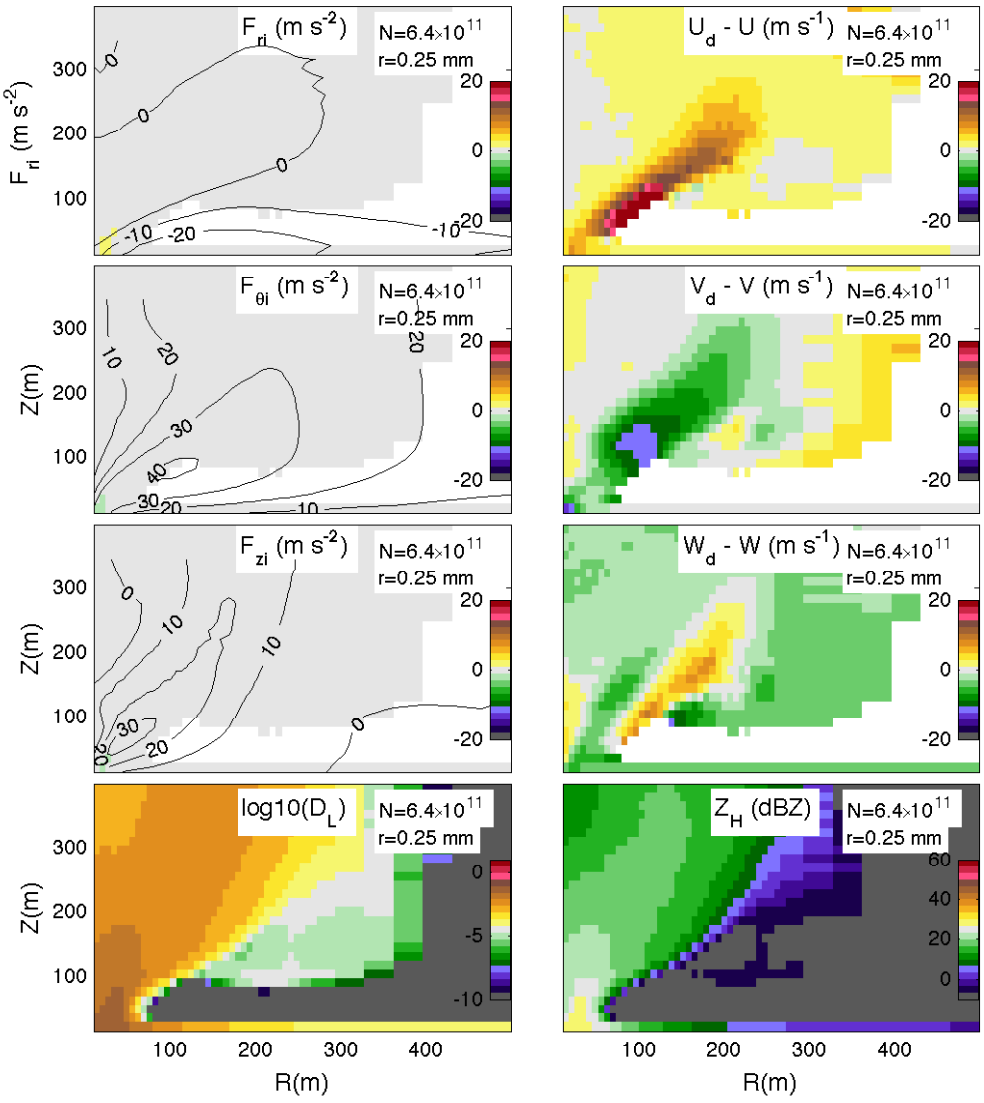

Figure 5.10: Same as Fig. 5.6, except for 6.4×10^{11} 0.25-mm radius sand particles. Debris loading in the corner flow region is less than 0.1, causing small magnitude accelerations.

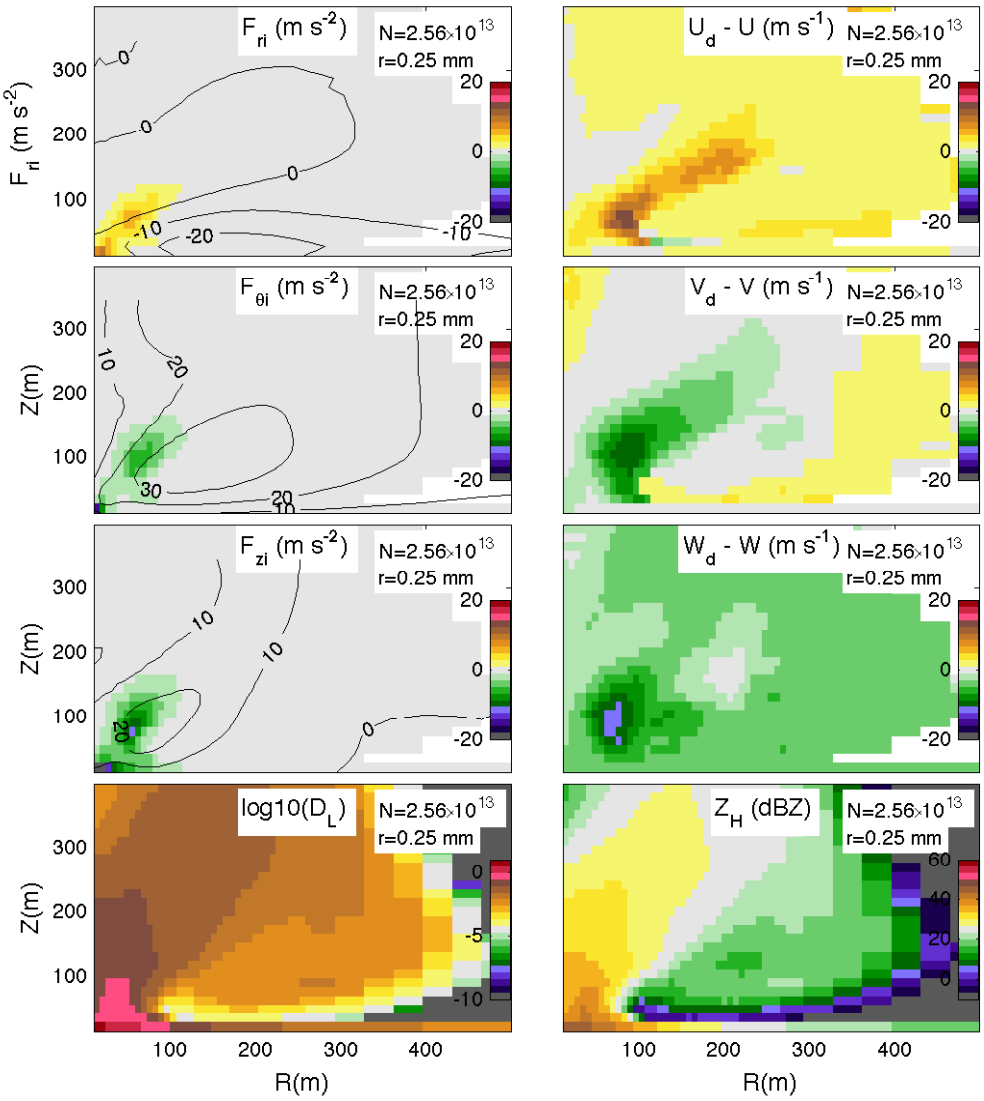

Figure 5.11: Same as Fig. 5.6, except for 2.56×10^{13} 0.25-mm radius sand particles. Large debris loading ($D_L < 1$) in the corner flow region causes large magnitude accelerations in the corner flow region. In contrast to the 10^{11} 1-mm particle simulation with similar corner flow peak debris loading, large magnitude accelerations extend to a greater height because 0.25-mm radius particles are not centrifuged outward as quickly.

and equivalent radar reflectivity factor are shown for the 6.4×10^{11} and 2.56×10^{13} in Figs. 5.10 and 5.11. Simulations for 6.4×10^{11} and 2.56×10^{13} are shown to examine cases with similar debris loading in the lowest grid cell as the 10^{10} and 10^{11} 1-mm radius sand particle cases. Peak mean debris loading for the 10^{10} 1-mm and 6.4×10^{11} 0.25-mm radius particle simulations are 0.06 and 0.07, respectively, and peak mean debris loading for the 10^{11} 1-mm and 2.56×10^{13} 0.25-mm radius particle simulations are 3.93 and 3.51, respectively. The 6.4×10^{11} 0.25-mm radius sand particle simulation has the same total mass as the 10^{10} 1-mm sand particle simulation while the mass of the 2.56×10^{13} simulation is a factor of 4 larger than the 10^{11} 1-mm sand particle simulation. To obtain similar corner flow mass loading in the 0.25-mm sand particle simulation, a higher surface flux of sand particles is required because 0.25-mm sand particles are evacuated from the corner flow region more quickly than 1-mm sand particle, particularly as lowest-grid cell vertical velocities decrease due to debris loading effects.

Significant differences exist in the spatial distributions of drag forces between the 10^{11} 1-mm radius and the 2.56×10^{13} 0.25-mm radius sand particle simulations. Larger radial accelerations and vertical decelerations are observed in the lowest grid cell for the 10^{11} 1-mm radius particle simulation even though peak debris loading is similar, likely resulting from greater relative velocity differences due to larger particle sizes. In the 2.56×10^{13} 0.25-mm radius sand simulation, large radial accelerations and tangential and vertical decelerations extend to

greater heights compared to the 10^{11} 1-mm radius sand particle simulation even though centrifugal forces and associated radial air-debris relative velocities are smaller for the 0.25-mm sand particles because debris loading is an order of magnitude larger above the lowest grid cell compared to the 10^{11} 1-mm particle simulation.

Given that the spatial distribution of drag forces differs between the 1-mm and 0.25-mm radius sand simulations, the spatial distribution of velocity change from the control simulation should exhibit differences as well. Radial, tangential, and vertical velocities, and pressure, and changes in the aforementioned variables from the control simulation are shown in Figs. 5.12 and 5.13. Similar to the 10^{10} 1-mm sand particle simulation, debris loading in the 6.4×10^{11} simulation is insufficient to cause significant effects on vortex dynamics. In the 2.56×10^{13} simulation, large increases in radial velocities and large decreases in tangential and vertical velocities are observed in the lowest grid cell, with maximum values of 13.2, -33.4, and -12.2 m s^{-1}, respectively. In contrast to the 1-mm particle simulation, large velocity changes are not only observed in the corner flow region, but extend through the vortex core flow. Negative tangential and vertical accelerations in the corner flow extend through a sufficient depth to cause downstream reductions in core tangential and vertical velocities. Core tangential and vertical velocities are reduced by as much as 4.8 and 8.2 m s^{-1}, respectively.

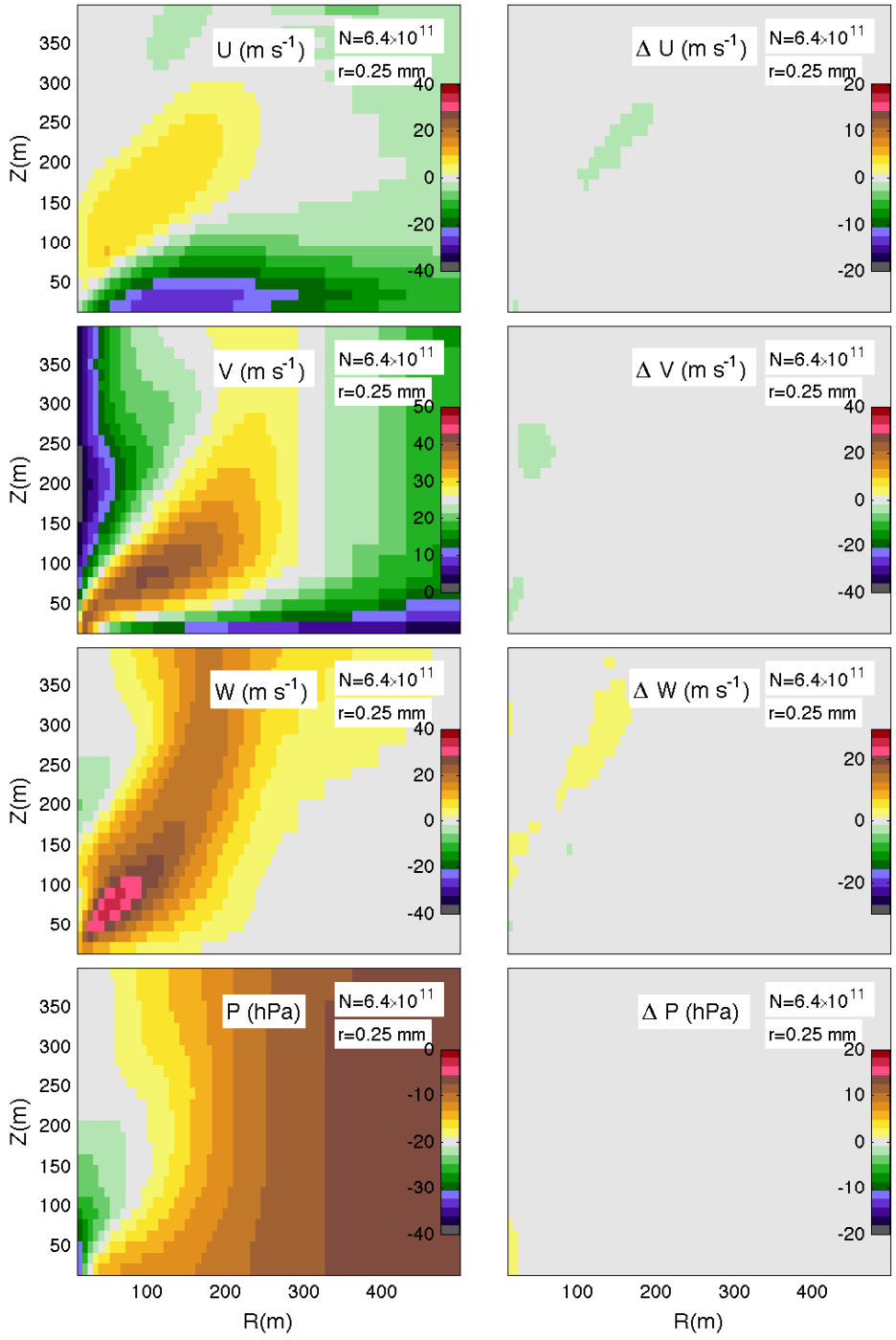

Figure 5.12: Same as Fig. 5.7, except for 6.4×10^{11} 0.25-mm radius sand particles. Velocity and pressure changes are small because debris loading and associated drag forces are relatively small.

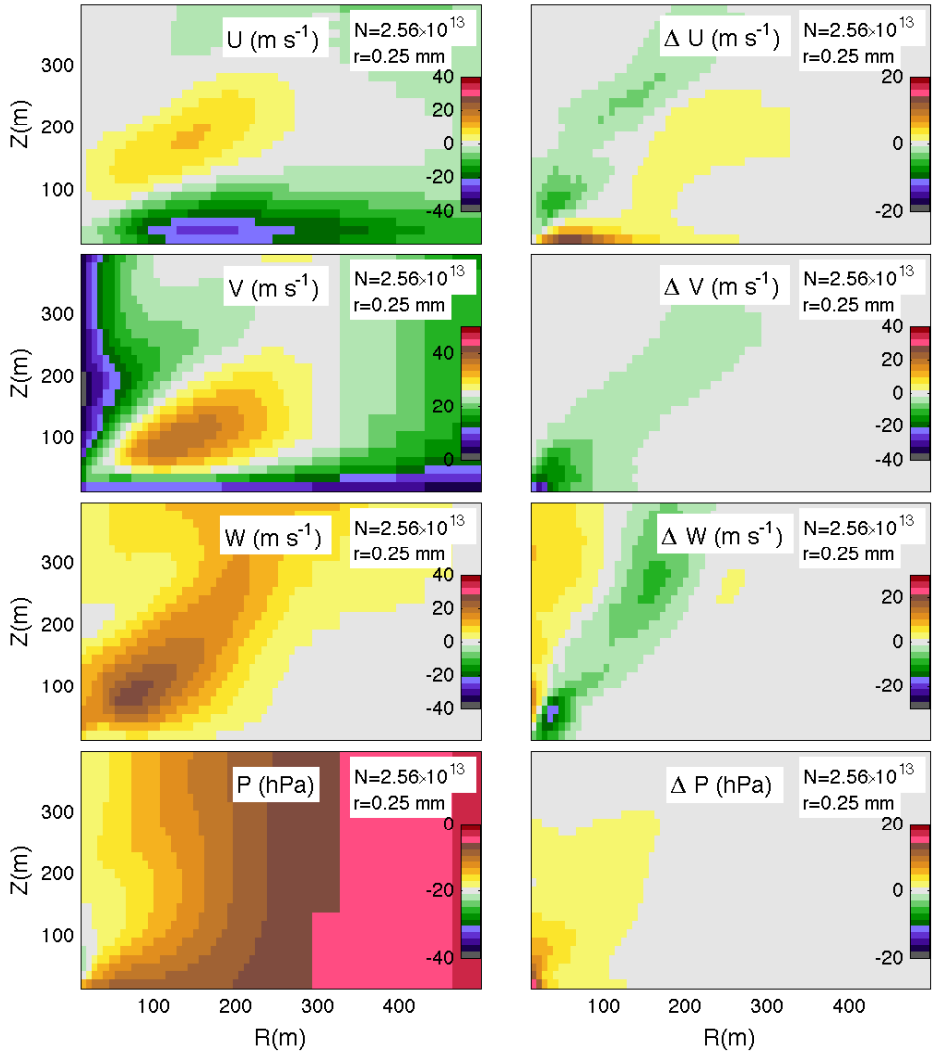

Figure 5.13: Same as Fig. 5.7, except for 2.56×10^{13} 0.25-mm radius sand particles. In comparison to the 10^{11} 1-mm radius sand simulation, greater magnitude radial, tangential and vertical accelerations are observed because the large drag forces occur through a greater depth of the corner flow region.

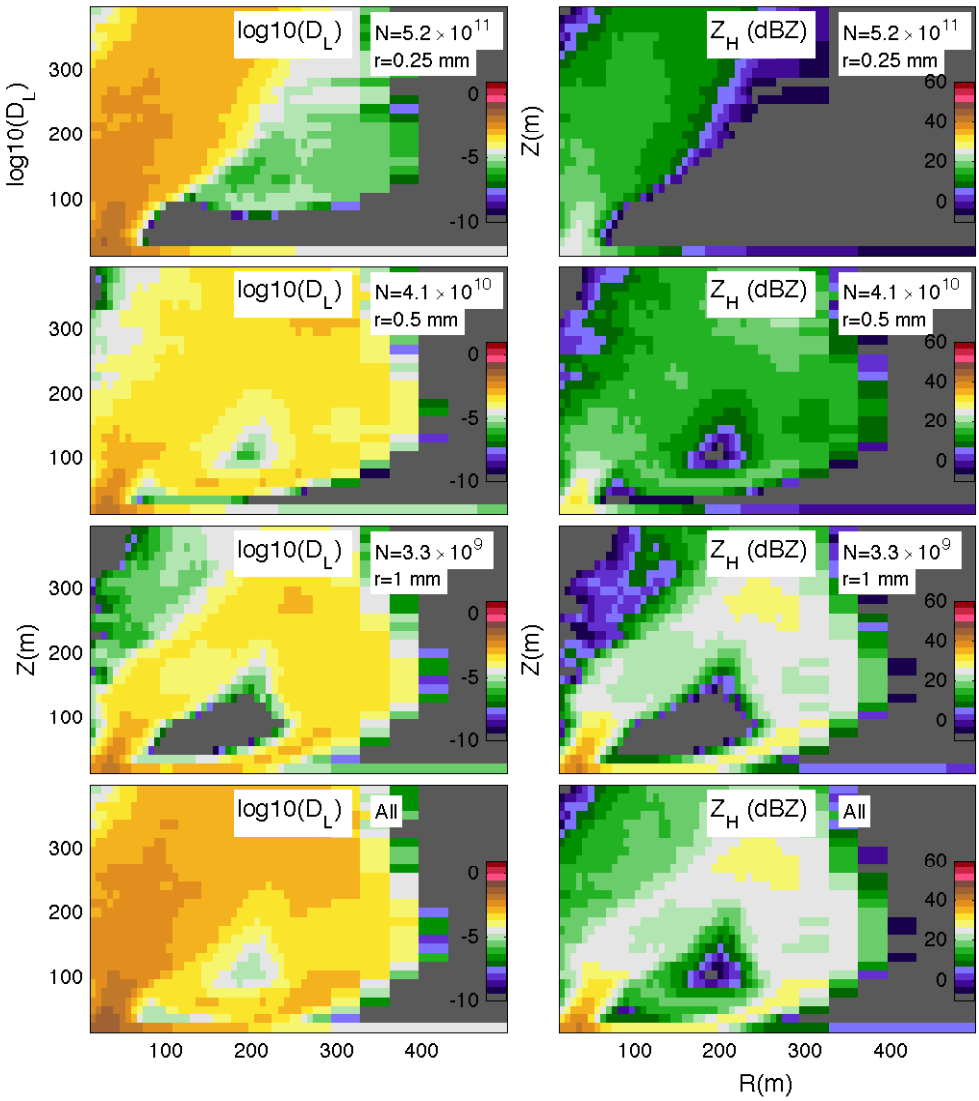

Figure 5.14: Log_{10} of debris loading (D_L) and equivalent radar reflectivity factor for simulation M1. Log_{10} of debris loading (D_L) for 0.25-, 0.5-, and 1-mm radius sand particles, and all particles are shown in the left column, and equivalent radar reflectivity factor at S-band for 0.25-, 0.5-, and 1-mm radius sand particles, and all particles are shown in the right column.

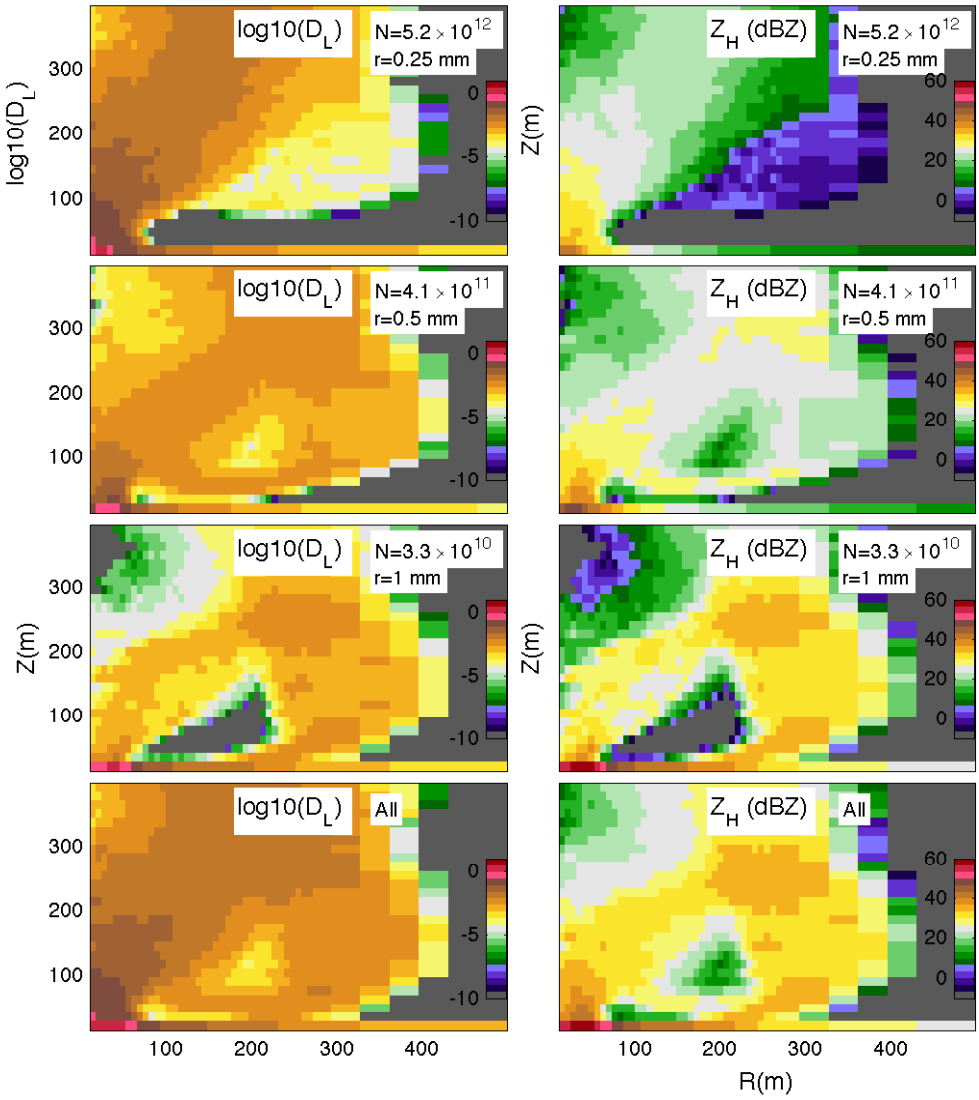

Figure 5.15: Same as Fig. 5.14, except for simulation M2 (number of particles is a factor of 10 larger than simulation M1). Equivalent radar reflectivity factor exhibits greater contributions from smaller particles because fewer large particles are lofted due to reduced near-surface vertical velocities.

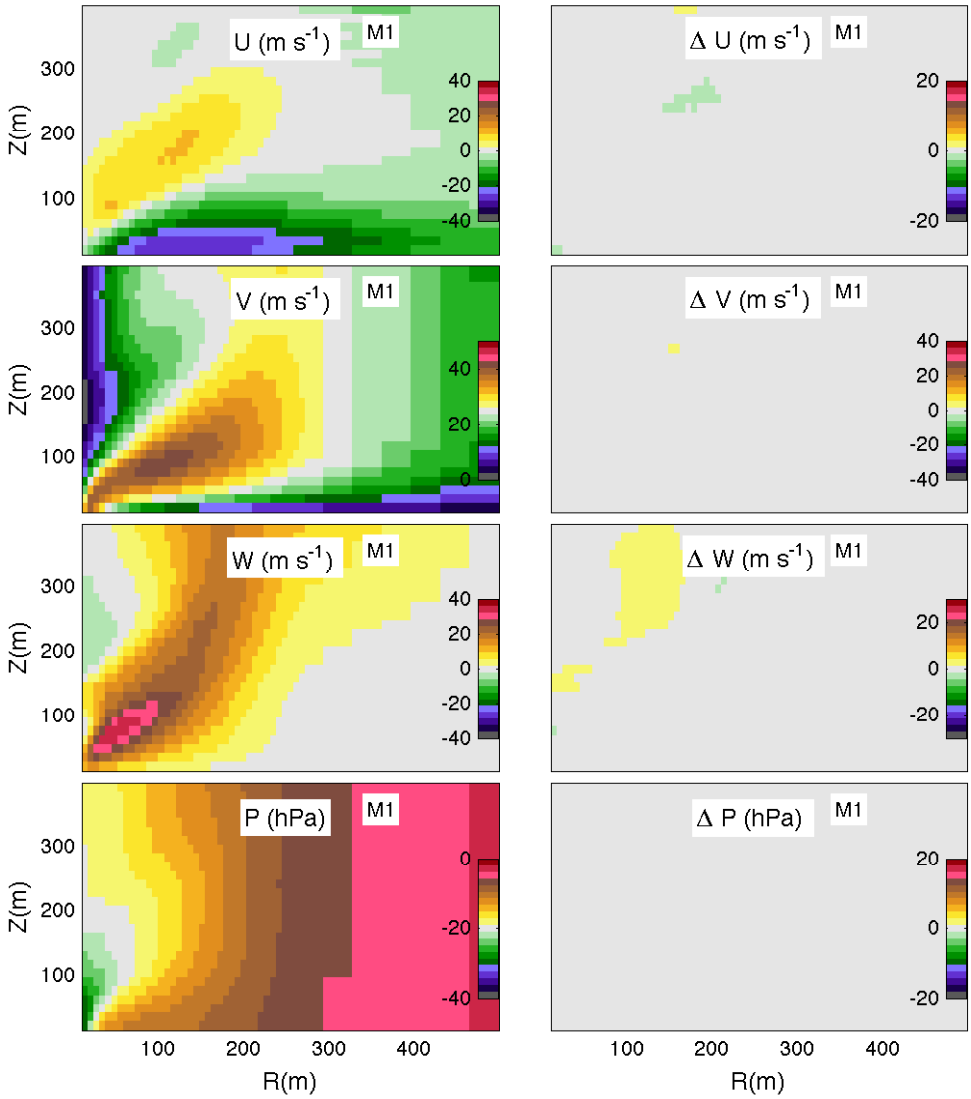

Figure 5.16: Same as Fig. 5.7, except for simulation M1 which uses a sandy loam particle distribution comprised of 0.25-, 0.5-, and 1-mm radius sand particles. Because peak debris loading in corner flow is small (0.05), insufficient momentum transfer occurs to create significant changes in near-surface velocities.

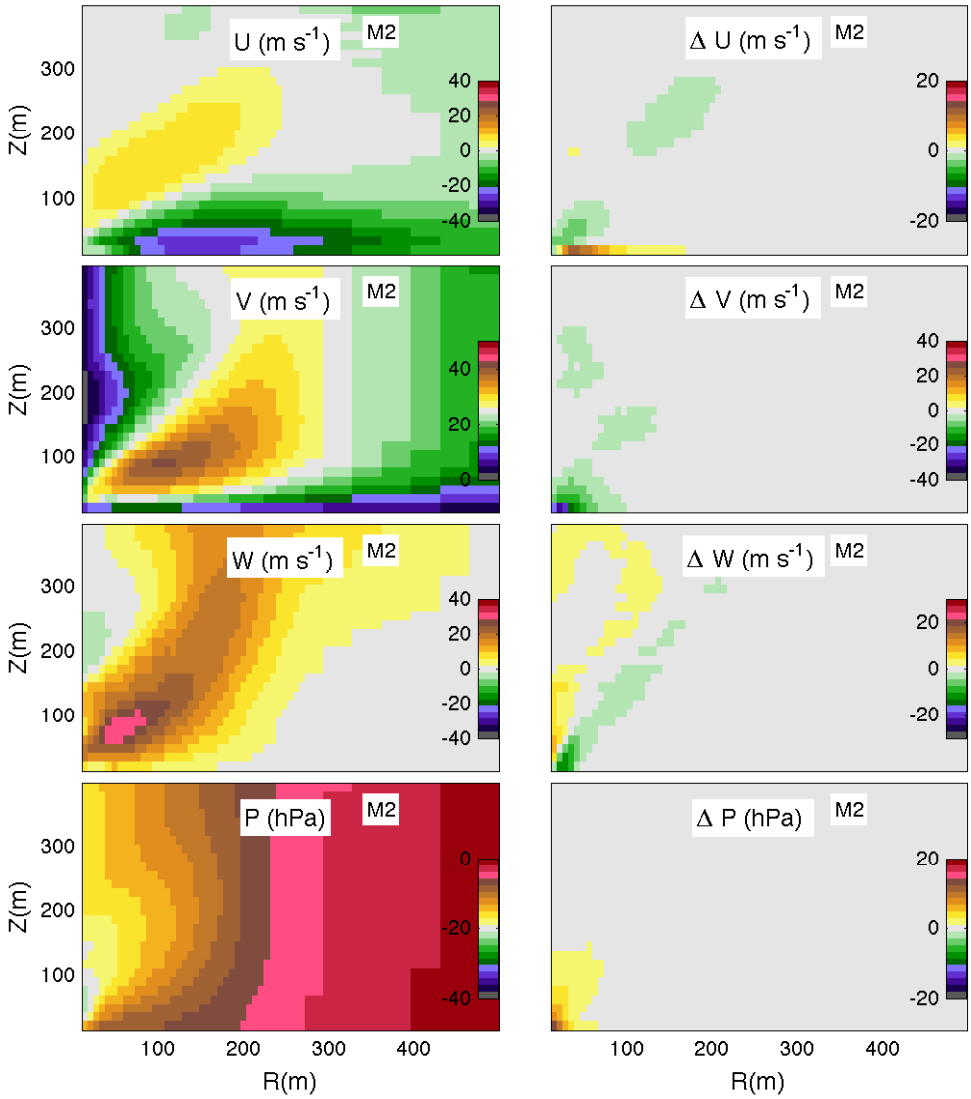

Figure 5.17: Same as Fig. 5.7, except for simulation M2 which uses a sandy loam particle distribution comprised of 0.25-, 0.5-, and 1-mm radius sand particles. Greater reductions in magnitudes of near-surface radial, tangential and vertical velocities are observed compared to simulation M1.

To examine debris loading effects on tornado dynamics using a more realistic particle size distribution, simulations are performed with 0.25-, 0.50-, and 1-mm radius sand particles based on the size distribution for sandy loam soil ($N_s = 9.4 r_s^{-2.646}$). The first simulation (hereafter called M1), contains 5.16×10^{11} 0.25-mm, 4.12×10^{10} 0.5-mm, and 3.29×10^{9} 1-mm radius sand particles. In the second simulation (hereafter called M2), the number of sand particles for each size is increased by a factor of 10. Peak values of debris loading for M1 and M2 are 0.05 and 3.34, respectively. Thus, simulation M1, 10^{10} 1-mm and 6.4×10^{11} 0.25-mm radius sand simulations have similar peak debris loadings between 0.05 – 0.07, and simulations M2, 10^{11} 1-mm and 2.56×10^{13} 0.25-mm radius sands also have similar peak debris loadings between 3.34 – 3.93.

Simulations M1 and M2 present small and large debris loading cases. Debris loading for each sand particle size, total debris loading, and equivalent radar reflectivity factor for each sand particle size and total equivalent radar reflectivity factor are shown for simulations M1 and M2 in Figs. 5.14, 5.15, respectively. For simulation M1, maximum total debris loading occurs within a cylindrical region centered around the vortex with a 50-m radius and 50-m height. For simulation M2, the maximum total debris loading occurs near the surface due to the reduction in radial and vertical velocities. Because air-debris relative velocities caused by centrifuging are smaller for 0.25-mm radius particles, 0.25-mm particles accumulate in the vortex center in both simulations and create high debris loading inside the vortex core. Centrifugal forces eject larger particles

more quickly, dispersing the sand particles into a larger sand cloud and some sand particles are recycled into the inflow after falling out of the updraft.

Total equivalent radar reflectivity factor exhibits contributions from each particle size, but most closely resembles the 1-mm equivalent radar reflectivity factor because of radar reflectivity factor's D^6 dependence. In some areas where 1-mm particles are sparse (e.g., inside the vortex core above 200 m), 0.25-mm and 0.5-mm particles exhibit the greatest contributions to equivalent radar reflectivity factor. For interpreting Doppler velocity data and correcting errors in debris centrifuging, such variations in dominant scatterers would necessitate a method to identify the dominant scatter's sizes because air-debris relative velocities vary depending on scatterer size. Some subtle differences are observed between simulations M1 and M2. Because fewer 1-mm radius particles are lofted in simulation M2, total equivalent radar reflectivity factor exhibits larger contributions from smaller particles compared to simulation M1. For example, between 20 – 100 m AGL within a 100-m radius of the vortex center, 0.5-mm equivalent radar reflectivity factor is greater than 1-mm equivalent radar reflectivity factor.

Debris loading effects on tornado dynamics differ for simulations M1 and M2. Radial, tangential and vertical velocities, and pressure, and changes in aforementioned variables are shown for simulations M1 and M2 in Figs. 5.16 and 5.17, respectively. In simulation M1, changes in radial, tangential, and vertical velocities are small due to small drag and reaction forces. In simulation M2, larger drag forces significantly reduce near-surface wind speeds. The largest

velocity changes in lowest grid cell radial, tangential, and vertical velocities are 11.2, -28.6, and -15.3 m s^{-1}, respectively. In contrast to the 2.56×10^{13} 0.25-mm sand particle simulations, reductions in tangential and vertical velocities in the vortex core are smaller because mass loading in the vortex core is reduced and large tangential and vertical velocities reductions occur through a more shallow depth. However, reductions in tangential and vertical velocity extend higher than the 10^{11} 1-mm radius sand simulation. Thus, simulation M2 combines some effects of the small and large sand particle cases.

5.2.1.2 Wood

Debris loading appears to increase in urban areas based on polarimetric radar observations (Ryzhkov et al. 2005; Bodine et al. 2013), which show higher Z_{HH} values in urban areas. Debris loading effects in urban areas are particularly important as changes in tornado dynamics and debris loading could significantly affect a tornado's damage potential and thus hazards posed to life and property. To simulate debris loading effects in urban areas, sensitivity tests are performed in the LES model for wood debris. Additional influences on tornado dynamics in urban areas, such as changes in corner flow structure caused by greater surface roughness (and greater variability of surface roughness), will be considered in future simulations. To determine how much debris loading might occur in an urban area, it is useful to consider the amount of materials used in construction.

According to the National Association of Home Builders (Yamarone 2012), a 2,000-sq. ft. single-family residence requires:

- 31 m^3 of framing wood (e.g., "2 X 4s")
- 577 m^2 of sheathing (e.g., plywood boards)
- 284 m^2 of insulation
- 288 m^2 of roofing materials (e.g., shingles)

LES model simulations were conducted for 4-foot long "2 X 4s" with 10^4 and 10^5 wood boards. As a reference point, based on a typical home concentration, the 31 m^3 of framing wood is equivalent to ∼6,400 4-foot "2 X 4" wood boards. The wood board debris trajectories are initialized in the lowest two grid cells, allowing for debris to originate at a greater range of heights as expected for man-made structures.

Significant amounts of wood debris are needed to affect tornado dynamics. In the 10^4 "2 X 4" simulation, debris loading in the corner flow is quite small (peak value of 0.2), and thus magnitudes of radial, tangential and vertical accelerations are also small (Fig. 5.18). As a result, debris loading effects on corner flow radial, tangential and vertical velocities are relatively small. In the lowest grid cell, radial, tangential and vertical velocities are reduced by a maximum of 0.2, -1.8, and -0.3 m s^{-1}, respectively. In the 10^5 "2 X 4" simulation, larger radial accelerations and tangential and vertical decelerations occur in response to higher debris loading, with a maximum debris loading of 1.1. The maximum changes

in lowest grid cell radial, tangential and vertical velocities are 2.3, -11.3 and -2.5 m s^{-1}, respectively. The maximum tangential wind speeds at the lowest grid cell are also reduced by 11.2 m s^{-1}.

Equivalent radar reflectivity factor is computed for the 10^4 and 10^5 wood board simulation using T-matrix calculations for a wood prolate spheroid of diameter 0.1048 m (same volume as a 4-foot "2 X 4"). While radar reflectivity factor contributions for sand may be obscured by larger debris, large wood boards would likely be dominant scatterers in a TDS, and hence radar reflectivity factor may provide a more useful upper-bound on maximum wood debris concentration. Maximum equivalent radar reflectivity factors for the 10^4 simulation for the entire domain, 50 m, and 100 m are 94.6, 77.8 and 63.7 dBZ, respectively. For the 10^5 simulation, maximum equivalent radar reflectivity factors for the entire domain, 50 m and 100 m are 104.0, 84.4, and 70.5 dBZ, respectively. It is evident that wood debris of sufficient concentration would produce extremely high equivalent radar reflectivity factor values, which are on the fringe of observed values for TDSs. The number of cases where tornadoes lofted substantial amounts of wood debris sufficiently close to a WSR-88D to provide beam heights below 100 m is probably small (none to the author's knowledge). But, such data could illuminate if such debris concentrations are possible. Beam heights from the TDS cases discussed previously (e.g., see Table 3.2) are typically too high to draw substantial conclusions about near surface debris loading, but indicate that the upper end of 90th percentile Z_{HH} is 61 – 66 dBZ. If radar measurements were

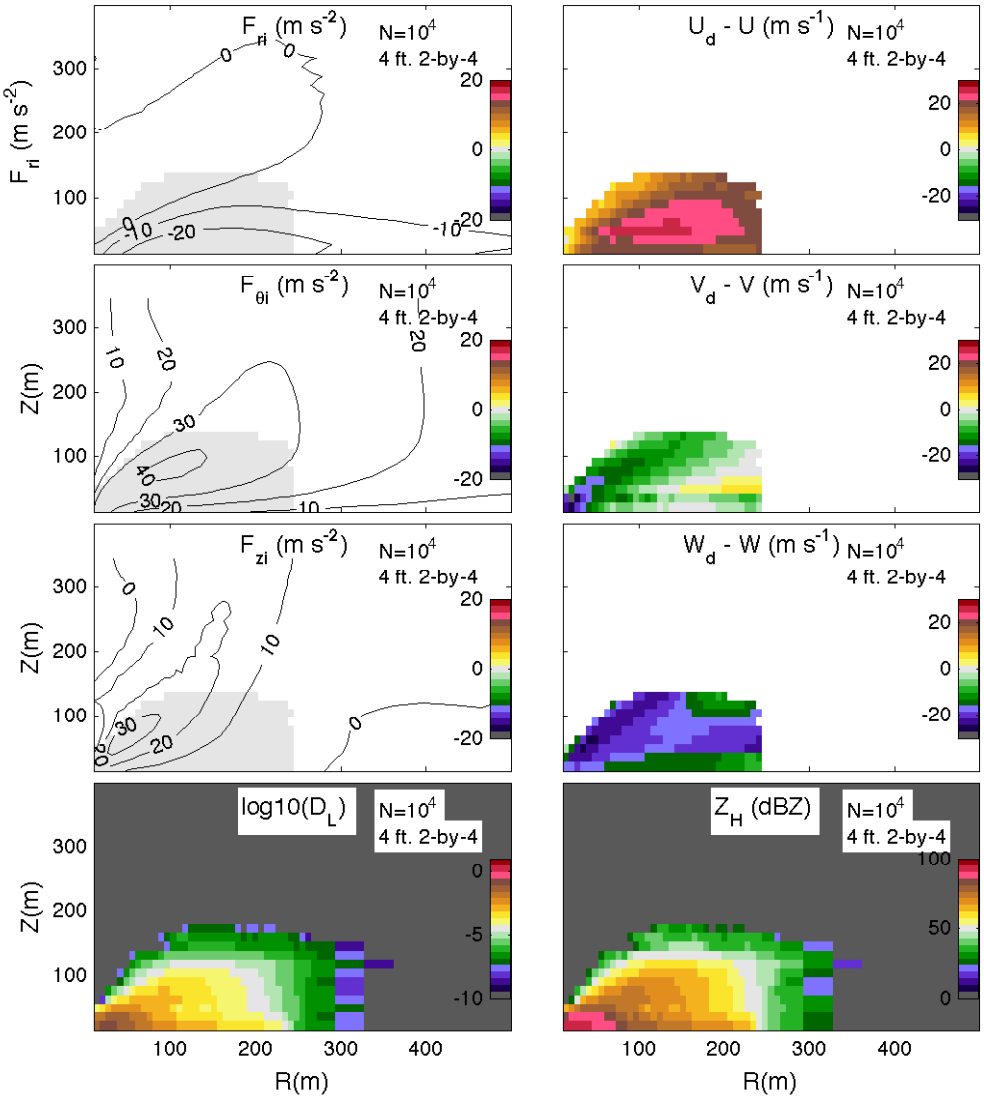

Figure 5.18: Same as Fig. 5.6, except for 10,000 "2 X 4" 4-foot long boards. Note that the color scales have been adjusted to account for greater range of relative velocities and equivalent radar reflectivity factors for wood compared to sand. Drag forces produce small magnitude radial, tangential, and vertical accelerations because debris loading is small.

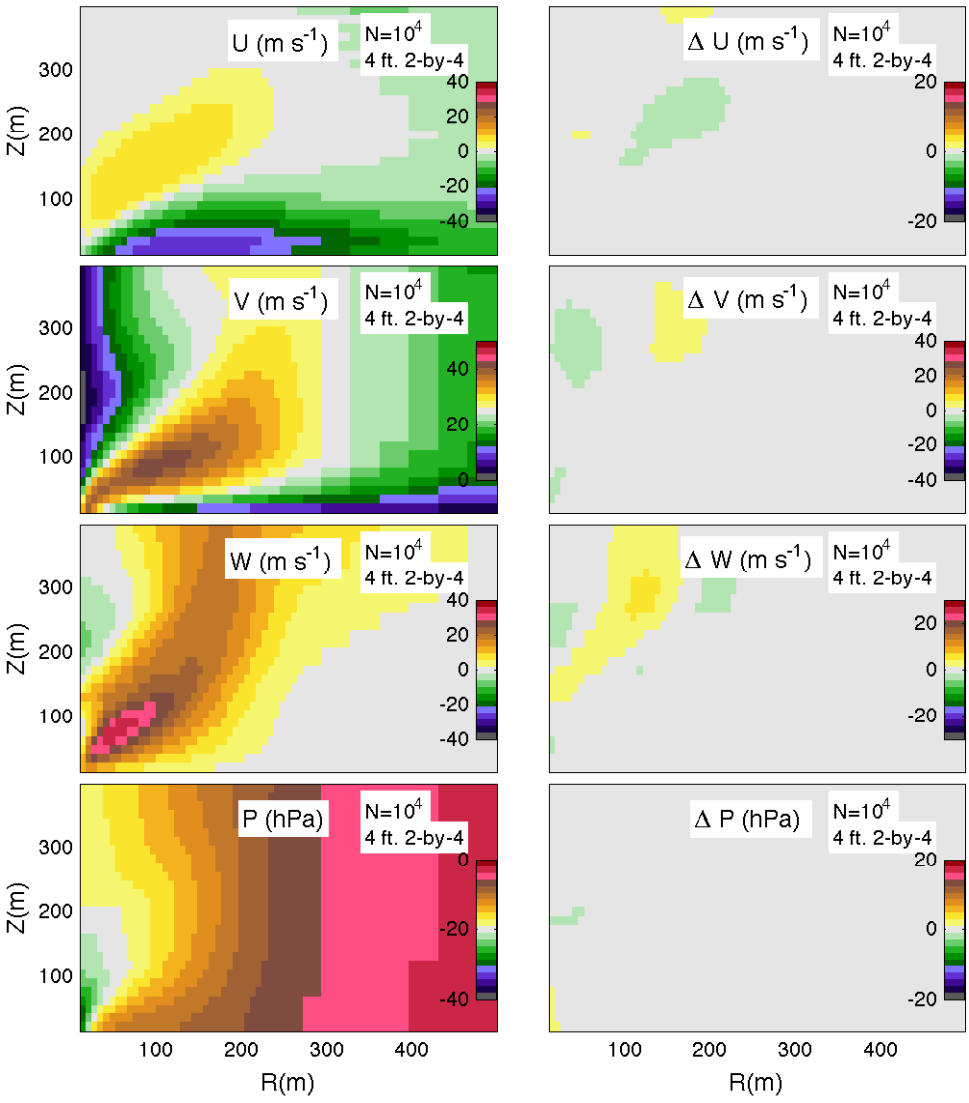

Figure 5.19: Same as Fig. 5.6, except for 10,000 "2 X 4" 4-foot long boards. Due to the small accelerations in the corner flow region, small changes in radial, tangential, and vertical wind speeds are observed.

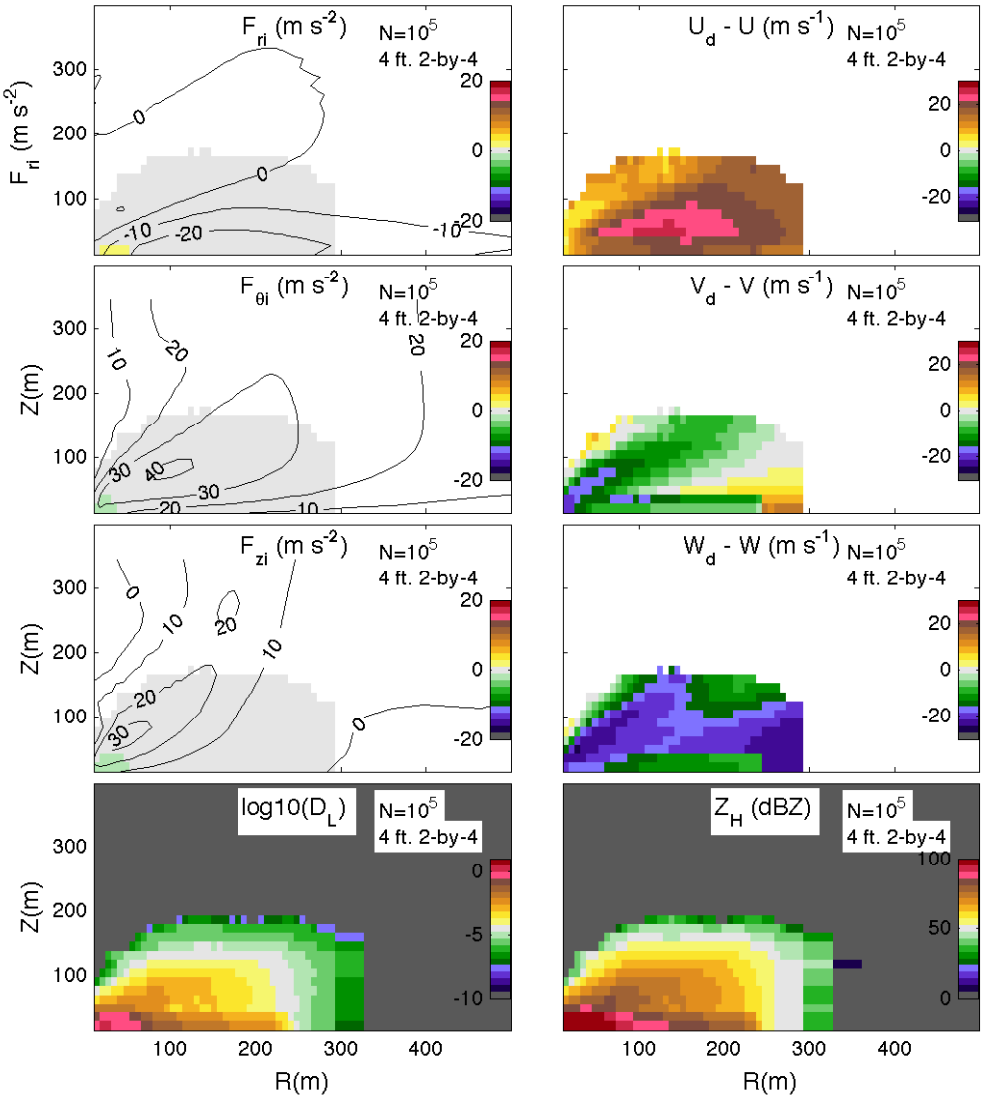

Figure 5.20: Same as Fig. 5.6, except for 100,000 "2 X 4" 4-foot long boards. Note that the color scales have been adjusted to account for greater range of relative velocities and equivalent radar reflectivity factors for wood compared to sand.

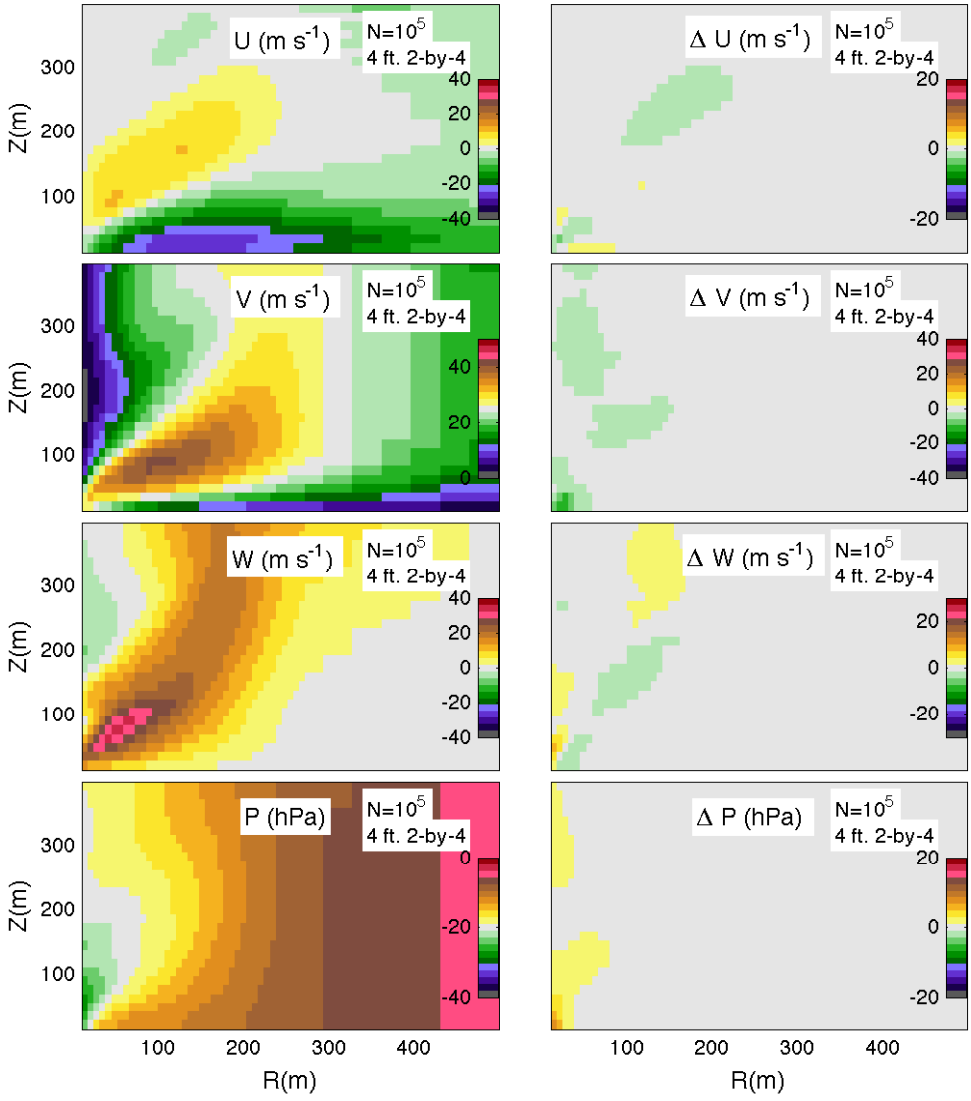

Figure 5.21: Same as Fig. 5.6, except for 100,000 "2 X 4" 4-foot long boards. Corner flow tangential wind speeds decrease and pressure increases compared to the 10^4 wood board simulation.

made at lower altitudes for these tornadoes, it is possible that higher Z_{HH} might be observed. The 20 May 2013 Moore, Oklahoma tornado occurred relatively close to KTLX, but beam heights are about 200 m at the lowest elevation angle as the tornado crosses I-35. Nonetheless, KTLX Z_{HH} values range from 65 – 70 dBZ during the period of EF-4 and 5 damage before and just after crossing I-35.

Unlike sand particles which are easily lofted by the wind, the greater terminal fall speeds of the wood boards require greater aerodynamic forces and vertical velocities to loft wood boards. Accordingly, debris loading effects for wood boards (and other large debris) are probably more dependent on vertical velocity. In tornadoes with weak vertical velocities near the surface, wood boards may be aerodynamically lifted for a short distance while its aerodynamic force exceeds gravity, or not lifted at all. If strong vertical velocities are present, wood boards may be lofted and quickly transported out of the corner flow region. In both cases, momentum transfer will occur as the wood board is accelerated by the near-surface flow, but the amount of momentum transfer and its location may vary significantly. Hence, accumulating significant amounts of wood in the corner flow region might require vertical velocities to be sufficiently strong to loft wood boards, but not strong enough to loft them quickly out of the corner flow.

Based on this exploratory analysis of wood debris loading effects, it appears that wood debris would create a TDS with extremely high Z_{HH} that approaches

the upper limits of values observed in TDSs. Even in such cases, effects on tornado dynamics are relatively small except in the grid cell closest to the surface. It is possible that debris loading effects from wood debris may be more localized in tornadoes, and occur primarily at the location of debris dispersion. Unlike sand particles, debris sources for wood boards would exhibit a more spatially inhomogeneous distribution. To examine this effect, simulations should be performed to examine localized debris lofting and its effect on nearby airflow.

5.2.2 Theory and simulations of debris loading measurements

Because sand-sized debris loading may affect tornado dynamics, measurements of near-surface debris loading of such particles is needed. As discussed previously, while equivalent radar reflectivity factor can provide an upper-bound on debris loading, a small concentration of large scatterers contribute significantly greater backscattered power than a higher concentration of larger scatterers. Thus, other measurements are needed to better constrain estimates of debris loading.

Previous studies have suggested using attenuation differences between wavelengths to estimate scatterer concentrations (Wexler and Atlas 1963; Bluestein and Pazmany 2000). For sand particles, a complicating factor in determining attenuation patterns between wavelengths is that soil wetness is unknown, and perhaps changes as particles are lofted and collide with rain drops (estimates of liquid water content near tornadoes could perhaps aid in estimating this effect).

As noted in Section 2.1.3.1, the complex relative permittivity of sand varies as a function of water content. The dielectric loss factor for dry sand decreases as a function of frequency (from 3 – 10 GHz), but even for small water contents this effect is reversed and dielectric loss factor increases as a function of frequency.

For Rayleigh scatterers, absorption of incident power energy is greater than scattering. Using the absorption and scattering cross-sections, one-way attenuation (dB km^{-1}) can be calculated as follows:

$$K = 4.343 \times 10^3 \int_0^\infty N(D)\,(\sigma_a + \sigma_s)\,dD \tag{5.14}$$

where $N(D)$ is the number of density of scatterers per unit diameter (Doviak and Zrnić 1993). The mass density of scatterers can be expressed similarly to the liquid water content as:

$$M_d = \frac{\rho_d \pi}{6} \int_0^\infty N(D) D^3 dD. \tag{5.15}$$

For Rayleigh scatterers, σ_s (2.2) is much smaller than σ_a (2.4), and therefore M_d is approximately proportional to K. This observation allows more meaningful observations about sand attenuation patterns because detailed knowledge about the sand particle size distribution is not required.

Attenuation patterns exhibit some differences in frequency between 3 – 10 GHz. Attenuation varies as a function of wavelength proportional to $\mathrm{Im}\{-K_m\}/\lambda$, which is 5.80 $\times 10^{-5}$, 5.27 $\times 10^{-5}$, 4.52 $\times 10^{-5}$, at S, C, and X bands, and thus attenuation for dry sand decreases with increasing frequency between 3 – 10 GHz. T-matrix calculations confirm these observations, and demonstrate

that for Rayleigh scatterers attenuation differences exhibit only slight sensitivity to sand particle size for constant sand mass density. For example, two-way attenuation rates for 0.1-mm diameter sand particles with a mass density of 1.2 kg m^{-3} (D_L=1) at S, C and X bands are 2.004, 1.966, and 1.716 dB km^{-1}, respectively. For 0.37-mm diameter sand particles with the same mass density, two-way attenuation rates are 2.004, 1.965, 1.722 dB km^{-1}. As an example, a 100-m (1000-m) diameter debris cloud with D_L=1 would produce a total attenuation of 0.2 (2) dB. If the debris loading increases to D_L=10, the total attenuation increases to 2 (20) dB for a 100 (1000-m) diameter debris cloud.

Attenuation rates for these debris loading cases are much greater than typical values for rain because such large debris loadings require an extremely high concentration of sand particles. For example, consider a convective updraft with a liquid water content (LWC) of 10 g m^{-3}. Two-way attenuation rates for this LWC at S and X band are 0.18 and 1.76 dB km^{-1}, respectively. Using a similar mass density for sand and water of 1.2 kg m^{-3} (i.e., using a unrealistically high LWC of 1200 g m^{-3}), attenuation rates for rain at S and X are 21.6 and 211.0 dB km^{-1}. For 1200 g m^3 of sand, attenuation rates are on the order of 2 dB km^{-1}, which are lower than rain because the dielectric loss factor of sand is smaller than water.

While the preceding discussion has focused on frequencies where Rayleigh scattering is dominant, the discussion now shifts to higher frequencies where sand particles exhibit Mie scattering effects. For these sand particles, scattering

cross-sections become larger than the absorption cross-section and cause the extinction cross-section to increase more quickly as particle size increases, leading to much higher attenuation rates. Two-way attenuation rates for a monodispersive distributions of different sand particle sizes with $D_L = 1$ and 10 are shown in Figs. 5.22 and 5.23. As scattering effects on attenuation become greater due to Mie scattering effects, attenuation rates increase as a function of sand particle size for the monodispersive sand distribution. The onset of Mie scattering effects occurs for smaller sand particle sizes at higher frequencies (Figs. 5.22 and 5.23). In addition to Mie scattering effects, attenuation rates are further increased at W band because the $\mathrm{Im}\{-K_m\}/\lambda$ term is a factor of 7 greater compared to Ka band because the dielectric loss factor is greater at W band compared to Ka band.

Using T-matrix calculations and mean debris concentrations from the LES model runs, attenuation through tornado debris clouds is simulated at S, C, X, Ka, and W bands. Two-way attenuation through the center of the vortex in the 10^{10} sand particle simulation is shown in Table 5.5. In this simulation, debris loading effects on tornado dynamics were quite small and peak debris loading was 0.06. Total two-way attenuations at S, C, and X bands are small (< 0.02 dB), and attenuation at Ka band is less than 1 dB. Hence, attenuation would likely not be noticeable at these wavelengths for these concentrations of sand particles. At W band, however, the lowest grid cell attenuation is 15.5 dB,

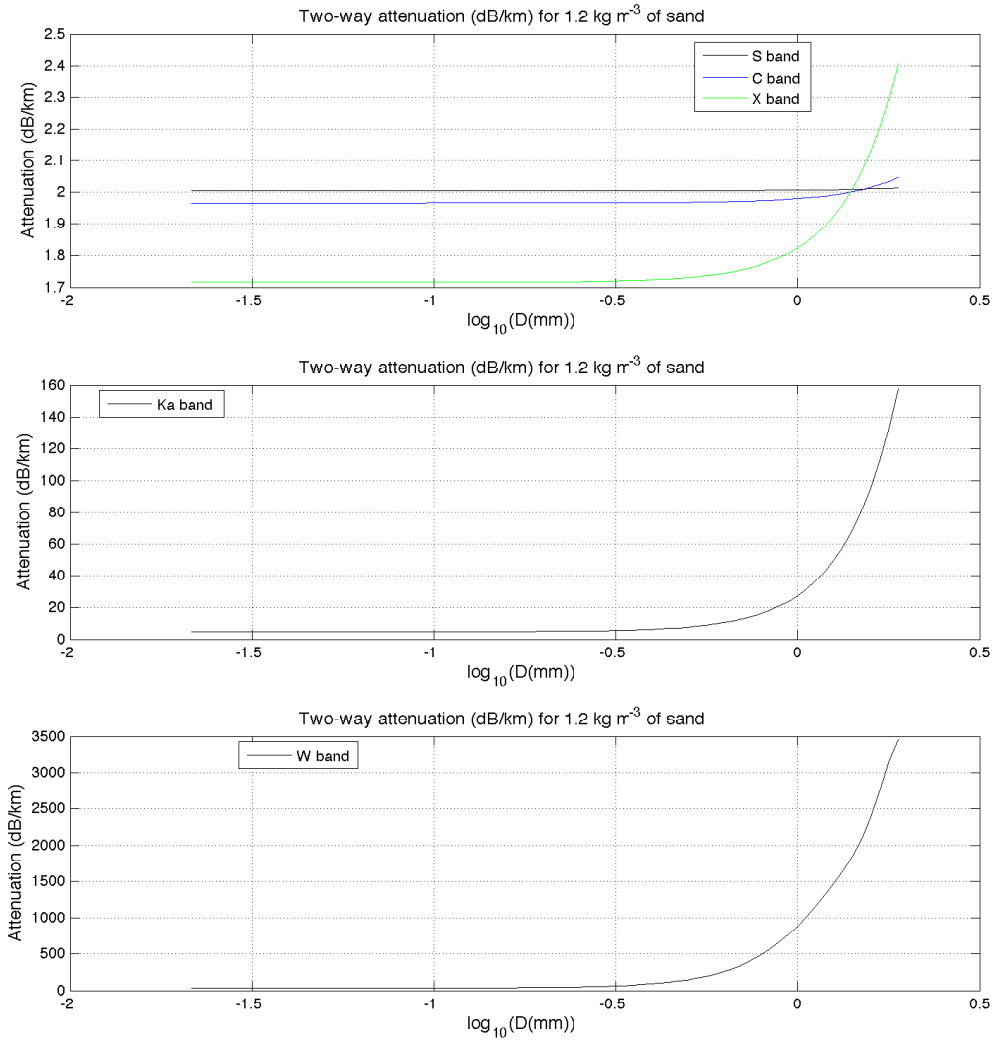

Figure 5.22: Two-way attenuation rate (dB km^{-1}) of a monodispersive distribution of sand particles with a mass density of 1.2 kg m^{-3} at S, C, X, Ka, and W bands. Attenuation rates are constant for the diameter range where Rayleigh scattering is valid, but increasing significantly for larger diameters due to attenuation due to scattering.

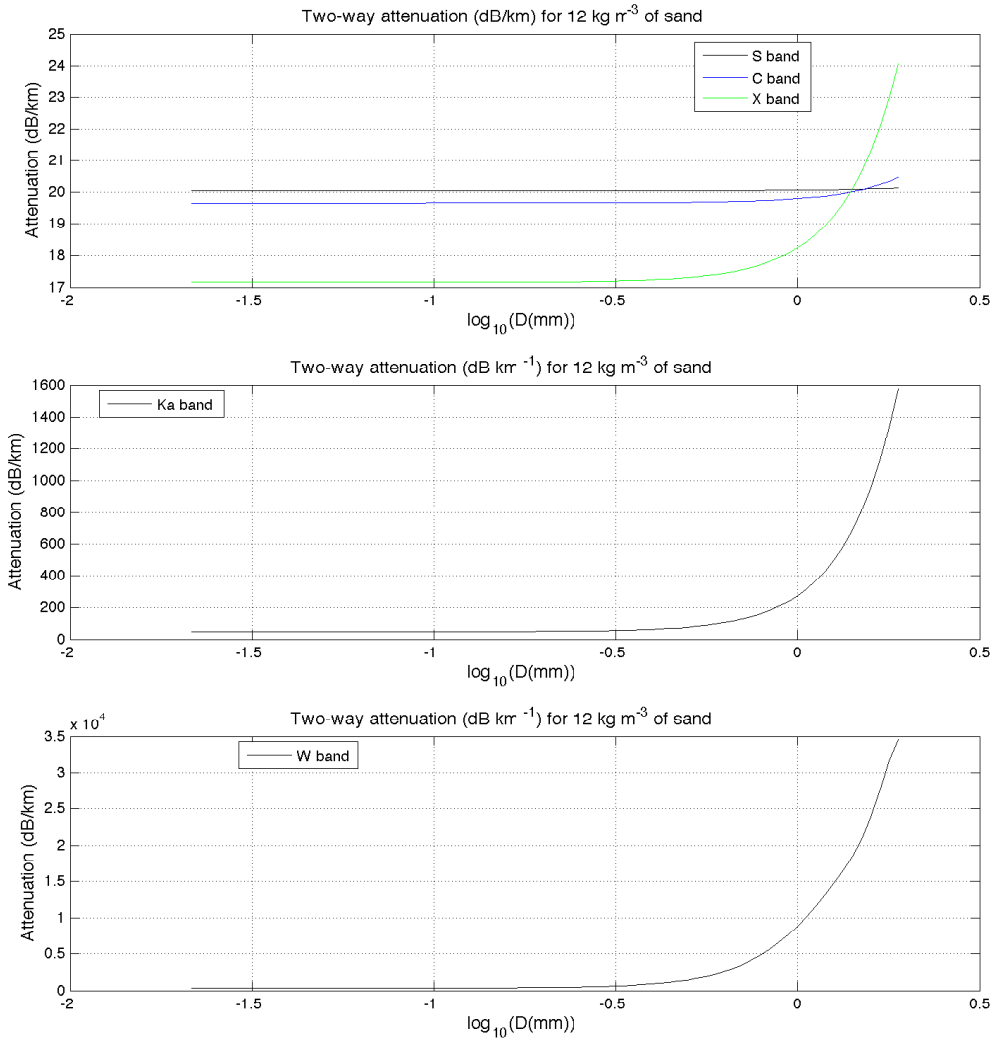

Figure 5.23: Two-way attenuation rate (dB km^{-1}) of a monodispersive distribution of sand particles with a mass density of 12 kg m^{-3} at S, C, X, Ka, and W bands. Attenuation rates are constant for the diameter range where Rayleigh scattering is valid, but increasing significantly for larger diameters due to attenuation due to scattering.

Table 5.5: Two-way attenuation (dB) through the center of the tornado for the 10^{10} 1-mm radius sand particle simulation at S, C, X, Ka and W bands. Attenuation through the lowest grid cell ($A_{H,i=1}$) and mean attenuation through the lowest 50 ($A_{H,50-m}$) and 100 m ($A_{H,100-m}$) are shown.

Frequency Band	$A_{H,i=1}$ (dB)	$A_{H,50-m}$ (dB)	$A_{H,100-m}$ (dB)
S	0.009	0.004	0.003
C	0.009	0.004	0.003
X	0.011	0.005	0.003
Ka	0.706	0.321	0.222
W	15.503	7.044	4.864

Table 5.6: Two-way attenuation (dB) through the center of the tornado for the 10^{11} 1-mm radius sand particle simulation at S, C, X, Ka and W bands. Attenuation through the lowest grid cell ($A_{H,i=1}$) and mean attenuation through the lowest 50 ($A_{H,50-m}$) and 100 m ($A_{H,100-m}$) are shown.

Frequency Band	$A_{H,i=1}$ (dB)	$A_{H,50-m}$ (dB)	$A_{H,100-m}$ (dB)
S	0.722	0.185	0.108
C	0.734	0.189	0.109
X	0.864	0.222	0.129
Ka	56.496	14.542	8.407
W	1240.361	319.270	184.572

and mean attenuation through the 50- and 100-m depths are 7.0 and 4.9 dB, and thus attenuation effects at W band would be observed.

In the 10^{11} 1-mm sand particle simulations, debris loading causes significant changes in near-surface wind speeds. For the 10^{11} 1-mm radius simulation, two-way attenuation through the vortex center is calculated for the lowest grid cell, and for the lowest 50 and 100 m AGL (Table 5.6). The 1-mm radius particles exhibit greater contributions to attenuation from scattering at small wavelengths, leading to higher attenuation at higher frequencies. Although peak debris loading values exceed 3 in the corner flow region, two-way attenuation is small at S, C, and X bands because large debris loading occurs within a narrow radius and a shallow depth. Accordingly, mean attenuation measured over a 50-m and 100-m depth is small for both simulations at those frequencies (less than 0.3 dB). However, Ka and W bands exhibit significant attenuation through the center of the simulated tornado. In the 10^{11} 1-mm sand particle simulation, incident energy passing through the lowest 50- (100-m) is attenuated 14.5 dB (8.4 dB) at Ka band. At W band, attenuation would cause complete extinction of the incident energy passing through the tornado with two-way attenuations of 185 dB in the lowest 100-m.

Attenuation characteristics of smaller particles are also examined for the 6.4×10^{11} and 2.56×10^{13} 0.25-mm radius sand particle simulations, which had peak values of debris loading of 0.06 and 3.51, respectively. Total two-way attenuation through the vortex center is computed for the 6.4×10^{11} (Table 5.9)

Table 5.7: Two-way attenuation (dB) through the center of the tornado for the 6.4×10^{11} 0.25-mm radius sand particle simulation at S, C, X, Ka and W bands. Attenuation through the lowest grid cell ($A_{H,i=1}$) and mean attenuation through the lowest 50 ($A_{H,50-m}$) and 100 m ($A_{H,100-m}$) are shown.

Frequency Band	$A_{H,i=1}$ (dB)	$A_{H,50-m}$ (dB)	$A_{H,100-m}$ (dB)
S	0.009	0.007	0.006
C	0.009	0.007	0.006
X	0.008	0.006	0.005
Ka	0.034	0.022	0.021
W	0.660	0.509	0.414

Table 5.8: Two-way attenuation (dB) through the center of the tornado for the 2.56×10^{13} 0.25-mm radius sand particle simulation at S, C, X, Ka and W bands. Attenuation through the lowest grid cell ($A_{H,i=1}$) and mean attenuation through the lowest 50 ($A_{H,50-m}$) and 100 m ($A_{H,100-m}$) are shown.

Frequency Band	$A_{H,i=1}$ (dB)	$A_{H,50-m}$ (dB)	$A_{H,100-m}$ (dB)
S	0.669	0.259	0.181
C	0.656	0.254	0.178
X	0.577	0.224	0.156
Ka	2.504	0.971	0.678
W	48.581	18.829	13.149

and the 2.56×10^{13} (Table 5.10) 0.25-mm radius sand particle simulations. Differences among S, C, and X band remain comparatively small to higher frequencies. Total two-way attenuation of sand particles in the 0.25-mm radius simulations are reduced compared to the 1-mm simulations at both Ka and W bands. However, significant attenuation still occurs at W band in the 2.56×10^{13} 0.25-mm radius simulation.

Attenuation is also computed for simulations M1 and M2 to examine attenuation effects of more realistic soil particle size distributions. Two-way attenuation through the vortex center for simulations M1 and M2 are shown in Tables 5.11 and 5.12, respectively. As observed in other small debris loading cases, simulation M1 exhibits small two-way attenuation except at W band where values

Table 5.9: Two-way attenuation (dB) through the center of the tornado for the 6.4×10^{11} 0.25-mm radius sand particle simulation at S, C, X, Ka and W bands. Attenuation through the lowest grid cell ($A_{H,i=1}$) and mean attenuation through the lowest 50 ($A_{H,50-m}$) and 100 m ($A_{H,100-m}$) are shown.

Frequency Band	$A_{H,i=1}$ (dB)	$A_{H,50-m}$ (dB)	$A_{H,100-m}$ (dB)
S	0.009	0.007	0.006
C	0.009	0.007	0.006
X	0.008	0.006	0.005
Ka	0.034	0.022	0.021
W	0.660	0.509	0.414

exceed 1 dB. Two-way attenuation in simulation M2 causes higher attenuation at Ka band, and would likely lead to complete attenuation of transmitted energy at W band.

Soil moisture or sand colliding with rain drops would increase the complex relative permittivity, and lead to higher attenuation rates. While two-way attenuation values at S, C, and X band were similar for dry sand, water content causes attenuation rates to increase between 3 – 10 GHz. Although attenuation increases by approximately an order of magnitude at X band, sand wetting or soil moisture content has the most significant effect at Ka and W bands because significant attenuation already occurs for dry sand. In simulation M2, lowest grid cell attenuation at Ka band increases from 14.8 to 99.6 dB as the fractional

Table 5.10: Two-way attenuation (dB) through the center of the tornado for the 2.56×10^{13} 0.25-mm radius sand particle simulation at S, C, X, Ka and W bands. Attenuation through the lowest grid cell ($A_{H,i=1}$) and mean attenuation through the lowest 50 ($A_{H,50-m}$) and 100 m ($A_{H,100-m}$) are shown.

Frequency Band	$A_{H,i=1}$ (dB)	$A_{H,50-m}$ (dB)	$A_{H,100-m}$ (dB)
S	0.669	0.259	0.181
C	0.656	0.254	0.178
X	0.577	0.224	0.156
Ka	2.504	0.971	0.678
W	48.581	18.829	13.149

volume of water increases from 0 to 20%. Hence, a tornado lofting dry sand with no precipitation entrainment would exhibit much lower attenuation compared to a tornado lofting moist soil or soil becoming wet due to precipitation entrainment.

Sand or soil particle distributions are not monodispersive, so sand or soil particle distributions provide a more realistic assessment of sand or soil attenuation rates in tornadoes. Two-way attenuation rates for dry clay and sandy soils at shown for debris loadings of 1 and 10 in Tables 5.13. Soil particle radii in these calculations range from 0.01 – 1 mm, enabling an examination of smaller particle sizes than those examined in the previous simulations. For dry soils, attenuation rates at S, C, and X band are similar to monodispersive attenuation rates due to

Table 5.11: Two-way attenuation (dB) for dry and wet sand (20% fractional volume of water) through the center of the tornado for simulation M1 at S, C, X, Ka and W bands. Attenuation through the lowest grid cell ($A_{H,i=1}$) and mean attenuation through the lowest 50 ($A_{H,50-m}$) and 100 m ($A_{H,100-m}$) are shown.

Frequency Band	$A_{H,i=1}$ Dry (dB)	$A_{H,50-m}$ Dry (dB)	$A_{H,100-m}$ Dry (dB)	$A_{H,i=1}$ Wet (dB)	$A_{H,50-m}$ Wet (dB)	$A_{H,100-m}$ Wet (dB)
S	0.008	0.005	0.004	0.013	0.008	0.006
C	0.008	0.005	0.004	0.031	0.019	0.015
X	0.008	0.005	0.004	0.083	0.051	0.040
Ka	0.203	0.104	0.076	1.710	0.971	0.736
W	4.704	2.425	1.778	11.023	6.263	4.753

Table 5.12: Two-way attenuation (dB) for dry and wet sand (20% fractional volume of water) through the center of the tornado for simulation M2 at S, C, X, Ka and W bands. Attenuation through the lowest grid cell ($A_{H,i=1}$) and mean attenuation through the lowest 50 ($A_{H,50-m}$) and 100 m ($A_{H,100-m}$) are shown.

Frequency Band	$A_{H,i=1}$ Dry (dB)	$A_{H,50-m}$ Dry (dB)	$A_{H,100-m}$ Dry (dB)	$A_{H,i=1}$ Wet (dB)	$A_{H,50-m}$ Wet (dB)	$A_{H,100-m}$ Wet (dB)
S	0.358	0.118	0.080	0.603	0.199	0.134
C	0.358	0.118	0.079	1.415	0.467	0.317
X	0.369	0.118	0.078	3.859	1.260	0.844
Ka	14.778	3.970	2.383	99.560	29.277	18.563
W	336.428	90.976	54.834	645.287	189.562	120.016

Table 5.13: Two-way attenuation rates (dB km^{-1}) for dry clay and sandy soils at S, C, X, Ka and W bands for D_L of 1 and 10.

Frequency Band	Clay, D_L=1 (dB km^{-1})	Sand, D_L=1 (dB km^{-1})	Clay, D_L=10 (dB km^{-1})	Sand, D_L=10 (dB km^{-1})
S	2.00	2.00	20.04	20.04
C	1.97	1.97	19.66	19.67
X	1.72	1.73	17.23	17.28
Ka	6.23	7.31	62.33	73.13
W	80.05	111.84	800.46	1118.40

Table 5.14: Two-way attenuation rates (dB km^{-1}) for wet clay and sandy soils at S, C, X, Ka and W bands for D_L of 1 and 10 (fractional water content of 20%).

Frequency Band	Clay, D_L=1 (dB km^{-1})	Sand, D_L=1 (dB km^{-1})	Clay, D_L=10 (dB km^{-1})	Sand, D_L=10 (dB km^{-1})
S	3.37	3.37	33.73	33.72
C	7.80	7.80	77.98	77.95
X	20.29	20.27	202.91	202.68
Ka	254.24	249.47	2542.40	2494.70
W	1098.30	1019.23	10982.98	10192.29

Rayleigh scattering (i.e., attenuation is independent of soil particle distribution). At Ka and W bands, however, attenuation rates become increasingly sensitive to differences in soil particle distributions. Sandy soils consist of a higher concentration of larger particles, leading to higher attenuation rates. For both soil types, significant attenuation rates occurs at Ka band for debris loading of D_L = 1, and complete attenuation of incident energy may occur for D_L = 10 for a sufficiently wide tornado. At W band, D_L = 1 produces significant attenuation and may completely attenuate the incident energy similar to Ka band for D_L = 10. At W band for D_L = 10, attenuation rates are sufficiently large that incident energy could be completely attenuated even for a relatively small debris cloud.

Two-way attenuation rates for wet clay and sandy soils are shown in Table 5.14. For a 20% fractional water content, attenuation rates for moist soils

are higher than dry soils owing to the greater imaginary part of the refractive index with greater moisture content. Attenuation rates also increase significantly at higher frequencies, with X, Ka and W band attenuations increasing by a factor of 10 or greater. Thus, attenuation rates observed for $D_L = 10$ for dry soil are observed for $D_L = 1$. Thus, soil wetting effects should be accounted for when estimating sand debris loading and creating a maximum bound for debris loading.

5.2.3 Conclusions and recommendations

Debris loading effects on tornado dynamics are examined using an LES model with a drag force coupling parameterization based on debris trajectories. Simulations are performed for a range of sand particle sizes, and wood boards. Large amounts of sand-sized debris are required to significantly affect tornado dynamics, particularly above the corner flow region. As debris loading increases, corner flow radial velocities increase, and tangential and vertical velocities decrease because debris gain momentum from the air through drag forces. As the wind speeds are reduced, a negative feedback mechanism results because air parcels spend greater periods of time in near-surface corner flow with large radial accelerations, and large tangential and vertical decelerations, further increasing radial velocities and decreasing tangential and vertical velocities (i.e., increased parcel residency times allow greater angular and vertical momentum transfer from the air to the debris). Moreover, near-surface pressure increases, leading to a

upward-directed perturbation pressure gradient force and decreased radial pressure gradients. Consequently, axial downdrafts are reduced in magnitude and spatial coverage, and near-surface inflow velocities are reduced further, including at greater radii where radial accelerations caused by drag forces are small.

LES debris simulations reveal similar effects on tornado dynamics to the simulations by Lewellen et al. (2008). While their simulations used wind tunnel measurements to specify debris fluxes as a function of wind speed, the simulations conducted in this study examine the sensitivity of tornado dynamics to varying debris loads without specifying a specific debris flux to a wind speed. Such sensitivity tests are needed because differences in surface debris fluxes vary order several orders of magnitude depending on surface characteristics, such as sand or soil type or wetness, or vegetation cover. Given the large variability of surface particle fluxes, surface roughness and soil types may determine if debris loading affects are important in tornadoes. In addition to sensitivity tests for sand particles, large debris simulations are conducted for "2 X 4" boards. These simulations reveal that a large number of wood boards are needed to produce a modest effect on near-surface wind speeds. Such high concentrations of wood boards would produce extremely high equivalent radar reflectivity factors higher than typical values in TDSs.

Equivalent radar reflectivity factor and attenuation are calculated for a range of common weather radar frequencies to develop a methodology for measuring debris loading in tornadoes. Equivalent radar reflectivity factor and attenuation

can provide an upper-bound of debris loading by assuming a single particle type produces the backscattered radar signal. This creates an upper-bound on debris loading because even though other scatterers are likely present (in unknown contributions), they also contribute to equivalent radar reflectivity factor or attenuation. Hence, the equivalent radar reflectivity factor or attenuation from the scatterers of interest must be equal or less than the actual equivalent radar reflectivity factor or attenuation. Such analyses are shown to be useful for estimating sand debris concentrations in actual tornadoes. For debris loading values that produce significant changes in tornado dynamics, significant attenuation occurs, particularly at Ka and W bands. In many cases, complete extinction of the W band incident energy would occur, and no measurements would be observed beyond the debris cloud. *Thus, if sufficient sand-sized debris loading is present to cause significant changes in tornado dynamics (e.g., $D_L \geq 1$), significant attenuation will be observed by W-band and sometimes Ka-band radars.* Numerous cases of close range observations of tornadoes exist at W and Ka bands (e.g., Bluestein et al. 2003, 2004; Weiss 2009), providing an opportunity to study debris loading effects.

Given the large number of tornado measurements at W and Ka bands, analyses of attenuation rates at these frequencies would be useful. Given that W, Ka, and lower frequencies do not have the same equivalent radar reflectivity factor due to resonance effects, direct comparisons of attenuation based on comparing W or Ka band with lower frequencies may be difficult. However, it may be

possible to infer attenuation across the TDS by assuming the debris signature possesses axisymmetric equivalent radar reflectivity factor, and examining the reduction in equivalent radar reflectivity factor along the radial. Lidar measurements in tornadoes (Bluestein et al. 2013) could also be useful for assessing debris loading of small particles which could contribute to debris loading in tornadoes, and perhaps provide between low-level observations. Factors affecting debris loading could be examined for a large number of cases to assess differences caused by different soil types or vegetation cover.

New methods are needed to estimate debris concentration and size, and will require a fundamental examination of polarimetric scattering characteristics of a wide range of debris using T-matrix calculations, more advanced electromagnetic simulations, and anechoic chamber measurements. New methods could exploit polarimetric radar observations at multiple wavelengths (time series and/or moment data), and may benefit from utilizing different polarizations (e.g., linear, circular). As discussed previously, using Z_{HH} and ρ_{HV} at multiple wavelengths may help illuminate characteristics of the size distribution (i.e., the presence of sufficiently large sizes to produce non-Rayleigh scattering). To acquire debris size and concentration estimates, attenuation measurements could provide a useful second measurement because attenuation is less sensitive to scatterer size compared to radar reflectivity factor. For estimating sand or soil loading, measurements of relative permittivity over the range of weather radar frequencies are needed for different sand or soil types with varying wetness. It may be

helpful to acquire soil or vegetation samples to determine size distributions (e.g., using sieving) or estimate soil wetness to enable more accurate comparisons to radar observations or model simulations. To validate debris size or concentration retrievals, video observations may be useful for estimating size, type and concentration of larger scatterers. Estimates of sand debris loading might also be possible from optical attenuation from photographs or videos (such methods have been applied to dust devils on Mars).

Radar observations and damage surveys frequently indicate that tornado wind speeds increase after tornado formation. Concomitantly, visual observations frequently reveal a growing debris cloud and radar observations show increasing radar reflectivity factor, suggesting increasing debris loading during this period of intensification. If the tornado is intensifying during this period of increasing debris loading, does debris loading limit the amount of intensification that occurs, or are debris concentrations insufficient to substantially affect tornado dynamics? Do variations in surface type variations lead to debris flux differences and accordingly, differences in tornado evolution? Similarly, if debris loading inhibits tornado intensification during the transition from developing to mature tornadoes, debris loading might accelerate the dissipation phase of the tornado.

Chapter 6

Conclusions and Recommendations For Future Work

In this chapter, conclusions from the study are presented from the T-matrix calculations, polarimetric radar observations and numerical simulations of tornadic debris. Then, recommendations for future work are discussed.

6.1 Conclusions

The objective of this study is to examine polarimetric radar characteristics of tornadic debris using radar observations and numerical simulations. A background on electromagnetic scattering and polarimetric variables is provided, including T-matrix calculations of polarimetric variables for different types of debris. In Chapter 3, TDS parameters are compared to damage surveys to investigate the application of TDS parameters for near real-time damage estimation. Then, dual-wavelength comparisons between S- and C-band polarimetric TDSs are discussed in Chapter 4 to illuminate similarities and difference between wavelengths. In Chapter 5, LES model runs are presented which incorporate a trajectory-based drag force feedback model to permit momentum exchange between air and debris.

T-matrix calculations of idealized tornadic debris reveal complex relationships between debris size and polarimetric radar variables. Large oscillations in

Z_{HH} in the Mie scattering region create non-monotonic relationships between Z_{HH} and debris size for both rocks and wood particles. Large dual-wavelength Z_{HH} differences occur between S, C, and X band, and debris exhibit similar dual-wavelength Z_{HH} differences to hail. Dual-wavelength Z_{HH} differences are further complicated by a superposition of Z_{HH} oscillations due to Mie scattering, but modest positive correlations exist between S- and X-band Z_{HH} dual-wavelength differences. When debris become wetted, an increase in equivalent radar reflectivity factor is observed for both sand and wood. An important limitation to the T-matrix study is that the types of debris simulated are restricted to spheroidal shapes whereas actual debris may be much higher aspect ratio and exhibit irregular, non-spherical shapes. Consequently, polarimetric radar variables for actual debris could differ significantly depending on the physical characteristics of the debris.

Polarimetric radar observations of TDSs not only improve remote tornado detection, but provide a useful estimate of near real-time damage severity and extent. This study examines the use of TDS parameters to estimate tornado damage severity using S-band polarimetric radar data. Modified TDS parameters from Ryzhkov et al. (2005) and new TDS parameters are used, and are compared to detailed damage surveys provided by the NWS. In comparisons of along-path EF-rating, 90th percentile radar reflectivity factor, TDS height, and TDS volume increase during tornado intensification and decrease during tornado

dissipation. For 14 tornado cases, maximum and minimum TDS parameter values are compared to tornado EF ratings. An increase in 90th percentile Z_{HH}, TDS height, and TDS volume, and a decrease in 10th percentile ρ_{HV} and Z_{DR} are observed as tornado EF-rating increases. These results suggest that TDS parameters could help forecasters obtain near-real-time information about tornado damage severity and spatial coverage.

Statistical analyses of dual-wavelength radar observations illuminate interesting differences between S- and C-band polarimetric radar data. KOUN and OU-PRIME exhibited close temporal and spatial matching during the 10 May 2010 Moore-Oklahoma City EF-4 tornado. Dual-wavelength comparisons reveal that S-band TDSs have higher Z_{HH} and ρ_{HV} compared to C-band TDSs. Higher S-band ρ_{HV} is attributed to a smaller ratio of non-Rayleigh scatterers to total scatterers due to smaller electrical sizes, reduced resonance effects, and less sensitivity to deviations from spherical shapes at longer wavelengths. A negative Z_{DR} signature is also observed nearly simultaneously at S and C bands as a tornado passes over a vegetated area near Lake Stanley Draper. To investigate relationships between polarimetric variables and tornado wind fields, range profiles of radial and tangential wind speeds are calculated using KOUN and OU-PRIME data. Radial velocity profiles reveal radial divergence within vortex core flow through 700 m AGL collocated with the TDS. Formation of a weak-echo hole and higher ρ_{HV} in the vortex center aloft suggests debris centrifuging,

outward motion of scatterers due to radial divergence (i.e., two-cell vortex flow), or both.

Debris loading effects may affect tornado dynamics because large concentrations of debris are lofted in the corner flow region. To examine this effect, a drag force feedback parameterization is developed and incorporated into an LES model. Sensitivity tests are performed with varying concentrations and sizes of debris to determine the amount of debris needed to affect corner flow and core velocities. To provide a realistic constraint on debris loading, equivalent radar reflectivity factor and attenuation at multiple frequencies are calculated for model simulations using T-matrix calculations. Because a very large concentration of sand particles is required to create significant momentum change between air and debris, attenuation rates in sand clouds are much higher than those observed for rain, and would cause significant attenuation or complete extinction of incident energy for W-band and sometimes Ka-band radars.

6.2 Recommendations for future work

To understand relationships between TDSs and surface damage characteristics, a larger number of comparisons between detailed damage surveys and TDSs are needed. Although this study suggests that TDS parameters tend to be correlated with surface damage severity and extent, a larger set of cases are needed to further examine this relationship and determine the strengths and weaknesses of different TDS parameters as a near real-time damage severity

estimator. Geographic differences may result in different TDS characteristics depending on population density, vegetation type, etc., and may require different TDS thresholds or parameters for different locations. Using the recently upgraded polarimetric WSR-88D network, a large sample size of TDS cases can be obtained. More fundamentally, the relationship between surface damage, debris lofting, and characteristics of tornado wind fields needs to be examined. With high-resolution polarimetric mobile radars, relationships between the TDS, surface damage, and tornado wind fields can be investigated.

Debris electromagnetic scattering characteristics are poorly understood, but are a critical component of understanding TDSs and developing applications for TDSs. While general characteristics of the TDS is known, the behavior of polarimetric variables for specific debris types is unknown. To address this need, a systematic study of electromagnetic characteristics of debris is underway using T-matrix calculations, HFSS simulations, and anechoic chamber measurements for a wide range of debris types (e.g., sand, leaves, wood boards, bricks, etc.). Using a realistic radar simulator (Cheong et al. 2008) and simulations from the LES model or the Straka Atmospheric Model (SAM), TDSs will be simulated for different vortex flows and different combinations of debris types, sizes, and orientations.

Developing a debris classification algorithm remains a desirable, yet elusive goal, particularly for mitigating Doppler velocity errors due to debris centrifuging. Given that tornadic debris distributions are a multiple parameter problem,

determining physical characteristics of the debris field will require multiple independent measurements that are sensitive to debris size, concentration, etc. For debris exhibiting Rayleigh scattering, radar reflectivity factor and attenuation provide two measurements with dependence on debris size and concentration. In the Mie scattering region, however, radar reflectivity factor and attenuation exhibit non-monotonic relationships with debris size and thus additional information is needed. Multiple radar frequencies may be useful to obtain estimates of debris size, perhaps using dual-wavelength Z_{HH} or ρ_{HV} differences. Polarimetric radar data collected in different polarizations or full measurements of the covariance matrices may also provide useful information about debris characteristics. Finally, simulations or experiments with multi-static radar or multi-receiver networks could be useful given the anisotropic scattering characteristics of large debris, and possible applications of line-of-sight attenuation measurements for estimating debris concentrations or size.

To mitigate debris centrifuging effects on Doppler velocity, it may be desirable to design weather radars that minimize sensitivity to large particle sizes. T-matrix calculations indicate that Z_{HH} increases for large particles as radar wavelength increases. Thus, at shorter wavelengths, differences between Z_{HH} for larger debris and small particles becomes smaller, and thus the power-weighted contributions of the smaller scatterers increase. Thus, their contribution to mean velocity also increases. Given that large debris (e.g., wood boards) are present in much smaller concentrations than rain drops or sand particles, high frequencies

(W or Ka band) may reduce debris centrifuging effects if Z_{HH} differences between small scatterers and large objects can be minimized, allowing the higher concentrations of small particles to dominate the backscattered radar signal. However, higher frequencies are more susceptible to attenuation, thus requiring very close radar measurements and may preclude some observations of tornadoes enshrouded by heavy precipitiation. Radar simulations should be conducted to examine frequency dependence of air-debris velocity differences, and determine what radar frequencies may be optimal for minimizing debris centrifuging effects on Doppler velocity.

Circular polarization measurements may also have utility for correcting air-debris velocity differences or examining debris characteristics. Because spherical particles backscatter radiation in the opposite handedness, differences in power spectra from received channels in the parallel and orthogonal polarizations may illuminate where spherical and non-spherical scatterers are present. Given that spherical scatterers are likely smaller particles (e.g., rain drops or sand), identifying velocities at which spherical particles are present could reduce air-debris velocity differences and facilitate corrections because the physical characteristics of such small spherical scatterers are easier to characterize.

Several extensions of the current LES studies are planned. Sensitivity tests for a larger range of particle sizes and types are need to assess debris loading effects, coupled with improved electromagnetic scattering calculations to determine maximum bounds on number concentrations. The six degree-of-freedom

model will be employed to more accurately simulate trajectories for non-spherical debris. Given that tornado wind speeds are affected by debris loading, the boundary conditions in the LES model should be modified to account for decreased mass flux associated with reduced velocities in the radial-vertical plane. LES debris studies could also examine the generation of electric fields in tornadoes. In dust devils, electric fields as strong as 10 kV m^{-1} are generated (e.g., Renno and co-authors 2004). Visual observations of tornadoes have revealed glowing funnel clouds and frequent lightning strikes (Vonnegut and Weyer 1966; MacGorman and Rust 1998), suggesting that such electrical phenomena could be related to a significant electric field generated by tornadoes and associated debris clouds.

While the LES model provides a useful tool for examining debris centrifuging and loading effects within a tornado vortex, the axisymmetric boundary conditions do not simulate the asymmetric, three-dimensional flow of the parent thunderstorm. Hence, to examine storm-scale debris transport, a storm-scale model with sufficient resolution to resolve the tornado-scale vortex is required. To address this need, future debris studies will use very high-resolution simulations from the SAM to examine storm-scale debris characteristics and simulate TDSs.

The storm-scale model will address several important questions about TDSs, and improve our understanding of TDS applications. During the developing stages of tornadoes, debris columns appear to ascend more quickly as tornado

intensity increases. Using radar simulations based on trajectories calculated with SAM data, TDSs can be simulated during developing stages of tornadoes to assess how quickly debris are lofted, and assess any correlation between low-level storm-scale updraft and tornado intensity. With high-temporal resolution polarimetric radar data from mobile radars (Pazmany et al. 2013) and phased array radars (Zhang et al. 2011), sufficiently high temporal resolution exists to calculate debris column ascent rates and perhaps estimate vertical velocity. Storm-scale TDS simulations could be used to explore the potential of using debris column ascent rates as a proxy for vertical velocities. If the scatterer types in the updraft could be determined, then a proper correction for terminal fall speed may be possible.

Storm-scale debris transport patterns evolve throughout the tornado's lifetime, leading to high-temporal variability of the TDS. Debris fallout occurs at times through the rear-flank downdraft, often after large periods of debris accumulate in the storm-scale updraft. Are periods of debris fallout through the rear-flank downdraft driven by variations in storm-scale updraft intensity, or enhancements in rear-flank downdraft intensity, or both? In addition, the variability of debris deposition patterns described by Magsig and Snow (1998) could be explored. In addition to the storm-scale model, debris trajectories calculated using dual-Doppler analyses from TDS cases could help illuminate characteristics of storm-scale debris transport.

Bibliography

Anderson, C. E., 1985a: The Barneveld tornado: A new type of tornadic storm in the form of a spiral mesolow. *Preprints, 14th Conf. on Severe Local Storms*, Amer. Meteor. Soc., Ed., 289–292.

Anderson, C. E., 1985b: The fall-out pattern for debris for the Barneveld, WI tornado: An F-5 storm. *Preprints, 14th Conf. on Severe Local Storms*, Amer. Meteor. Soc., Ed., 264–266.

Andsager, K., K. V. Beard, and N. F. Laird, 1999: Laboratory measurements of axis ratios for large raindrops. *J. Atmos. Sci.*, **56 (15)**, 2673–2683.

Atlas, D. and F. H. Ludlam, 1961: Multi-wavelength radar reflectivity of hailstorms. *Quart. J. Roy. Meteor. Soc.*, **87**, 523–534.

Balakrishnan, N. and D. S. Zrnić, 1990: Use of polarization to characterize precipitation and discriminate large hail. *J. Atmos. Sci.*, **47**, 1525–1540.

Batt, R. G., M. P. Petach, S. A. Peabody II, and R. R. Batt, 1999: Boundary layer entrainment of sand-sized particles at high speed. *J. Fluid Mech.*, **392**, 335–360.

Beard, K. V. and C. Chuang, 1987: A new model for the equilibrium shape of raindrops. *J. Atmos. Sci.*, **44 (11)**, 1509–1524.

Beard, K. V. and A. R. Jameson, 1983: Raindrop canting. *J. Atmos. Sci.*, **40 (2)**, 448–454.

Benjamin, T. B., 1962: Theory of the vortex breakdown phenomenon. *J. Fluid Mech.*, **14**, 593–629.

Bickel, S. H., 1965: Some invariant properties of the polarization scattering matrix. *Proceedings of the IEEE*, **53 (8)**, 1070–1072.

Bluestein, H., J. Houser, M. French, J. Snyder, G. Emmitt, I. PopStefanija, C. Baldi, and R. Bluth, 2013: Observations of the boundary layer near tornadoes and in supercells using a mobile, co-located, pulsed Doppler lidar and radar. *J. Atmos. Oceanic Technol.*, in press.

Bluestein, H. B., M. M. French, R. L. Tanamachi, S. Frasier, K. Hardwick, F. Junyent, and A. Pazmany, 2007: Close-range observations of tornadoes in supercells made with a dual-polarization, X-band, mobile Doppler radar. *Mon. Wea. Rev.*, **135**, 1522–1543.

Bluestein, H. B., W.-C. Lee, M. Bell, C. C. Weiss, and A. L. Pazmany, 2003: Mobile Doppler radar observations of a tornado in a supercell near Bassett, Nebraska, on 5 June 1999. part II: Tornado-vortex structure. *Mon. Wea. Rev.*, **131**, 2968–2984.

Bluestein, H. B. and A. L. Pazmany, 2000: Observations of tornadoes and other convective phenomena with a mobile, 3-mm wavelength, Doppler radar: The Spring 1999 Field Experiment. *Bull. Amer. Meteor. Soc.*, **81**, 2939–2951.

Bluestein, H. B., C. C. Weiss, and A. L. Pazmany, 2004: The vertical structure of a tornado near Happy, Texas, on 5 May 2002: High-resolution, mobile, W-band, Doppler radar observations. *Mon. Wea. Rev.*, **132**, 2325–2337.

Bodine, D., M. R. Kumjian, R. D. Palmer, P. L. Heinselman, and A. V. Ryzhkov, 2013: Tornado damage estimation using polarimetric radar. *Wea. Forecasting*, **28**, 139–158.

Bodine, D., M. R. Kumjian, A. J. Smith, R. D. Palmer, A. V. Ryzhkov, and P. L. Heinselman, 2011: High-resolution polarimetric observations of an EF-4 tornado on 10 May 2010 from OU-PRIME. *35th Conf. on Radar Meteorology*, Amer. Meteor. Soc., Ed., 3B.4.

Bohonos, J. J. and D. E. Hogan, 1999: The medical impact of tornadoes in North America. *J. Emerg. Med.*, **17**, 67–73.

Bringi, V. N. and V. Chandrasekar, 2001: *Polarimetric Doppler Weather Radar: Principles and Applications*. Cambridge University Press, 636 pp.

Bringi, V. N. and A. Hendry, 1990: Technology of polarization diversity radars for meteorology. *Radar in Meteorology – Battan Memorial and 40th Anniversary Radar Meteorology Conference*, Amer. Meteor. Soc., Ed., 153–190.

Bringi, V. N. and T. A. Seliga, 1977: Scattering from non-spherical hydrometeors. *Ann. Telecomm.*, **32**, 392–397.

Brown, R. A., B. A. Flickinger, E. Forren, D. M. Schultz, D. Sirmans, P. L. Spencer, V. T. Wood, and C. L. Ziegler, 2005a: Improved detection of severe storms using experimental fine-resolution WSR-88D measurements. *Wea. Forecasting*, **20**, 3–14.

Brown, R. A., R. M. Steadham, B. A. Flickinger, R. R. Lee, D. Sirmans, and V. T. Wood, 2005b: New WSR-88D volume coverage pattern 12: Results of field tests. *Wea. Forecasting*, **20**, 385–393.

Bunkers, M. J. and M. A. Baxter, 2011: Radar tornadic debris signatures on 27 April 2011. *Electronic J. Operational Meteor.*, **12**, 1–6.

Carbone, R. E., M. J. Carpenter, and C. D. Burghart, 1985: Doppler radar sampling limitations. *J. Atmos. Oceanic Technol.*, **2**, 357–361.

Cheong, B. L., R. D. Palmer, and M. Xue, 2008: A time series weather radar simulator based on high-resolution atmospheric models. *J. Atmos. Oceanic Technol.*, **25**, 230–243.

Chorin, A. J., 1967: A numerical method for solving incompressible viscous flow problems. *J. Comput. Phys.*, **2**, 12–26.

Chorin, A. J., 1968: Numerical solution of the Navier-Stokes equations. *Math. Comput.*, **22**, 745–762.

Church, C. R. and J. T. Snow, 1993: Laboratory models of tornadoes. *The Tornado: Its Structure, Dynamics, Prediction and Hazards*, Amer. Geophys Union, No. 79, 19–39.

Church, C. R., J. T. Snow, G. L. Baker, and E. M. Agee, 1979: Characteristics of tornado-like vortices as a function of swirl ratio: A laboratory investigation. *J. Atmos. Sci.*, **36**, 1755–1776.

Daian, G., A. Taube, A. Birnboim, M. Daian, and Y. Shramkov, 2006: Modeling the dielectric properties of wood. *Wood Sci. Technol.*, **40 (3)**, 237–246.

Davies-Jones, R. P., 1973: The dependence of core radius on swirl ratio in a tornado simulator. *J. Atmos. Sci.*, **30**, 1427–1430.

Davison, A. C. and D. V. Hinkley, 1997: *Bootstrap methods and their application*. Cambridge University Press, 582 pp.

Dobson, M., F. Ulaby, M. Hallikainen, and M. El-Rayes, 1985: Microwave dielectric behavior of wet soil-part II: Dielectric mixing models. *IEEE Tran. Geosci. Remote Sensi.*, **GE-23 (1)**, 35–46.

Doviak, R. J., V. Bringi, A. Ryzhkov, A. Zahrai, and D. Zrnić, 2000: Considerations for polarimetric upgrades to operational WSR-88D radars. *J. Atmos. Oceanic Technol.*, **17**, 257 – 278.

Doviak, R. J. and D. S. Zrnić, 1993: *Doppler Radar and Weather Observations*. 2d ed., Dover Publications, Mineola, New York.

Dowell, D. C., C. R. Alexander, J. M. Wurman, and L. J. Wicker, 2005: Centrifuging of hydrometeors and debris in tornadoes: Radar-reflectivity patterns and wind-measurement errors. *Mon. Wea. Rev.*, **133**, 1501–1524.

Efron, B., 1979: Bootstrap methods: Another look at the jackknife. *Annals of Stat.*, **7**, 1–26.

Efron, B. and R. J. Tibshirani, 1993: *An Introduction to the Bootstrap*. Chapman and Hill, 436 pp.

Fiedler, B. H., 1989: Conditions for laminar flow in geophysical vortices. *J. Atmos. Sci.*, **46 (2)**, 252–260.

Fiedler, B. H., 1994: The thermodynamic speed limit and its violation in axisymmetric numerical simulations of tornadolike vortices. *Atmos.-Ocean*, **32 (2)**, 335–359.

Flandro, G. A., H. M. McMahon, and R. L. Roach, 2011: *Basic aerodynamics - incompressible flow*. Cambridge University Press, 432 pp.

Flay, R. G., 2013: Bluff body aerodynamics. *Advanced Structural Wind Engineering*, Y. Tamura and A. Kareem, Eds., Springer Japan.

Fujita, T. T., 1967: Estimated wind speed of the Palm Sunday tornadoes. SMRP Res. Pap. 53, University of Chicago.

Fujita, T. T., 1970: The Lubbock tornadoes: A study of suction spots. *Weatherwise*, **23 (4)**, 161–173.

Fujita, T. T., 1981: Tornadoes and downbursts in the context of generalized planetary scales. *J. Atmos. Sci.*, **38**, 1511–1534.

Gatesman, A. J., T. M. Goyette, J. C. Dickinson, R. H. Giles, J. Waldman, J. Sizemore, R. M. Chase, and W. E. Nixon, 2005: Polarimetric backscattering behavior of ground clutter at X, Ka, and W band. *Proc. SPIE 5808*, 428–439.

Gong, B., 2006: Large-eddy simulation of the effects of debris on tornado dynamics. Ph.D. thesis, West Virginia Univ.

Harlow, F. H. and J. E. Welch, 1965: Numerical calculation of time-dependent viscous incompressible flow of fluids with free surface. *Phys. Fluids*, **8**, 2182–2189.

Hoerner, S. F., 1965: *Fluid-dynamic drag: Practical information on aerodynamic drag and hydrodynamic resistance*. Brick Town, 438 pp.

Holmes, J. D., 2001: *Wind loading of structures*. Spon Press, 356 pp.

Holmes, J. D., C. J. Baker, and Y. Tamura, 2006: Tachikawa number: A proposal. *J. Wind Eng. Ind. Aerodynamics*, **94**, 41–47.

Holt, A. R., 1984: Some factors affecting the remote sensing of rain by polarization diversity radar in the 3- to 35-GHz frequency range. *Radio Sci.*, **19**, 1399–1412.

Houser, J. B., 2013: Observations of supercell tornado evolution using a mobile, rapid-scan, X-band radar. Ph.D. thesis, University of Oklahoma.

Jameson, A. R., 1987: Relations among linear and circulur polarization parameters measured in canted hydrometeors. *J. Atmos. Ocean. Tech.*, **4 (4)**, 634–646.

Jameson, A. R. and J. H. Davé, 1988: An interpretation of circular polarization measurements affected by propagation differential phase shift. *J. Atmos. Ocean. Tech.*, **5 (3)**, 405–415.

Jebbor, N., S. Bri, A. Nakheli, L. Bejjit, M. Hdddad, and A. Mamouni, 2011: Complex permittivity determination with the transmission/reflection method. *Int. J. Emerg. Sci.*, **4**, 682–695.

Kumjian, M. R. and A. V. Ryzhkov, 2008: Polarimetric signatures in supercell thunderstorms. *J. Appl. Meteor. Climatol.*, **48**, 1940–1961.

Lee, W. C., B. J.-D. Jou, P.-L. Chang, and S.-M. Deng, 1999: Tropical cyclone kinematic structure retrieved from single-Doppler radar observations. Part I: Doppler velocity patterns and the GBVTD technique. *Mon. Wea. Rev.*, **127**, 2419–2439.

Lee, W.-C. and J. Wurman, 2005: Diagnosed three-dimensional axisymmetric structure of the Mulhall tornado on 3 May 1999. *J. Atmos. Sci.*, **62**, 2373–2393.

Lei, L., G. Zhang, R. J. Doviak, R. Palmer, B. L. Cheong, M. Xue, Q. Cao, and Y. Li, 2012: Multilag correlation estimators for polarimetric radar measurements in the presence of noise. *J. Atmos. Ocean. Tech.*, **29 (6)**, 772–795, doi:10.1175/JTECH-D-11-00010.1.

Lewellen, D. C., B. Gong, and W. S. Lewellen, 2008: Effects of finescale debris on near-surface tornado dynamics. *J. Atmos. Sci.*, **65**, 3247–3262.

Lewellen, D. C. and W. S. Lewellen, 2007a: Near-surface intensification of tornado vortices. *J. Atmos. Sci.*, **64**, 2176–2194.

Lewellen, D. C. and W. S. Lewellen, 2007b: Near-surface vortex intensification through corner flow collapse. *J. Atmos. Sci.*, **64**, 2195–2209.

Lewellen, D. C., W. S. Lewellen, and J. Xia, 2000: The influence of a local swirl ratio on tornado intensification near the surface. *J. Atmos. Sci.*, **57**, 527–544.

Lin, N., J. D. Holmes, and C. W. Letchford, 2007: Trajectories of wind-borne debris in horizontal winds and application to impact testing. *J. Struct. Engr.*, **133**, 274–282.

Lin, N., C. Letchford, and J. Holmes, 2006: Investigation of plate-type wind-borne debris. Part I. Experiments in wind tunnel and full scale. *J. Wind Eng. Ind. Aerodynamics*, **94**, 51–76.

MacGorman, D. R. and W. D. Rust, 1998: *The Electrical Nature of Storms*. Oxford University Press, 403 pp.

Magsig, M. A. and J. T. Snow, 1998: Long-distance debris transport by tornadic thunderstorms. Part I: The 7 May 1995 supercell thunderstorm. *Mon. Wea. Rev.*, **126**, 1430–1449.

Marshall, J. S. and W. M. K. Palmer, 1948: The distribution of raindrops with size. *J. Meteor.*, **5**, 165–166.

Maruyama, T., 2011: Simulation of flying debris using a numerically generated tornado-like vortex. *J. Wind Eng. Ind. Aerodynamics*, **99**, 249–256.

Matzler, C., 1998: Microwave permittivity of dry sand. *IEEE Tran. Geosci. Remote Sensi.*, **36**, 317–319.

Matzler, C., 2002: MATLAB functions for Mie scattering and absorption, version 2. Tech. rep., Institute of Applied Physics, University of Bern, 11 pp.

McCormick, G. C. and A. Hendry, 1975: Principles for the radar determination of the polarization properties of precipitation. *Radio Sci.*, **10**, 421–434.

McCormick, G. C. and A. Hendry, 1985: Optimal polarizations for partially polarized backscatter. *IEEE Trans. Ant. Prop.*, **33**, 33–40.

McDonald, J. R., G. S. Forbes, and T. P. Marshall, 2004: The Enhanced Fujita (EF) scale. *22nd Conf. on Severe Local Storms*, Amer. Meteor. Soc., Ed., 3B.2.

McLaughlin, D. and co-authors, 2009: Short-wavelength technology and the potential for distributed networks of small radar systems. *Bull. Amer. Meteor. Soc.*, **90**, 1797–1817.

Metzger, S. M., M. R. Balme, M. C. Towner, B. J. Bos, T. J. Ringrose, and M. R. Patel, 2011: In situ measurements of particle load and transport in dust devils. *Icarus*, **214**, 766–772.

Minor, J. E., J. R. McDonald, and K. C. Mehta, 1977: The tornado: An engineering oriented perspective. NOAA Technical Memo ERL NSSL-82, National Severe Storms Laboratory, Norman, OK.

Mischenko, M. I., 2000: Calculation of the amplitude matrix for a nonspherical particle in a fixed orientation. *Appl. Optics*, **39**, 1026–1031.

Mischenko, M. I., L. D. Travis, and D. W. Mackowski, 1996: T-matrix computations of light scattering by nonspherical particles: a review. *J. Quant. Spectrosc. Radiat. Transfer*, **55**, 535–575.

Neakrase, L. D. V. and R. Greeley, 2010: Dust devils in the laboratory: Effect of surface roughness on vortex dynamics. *J. Geophys. Res.*, **115 (E5)**.

NOAA National Climatic Data Center, 2010: Storm events database, http://www.ncdc.noaa.gov/stormevents/eventdetails.jsp?id=231939. URL http://www.ncdc.noaa.gov/stormevents/eventdetails.jsp?id=231939, URL http://www.ncdc.noaa.gov/stormevents/eventdetails.jsp?id=231939.

Nolan, D. S., 2013: On the use of Doppler radar-derived wind fields to diagnose the secondary circulations of tornadoes. *J. Atmos. Sci.*, **70**, 1160–1171.

Oguchi, T., 1983: Electromagnetic wave propagation and scattering in rain and other hydrometeors. *Proceedings of the IEEE*, **71 (9)**, 1029–1078, doi: 10.1109/PROC.1983.12724.

Oye, R. C., K. Mueller, and S. Smith, 1995: Software for radar translation, editing, and interpolation. *Preprints, 27th Conf. on Radar Meteorology*, Vail, CO, Amer. Meteor. Soc., 359–361.

Palmer, R. D., et al., 2011: The 10 May 2010 tornado outbreak in central Oklahoma: Potential for new science with high-resolution polarimetric radar. *Bull. Amer. Meteor. Soc.*, **92**, 871–891.

Pazmany, A. L., J. B. Mead, H. B. Bluestein, J. C. Snyder, and J. B. Houser, 2013: A mobile rapid-scanning X-band polarimetric (RaXPol) Doppler radar system. *J. Atmos. Oceanic Technol.*, **30 (7)**, 1398–1413.

Picca, J. and A. Ryzhkov, 2012: A dual-wavelength polarimetric analysis of the 16 May 2010 Oklahoma City extreme hailstorm. *Mon. Wea. Rev.*, **140**, 1385–1403.

Pruppacher, H. R. and R. L. Pitter, 1971: A semi-empirical determination of the shape of cloud and rain drops. *J. Atmos. Sci.*, **28 (1)**, 86–94.

Ray, P. S., 1972: Broadband complex refractive indices of ice and water. *Appl. Optics*, **11**, 1836–1844.

Renno, N. O. and co-authors, 2004: MATADOR 2002: A pilot field experiment on convective plumes and dust devils. *J. Geophys. Res.*, **109**, E07 001.

Richards, P. J., 2012: Dispersion of windborne debris. *J. Wind Eng. Ind. Aerodynamics*, **104**, 594–602.

Richards, P. J., N. Williams, B. Laing, M. McCarty, and M. Pond, 2008: Numerical calculation of the three-dimensional motion of wind-borne debris. *J. Wind Eng. Ind. Aerodynamics*, **96**, 2188–2202.

Rotunno, R., 1978: A note on the stability of a cylindrical vortex sheet. *J. Fluid Mech.*, **87**, 761–771.

Ryzhkov, A., D. Burgess, D. Zrnić, T. Smith, and S. Giangrande, 2002: Polarimetric analysis of a 3 May 1999 tornado. *Preprints, 21th Conf. on Severe Local Storms*, Amer. Meteor. Soc., Ed., San Antonio, TX.

Ryzhkov, A. V., T. J. Schuur, D. W. Burgess, and D. S. Zrnić, 2005: Polarimetric tornado detection. *J. Appl. Meteor.*, **44**, 557–570.

Sachidananda, M. and D. S. Zrnić, 1985: Zdr measurement considerations for a fast scan capability radar. *Radio Science*, **20 (4)**, 907–922.

Scharfenberg, K. A., D. J. Miller, T. J. Schuur, P. T. Schlatter, S. E. Giangrande, V. M. Melnikov, and D. W. Burgess, 2005: The Joint Polarimetric Experiment: Polarimetric radar in forecasting and decision making. *Wea. Forecasting*, **20**, 775–788.

Schultz, C. J. and co-authors, 2012a: Dual-polarization tornadic debris signatures Part I: Examples and utility in an operational setting. *Electronic J. Operational Meteor.*, **13**, 120 – 137.

Schultz, C. J. and co-authors, 2012b: Dual-polarization tornadic debris signatures Part II: Comparisons and caveats. *Electronic J. Operational Meteor.*, **13**, 138–158.

Schwarz, C. M. and D. W. Burgess, 2011: Supercell polarimetric signatures at X-band: Data from VORTEX2. *35th Conf. on Radar Meteorology*, Amer. Meteor. Soc., Ed., 7B.4.

Scruton, C., 1981: *An introduction to wind effects on structures*. Oxford University Press.

Seliga, T. A., K. Aydin, and V. N. Bringi, 1984: Differential reflectivity and circular depolarization ratio radar signals and related drop oscillation and propagation effects in rainfall. *Radio Sci.*, **19 (1)**, 81–89.

Seliga, T. A. and V. N. Bringi, 1976: Potential use of radar differential reflectivity measurements at orthogonal polarizations for measuring precipitation. *J. Appl. Meteor.*, **15 (1)**, 69–76.

Seliga, T. A. and V. N. Bringi, 1978: Differential reflectivity and differential phase shift: Applications in radar meteorology. *Radio. Sci.*, **13 (2)**, 271–275.

Shapiro, A., 2005: Drag-induced transfer of horizontal momentum between air and raindrops. *J. Atmos. Sci.*, **62**, 2205–2219.

Simiu, E. and R. H. Scanlan, 1996: *Wind effects on structures: Fundamentals and applications to design*. 3d ed., John Wiley, 688 pp.

Smagorinsky, J., 1963: General circulation experiments with the primitive equations I: The basic experiment. *Mon. Wea. Rev.*, **91**, 99–162.

Snow, J. T., 1978: On inertial instability as related to, the multiple-vortex phenomenon. *J. Atmos. Sci.*, **35 (9)**, 1660–1677.

Snow, J. T., 1984: On the formation of particle sheaths in columnar vortices. *J. Atmos. Sci.*, **41**, 2477–2491.

Snow, J. T., A. L. Wyatt, A. K. McCarthy, and E. K. Bishop, 1995: Fallout of debris from tornadic thunderstorms: A historical perspective and two examples from VORTEX. *Bull. Amer. Meteor. Soc.*, **76**, 1777–1790.

Snyder, J. C. and H. B. Bluestein, 2014: Some considerations for the use of high-resolution mobile radar data in tornado intensity determination. *Wea. Forecasting*, **in press**.

Snyder, J. C., H. B. Bluestein, G. Zhang, and S. J. Frasier, 2010: Attenuation correction and hydrometeor classification of high-resolution, X-band, dual-polarized mobile radar measurements in severe convective storms. *J. Atmos. Oceanic Technol.*, **27**, 1979–2001.

Tachikawa, M., 1983: Trajectories of flat plates in uniform flow with application to wind-generated missiles. *J. Wind Eng. Ind. Aerodynamics*, **14**, 443–453.

Tanamachi, R. L., H. B. Bluestein, J. B. Houser, S. J. Frasier, and K. M. Hardwick, 2012: Mobile X-band, polarimetric Doppler radar observations of the 4 May 2007 Greensburg, Kansas, tornadic supercell. *Mon. Wea. Rev.*, **140**, 2103–2125.

Tannehill, J. C., D. A. Anderson, and R. H. Pletcher, 1997: *Computational fluid mechanics and heat transfer*. 2d ed., Taylor and Francis.

Thurai, M. and V. N. Bringi, 2005: Drop axis ratios from a 2d video disdrometer. *J. Atmos. Oceanic Technol.*, **22 (7)**, 966–978.

Thurai, M., G. J. Huang, V. N. Bringi, W. L. Randeu, and M. Schönhuber, 2007: Drop shapes, model comparisons, and calculations of polarimetric radar parameters in rain. *J. Atmos. Ocean. Tech.*, **24 (6)**, 1019–1032.

Turcotte, D. L., 1986: Fractals and fragmentation. *J. Geophys. Res.*, **91**, 1921–1926.

Tyler, S. W. and S. W. Wheatcraft, 1989: Application of fractal mathematics to soil water retention estimation. *Soil. Sci. Soc. of America*, **53**, 987–995.

Tyler, S. W. and S. W. Wheatcraft, 1992: Fractal scaling of soil particle-size distributions: Analysis and limitations. *Soil. Sci. Soc. of America*, **56**, 362–369.

Uchida, T. and Y. Ohya, 2003: Large-eddy simulation of turbulent airflow over complex terrain. *J. Wind Eng. Ind. Aerodynamics*, **91 (1–2)**, 219 – 229.

Ulaby, F., T. Bengal, M. Dobson, J. East, J. Garvin, and D. Evans, 1990: Microwave dielectric properties of dry rocks. *IEEE Tran. Geosci. Remote Sensi.*, **28**, 325–336.

Ulaby, T. B., K. Sarabandi, and F. T. Ulaby, 1987: Measuring and modeling the backscatter cross-section of a leaf. *Radio Sci.*, **22**, 1109–1116.

Ulbrich, C. W., 1983: Natural variations in the analytical form of the raindrop size distribution. *J. Appl. Meteor.*, **22**, 1764–1775.

Van Dyke, M., 1982: *An album of fluid motion*. The Parabolic Press, 176 pp.

Vivekanandan, J., W. M. Adams, and V. N. Bringi, 1991: Rigorous approach to polarimetric radar modeling of hydrometeor orientation distributions. *J. Appl. Meteor.*, **30**, 1053–1063.

Vonnegut, B. and J. R. Weyer, 1966: Luminous phenomena in nocturnal tornadoes. *Science*, **153**, 1213–1220.

Wakimoto, R. M., N. T. Atkins, and J. Wurman, 2011: The LaGrange tornado during VORTEX2. Part I: Photogrammetric analysis of the tornado combined with single-doppler radar data. *Mon. Wea. Rev.*, **139**, 2233–2258.

Wakimoto, R. M., P. Stauffer, W. C. Lee, N. T. Atkins, and J. Wurman, 2012: Finescale structure of the LaGrange, Wyoming tornado during VORTEX2: GBVTD and photogrammetric analyses. *Mon. Wea. Rev.*, **140**, 3397–3418.

Walko, R. and R. Gall, 1984: A two-dimensional linear stability analysis of the multiple vortex phenomenon. *J. Atmos. Sci.*, **41 (24)**, 3456–3471.

Wang, J. and T. Schmugge, 1980: An empirical model for the complex dielectric permittivity of soils as a function of water content. *IEEE Tran. Geosci. Remote Sensi.*, **GE-18**, 288–295.

Ward, N. B., 1972: The exploration of certain features of tornado dynamics using a laboratory model. *J. Atmos. Sci.*, **29**, 1194–1204.

Waterman, P. C., 1969: Scattering by dielectric obstacles. *Alta Frequenza*, **(Speciale)**, 348–352.

Waterman, P. C., 1971: Symmetry, unitarity and geometry in electromagnetic scattering. *Phys. Rev. D*, **3**, 825 – 839.

Weiss, C. C., 2009: The TTUKa mobile Doppler radar: Coordinated radar and in situ measurements of supercell thunderstorms during project VORTEX2. *34th Conf. on Radar Meteorology*, Amer. Meteor. Soc., Ed.

Wexler, R. and D. Atlas, 1963: Radar reflectivity and attenuation in rain. *J. Appl. Meteor.*, **2**, 276–280.

White, F. M., 2006: *Viscous Fluid Flow*. 3d ed., McGraw-Hill, 629 p.

Wills, J. A. B., B. E. Lee, and T. A. Wyatt, 2002: A model of windborne debris damage. *J. Wind Eng. Ind. Aerodynamics*, **90**, 555–565.

Wilson, J. W., 1986: Tornadogenesis by nonprecipitation induced wind shear lines. *Mon. Wea. Rev.*, **114**, 270–284.

WSEC, 2006: A recommendation for an enhanced Fujita scale (EF-scale). Tech. rep., Wind Science and Engineering Center, Texas Tech University, [Available online at http://www.depts.ttu.edu/weweb/EFScale.pdf].

Wurman, J., 2002: The multiple-vortex structure of a tornado. *Wea. Forecasting*, **17**, 473–505.

Wurman, J. and S. Gill, 2000: Fine-scale radar observations of the Dimmitt, Texas (2 June 1995), tornado. *Mon. Wea. Rev.*, **128**, 2135–2164.

Wurman, J., K. Kosiba, and P. Robinson, 2013: In situ, Doppler radar, and video observations of the interior structure of a tornado and the wind-damage relationship. *Bull. Amer. Meteor. Soc.*, **94**, 835–846.

Wurman, J., J. M. Straka, and E. N. Rasmussen, 1996: Fine-scale Doppler radar observations of tornadoes. *Science*, **272**, 1774–1777.

Yamarone, R., 2012: *The trader's guide to key economic indicators*, Vol. 151. John Wiley & Sons.

Zhang, G., R. J. Doviak, D. S. Zrnić, R. Palmer, L. Lei, and Y. Al-Rashid, 2011: Polarimetric Phased-Array Radar for weather measurement: A planar or cylindrical configuration? *J. Atmos. Oceanic Technol.*, **28**, 63–73.

Zhang, G., J. Vivekanandan, and E. Brandes, 2001: A method for estimating rain rate and drop size distribution from polarimetric radar measurements. *IEEE Tran. Geosci. Remote Sensi.*, **39**, 830–841.

Zrnić, D. S. and A. V. Ryzhkov, 1999: Polarimetry for weather surveillance radars. *Bull. Amer. Meteor. Soc.*, **80**, 389–406.

Appendix A

Large-Eddy Simulation

A.1 Governing equations

LES uses two governing equations, the Navier-Stokes equations and the continuity equation. The Navier-Stokes equation in tensor notation is given as follows:

$$\frac{\partial \rho u_i}{\partial t} + \frac{\partial}{\partial x_j}\left(\rho u_i u_j\right) = -\frac{\partial p}{\partial x_i} + \frac{\partial \rho \tau_{ji}}{\partial x_j} + \rho f_i \tag{A.1}$$

where τ_{ij} is the stress tensor, and f_i is body force per unit mass acting on the fluid (e.g., gravity), and i, j =1, 2, 3. The left-hand side of (A.1) describes the partial derivative of the velocity vector w.r.t. time and the advection of momentum. The terms on the right-hand side of (A.1) describe the three-dimensional pressure gradient force, viscous stress forces, and body forces, respectively.

The mass continuity equation describes the conservation of mass of the fluid,

$$\frac{\partial \rho}{\partial t} + \frac{\partial}{\partial x_i}\left(\rho u_i\right) = 0. \tag{A.2}$$

Using the product rule to expand the $\frac{\partial}{\partial x_i}\left(\rho u_i\right)$ term in (A.2), one can show that (A.2) becomes:

$$\frac{\partial \rho}{\partial t} + u_i \frac{\partial \rho}{\partial x_i} + \rho \frac{\partial u_i}{\partial x_i} = 0. \tag{A.3}$$

The first two terms in (A.3) represent the Lagrangian change in density following an air parcel. For meteorological flow conditions, it is commonly assumed

that the density of the fluid does not change with time (i.e., no expansion or compression of the fluid within a fixed volume). Such an assumption is called the incompressibility condition. The incompressibility condition states that the Lagrangian density change with represent to time, $\frac{D\rho}{Dt}$, is 0, where $\frac{D\rho}{Dt}$ is

$$\frac{D\rho}{Dt} = \frac{\partial \rho}{\partial t} + u_i \frac{\partial \rho}{\partial x_i}. \tag{A.4}$$

The governing equations for the LES model assume that the flow is incompressible. By substituting (A.4) into (A.3), the first two terms of (A.3) become zero. This results in the incompressible continuity equation,

$$\frac{\partial u_i}{\partial x_i} = 0. \tag{A.5}$$

The incompressible form of the Navier-Stokes equation is

$$\frac{\partial u_i}{\partial t} + \frac{\partial}{\partial x_j}\left(u_i u_j\right) = -\frac{1}{\rho}\frac{\partial p}{\partial x_i} + \frac{\partial \tau_{ij}}{\partial x_j} + f_i. \tag{A.6}$$

A.2 Filtered governing equations

The goal of LES is to numerically compute the large-scale flow and model the subgrid-scale (SGS) or residual turbulence which is not resolved explicitly by the model. Therefore, the Navier-Stokes and continuity equations must be filtered to remove smaller scale flows (or numerical noise) which are not resolved explicitly through LES. Maruyama (2011) define the filter length, L for the LES model. L depends on the width of the individual grid points in the x, y, and z-dimensions (ΔX_1, ΔX_2, ΔX_3). The filter length is computed using

$$L = \left(\Delta X_1 \Delta X_2 \Delta X_3\right)^{\frac{1}{3}}. \tag{A.7}$$

The velocity, pressure, and stress fields are filtered, and given the notation $\overline{u}_i$, $\overline{p}$, $\overline{\tau}_{ij}$, and so on, to denote filtered fields. After filtering, the continuity equation becomes

$$\frac{\partial \overline{u}_i}{\partial x_i} = 0, \tag{A.8}$$

and the Navier-Stokes equation becomes

$$\frac{\partial \overline{u}_i}{\partial t} + \frac{\partial}{\partial x_j}\left(\overline{u}_i \overline{u}_j\right) = -\frac{1}{\rho}\frac{\partial \overline{p}}{\partial x_i} + \frac{\partial \overline{\tau}_{ij}}{\partial x_j} + \frac{\partial\left(\overline{u}_i \overline{u}_j - \overline{u_i u_j}\right)}{\partial x_j}. \tag{A.9}$$

The second and third terms on the right-hand side of (A.9) are the filtered viscous stress term and residual of the stress term. The filtered viscous stress term can be expressed as

$$\overline{\tau}_{ij} = -\frac{2}{3}\frac{\mu}{\rho}\frac{\partial \overline{u}_i}{\partial x_i} + \frac{\mu}{\rho}\overline{D}_{i,j}, \tag{A.10}$$

where μ is the viscosity coefficient and the rate of strain tensor, $\overline{D}_{i,j}$ is

$$\overline{D}_{i,j} = \left(\frac{\partial \overline{u}_j}{\partial x_i} + \frac{\partial \overline{u}_i}{\partial x_j}\right). \tag{A.11}$$

The residual of the stress term can not be solved numerically in the form presented in (A.9), so it will be modeled in a numerically solvable form.

A.3 LES sub-grid scale model

The $\overline{u_i u_j}$ term of the sub-grid scale (SGS) stress term can be expanded using Reynolds averaging of u_i and u_j (e.g., $u_i = \overline{u}_i + u_i^{'}$). After expanding the u_i and u_j terms, the following equation results,

$$\overline{u_i u_j} = \overline{\overline{u}_i \overline{u}_j} - \overline{u_i^{'} u_j^{'}} + \overline{\overline{u}_i u_j^{'}} + \overline{u_i^{'} \overline{u}_j^{'}}. \tag{A.12}$$

In the LES model, the SGS stress term is modeled using the Smagorinsky model (Smagorinsky 1963). The Smagorinsky model assumes that turbulence is isotropic and spatially homogeneous. The SGS viscosity, ν_{SGS}, is defined as

$$\nu_{SGS} = (C_s L)^2 \sqrt{2\overline{D}_{ij}\overline{D}_{ij}}, \tag{A.13}$$

where C_s is the Smagorinsky constant and L is the filter length. The LES model uses a Smagorinsky constant of 0.1 (Maruyama 2011). The SGS stress term is modeled using ν_{SGS} as follows,

$$\overline{u_i u_j} - \overline{u}_i \overline{u}_j = -\nu_{SGS}\overline{D_{ij}}. \tag{A.14}$$

Equation (A.9) can be rewritten using the new SGS stress term as follows,

$$\frac{\partial \overline{u}_i}{\partial t} + \frac{\partial}{\partial x_j}\left(\overline{u}_i \overline{u}_j\right) = -\frac{1}{\rho}\frac{\partial \overline{p}}{\partial x_i} + 2\frac{\partial\left(\nu + \nu_{SGS}\right) D}{\partial x_i}. \tag{A.15}$$

A.4 Numerical calculation of the LES

In this section, the numerical calculation of the LES is discussed using the governing equations discussed in the previous section. There are two common approaches for solving the incompressible Navier-Stokes equations (Tannehill et al. 1997). The vorticity-stream approach employs a change of variables to rewrite velocity as vorticity and stream functions. The primitive-variable approach solves the Navier-Stokes equations using the components of the wind and pressure without a change of variables. The LES model employs the latter approach, which is most common for three-dimensional Navier-Stokes calculations.

There are two subsets of approaches for the primitive-variable approach: coupled approach and pressure-correction approach (Tannehill et al. 1997). In the coupled approach, an artificial compressibility term is added to the continuity equation (Chorin 1967). The continuity equation includes an artificial pressure and artificial time term which approach zero as the solution converges. The LES numerical calculations use the pressure-correction approach. The pressure-correction approach first solves the terms of the Navier-Stokes equations independently without using the continuity equation (Harlow and Welch 1965; Chorin 1968). Without the continuity equation, however, the pressure (or density) distribution will not satisfy the continuity equation. To satisfy the continuity equation, a Poisson equation is formulated for the pressure field and solved until the field divergence is zero (i.e., $\frac{\partial u_i}{\partial x_i} = 0$).

The pressure-correction approach used in the LES model is the fractional step method or projection method (Chorin 1968). The calculation of the velocity and pressure fields at the next time step, $n + 1$, involves the following steps. The Navier-Stokes equation can be rewritten as follows for time n,

$$\frac{\partial u^n}{\partial t} + A^n = -\nabla p + S^n \tag{A.16}$$

where n is the current time step, A is the advection term, and S is the stress term. The first term can be expanded into finite difference notation,

$$\frac{\partial u^n}{\partial t} = \frac{u^{n+1} - u^n}{\Delta t}. \tag{A.17}$$

After some algebraic manipulation, the equation for the velocity field at time $n+1$ is

$$u^{n+1} = u^n + \Delta t \left(-\nabla p - A^n + S^n\right). \tag{A.18}$$

In order to solve for the velocity field at time $n+1$, the velocity, u^F, is calculated first without including the pressure term,

$$u^F = u^n + \Delta t \left(-A^n + S^n\right). \tag{A.19}$$

Using (A.19), (A.18) can be rewritten as,

$$u^{n+1} = u^F - \Delta t \nabla p^{n+1}, \tag{A.20}$$

To satisfy the mass continuity equation, a Poisson equation is formed by taking the divergence of both sides. The divergence of u^{n+1} is zero because of the incompressibility condition. Hence, (A.20) becomes

$$\nabla^2 p^{n+1} = \frac{\nabla \cdot u^F}{\Delta t}, \tag{A.21}$$

which is a Poisson equation. After solving the Poisson equation, the velocity field at time $n+1$ can be solved using (A.20).

After the generation of the model initial conditions and grid, the calculation of the LES can be summarized by the following steps:

1. Calculation of the SGS viscosity

2. Calculation of the Navier-Stokes equation terms

3. Pressure correction of the velocity field

Appendix B

List of Acronyms

ATSR	Alternating Transmit Simultaneous Receive
BC	Boundary Conditions
CDR	Circular Depolarization Ratio
CI	Confidence Interval
DSD	Drop-size distribution
EF	Enhanced Fujita
EM	Electromagnetic
GBVTD	Ground-Based Velocity Tracking Display
HFSS	High Frequency Structural Simulator
LES	Large-Eddy Simulation
LWC	Liquid Water Content
MAD	Median Absolute Deviation
NWS	National Weather Service

OU-PRIME	University of Oklahoma Polarimetric Radar for Innovations in Meteorology and Engineering
RFD	Rear-Flank Downdraft
RMW	Radius of Maximum Wind
SGS	Subgrid-Scale
STSR	Simultaneous Transmit Simultaneous Receive
TDS	Tornadic Debris Signature
TVS	Tornadic Vortex Signature
VCP	Volume Coverage Pattern
WEH	Weak Echo Hole
WFO	Weather Forecast Office
WSR-88D	Weather Surveillance Radar 1988 Doppler

Appendix C

List of Symbols

a	Major axis (m)
A^i_{TDS}	TDS Area (m^2)
A	Debris cross-sectional area (m^2)
b	Minor axis (m)
$\mathbf{C}$	Covariance matrix
c_{deb}	Proportionality constant for debris flux
C_D	Drag force coefficient
C_F	Aerodynamic force coefficient
C_L	Lift force coefficient
C_M	Aerodynamic moment coefficient
C_N	Normal force coefficient
C_P	Pressure coefficient
C_S	Smagorinsky constant
D	Diameter (m)
D_L	Debris loading
e	Turbulent kinetic energy ($m^2\ s^{-2}$)
$\mathbf{E^i}$	Incident electric field ($V\ m^{-1}$)
$\mathbf{E^b}$	Backscattered electric field ($V\ m^{-1}$)

F_A	Aerodynamic force (N)
f_{xi}	Body force exerted by one debris element (N)
F_{xi}	Body force per unit mass (m s^{-2})
f_v	Fractional volume
g	Gravitational acceleration (m s^{-2})
$\mathbf{G}$	Rotation matrix
$\hat{h_i}$	Horizontal polarization vector
Δh_i	Height between elevation angles (m)
h_{cvg}	Height of the convergence region (m)
h_{cvt}	Height of the convection region (m)
h_{max}	Maximum TDS height (m)
$\hat{i}$	Vector oriented in the direction of incident EM wave
$\hat{l}$	Left-hand circular polarization vector
I	Fixing integrity parameter
I_v	Intensification parameter
l	Debris length (m)
L	LES filter length (m)
l_{inf}	Inflow region length (m)
k	Wavenumber (m^{-1})
K_m	Complex dielectric factor
L_{DR}	Linear depolarization ratio (dB)
m	Complex refractive index

$\overline{m_d}$	Mean debris mass (kg)
N	Number of scatterers
N_s	Number of soil particles greater than radius, r_s
N_{flux}	Vertical flux of debris ($\#m^{-2}s^{-1}$)
$q_{0.1}\{\rho_{HV}\}$	10th percentile co-polar cross-correlation coefficient
$q_{0.1}\{Z_{DR}\}$	10th percentile differential reflectivity (dB)
$q_{0.9}\{Z_{HH}\}$	90th percentile radar reflectivity factor (dBZ)
p	Pressure (Pa)
p_o	Ambient pressure (Pa)
r	Radius (m)
r_s	Soil particle radius (m)
r_{cvt}	Convection region radius (m)
r_{up}	Radius between the convergence and convection regions (m)
r_{top}	Top outlet radius (m)
$\hat{r}$	Right-hand circular polarization vector
Re	Reynolds number
Re_p	Particle Reynolds number
S	Scaling factor
$\mathbf{S}$	Scattering matrix
$\mathbf{S_c}$	Scattering matrix for circular polarization
S_c	Corner flow swirl ratio
S_i	Incident power density (W m^{-2})

S_r	Returned power density (W m^{-2})
t	Plate thickness (m)
$T1$	First set of TDS thresholds
$T2$	Second set of TDS thresholds
Ta	Tachikawa Parameter
U	Wind speed (m s^{-1})
u_i	Wind speed in tensor notation (m s^{-1})
u_{min}	Minimum radial velocity (m s^{-1})
u_{di}	Debris speed in tensor notation (m s^{-1})
u_d	Radial debris velocity (m s^{-1})
u_p	Radial particle velocity (m s^{-1})
U_o	Ambient wind speed (m s^{-1})
U_r	Relative wind speed between object and the air (m s^{-1})
v_c	Core tangential velocity (m s^{-1})
v_d	Tangential debris velocity (m s^{-1})
V_{grid}	Grid cell volume (m^3)
V_{ij}	Complex received signal voltage (V)
V_0	Characteristic velocity (m s^{-1})
v_{max}	Maximum tangential velocity (m s^{-1})
v_r	Radial velocity (m s^{-1})
V_{TDS}	TDS volume (m^3)
w	Vertical velocity (m s^{-1})

w_d	Vertical debris velocity (m s^{-1})
w_{min}	Minimum vertical velocity (m s^{-1})
w_{max}	Maximum vertical velocity (m s^{-1})
w_p	Tangential particle velocity (m s^{-1})
Z_{DR}	Differential reflectivity (dB)
$\hat{Z}_{DR}$	Differential reflectivity threshold (dB)
Z_{HH}	Horizontal radar reflectivity factor (dBZ)
Z_{VV}	Vertical radar reflectivity factor (dBZ)
Z_E	Equivalent radar reflectivity factor (dBZ)
$\hat{Z}_{HH}$	Radar reflectivity threshold (dBZ)
z_L	Lower midpoint (m)
z_{top}	Top of the inflow layer (m)
z_U	Upper midpoint (m)
β	Canting angle of a spheroid in the polarization plane (°)
δ_{dp}	Backscatter differential phase (°)
ϵ_e	Effective complex relative permittivity
ϵ_r	Complex relative permittivity
γ	Depleted angular momentum (m^2 s^{-1})
Γ	Angular momentum (m^2 s^{-1})
Γ_∞	Far-field angular momentum (m^2 s^{-1})
λ	Wavelength (m)
μ	Air viscosity (Pa s)

ν	Kinematic viscosity (m^2 s^{-1})
ϕ	Angle between the incident EM wave and spheroid's symmetry axis (°)
Φ_{dp}	Propagation differential phase (°)
ρ	Air density (kg m^{-3})
ρ_{HV}	Co-polar cross-correlation coefficient
$\hat{\rho}_{HV}$	Co-polar cross-correlation coefficient threshold
σ	Radar cross-section (m^2)
σ_a	Absorption cross-section (m^2)
σ_b	Backscatter cross-section (m^2)
σ_D	Proturbence of a sphere (m)
θ	Debris attack angle (°)

Index